Von der Fakultät für
Bauingenieurwesen und Geodäsie der
Gottfried Wilhelm Leibniz Universität Hannover
zur Erlangung des Grades
Doktor-Ingenieur genehmigte Dissertation

Inverse Load Calculation for Offshore Wind Turbines

vorgelegt von:
Dipl.-Ing. Thomas Pahn

Tag der mündlichen Prüfung:
21. Oktober 2013

Hauptreferent:
Prof. Dr.-Ing. habil. Raimund Rolfes,
Leibniz Universität Hannover, Deutschland

Korreferent:
Prof. Dr.-Ing. Andreas Reuter,
Leibniz Universität Hannover, Deutschland

Gutachter:
Ph.D. Jason Jonkman,
National Renewable Energy Laboratory,
Golden CO, USA

ISD
INSTITUT FÜR STATIK
UND DYNAMIK

Herausgeber:
Prof. Dr.-Ing. habil. R. Rolfes

Institut für Statik und Dynamik
Leibniz Universität Hannover

Appelstraße 9A
30167 Hannover

Tel: 0511 - 762 3867
Fax: 0511 - 762 2236

www.isd.uni-hannover.de
info@isd.uni-hannover.de

ISSN 1862-4650

Abstract

Knowing the loads that occur at wind turbines during operation allows for the verification of the assumptions made in the design process or for making lifetime predictions. Both of these goals require realistic load values. Such load values can be determined by applying an inverse load calculation procedure that uses measured structural responses. In the case of offshore wind turbines, the inverse load calculation is a complex dynamical problem in which coupled aerodynamics, elasticity, hydrodynamics, and the wind turbine control have to be considered. Although the inverse load calculation at wind turbines is a research field of increasing interest, a comprehensive overview of this method's potential and its resulting accuracy is still missing.

This work presents an investigation of the inverse load calculation at wind turbines. Single steps of increasing complexity are chosen in order to discuss the influence of the ill-conditioning on the inverse calculation procedure, the dynamic coupling effects, effects due to the wind turbine control, and the occurrence of combined wind and wave loads. A frequency-domain based inverse calculation procedure is used – the Deconvolution in the Frequency Domain. The comprehensive simulation code FAST is used for verification purposes. Conclusions are derived from simulations with 5 MW wind turbine models, in which the inversely calculated loads are compared to the applied loads. The ensuing verifications show that the inverse load calculation procedure produces promising results.

In addition, the application of the inverse load calculation procedure to a real-world 5 MW onshore wind turbine is presented. Special focus lies on determining a realistic system description of the structure. With the Frequency Domain Decomposition, a frequency-domain based output-only system identification method is used. Eigenfrequencies, mode shapes, and damping ratios – including aerodynamic effects – are determined for standstill and several operation states. Using the inversely calculated load, structural strains are calculated that are compared to measured strains. This verification shows the capability of the inverse load calculation for producing very good results when applied to a real-world structure.

Keywords: Inverse load calculation, load measurement, Deconvolution in the Frequency Domain, FAST, system identification, Frequency Domain Decomposition, aerodynamic damping, lifetime prediction

Kurzfassung

Die Kenntnis der im Betrieb von Windenergieanlagen auftretenden Belastungen ermöglicht die Überprüfung der Annahmen aus dem Entwurfsprozess oder die Erstellung einer Lebensdauerprognose. Die auftretenden Belastungen können mittels einer inversen Lastermittlung auf der Basis gemessener Strukturantworten berechnet werden. Die inverse Lastermittlung bei Offshore-Windenergieanlagen ist ein komplexes dynamisches Problem, in dem aerodynamische, strukturelastische und hydrodynamische Kopplungseffekte sowie die Steuerung der Windenergieanlage berücksichtigt werden müssen. Obwohl die inverse Lastermittlung für Windenergieanlagen ein Forschungsfeld von steigendem Interesse ist, existieren bisher wenig Aussagen über das Potential und die Genauigkeit dieser Methode.

Die vorliegende Arbeit befasst sich mit der inversen Lastermittlung für Windenergieanlagen. Die Lastermittlung wird an Modellen durchgeführt, deren Komplexität sukzessive gesteigert wird. Anhand dieses Vorgehens werden die Einflüsse aus der schlechte Kondition des inversen Problems, den dynamischen Kopplungseffekten, der Anlagensteuerung der Windenergieanlage sowie das Auftreten kombinierter Wind- und Wellenlasten diskutiert. Eine Frequenzraummethode – Deconvolution in the Frequency Domain – wird bei der inverse Berechnung verwendet. Mittels der Software FAST, die eine ganzheitliche Berechnung von Windenergieanlagen erlaubt, wird die Verifikation der inversen Berechnung vorgenommen. Anhand der Simulationen von 5 MW Windenergieanlagen werden invers berechnete Belastungen ermittelt, die mit den in der Simulation definierten Lasten verglichen werden. Die durchgeführten Verifikationen zeigen, dass die inverse Lastermittlung in der Lage ist, sehr gute Ergebnisse zu erzielen.

Zudem wird die Anwendung der inversen Lastermittlung auf eine reale 5 MW Onshore-Windenergieanlage vorgestellt. Der Schwerpunkt liegt auf der Erstellung einer wirklichkeitsnahen Systembeschreibung. Verwendet wird dazu eine frequenzraumbasierte output-only Methode zur Systemidentifikation – die Frequency Domain Decomposition. Die Eigenfrequenzen, Eigenvektoren und die Dämpfungswerte – inklusive aerodynamischer Effekte – werden im Stillstand und für verschiedene Betriebsbedingungen der Anlage ermittelt. Unter Verwendung der inversen Belastungen werden Strukturdehnungen berechnet und mit Dehnungsmessungen verglichen. Die guten Ergebnisse dieses Vergleichs zeigen das Potential der inversen Lastermittlung, realistische Strukturdehnungen zu berechnen.

Schlagwörter: Inverse Lastermittlung, Deconvolution in the Frequency Domain, FAST, Systemidentifikation, Frequency Domain Decomposition, Aerodynamische Dämpfung, Restlebensdaueranalyse

Acknowledgment

This dissertation is not only a scientific work; it represents a complete period of my life. I am deeply gratful that my beloved wife Simone always was a fundamental part of this life and that you are still with me. I also want to express my appreciation to my parents and my brother Matthias. Thank you all for being such a helping and supporting family.

I also want to express my gratitude to Prof. Raimund Rolfes, Head of the Institute of Structural Analysis at the Leibniz Universität in Hannover. Thanks for giving me the opportunity to realize this work. The major part of this work is a product of my scientific work at your Institute. In retrospect, it was an outstanding time in which I learned much more than the content I wrote down in this work.

Thanks to Prof. Andreas Reuter that you assume the responsibility for being the second examiner of my dissertation.

In 2011, I have had the great pleasure to be a guest at the National Renewable Energy Laboratory (NREL) in Boulder, Colorado. Thanks to Ph.D. Jason Jonkman that you gave me the possibility to temporarily become a member of your team and for your outstanding technical support. I extraordinarily enjoyed the stay in Boulder, not only because of the scientific work but also due to the fantastic people and the awesome countryside. Thanks also to the DAAD that funded my stay with a scholarship.

A general thank is due to all my collegues – both at ISD in Hannover and at NREL in the USA. The coffee and cake breaks with Matze were essential for keeping perseverance. Thanks also to Gerald and Moritz and to my roommates Anne and Martin for all the time and discussions and for the help. Thanks to Amy and Beckie and especially to Dana and Aaron for the tremendous soccer matches at Carroll Butts. Furthermore, I want to mention all the OGOWin-researcher. The scientific and personel collaboration was an invalueable experience.

A special thank goes to my sister-in-law Emmi Luisa for proofreading my dissertation. I am sure that this was hard work. And finally some words to Stefan and Andi: I appreciate that.

Thomas Pahn – Cottbus, im November 2013.

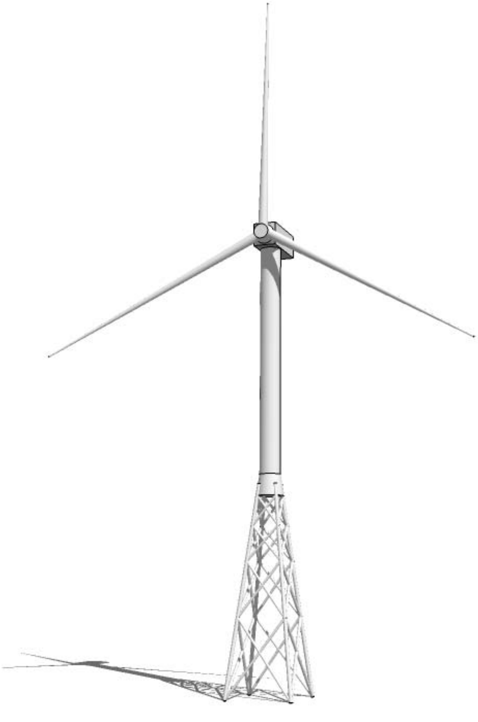

Except the Lord build the house,
they labour in vain that build it.

Psalms 127, 1

Content

List of figures

List of tables

Nomenclature

Abbreviations

BEM	blade element momentum
CM	center of mass
DFD	Deconvolution in the Frequency Domain
DLC	design load case
DOF	degree of freedom
DP	Dynamic Programming
EoM	equation of motion
FAST	Fatigue, Aerodynamics, Structures, and Turbulence – software code for three-bladed horizontal-axis wind turbines
FDD	Frequency Domain Decomposition
FE	finite element
FFT	Fast Fourier Transform
FRF	frequency response function
GDW	generalized dynamic wake
HAWT	horizontal-axis wind turbine
HSS	high-speed shaft
ISF	Inverse Structural Filter
LC	load case
LMI	linear matrix inequality
MDOF	multi-degree of freedom
MLC	measurement load case
NREL	National Renewable Energy Laboratory, Golden, USA
ODE	ordinary differential equation
PM	Pierson-Moskowitz
PMM	Partial Modal Matrix
PSD	power spectral density

RNA	rotor-nacelle assembly
SDOF	single-degree of freedom
SNR	signal-to-noise ratio
SVD	singular value decomposition
SWL	still water level
UIO	Unknown Input Observer
w.r.t.	with respect to

Variables

D	damping ratio as percentage of critical damping
D_i	modal damping ratio of the i-th mode of vibration
E_S	soil layer stiffness modulus
F_{ik}^{Hydro}	total hydrodynamic load at node k, i-th force component
F_{ik}^{prtHyd}	portion of the hydrodynamic load at node k that does not depend on acceleration, i-th force component
$F^R(t)$	resulting wave load
H	wave height
H_S	significant wave height
L	wave length
N	number of samples in the signal
T	period / wave period
T_P	peak spectral period
$S_{JS}(f)$	spectral density function of the JONSWAP spectrum
TwrFlex	flexible height of the tower
TwrNodes	number of tower nodes
V_r	noise ratio
WaveNodes	approximation of the node number that is loaded with hydrodynamic forces
a	water particle acceleration, normal to the structure
c_S	thrust coefficient

d	diameter
dz	element length
f	frequency
f_{max}	length of a signal in frequency domain
f_S	resolution of a signal in frequency domain
f_{Sample}	sampling frequency
$f(\,)$	non-linear forcing function
f_{0i}	eigenfrequency of the i-th mode of vibration in Hz
h	water depth
h_k	node coordinate along the height of the structure
$h^R(t)$	points of application of the resulting wave load
$\overline{h}^R$	sensor location for the resulting wave load
t_{max}	length of a time signal
t_S	resolution of a time signal
v	water particle velocity, normal to the structure
v_{Hub}	mean wind speed at hub height
Ω	MAC value
α	angle of attack, angle between the vector of the wind forces and the vector of the reacting forces in the rotor plane
γ	peak-shape parameter of the JONSWAP spectrum
δ	decay constant
ε	error in time
ε_{aero}	error in time for the aerodynamic (wind) load
ε_{hydro}	error in time for the hydrodynamic (wave) load
ϑ	logarithmic decrement
λ	tip speed ratio
ρ	water density
σ	scaling factor for the JONSWAP spectrum
$\hat{\phi}$	mode shape estimate

ω	frequency in s^{-1}
ω_{0i}	eigenfrequency of the i-th mode of vibration in s^{-1}

Vectors and matrices

$\mathbf{a}$	vector of accelerations
$\mathbf{s}_{ij}$	singular value of the PSD
$\mathbf{u}_{ij}$	singular vector of the PSD

A_{ijk}	hydrodynamic added-mass matrix at node k, i-th force component and j-th acceleration component
$\mathbf{F}^{Hydro}$	matrix of hydrodynamic forces
$\mathbf{G}_{\mathbf{xx}}(j\omega)$	PSD matrix of the inputs
$\mathbf{G}_{\mathbf{yy}}(j\omega)$	PSD matrix of the responses
$\mathbf{F}_{inv}$, $F_{inv,aero}$	inversely calculated aerodynamic load (wind load)
$F_{inv,hydro}$	inversely calculated hydrodynamic load (wave load)
$\mathbf{F}_{xN}$	estimation for the rotor thrust force based on Betz law
FTHydro	matrix of the applied hydrodynamic forces in FAST
$\mathbf{S}$	singular value matrix of the SVD
$\mathbf{U}$	singular vector matrix of the SVD

First-order state space system

$\mathbf{f}$	input/force vector (m, 1)
$\mathbf{q}$	vector of displacements
$\dot{\mathbf{q}}$	vector of velocities
$\ddot{\mathbf{q}}$	vector of accelerations
$\mathbf{u}$	vector of control inputs
$\mathbf{u}_d$	vector of wind input disturbances
$\mathbf{x}$	state vector (n, 1)
$\mathbf{y}$	output/response vector (l, 1)

$\mathbf{A}$	state matrix (n, n)
$\mathbf{B}$	input matrix (n, m)

$\mathbf{C}$	output matrix (l, n)
$\mathbf{D}$	feedthrough matrix (l, m)

Second-order ordinary differential equation

$\mathbf{a}$	acceleration vector (n, 1)
b_{Ei}	entry of the generalized diagonal damping matrix
$\mathbf{f}$	force vector (n, 1)
k_{gi}	entry of the generalized stiffness matrix
m_{gi}	entry of the generalized mass matrix
$\mathbf{p}$	vector of the applied load
$\mathbf{u}_{0i}$	eigenvector of the i-th mode of vibration (n, 1)
$\mathbf{y}$	displacement vector (n, 1)
ϕ_i	eigenvector of the i-th mode of vibration, scaled to $m_{gi} = 1$ (n, 1)
λ_{0i}	eigenvalue of the i-th mode of vibration

$\mathbf{B}_E$	generalized diagonal damping matrix (n, n)
$\mathbf{B}_g$	generalized damping matrix (n, n)
$\mathbf{D}$	damping matrix (n, n)
$\mathbf{F}(j\omega)$	force vector (n, 1)
$\mathbf{F}_g(j\omega)$	modal force vector (n, 1)
$\mathbf{H}(j\omega)$	frequency response function FRF matrix (n, n)
$\mathbf{K}$	stiffness matrix (n, n)
$\mathbf{K}_g$	generalized stiffness matrix (n, n)
$\mathbf{K}^{red}$	reduced stiffness matrix
$\mathbf{M}$	mass matrix (n, n)
$\mathbf{M}_g$	generalized mass matrix (n, n)
$\mathbf{M}^{red}$	reduced mass matrix
$\mathbf{Q}(j\omega)$	modal displacement vector (n, 1)
$\mathbf{Q}_i(j\omega)$	modal displacement vector of the i-th mode of vibration (n, 1)
$\mathbf{U}_0$	modal matrix (n, n)
$\mathbf{Y}(j\omega)$	Fourier transform of the displacement vector (n, 1)

$\ddot{Y}(j\omega)$	Fourier transform of the acceleration vector (n, 1)
$\mathbf{\Phi}$	generalized modal matrix, scaled to $m_{gi} = 1$ (n, n)
Λ_0	spectral matrix, containing the eigenvalues of a system (n, n)

Glossary

Cut-in wind speed	minimum wind speed at which a wind turbine will generate usable power
Rated wind speed	minimum wind speed at which a wind turbine will generate its designated rated power
Cut-out wind speed	maximum wind speed at which a wind turbine will generate power
Fore-aft	in direction of the rotor axis
Side-side	horizontally sideways, orthogonal to the rotor axis

Basic units and dimensions

Acceleration	m/s^2
Displacement	m
Force	N, kN
Frequency	Hz, s^{-1}
Length	mm, m
Power	MW, kW
Time	s, min
Velocity	m/s

1 Introduction

1.1 Motivation

Renewable energies are becoming increasingly important to ensure a steady supply of energy. The Renewable Energy Directive, adopted by the European Parliament in 2009, sets binding targets. By 2020, 20 % of the overall energy mix in the EU is intended to be produced from renewable energy. For example, Germany, being part of the EU, decided to phase out nuclear power completely by the end of 2022, at the latest. The occurring gap in the power supply shall be covered by renewable energies. In 2011 Germany already reached the target to produce 20 % of its electrical power supply by renewable energies. And further growth is expected. As stated in the German government's energy concept in 2010[1], Germany seeks to increase the contribution of renewable energies to 60 % by 2050. Aside from the European countries, other important industrial nations also mark ambitious goals. The US aims to get 80 % of America's electricity from clean energy sources. China plans to change its coal-dependent energy concept and seeks to generate at least 15 % of its energy capacity from wind, solar and other renewable energy sources by 2015.

One form of renewable energy is wind energy. Wind energy plays an essential role for achieving the goals defined by several governments. The EWEA gives a closer look into the development of wind energy in the EU[2] in its 2007 report. In the last 20 years, wind energy has shown a dramatic growth, with an annual averaged increase of 25 %. About 30 % of all new power capacity between 2000 and 2007 came from wind energy. Thus, in 2007 wind energy reached a 7 % share of the total energy capacity in the EU.

The growth in wind energy continues. Costs, efficiency in power production and reliability of wind turbines still need to be enhanced. Key questions[3] to be solved or developed are:

- The development of appropriate materials
- Enhanced understanding of aerodynamics and wind physics
- Grid integration
- Production, logistics and maintenance, especially for offshore wind turbines
- Innovative concepts for nacelles, optimization of drive trains
- Improvement of rotor blades according to aerodynamics, acoustics and structural weight
- New support structure and foundation concepts both for onshore and offshore wind turbines

---

[1] Source: Federal Ministry for the Environment, Nature Conservation and Nuclear Safety [20].

[2] Source: European Wind Energy Association [17].

[3] See report of Deutsches Bundesministerium für Wirtschaft und Technologie [12], section 4.1.

Today, research must generate a quantifiable outcome.[4] To compete with conventional energy sources, wind energy concepts need to stay innovative and to become even more cost efficient. Usually, wind turbines are gathered in wind parks consisting of up to hundreds of turbines. Similar support structures are manufactured in series. Support structures form a significant proportion of the development costs for wind parks, which is true both for onshore and offshore wind turbines. Consequently, the optimization of support structures may enormously enhance economic efficiency.

Wind turbine support structures have to withstand high dynamic forces. Excitations come from wind forces, gravity and inertia forces, and hydrodynamic forces. In addition, coupling effects between wind inflow, aerodynamics, hydrodynamics, elasticity and turbine control need to be taken into account. Comprehensive simulation software is successfully used for the design of support structures. Nevertheless, the force-to-structure interaction with its coupling effects is complex. For this reason, the testing and the monitoring of support structures is necessary. This imperative is underlined by the IEC Standard 61400-13 [109], which describes the measurement of mechanical loads at wind turbine generator systems. The standard states: "*In the design stage loads can be predicted with aeroelastic models and codes. However, such models have their shortcomings and uncertainties, and they need to be validated by measurement.*" The Germanischer Lloyd – one of the most important certifying institutions for wind turbines in Germany – also points out a demand for on-site checking of design assumptions:[5] It is a matter of fact that real occurring loads can differ drastically from those simulated, depending on the specific site of the wind turbine. This fact is valid both in the design stage and in remaining lifetime predictions.[6] Furthermore, one of the leading German research institutes in wind energy – the Fraunhofer IWES – also emphasizes that the knowledge of realistic wind and wave loads is essential for the further development of wind turbines.[7]

For the purpose of detecting realistic load values of structures or systems that are dynamically loaded, a so-called inverse load calculation can be used. This inverse process uses measured dynamical responses of the structure, e.g. accelerations, to calculate the acting loads. A mechanical description of the structure is needed. On the basis of measured dynamical system properties such as eigenfrequencies, eigenvectors, and damping ratios, the frequency response function (FRF) matrix can be generated. The FRF matrix fully describes the realistic dynamic behavior of the structure. Consequently, the measured responses combined with the realistic description of the structure lead to realistic load values that can serve for a verification of the assumptions from the design process and can be used for remaining lifetime predictions.

---

[4] See Reuter (2013) [87].

[5] See Faber (2008) [19].

[6] Translated from German.

[7] See Reuter and Busmann (2010) [86].

1.2 Load Measurement on Wind Turbines – State of the Technology

1.2.1 Survey through existing Design Codes, Standards and Guidelines

There exist a couple of design codes, standards, and guidelines for onshore and offshore wind turbines. They primarily focus on standardizing the appropriate requirements needed for the design of wind turbines. But most of them also give recommendations for measurements. This fact underlines the importance of measurements. The proposed measurements serve for different purposes. A review shall give an overview about the proposed practice for load measurements at wind turbine support structures. To clarify the denomination of the several structural sections of wind turbines, Figure 1.1 shows the definition from the GL guideline (2004) [106] that serve as the basis for all denominations in this work.

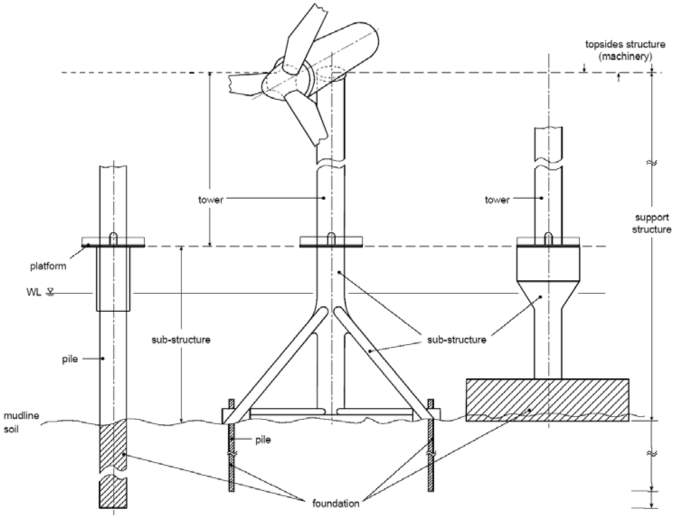

Figure 1.1: Definition of offshore wind turbine sections (from GL guideline (2004) [106])

<u>The German standard VDI 3834 (2009)</u> [110] aims to evaluate mechanical vibrations at onshore wind turbines and their components. The components taken into account are the nacelle-tower system, the rotor bearing with the roller bearings, the gearbox, and the generator. Neither applied loads nor structural loads are measured. The VDI 3834 concludes that the vibration level highly influences the stresses of all components and thus the operational reliability and the service live. For this reason, evaluation criteria are given on the basis of vibration velocities and vibration accelerations.

<u>The German BSH standard (2007)</u> [103], published by the Federal Maritime and Hydrographic Agency, states that offshore wind turbines have to be equipped with monitoring

systems. Looking at the support structures in particular, monitoring systems on at least 1/10 of the wind turbines are required. Appropriate equipment or procedures are not defined. Thus, the BSH standard does not focus on load measurement in particular. But the demand for measurements and monitoring is clearly pointed out.

The Norwegian design code DNV-OS-J101 (2004) [105] is valid for onshore wind turbines. The design code describes wind turbine loads during power production and states that selected transient events should be verified by load measurements. These measurements are recommended in the intended operational range of the wind turbine, i.e. wind speeds between cut-in and cut-out. Detailed instructions for these verification measurements are missing. However, the DNV standard recommends that measurements shall be carried out by accredited testing laboratories.

The IEC 61400-1 (2005) [107] sets design requirements for onshore wind turbines. Load measurements are required for the ultimate strength analysis. The use of the partial safety factors for loads for normal and abnormal design situations requires that the load calculation model is validated by load measurements. These measurements shall be made on a wind turbine that is similar to the wind turbine design under consideration of aerodynamics, control, and the dynamic response. In addition, measurements may be used for a determination of lower partial safety factors for loads. In that case, the magnitudes of loads have to be established by measurements or by analysis confirmed by measurements to a higher than normal degree of confidence.

The IEC 61400-3 (2009) [108] is the design code for offshore wind turbines in the IEC series. Special recommendations to load measurements are absent. But oftentimes references to the onshore design code IEC 61400-1 are given. The requirements on load measurements in part 1 are similar to part 3, except the demand for using a validated load calculation model.

The DIBt Richtlinie (2004) [104] addresses onshore wind turbines with tubular towers and their foundations. The guideline mentions the option to control the assumptions for the fatigue analysis with the use of measurements. If the fatigue analysis is based on stress collectives, the stress collectives have to be simulated at the crucial cross-sections. These simulations can be verified by measurements. The measurements shall be carried out in accordance with the IEC 61400-13 (2001) [109].

The GL guideline (2004) [106] is published by the Germanischer Lloyd and contains design requirements for the certification of offshore wind turbines. An entire chapter is dedicated to the testing of offshore wind turbines. Amongst others, load measurements are recommended. The load measurements shall be carried out in accordance with the IEC 61400-13.

1.2.2 Load Measurement according to IEC 61400-13

The survey of various design codes, standards, and guidelines clarifies the demand for load measurements at wind turbines and at wind turbine support structures in particular. The information gained via measurements is principally used to verify the assumptions made in the design calculations. Such verification is needed in a broad range of operational conditions, summarized in specific load cases. In addition, it is used for monitoring purposes. In general, the design codes, standards, and guidelines do not explain in detail the process of load measurement. But most of them refer to the IEC 61400-13, so that a closer look at its specifications seems adequate.

The IEC 61400-13 (2001) [109] gives detailed description for the measurement of mechanical loads on wind turbines. This is motivated by the fact that load measurements can serve as a basis for the design and the certification or for the verification of simulation codes. For these purposes, measurements of different steady-state operations (e.g. power production, power production with occurrence of fault, parked/idling) and different transient effects (e.g. start-up, normal shutdown, emergency shutdown) are required. Recommendations with respect to the measurement techniques are also given. For large wind turbines, it will rarely be possible to place a load cell in a main load path. But, loads can be measured indirectly. The recommended types of sensors are:

- Strain gauge bridges
- Load cells / torque tubes (including piezoelectric cells)
- Accelerometers, velocity, rotation and displacement transducers

Recent research e.g. VERBRUGGEN (2009) [100] or OGOWin (2011) [74] show fiber optical sensors as an adequate alternative to strain gauges.

The IEC 61400-13 (2001) proposes two alternatives for the measurement of mechanical loads. The IEC Standard does not deal with specific denotations. In order to distinguish between both alternatives, it will subsequently be referred to as "Direct determination of structural loading" and "Inverse calculation of applied loading".

The direct determination of structural loading is the method that is recommended by the IEC. The main advantage of this method is its easy application. Furthermore, the method allows an easy-to-handle, straight-forward determination of the loads. Strain gauge bridges are used as sensors and are applied to crucial structural components / cross-sections. At minimum, the measurement of at least one blade-root load (flapwise and edgewise), rotor loads (tilt and yaw moment, torque), and tower loads (bottom bending in two directions) shall be carried out.

Based on the mechanical principles of the linear statics of shells, the measured strains are used to calculate structural loadings (also referred to as internal loadings) at the particular cross-sections. Due to the characteristics of strain gauges, temperature effects and cross-sensitivity[8] have to be taken into account. The use of full strain gauge bridges offers good scope for reducing both effects. In addition, further drawbacks have to be taken into consideration.

---

[8] Cross-sensitivity is the undesirable characteristic of a measurement system of being sensitive to different load sources, making it difficult or impossible for the system to differentiate between them.

- The load measurement is limited to the cross-sections equipped with sensors. No information at intermediate cross-sections is available.
- The strain gauge output is related to an applied load level. This relationship is achieved by a static calibration of the sensors. The dynamic behavior of the structure causes an amplification of measured strains so that the strain gauge can indicate gross internal loads rather then externally applied loads. Thus, information about externally applied loads cannot be gained.
- The sensor positions have to be chosen so that sufficient strains per unit load levels exist.
- Sensor positions have to be selected that provide linear stress-to-load relationships, for which reason load introduction paths should be avoided. Load introduction paths may occur at tower flanges as demonstrated in SEIDEL (2001) [93].
- Sensors need to be placed in regions of uniform stresses, i.e. regions not subjected to high stress or strain gradients. Places with localized stress raisers or concentrations should be avoided.

The second method mentioned by the IEC 61400-13 is the inverse calculation of applied loading. This method is more complex than the direct determination of structural loading. Accelerometers and displacement transducers can be used to measure applied load indirectly, relying on the knowledge of inertia or stiffness of the structure. This method is difficult. It requires very accurate descriptions of the structural mass and stiffness. Otherwise it is prone to significant errors.

If the mentioned drawbacks can be satisfactorily solved, this method offers the following advantages.

- The method gives applied loads rather than internal forces which results in an easier verification of simulation codes, because applied loads can be compared directly. The knowledge of applied loads allows the calculation of internal loadings at arbitrary cross-sections. An appropriate model of the structure is needed.
- The inverse calculation offers the possibility of measuring complex configurations of applied loads, e.g. from combined wind and wave loads.
- A different set of sensor types and sensor locations is used that promises to be more robust and reliable under rough offshore conditions. Due to the fact that mostly accelerometers are used and strain measurement is only necessary at one cross-section, an application in regions of load introduction paths or regions of non-uniform stresses can easily be avoided.

A comparison of both methods shows the direct determination of structural loading to be a user-friendly approach that is convenient in its practical application and its corresponding calculation procedures. But this leads to some limitation, e.g. the limitation to few cross-sections. On the other hand, the inverse calculation is a much more complex approach that requires accurate calculation inputs, such as the structural inertia and mass distribution.

This comparatively greater effort allows a more complex appraisal of the load situation. As will be pointed out in the following section 1.2.3, there is a demand for more detailed research to assure that the inverse load calculation is capable to gain reliable and accurate results. In particular, this fact counts for the dynamic interaction between loads and structures of wind turbines as well as for complex load situations due to combined wind and wave loads.

1.2.3 Load Measurement at Wind Turbine Support Structures

Both methods, the direct determination of structural loadings and the inverse calculation, are used in practice. Camp et al. (2002) [13] gives an illustrating example of the application of the direct determination method using strain gauges. Load measurements at a 2 MW offshore wind turbine with tubular steel tower and monopile foundation are described. The wind turbine is located in the wind park Blyth in the North Sea, in north-eastern England, with a mean water depth of approximately 9 m. The measurements are carried out in the project OWTS project (Offshore Wind Turbines at Exposed Sites). A large array of strain gauges is applied to every major structural element in order to detect structural loadings. The sensors are used to measure structural loads at the tower pile and the foundation. Strains at eight levels over the tower height are recorded to calculate bending moments in two directions and torsional moments. Cross-sections of interest are tower top, tower base, under sea level, and under mudline. In addition, blade root bending moments as well as torque and bending moment at the low-speed shaft are determined. Although it is not mentioned explicitly, the measurements are in accordance with the specifications for the direct determination of structural loadings, given in the IEC 61400-13. Hence, applied loadings are not determined. The measured structural loadings are used to get information about wind and wave loading.

Engineers try to reduce instrumentation effort without losing information. Thus, alternative methods, other than the direct determination of structural loadings are investigated. Lange (2010) [60] proposes a condition monitoring system with two objectives. A structural condition monitoring system is developed to detect damages at the support structure that may occur during operation. The monitoring system is based on strain and acceleration measurements. The second objective is the development of a lifetime condition monitoring system that monitors the fatigue condition during operation to predict the remaining lifetime of the structure. An approach that uses measured pitch angles, rotor speed, and generated power is described. Based on theses operational parameters, a rotor thrust force is calculated using the equation of motion. The λ-c_s-matrix is required for this calculation. Internal forces are determined using an aeroelastic simulation with the rotor thrust as externally applied load. The resulting time series are used for fatigue analysis. However, the λ-c_s-matrix is the relationship between the tip-speed ratio and the thrust coefficient of the rotor blades. This relationship is hardly known for a specific wind turbine. As an alternative, recommendations taken from literature sources might be used that neither assure a realistic representation of the aerodynamic conditions.

Cosack (2010) [15] introduces an approach for fatigue load estimation. The measured inputs for this approach are standard wind turbine signals, such as generator rotational speed, generator rotational acceleration, electrical power output, and pitch angles. A neural network is used to estimate loads. The neural network represents the transfer function between the measured inputs and the estimated loads. Because the neural network does not contain physical information about the structure, this approach is a so-called black-box-model. Consequently, the neural-network-approach is an alternative to the inverse load calculation, where structural information is used to set up the model (white-box-model). The neural-network-approach does not give applied loads, but directely estimates equivalent loads and load magnitudes.

Rebelo et al. (2008) [84] describes the concept for the long-term monitoring of an eighty-meter high onshore wind turbine steel tower. Strain gauges and accelerometers are applied at four cross-sections over the height of the structure. The concept aims to identify modal parameters. Using this information, applied loads from wind shall be calculated by solving the inverse problem. The current state of the work does not comprise any specific results regarding the load calculation. Thus, it still is part of ongoing research.

The final report of the IMO-Wind project (2010)[9] [41] outlines a further application that requires knowledge about the loading at wind turbine support structures. An automatic, real-time monitoring system for wind turbines is set up. This system aims at design verification and monitoring of the wind turbine support structure during operation. Results are demonstrated for a 5 MW wind turbine with an offshore tripod support structure, which is erected onshore as a prototype. The structural reliability and robustness is assessed using probabilistic approaches. This analysis is based on a dynamic simulation of the support structure in combination with a stochastic finite-element-analysis. This promising approach relies on the knowledge of realistic load values. Here, the use of internal forces at the tower top and external applied loads from the wind distribution over the tower height is shown. The tower-top forces are derived from strain gauge measurements – a cross-section that is prone to be influenced by load introduction paths. The calculation is based on the principles of linear shell statics. A procedure to determine loads under combined wind and wave excitation is absent.

Obviously, there is an interest and a demand for research that determines applied loads for wind turbines from measurements. For this purpose, the inverse load calculation represents an adequate approach. An investigation of inverse load calculations already has been done in the 1980's. Stevens (1987) [96] summarizes applications of a frequency-based method in various fields, such as the automotive industry, in aeronautics, or at dynamically operating machineries. Applications to wind energy just can be found in recent years.

Swartz et al. (2010) [97] reports an automated wind load characterization of wind turbine structures. The study's focus lies on the use of wireless sensors (accelerometers) to measure the structural dynamics. The vibration signals are post-processed automatically in order to identify the dynamical behavior of the support structure (eigenfrequencies, eigenvectors,

---

[9] See section 6 of the final report of the IMO-Wind project (2010) [41].

damping ratios). The wind loads are calculated inversely with these dynamic characteristics. In particular, a rotor thrust force and a lateral force from the gyroscopic effects that result from the rotor rotation is determined. A time-domain approach is chosen for the inverse calculation. At the current stage of the research, tests at a laboratory structure – a pile with head mass that represents an onshore wind turbine – are conducted. A stochastic load is applied to the head mass. In order to verify this approach, a comparison between the applied load at the head mass and the inversely calculated load is given. The accuracy of the calculation depends on the number of measured system properties, like e.g. eigenfrequencies. This research shows promising results. But the step to a real wind turbine structure or a consideration of combined wind and wave loads has not been yet investigated.

Thus far, the most advanced research regarding the inverse load calculation at offshore wind turbine support structures was done by Klinkov and Fritzen. The main goal of the work is a real-time load calculation by use of a robust observer, as described in KLINKOV AND FRITZEN (2007) [55]. The observer is a time-domain based set of matrices found with the help of the linear matrix inequality technique. The dynamic properties of the structure are described in a state-space-system. The dimension of the system relies on the number of measured system properties, such as eigenfrequencies. The objective of the inverse calculation is the determination of a rotor thrust force. Accelerometers and strain gauges are used as sensors. A series of laboratory tests is used to verify the inverse calculation procedure. The test arrangement is increased stepwise from simple to more complex structures and loadings. In KLINKOV AND FRITZEN (2006) [54], a test at a simply supported Euler-Bernoulli beam under a non-periodic single force at the middle of the beam is described. A test at a two-storey test rig with a stochastic wind load is shown in FRITZEN AND KLINKOV (2006) [23]. A scaled tripod structure, representing an offshore wind turbine support structure, is investigated in FRITZEN AND KLINKOV (2007) [24]. The structure is loaded with a stochastic single force at the tower top. On the basis of this investigation the inverse load calculation using a robust observer is applied to a wind turbine with a tripod offshore support structure that is erected as an onshore prototype (final report IMO-Wind project[10] (2010) [41]). A brief summary is presented in KLINKOV AND FRITZEN (2010) [56]. The different studies show very good results.

However, there are still open questions. A satisfactory appraisal of the inversely calculated load at the real wind turbine is not given. So far, the inversely calculated load is compared to an estimate gained from the relationship given by the Betz theory. This comparison only allows a rough estimate regarding the approximate magnitude of the calculated force. Moreover, the investigated laboratory structures neither account for aerodynamic coupling effects between the loading and the structure nor do they give information about the influence of different operational states of the wind turbine. Finally, an approach to handle combined wind and wave loads is not given.

---

[10] See section 5 of the final report of the IMO-Wind project (2010) [41].

1.3 Objective and Outline

The main objective of this work is the calculation of loads using measurements at wind turbine support structures during operation and the verification of the results of the inverse load calculation.

A general analysis problem can be described by the response, the system, and the input; see e.g. SHARPE (2008)[11] [94]. The load calculation is done by solving an inverse problem. In the context of this work, an inverse problem is one where the response and the system are known and needed in order to affect a solution for the unknown input. A scheme of the inverse problem is depicted in Figure 1.2.

Figure 1.2: Scheme of the inverse problem

Applying this scheme to the inverse load calculation at wind turbine support structures leads to a description of response, system, and input, as given subsequently.

The responses are measured structural vibrations, recorded as accelerations or displacements. Accelerations and displacements can be measured directly with appropriate sensors. Alternatively, strain gauges can be used to derive displacements. In this case, the stiffness of the structure is required. In addition, measured accelerations can be integrated twice to calculate displacements – and vice versa.

Wind turbines are dynamically loaded structures. Thus, a mechanical system describing the structural properties needs to take mass, damping, and inertia effects into account. A full description of the structural dynamics gives a FRF matrix. A FRF matrix can be composed of modal information. The modal information can be gained from measurements performing system identification.

The unknown input is represented by the externally acting loads, such as wind loads under onshore conditions or wind and wave loads under offshore conditions.

In this work, the inverse load calculation at wind turbine support structures is performed using the following approach: Structural responses are measured as accelerations over the height of the support structure. The accelerations serve to determine modal information of the wind turbine structure, such as eigenfrequencies, eigenvectors, and damping ratios. A system identification technique is used. A finite-element model of the structure is updated so that the updated model represents the realistic dynamical behavior of the wind turbine support structure. In contrast to the previous researches mentioned in section 1.2.3, the model updating approach allows to gain additional modal information than achieved only

---

[11] See section 10 in SHARPE (2008) [94].

by structural measurement. Finite-element models are not limited to a certain number of modal parameters. If the finite-element model is adjusted to all measured modal parameters, it is assumed that the further modal parameters also represent a more realistic dynamical behavior of the structure than a model that is not updated. With the updated model, an under-determined problem is prevented. This approach even allows setting up over-determined systems of equations that enables eliminating random errors using regression analysis.

The FRF matrix that describes the mechanical system of the structure is composed of the information of the updated model. Measured accelerations are transformed to displacements, so that the response is known. Both system and response are used to solve the inverse problem and to calculate the dynamic part of the unknown loads. In addition, strain gauges at one cross-section of the structure are used to add the static part of the loads.

In order to achieve reliable results and to verify the accuracy of the inverse calculation, this work investigates the following steps.

Section 2 summarizes the loadings that wind turbines need to withstand. The intended inverse load calculation is set in relation to the typical loadings. The types of loads that can be calculated inversely are discussed.

In **section 3**, the state of the art of inverse load calculation methods is given. An appropriate method is chosen and its theoretical basics are presented in detail. The method is applied to a simple 2-DOF system. A stochastic load is applied in order to calculate responses. This procedure corresponds to the solution of the forward problem and leads to the knowledge of loads, the system, and responses. Knowing the solution of the forward problem enables the verification of the inverse procedure. The system and the responses are used to calculate the applied load inversely. The inversely calculated load is compared to the applied load from the forward problem. Inverse calculations are notoriously ill-conditioned. An approach for dealing with this effect is discussed.

As pointed out previously about the inverse load calculation, the influence of the aerodynamic coupling effects between the loading and the structure has not yet been investigated. For this reason, in **section 4** numerical simulations at a 5 MW onshore wind turbine model with a tubular steel tower are run. The comprehensive simulation code FAST is used. FAST accounts for coupled dynamics of wind inflow, aerodynamics, elasticity, and turbine controls. The FAST simulations represent the solution of the forward problem. Thus, a numerical verification of the inverse calculation in consideration of these special wind turbine effects is done. Simulations are run in operational conditions between cut-in wind speed and rated wind speed, around rated wind speed, and between rated wind speed and cut-out wind speed. These operational conditions are assumed as representative for power production and as fatigue driving load cases.

Section 5 deals with requirements that occur when transferring the inverse load calculation to a real wind turbine. A 5 MW wind turbine with a lattice offshore support structure is investigated. The wind turbine is erected as an onshore prototype. Consequently, the externally applied loads are limited to wind loads. The measurement concept is specified. The conducted measurement campaigns are described. Theoretical basics of system identification techniques are discussed. An appropriate technique is described in detail and applied to the measurement data. The modal parameters (eigenfrequencies, eigenvectors, and damping ratios) of the support structure are identified in standstill and in operation. Thus, an entire description of the dynamical behavior of the support structure is given. Special emphasis lies on the determination of damping ratios for the first fore-aft mode of the turbine in operation. This mode is influenced by aerodynamic effects. Corresponding literature only contains rough information. Additionally, the model updating process of the finite-element model is shown. The results of the system identification are used. The integration of the measured acceleration signals is discussed. Finally, results of the inverse load calculation for the 5 MW wind turbine are presented.

Section 6 focuses on the inverse load calculation under offshore conditions. A numerical study using the simulation code FAST is used. Again, the forward problem is solved in order to verify the inverse calculation. This time, the 5 MW wind turbine model with a tubular steel tower is loaded with combined wind and wave loads. This presents a more complex inverse problem that needs to be solved. The related results are shown.

In **section 7**, a conclusion of the presented work and an outlook on continuing research is given.

2 Scope of the Inverse Load Calculation

Wind turbines must be able to withstand complex load situations. In order to clarify the scope and the capability of the inverse load calculation, a brief summary of loadings is given. Section 2.1.1 describes the sources of loads, both for onshore and offshore wind turbines. The summary is limited to the facts needed to discuss the load components that can be determined by the inverse load calculation. These load components are pointed out in section 2.2. More detailed information about the loading of onshore and offshore wind turbines is given in the corresponding technical literature. For instance, HAU (2000) [34] and GASCH AND TWELE (2005) [27] give a broad overview about nearly all aspects related to wind turbines, with an emphasis on onshore wind turbines. Also, UNGRAD (2004) [99] and BÖKER (2009) [6] describe the loadings of offshore wind turbines in detail. In addition, the related design codes, standards, and guidelines contain technical specifications. Regarding onshore wind turbines, the DIBt Richtlinie (2004) [104] and IEC 61400-1 (2005) [107] can be mentioned. For offshore conditions the GL guideline (2004) [106] and the IEC 61400-3 (2009) [108] present relevant literature.

This work focuses on horizontal axis three-bladed wind turbines with upwind rotor direction and active control. This configuration is the most common type used for modern wind turbines.

2.1 Sources of Loads

2.1.1 Loads on Onshore Wind Turbines

The loads on onshore wind turbines are caused by two main sources:

- Inertial and gravity loads due to the weight of the structural components of the wind turbine and the rotation of the rotor blades.
- Aerodynamic loads from wind.

Gravitational loads

The weight of the structural components leads to time-independent loadings. During operation of the wind turbine, additional loads occur due to the spinning rotor.

The rotation of the rotor blades at a uniform, stationary wind speed generates time-independent, stationary centrifugal forces that move in the radial direction. The centrifugal forces at wind turbines are small due to the low rotational speed. However, these forces are important for determining the natural frequencies of the rotor blades.

Furthermore, the rotation of the rotor induces time-dependent cyclic loads. Hence, the excitation frequency depends on the rotational speed of the rotor. The frequency that corresponds to the full rotation of one blade is the fundamental oscillation – the so-called 1P-frequency. Due to the characteristics of cyclic excitation, the higher multiples of the 1P-frequency have to be taken into account. For three-bladed wind turbines in particular, the higher harmonics 3P, 6P, 9P etc. are important to the support structure due to the cumulative effect of all blades. However, in the rotating frame of a blade, the 1P, 2P, 3P, 4P etc. are important.

The weight of the rotor blades causes gravity forces at each blade. Due to the rotation, the position of these gravity forces changes depending on the rotor speed. Cyclic loads in the rotor plane are induced. The effects of these loads are insignificant in terms of the global structure.

A change of the nacelle position leads to gyroscopic forces. These cyclic gyroscopic forces can be assumed as secondary for the support structure.

Mass imbalances of the rotor blades act like rotating eccentric masses. If one of the rotor blades shows a different mass distribution, a harmonic side-side force to the global structure with a 1P-excitation is the result.

Aerodynamic loads

Wind turbines are exposed to wind loads. Due to the physics of wind, the corresponding loads fluctuate. Thus, the structural components of a wind turbine have to be designed to withstand loads from extreme events and varying loads during operation. The varying character of the loads leads to fatigue of the structure. The wind forms a wind profile with an increasing wind speed over the height above ground. The support structure and the rotor in standstill are exposed to the loads caused by this wind profile. In case a certain wind speed at hub height – the cut-in wind speed – is reached, the rotor begins to rotate and the wind turbine will start power production. During power production the aerodynamic loads on the rotor substantially exceed the wind loads on the support structure.[12] Thus, the following discussion is limited to the load effects at the rotor.

The loads during power production are caused by the effects of wind, mass, and elastic forces acting on the rotor. Splitting the loads from wind into several components enables the description of the entire, complex load situation. Figure 2.1 shows the inflow from a wind field and illustrates the relation between the time-dependent effects and the components of the wind field. A discussion of the load components that result from the characteristics of a wind field is given subsequently.

---

[12] See KÜHN (2001) [58], p. 97 [58].

- Steady aerodynamic loads due to the mean wind speed.
- Periodic aerodynamic loads because of the steady increasing wind profile over the height.
- Stochastic and transient aerodynamic loads, e.g. induced by wind turbulences or gusts.

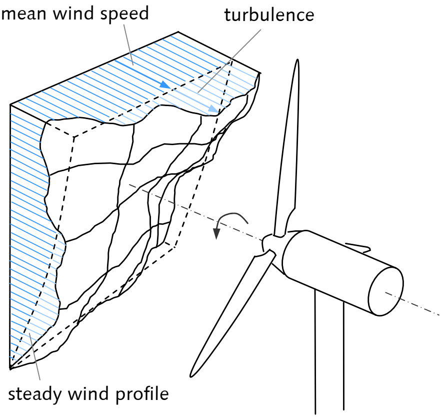

Figure 2.1: Inflow from a wind field

■ Steady aerodynamic loads

A stationary, uniform wind inflow of course does not exist in reality. But, as an idealization, the assumption of a stationary mean wind speed allows the determination of stationary aerodynamic forces along the rotor blades. The wind inflow generates axial forces and tangential forces at the rotor blades. The distribution of both aerodynamic forces depends on

- the effective wind speed increasing from blade root to the tip of the blades (see Figure 2.2a),
- the geometry of the blades, and
- the angle of attack, influenced by the pitch control of the blades.

The sum of the integrated axial forces results in the rotor thrust force. The integration of the tangential forces gives the driving torque (Figure 2.2). There are non-linear effects that have to be taken into account.

- The non-linear dependency of the axial force along the rotor blade on the wind speed. Figure 2.2a exemplarily shows the distribution of an axial force along the rotor blade below rated wind speed, at rated wind speed, and above rated wind speed.
- The rotor thrust force and the driving torque show a non-linear dependency on the wind speed, as depicted in Figure 2.2b. The non-linearity becomes even more crucial in case of active turbine control, such as pitch control of the rotor blades.

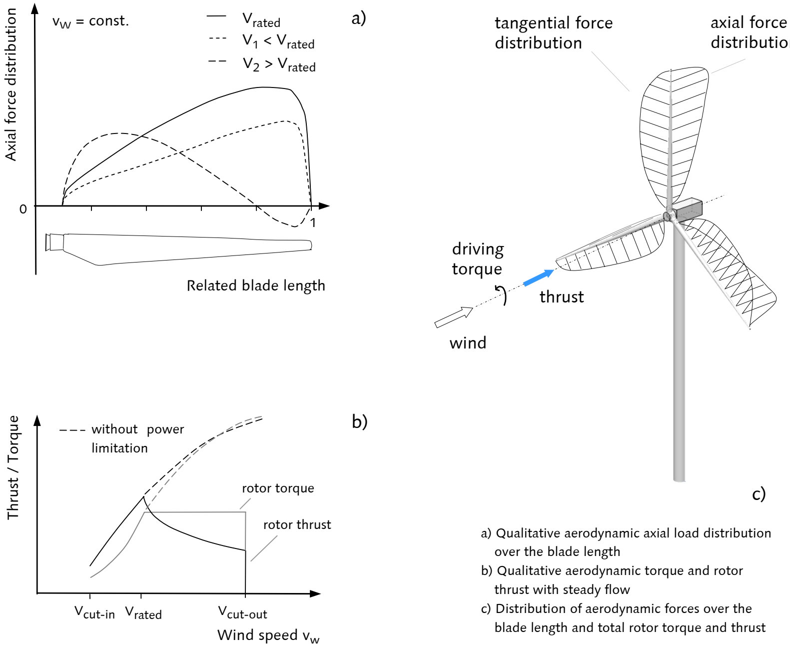

a) Qualitative aerodynamic axial load distribution over the blade length
b) Qualitative aerodynamic torque and rotor thrust with steady flow
c) Distribution of aerodynamic forces over the blade length and total rotor torque and thrust

Figure 2.2: Rotor blade loads (from HAU *(2000) [34])*

- Periodic aerodynamic loads

A stationary, spatially uneven inflow, i.e. a non-symmetric inflow, causes non-stationary, harmonic loads. Non-symmetric inflow occurs due to two phenomena: 1) the increasing wind speed over the height, and 2) cross winds flowing misaligned to the nacelle position. The loads on a rotor blade change with their position during rotation. Consequently, the rotational speed of the rotor is the excitation frequency, the 1P-frequency. Due to the harmonic characteristics, higher harmonics occur. Cyclic effects from the 1P, 2P, 3P, 4P etc. excitation occur in the rotating frame of the rotor blades. In the case of three-bladed rotors, the 3P excitation and its multiples 6P, 9P etc. are present in the frequency spectra of the support structure. The effects due to the non-symmetric inflow mainly lead to additional roll and yaw moments.

The wind speed decreases in front of the tower of the wind turbine. A rotor blade, passing this region of attenuated wind speed, is loaded by lower forces. Thus, a harmonic excitation (1P and its multiples) in fore-aft direction is generated.

- Stochastic and transient aerodynamic loads

The natural fluctuation of the wind speed generates a stochastic inflow, which is also referred to as wind turbulence. Wind turbulences show a broad range of frequencies. Hence, the excitation of the structure highly depends on the relation of the exciting frequencies to the eigenfrequencies.

Wind turbines can be affected by turbines located upwind. Wake effects might cause a higher turbulence level than an undisturbed wind flow generates.

Wind speed fluctuations with low frequencies are so-called gusts. Gusts are characterized by considerable deviations of the wind speed from the mean wind speed. Gusts show transient load characteristics. Further transient loads occur in wind turbine maneuvers, such as start, stop, and emergency breakdown of the turbine.

2.1.2 Loads of Offshore Wind Turbines

Offshore wind turbines are affected by the aerodynamic and the gravitational loads shown for onshore wind turbines. Additionally, hydrodynamic loads have to be considered for offshore wind turbines. Their main sources are wave loads and loads from sea currents.[13] The total hydrodynamic load results from a superposition of both sources.

<u>Wave loads</u>

- Regular wave

The most important hydrodynamic loads are waves generated by wind. The most fundamental description is a single, regular wave. A regular wave is a periodic oscillation of the water surface (Figure 2.3). If the propagation direction is assumed to be constant, a wave can be characterized by: 1) wave height, 2) wave length / wave period, and 3) water depth.

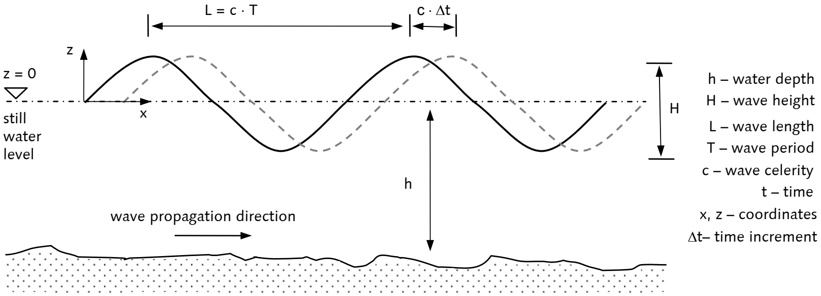

Figure 2.3: Propagation of a single, regular wave

---

[13] Icing and sea ice is not taken into consideration since it is not scope of this dissertation.

- Irregular sea state

A series of long-crested regular waves create a regular sea state. In reality, waves are irregular in shape. Their height, length, and speed of propagation vary, which can be described as a long-crested, irregular sea state. Due to environmental conditions, waves propagate in different directions simultaneously, which leads to a short-crested, irregular sea state (Figure 2.4).

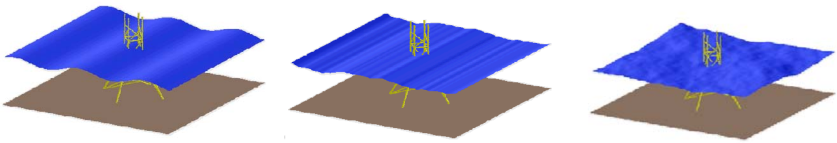

long-crested, regular sea state

long-crested, irregular sea state

short-crested, irregular sea state

Figure 2.4: Sea states (from Böker *(2009) [6])*

A design sea state can be described by a stochastic wave model that is assumed stationary over a certain time period. Such a long-crested, irregular sea state is formed by the superposition of many regular waves, each with its own frequency, amplitude, and phase angle. The mathematical description of the sea state is done by means of the spectral density of the surface elevation. The most common types are the Pierson-Moskowitz (PM) spectrum and the JONSWAP spectrum.[14] The JONSWAP spectrum $S_{JS}(f)$ is defined by the significant wave height H_S, the peak spectral period T_P, and the peak-shape parameter γ (Figure 2.5). The significant wave height is defined as the mean wave height of the highest third of the waves observed.

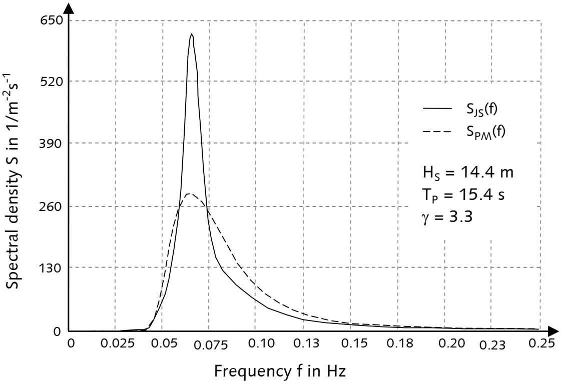

Figure 2.5: JONSWAP spectrum and PM spectrum

---

[14] The JONSWAP spectrum equals the PM spectrum in case of $\gamma = 1$.

Further mathematical descriptions of the wave spectra are given for instance in the IEC 61400-3 (2009), Annex B [108]. The long-crested, irregular sea state that is described by a wave spectrum can be developed to a short-crested, irregular sea state by means of a spreading function, which accounts for the different wave propagation directions.

- Wave theories

The water particles below the oscillating surface of a two-dimensional regular wave show specific velocities and accelerations. To predict the kinematics, several wave theories exist. All wave theories follow a periodic approach, so that the symmetric surface shape and the kinematics repeat at each time period. All theories are based on the same differential equation with the appropriate boundary conditions. They differ in their functional formulation and in the degree to which they satisfy the non-linear kinematic and dynamic boundary conditions at the wave surface. Common wave theories are the linear Airy theory, the Stokes theory, and the Stream Function theory.[15] The wave kinematics depend on the relation of the wave height H to the water depth d. Next to 3rd order Stokes theory, the linear Airy theory is the most important wave theory to approximate irregular sea states. The orbital velocities and accelerations in both horizontal and vertical direction are calculated.

The complex topic of wave theories and the calculation of wave kinematics is explained more detailed for instance in IEC 61400-3 (2009) [108], GL guideline (2004) [106], DNV-OS-J101 (2004) [105], KÜHN (2001) [58], and UNGRAD (2004) [99].

- Calculation of hydrodynamic loads

Knowing the water particle kinematics and the shape of the wave surface enables the calculation of hydrodynamic loads. For slender, cylindrical structures, as is often the case for offshore wind turbine support structures, the Morison equation is a widely used approach. The equation is applicable if the diameter d of the structure does not exceed one fifth of the wave length L, which then is called hydrodynamic transparency. If the hydrodynamic transparency is not fulfilled, effects like diffraction have to be taken into account.

Assuming a slender, bottom-mounted structure, the Morison equation calculates a wave load that is the sum of a drag force and an inertia force. Drag force and inertia force are phase-shifted, so that the wave load has to be calculated under consideration of the phase angle. The qualitative distribution of the wave load over the height of a structure is shown in Figure 2.6. The case of a wave with small amplitude and a slender structure is depicted, so that the requirement for hydrodynamic transparency is fulfilled. The Morison equation calculates hydrodynamic forces up to the elevation of the still water level. To extend the hydrodynamic force to the current wave surface, stretching needs to be applied. The most common approach is the Wheeler stretching.

---

[15] Different orders exist for each Stokes theory and stream function theory.

If the wave profile becomes steep-sided, the assumption of linear theories is not suitable anymore. A deformation of the wave profile may occur during extreme events or in shallow waters where the height of the wave crest above still water level (SWL) becomes greater than the depth of the trough below. At a certain point, the horizontal velocity of the water particles in the wave crest will exceed the wave velocity and the structure of the wave will break. Breaking waves induce transient loads at offshore structures.

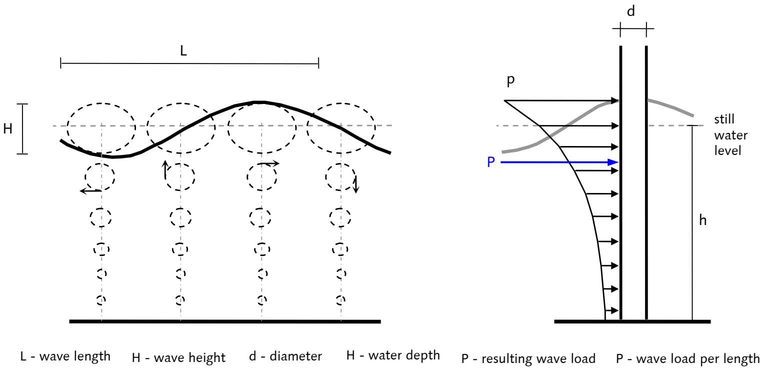

Figure 2.6: Surface and particle velocity of a wave with small amplitude and wave load at a slender cylindrical pile structure

Loads from sea currents

For the calculation of loads from sea currents, a horizontally uniform flow field of constant velocity and direction is assumed. The velocity of the sea current is varying over the depth. The total current velocity is the vector sum of the occurring types of currents.

Three types of currents are mentioned by the offshore wind turbine design code IEC 61400-3 (2009) [108]:

- Sub-surface currents generated by tides, storm surge and atmospheric pressure variations
- Wind generated near surface currents
- Near shore wave induced surf currents running parallel to the cost

The basic generating factors of sea currents are thermal gradients, tides, and wind. Thermal gradients result from insolation. Tides are cyclic water flows depending on the gravitational forces of the sun and the moon. If wind flows constantly in a uniform direction over the water surface, shear forces result in currents. Hence, the generating factors base on constant environmental conditions, at least for a certain time period that can be considered low frequent. Thus, the mathematical description of sea currents is formulated time-independently.

2.2 Inversely calculated Load Components

2.2.1 Classification of Load Types

The loads on offshore wind turbines are explained in section 2.1.1 and section 2.1.2 according to their time-dependency. Different load sources – aerodynamic, inertial, and hydrodynamic loads – are described in terms of their classification into steady, periodic, stochastic, and transient components. A summary of the load types is given in Table 2.1.

Table 2.1: Types of loads for wind turbines

Type of load		Aerodynamic loads	Inertial loads	Hydrodynamic loads
Quasi-static	Steady loads	Uniform, stationary mean wind speed.	Centrifugal forces from rotor running at a constant speed in rotating frame.	Sea currents.
Dynamic	Periodic loads	Stationary, but spatially uneven wind field over the swept rotor area. Caused by the increasing wind speed over the height (vertical shear) or by cross wind or rather yaw misalignment. 1) Effects from the tower shadow (downwind rotors) or tower dam (upwind rotors). 1)	Gravitational forces due to the weight of the rotor blades or mass imbalances. 1) Gyroscopic loads from the yaw of the nacelle.	Wave loads due to long-crested regular sea state. 2)
	Stochastic loads	Stochastic loads from wind turbulence.		Stochastic wave loads from long-crested irregular sea state.
	Transient loads	Transient loads from gusts or shutting down.		Transient loads from breaking waves.

1) Depending on rotational speed of the rotor.

2) Independent from rotational speed of the rotor.

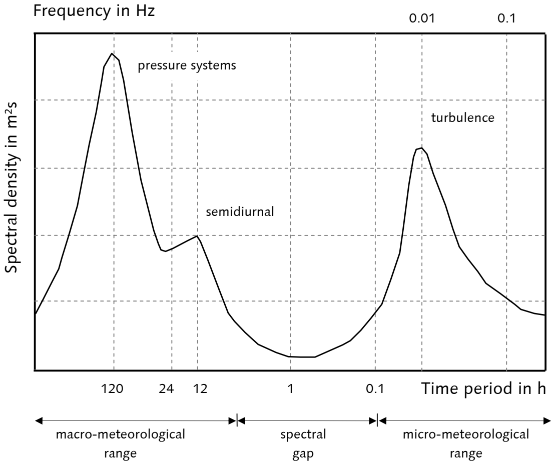

Figure 2.7: Qualitative wind energy spectrum (KÜHN (2001) [58][16])

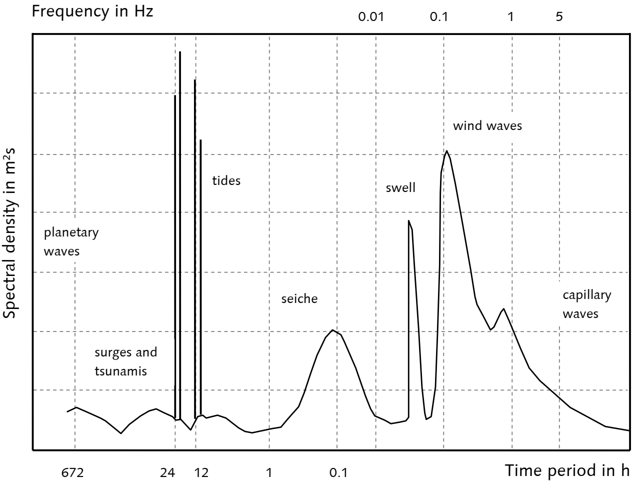

Figure 2.8: Qualitative energy spectrum of ocean waves (KÜHN (2001) [58][17])

---

[16] Originally taken from HOVEN (1957) [37].

[17] Originally taken from HOLTHUIJZEN (1992) [36].

As pointed out, different time-dependent loads act on the wind turbines. The structural components of a wind turbine are flexible. Hence, dynamic interaction between the structural components and the loads occurs. The dynamic interaction leads to amplifications of structural vibrations and structural strains, respectively. A closer look at typical frequency spectra of the loads on wind turbines allows to estimate the effects of dynamic interaction. A typical load spectrum due to wind is given in Figure 2.7 and a qualitative wave load spectrum is depicted in Figure 2.8.

The energy spectrum of wind (Figure 2.7) can be divided into the macro-meteorological range and the micro-meteorological range. A spectral gap without energy content opens between both ranges. The macro-meteorological range with its very low frequencies is the result of long-term wind characteristics. The corresponding loads can be considered quasi-static load components. Notable dynamic load components are visible in the micro-meteorological range at frequencies around 0.01 Hz and up to 0.1 Hz.

A typical wave spectrum (Figure 2.8) is the result of various influences. In accordance with the appraisal of the wind spectrum, the wave spectrum can be divided into quasi-static components and dynamic components. Whereas notable quasi-static load components are the result of surges, tsunamis, and tides, dynamic load components are mainly caused by wind waves. A significant frequency range occurs between 0.1 Hz and 3 Hz.

The lower bound of common eigenfrequencies for fixed-bottom wind turbines is around 0.1 Hz to 0.3 Hz; see for example PAHN ET AL. (2010) [77], IMO-Wind (2010) [41], and REBELO ET AL. (2008) [84]. The German DIBt Richtlinie states that the structural vibrations of wind turbines above 5 Hz are negligible. The comparison to the energy spectra, given in Figure 2.7 and Figure 2.8, clarifies that both typical excitations and structural vibrations coincide, which demands the consideration of dynamic interaction. Furthermore, the spectral gaps in the qualitative spectra of the excitations seem to make a division into quasi-static and dynamic load components reasonable. Consequently, the division into quasi-static and dynamic load types is also considered in Table 2.1.

Due to typical rotational speed of three-axis horizontal wind turbines, the 1-P harmonic excitation may lay around 0.1 Hz and its most prevalent multiples then range up to around 3 Hz.[18] As a rough estimate, blade eigenfrequencies can be assumed to occur around 0.5 Hz and 5 Hz.[19] Consequently, the structural dynamic interaction with the P harmonics or the blade eigenfrequencies has to be considered as well. Generally, excitations of the rotating generator are decoupled from the structural vibrations, because their typical range is much higher. In case of a 5 MW wind turbine generator frequencies of approximately 15 Hz may occur.

---

[18] These facts depend on the operational conditions of a wind turbine and the eigenfrequencies of the structure. The mentioned frequency ranges are derived from a 5 MW wind turbine.

[19] The blade eigenfrequencies highly depend on a specific blade type. The given value represents estimations for blades with a length of 60 m.

2.2.2 Scope of the Inverse Load Calculation

Basing on the load summary in Table 2.1, the ability of the inverse load calculation in terms of calculating the several load components shall be discussed.

Generally, the angle of attack of the loads is assumed to be known. This knowledge can be assured by measurements of environmental parameters such as wind and wave directions.

Because the main field of application of the inverse load calculation is seen for monitoring purposes or remaining lifetime predictions, this work focuses on load cases in operation. Although the inverse load calculation is applicable to standstill conditions and extreme events, both are not taken into account. In this way, transient loads due to shutdown or breaking waves are not considered.

The objective of the inverse load calculation is the determination of applied loads. For this reason, aerodynamic and hydrodynamic loads are of interest, whereas gravitational loads are neglected. In case of wind loads during operation, the significant forces occur in fore-aft direction applied to the spinning rotor blades. Additional hydrodynamic forces may occur from arbitrary directions. Due to the low damping of wind turbines, force components in side-side direction may induce highly amplified structural vibrations. The inverse load calculation is able to handle loads acting in different directions. However, it is not in the scope of this work to identify misaligned load configurations. Thus, this work focuses exclusively on aerodynamic and hydrodynamic loads acting in fore-aft direction simultaneously.

Consequently, cross wind effects or yaw misalignment are not parts of the calculation. Both effects mainly cause blade root moments and torsional bending of the support structure. The blade loads are not the scope in this work. SEIDEL (2001) [93] states that the bending moments in wind direction are the decisive internal forces, which is caused by the heights of the structures. Further internal forces such as normal forces, shear forces, and torsional forces are of minor importance. Hence, focusing on the loads in the fore-aft direction is a reasonable approach.

The influence of sea currents on the hydrodynamic fatigue loading of an offshore wind turbine may be insignificant in cases where the total current velocity is small compared to the wave induced water particle velocity in the wave crest.[20] For this reason, sea currents are neglected in this work.

Consequently, the result of the inverse load calculation consists of the following load components. First, the quasi-static load component due to a stationary mean wind speed is part of the result. Additionally, dynamic effects caused by the vertical wind shear and the stochastic loads from the wind turbulences can be calculated inversely. Dynamic effects of the tower dam that cause harmonic excitation are considered. In terms of hydrodynamic loads, wave loads are accounted for. Both calculations of long-crested regular and irregular sea states are feasible. A depiction of the loads that can be calculated inversely is given in Figure 2.9. The depiction is done exemplarily at a wind turbine with tubular steel tower, but generally the inverse load calculation is not limited to a specific type of structure.

---

[20] See IEC 61400-3 (2009) [108], p. 26, section 6.4.2.

The scope of the inverse load calculation is the identification of a rotor thrust force and a resulting wave load, as depicted in the load model in Figure 2.9. This approach is based on the following idea.

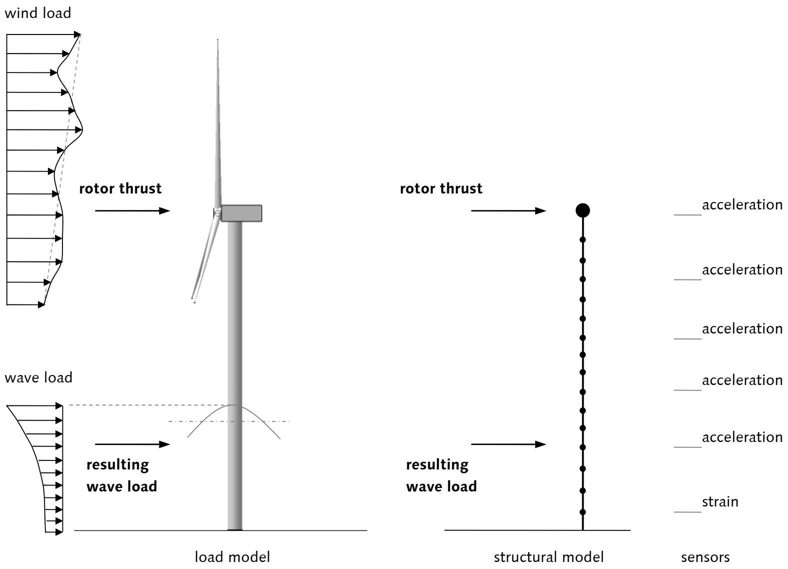

Figure 2.9: Load model and structural model for the inverse load calculation

The wind field causes forces distributed along the rotor blades, as described in Figure 2.2c. Reducing the axial blade forces to a rotor thrust force enables the wind force in fore-aft direction to be calculated by only measuring the structural motions of the tower. As long as the applied loads acting at the support structure are the point of interest, this approach provides sufficient load information. The influence of the stiffness and mass properties of the rotor blades is considered by additional inertia and mass terms at the tower top in the structural model (see Figure 2.9). Additionally, this approach matches practical requirements of the wind industry. Often, detailed information about the rotor blade properties is proprietary and withheld by manufacturing companies. Therefore, a simple modeling of the rotor blades is desirable. Consequently, the described approach does not cover the calculation of the load distribution along the blades.

The absence of rotor blade eigenfrequencies in the structural model causes an error in the inverse load calculation. The calculation procedure interprets the rotor blade eigenfrequencies as excitation frequencies. For this reason, they appear in the inversely calculated load spectrum. The effects of this modeling error will be discussed in this work.

The sea state generates a non-uniform wave load with time-varying load amplitudes and time-varying heights of the load, both depending on the current wave height. A detailed calculation of the wave load distribution would require an excessive number of sensors. Because the scope of the described approach for the inverse calculation is the use of a preferably simple arrangement of sensors, the wave load is reduced to a resulting wave load (see Figure 2.9).

A basic assumption of the chosen approach is knowledge about the load position of the rotor thrust and the resulting wave load. Additionally, the qualitative form of the distributed wave load is assumed to be known, so that a reconstruction based on the resulting wave load is possible, even though this reconstruction is not part of the work presented.

The measurement concept aims at recording only the vibrations of the support structure. Hence, the sensors are concentrated along the support structure (Figure 2.9). Accelerometers are used in order to determine the dynamic component of the loads. The sensor positions have to be chosen so that the dynamic behavior of the structure – i.e. the eigenfrequencies, the mode shapes, and the structural damping – can be recorded entirely. Additionally, the measurement of strains at one cross-section has to be accomplished to determine the quasi-static component of the rotor thrust. An appropriate cross-section for the strain measurement has to be chosen. The approach allows locating the strain sensor above water level. A discussion of the measurement concept in terms of its practical application is given in section 5.

As mentioned previously (see section 2.1.1, Stationary aerodynamic loads), there are non-linear dependencies between the wind speed and

(1) the force distribution along the rotor blades (Figure 2.2a) due to the geometric shape of the blades,

(2) the rotor blade forces due to pitching maneuvers,

(3) the rotor thrust and driving torque respectively, due to the wind turbine control (Figure 2.2b).

To deal with these non-linearities, the use of operating conditions that can be assumed as constant is proposed. That means for example, simulated or measured time series with a constant mean wind speed are used. In terms of measurement data, a mean wind speed with small variation is considered constant as well. In this way, during a single time period, the non-linearities do not affect the inversely calculated loads. Obviously, the inversely calculated loads are not proportional to the wind speed. But a correlation is possible while knowing the configuration of the wind turbine control.

The wake effects of adjacently located wind turbines may result a velocity deficit and in raised turbulence intensities that affect the stochastic aerodynamic loads. The inverse load calculation procedure will not be affected by varying turbulence intensities. However, calculations that focus especially on wake-effect influences are not part of this work.

3 Theory of the Inverse Load Calculation

On the basis of the description for the inverse problem in section 1.3 (see Figure 1.2), the mathematical solution of the inverse problem will subsequently be discussed. For this reason, section 3.1 gives an overview of inverse load calculation methods in order to highlight specific mathematical aspects. This overview also shows different approaches for dealing with these aspects. The approaches are reviewed according to the scope of the inverse load calculation at wind turbine support structures, as previously defined in section 2.2.2 (Figure 2.9). This review serves to choose an appropriate method for the inverse load calculation at wind turbine support structures. The mechanical fundamentals of the method chosen are described in section 3.2.1. Finally, the method is demonstrated by using a simple 2-DOF system.

3.1 Inverse Load Calculation Methods – State of the Art

Generally, an analysis problem is described by three basic components: system, response, and input. The forward problem is defined as one in which the system and the input are known and the response is unknown (Figure 3.1a). Typically, these kinds of problems occur in the design stage of structures. All system describing properties such as the material, the geometry, and boundary conditions are known. Additionally, the loads that define the input are known as well. The responses, for instance displacements or stresses, are required. The definition of an inverse problem is based on the forward problem. Thus, an inverse problem is one in which ether the system[21] or the response is unknown. This section focuses exclusively on inverse problems where the response and the system are known and the input is the unknown parameter, as depicted in Figure 3.1b.

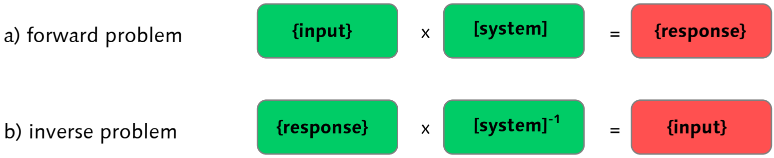

Figure 3.1: Scheme of the forward problem and the inverse problem

---

[21] An example for problems that aim on the determination of system properties is the system identification, which is discussed in section 5.

Solving inverse problems is a field of application in various disciplines. For example, Menke (1984) [64] describes the use of the discrete inverse theory in geophysical data analysis, for instance to determine ocean circulation, tectonic plate motions, earthquake locations, and to create representations of the earth's gravity and magnetic field. The inverse problem can be limited to cases where a discrete dynamic system generates time-dependent responses, like accelerations, velocities, displacements, or strains. The unknown inputs are forces or loads respectively. Then, the inverse problem is called *inverse load calculation*. Corresponding literature also uses the terms *load identification*, *indirect force measurement*, *force identification*, *force reconstruction*, or *force estimation*.

The inverse load calculation in structural dynamics is applied if dynamic loads cannot be measured directly or if the direct measurement demands a high level of effort. Successful applications to various fields of engineering are reported. For instance, in aviation ([4], [101]), automotive industry ([72], [73]), and dynamically operating machines ([75], [90]).

The literature clearly points out, that inverse problems are closely associated with two mathematical aspects: ill-conditioning and ill-posedness. Following the definition in Bader and Schenk (2001) [3], a problem is mathematically ill-conditioned if small variances in the calculation lead to large errors in the result. This characteristic is attributed to the fact that the inversion of an integration process (forward problem) implies a differentiation process (inverse problem). The integration in the forward solution has smoothing effects, whereas the opposite applies to the inverse solution.[22] Using measurement data a priori induces variances in the calculation, mainly caused by noise in the recorded response data. The ill-conditioning is a property of the system and not the data. Errors in the data only manifest the ill-conditioning.[23] A problem can be considered ill-posed if no unique solution exits. In terms of the inverse load calculation, different reasons may cause such an ill-posedness. First, the general formulation of the inverse problem is notoriously ill-posed because load locations and load magnitudes are unknown. Secondly, there is no unique solution if the locations of the loads are known, but there are too few sensors recording the responses, which leads to an under-determined system of equations.[24] Third, the inversion of the system matrix may produce a singular system description of the inverse problem. Especially near or at resonances, the response will be dominated by only a few modes. In this case, the system matrix contains a few dominant elements and many smaller elements.[22] Fourthly, so-called non-collocated problems cause ill-posedness. Non-collocation is given if at least one of the loads does not have instant or distinguishable influence on any of the sensors[24], e.g. if the load location does not coincide with the measurement location. The finite wave propagation implies that the input will have a delayed effect to the response.[25] In particular, real-time methods are affected. Such methods only use information from previous and current time steps. Thus, the first rows of the system matrix are filled with zeros.

---

[22] See Stevens (1987) [96] p. 839.

[23] See Doyle, J. F. in Sharpe (2008) [94], p. 234.

[24] See Nordberg (2004) [72], p. 11.

[25] See Nordström (2005) [73], p. 3.

Due to the time delay, the excitation waves need to reach the sensor positions.[26] This fact is particularly important in the case of transient loads.

Different numerical methods exist to calculate loads inversely. Generally, they can be divided into time-domain and frequency-domain approaches. The most common methods are discussed subsequently.

3.1.1 Time-Domain Methods

Linear time-invariant systems in structural dynamics can be described by either the first-order state space system (equation (3.1)) or by the second-order ordinary differential equation (ODE) (equation (3.2)). Both represent different mathematical descriptions for the same problem. The state space approach has a reduced order of the differential equation, which causes a doubling of the numbers of equations. The second-order description requires the solution of one ODE, which is doubled in terms of its order. The fundamental equations of both mathematical descriptions are given subsequently.

First-order state space system (Natke (1983) [70])

$$\begin{aligned} \dot{\mathbf{x}}(t) &= \mathbf{A}\mathbf{x}(t) + \mathbf{B}\mathbf{f}(t) \\ \mathbf{y}(t) &= \mathbf{C}\mathbf{x}(t) + \mathbf{D}\mathbf{f}(t) \end{aligned} \tag{3.1}$$

with **x** - state vector (n, 1)
f - input/force vector (m, 1)
y - output/response vector (l, 1)
A - state matrix (n, n)
B - input matrix (n, m)
C - output matrix (l, n)
D - feedthrough matrix (l, m)
n - number of states
m - number of forces
l -number of responses

Second-order ordinary differential equation (Rolfes et al. (2007) [89])

$$\mathbf{M}\ddot{\mathbf{y}}(t) + \mathbf{B}\dot{\mathbf{y}}(t) + \mathbf{K}\mathbf{y}(t) = \mathbf{f}(t) \tag{3.2}$$

with **y** - displacement vector (n, 1)
f - force vector (n, 1)
M - mass matrix (n, n)
B - damping matrix (n, n)
K - stiffness matrix (n, n)
n - number of DOF's

- Dynamic Programming (DP)

Dynamic Programming calculates the inverse problem by solving the first-order state space system using a least-squares approach, as explained in Nordberg (2004) [72] and Nordström (2005) [73]. DP is a recursive algorithm consisting of a backward and a forward sweep. The backward sweep defines the input-output relationship at each time step,

---

[26] See Klinkov and Fritzen (2007) [55], p. 463.

whereas the forward sweep sets the optimal input and state sequences based on the initial conditions and the relationships known from the backward sweep. The primary unknown is the incremental change of the force magnitude $\Delta\mathbf{f}_k$, so that an extended discrete linear time-invariant state space system is constituted as given in equation (3.3).

$$\begin{bmatrix}\mathbf{x}_{k+1}\\ \mathbf{f}_{k+1}\end{bmatrix}=\begin{bmatrix}\mathbf{A} & \mathbf{B}\\ 0 & \mathbf{I}\end{bmatrix}\begin{bmatrix}\mathbf{x}_k\\ \mathbf{f}_k\end{bmatrix}+\begin{bmatrix}0\\ \Delta\mathbf{f}_k\end{bmatrix} \quad \text{and} \quad \mathbf{y}_k=\mathbf{C}\mathbf{x}_k+\mathbf{D}\mathbf{f}_k \tag{3.3}$$

The state space matrices **A**, **B**, **C**, and **D** are constant. The vectors $\mathbf{x}_k$, $\mathbf{y}_k$, and $\mathbf{f}_k$ define state, output, and input at the time step k. The unknown $\Delta\mathbf{f}_k$ can be found by minimizing the weighted and regularized squared error function in equation (3.4).

$$E=\sum_{k=1}^{N}\left(\mathbf{y}_k-\hat{\mathbf{y}}_k\right)^T\mathbf{W}_w\left(\mathbf{y}_k-\hat{\mathbf{y}}_k\right)+\sum_{k+1}^{N}\left(\Delta\mathbf{f}_k\right)^T\mathbf{W}_r\Delta\mathbf{f}_k \tag{3.4}$$

The vector $\hat{\mathbf{y}}_k$ denotes the measured responses. Usually, the identity matrix $\mathbf{I}$ is chosen as weighting matrix $\mathbf{W}_w$. The regularization matrix $\mathbf{W}_r$ can be established using the L-curve method[27], which gives the diagonal elements ω_r in $\mathbf{W}_r = \omega_r\mathbf{I}$. Plotting the first sum in equation (3.4) versus the second sum in log-log scale produces an L-curve shape. The optimal regularization parameter can be chosen from the corner point of the L-curve, which now enables the calculation of the unknown force vector **f**.

DP facilitates the inverse load calculation for time-invariant and time-variant systems, as well as the handling of non-collocated force-to-sensor positions. Nordberg and Nordström illustrate a simple numerical example that demonstrates DP's application. First-order Tikhonov regularization is applied. The L-curve method is used to find the weighting terms. Using perfect data – which means the absence of noise in the data – the DP calculates a transient load perfectly. However, adding some noise to the data produces highly disturbed, useless load estimation results that are due to the ill-conditioned system behavior. By means of the Tikhonov regularization, the errors are drastically reduced.

Because of the use of forward and backward sweep, DP does not enable real-time load calculation. KLINKOV AND FRITZEN (2007) [55] also state, that the DP is not capable of handling non-linear systems.

- Inverse Structural Filter (ISF)

This method is introduced by STELTZNER AND KAMMER (1999) [95] for real-time load estimation purposes. The core idea of the ISF is the inversion of input and output of the discrete-time state space system. The inversion of the state space system requires an over-determined system with the number of sensors to be greater than the number of forces so that the feedthrough matrix **D** can be inverted. Additionally, **D** must be full column rank. For non-collocated sensor-to-force locations, the inverted state space formulation may lead to unstable systems in terms of an inverse plant matrix $\hat{\mathbf{A}}$. Even if the system is stable, the

---

[27] The used source refers to: HANSEN (1992) [32].

calculation of the inverse Markov parameters $\hat{\mathbf{h}}_i$ is numerically unstable due to the ill-conditioning. To overcome the ill-conditioning, the system is stepped forward in time before the inversion. Thus, the input force at the time k is a function of the response at future times k+1 to k+l. The non-causal, general l-lead inverse model in the form of equation (3.5) is developed.

$$\mathbf{f}_k = \sum_0^k \hat{\mathbf{h}}_i \mathbf{y}_{k+l-i} \tag{3.5}$$

Equation (3.5) contains the inverse Markov parameters $\hat{\mathbf{h}}_i$, which are calculated according to equation (3.6).

$$\hat{\mathbf{h}}_0 = \hat{\mathbf{D}} \quad \text{and} \quad \hat{\mathbf{h}}_i = \hat{\mathbf{C}}\hat{\mathbf{A}}^{i-1}\hat{\mathbf{B}} \tag{3.6}$$

The inverse Markov parameters are derived from the inverted state space matrices as given in equation (3.7), where + denotes the Moore-Penrose pseudo-inverse.

$$\begin{aligned} \hat{\mathbf{A}} &= \left[\mathbf{A} - \mathbf{B}\left(\mathbf{CA}^{l-1}\right)^{+}(\mathbf{CA})^{l}\right]; \qquad & \hat{\mathbf{B}} &= \mathbf{B}\left(\mathbf{CA}^{l-1}\mathbf{B}\right)^{+} \\ \hat{\mathbf{C}} &= -\left(\mathbf{CA}^{l-1}\mathbf{B}\right)^{+}\left(\mathbf{CA}^{l}\right); & \hat{\mathbf{D}} &= \left(\mathbf{CA}^{l-1}\mathbf{B}\right)^{+} \end{aligned} \tag{3.7}$$

Equation (3.5) represents the basic equation of the ISF. An approach that limits the length of the non-causal filter represents a further development of the ISF in order to deal with non-collocated cases that are still difficult to handle with the l-lead approach.

The inverse Markov parameters can be obtained analytically or from measurements. The responses are required in form of accelerations. The time span l needs to be chosen by the user. The ISF is prone to noise in the recorded data. For this reason, STELTZNER AND KAMMER (1999) [95] propose calculating the minimum norm of the ISF. NORDBERG (2004) [72] and NORDTSRÖM (2005) [73] show how to treat satisfactorily the errors produced by noise using Tikhonov regularization.

- Unknown Input Observer (UIO)

This time-domain approach was invented for control engineering purposes. KLINKOV AND FRITZEN (2007) [55] give a brief summary in order to apply this approach to civil engineering structures. The basic idea bases on the construction of a general observer for a first-order, non-linear state space system, as given in equation (3.8).

$$\begin{aligned} \dot{\mathbf{x}}(t) &= \mathbf{Ax}(t) + \mathbf{Bf}(t) + f\left((\mathbf{x},\mathbf{f}),\mathbf{y}\right) \\ \mathbf{y}(t) &= \mathbf{Cx}(t) + \mathbf{Df}(t) \end{aligned} \tag{3.8}$$

Here, $f(\ )$ is a vector function that contains the non-linear terms. The UIO allows simultaneous reconstruction of the inputs and states, i.e. velocities and positions. Both linear and non-linear systems can be handled. Time-invariance is a mandatory characteristic of the system. Therefore, the observer has the following form.

$$\begin{aligned}\dot{\omega}(t) &= \mathbf{N}\omega(t) + \mathbf{L}\mathbf{y}(t) + \mathbf{T}\mathbf{f}_L\left(\hat{\xi},\mathbf{y}\right) \\ \hat{\xi}(t) &= \omega(t) + \mathbf{Q}\mathbf{y}(t)\end{aligned} \qquad \text{with } \xi(t) = \begin{bmatrix}\mathbf{x}(t)\\ \mathbf{f}(t)\end{bmatrix} \tag{3.9}$$

$\hat{\xi}(t)$ is the estimate of the unknown vector $\xi(t)$ that contains the states and the inputs (forces). An appropriate set of observer matrices **N**, **L**, **T**, and **Q** is required to calculate the estimate of the states and inputs. The set is appropriate if the error between the estimation $\hat{\xi}(t)$ and the real states and inputs $\xi(t)$ converges to zero in time.

Finding the set of observer matrices is the crucial point of the UIO. One option is the use of a linear matrix inequality (LMI) technique. The matrices only need to be set up once. The feedthrough matrix **D** must have full column rank, which means that acceleration sensors must be used. Additionally, the number of sensors needs to be greater or equal to the number of unknown inputs plus the number of non-linear terms. Fulfilling all requirements makes the UIO an approach of robust performance even in the presence of noisy data.

FRITZEN AND KLINKOV ([23], [24], [56]) present a few laboratory tests that give promising results of an inverse load calculation at wind turbine support structures. Their research aims at a real-time load reconstruction.

- Partial Modal Matrix (PMM)

In contrast to the above-mentioned, time-domain approaches the PMM is based on the second-order ODE as introduced in equation (3.2). The idea of the PMM is the decoupling of the spatial system into a modal one, resulting in equation (3.10).

$$\mathbf{f}(t) = \left(\mathbf{U}_0^T\right)^+ \left\{\mathbf{M}_g\ddot{\mathbf{q}}(t) + \mathbf{B}_E\dot{\mathbf{q}}(t) + \mathbf{M}_g\Lambda_0\mathbf{q}(t)\right\} \tag{3.10}$$

In equation (3.10), $\mathbf{q}(t), \dot{\mathbf{q}}(t)$, and $\ddot{\mathbf{q}}(t)$ are the response vectors that contain the three kinetic quantities displacements, velocities, and accelerations – all in generalized (modal) coordinates. Hence, the three kinetic quantities need to be known. They can either be obtained by measurement directly or at least one kinetic quantity has to be measured and the others are calculated via differentiation or integration, respectively. The transformation from the spatial to the modal space is done by means of the modal matrix $\mathbf{U}_0$ according to the relations in equation (3.11). The superscript + denotes the Moore-Penrose pseudo-inverse of the matrix.

$$\begin{aligned}\mathbf{q}(t) &= \mathbf{U}_0^+\mathbf{y}(t) \text{ – displacements}\\ \dot{\mathbf{q}}(t) &= \mathbf{U}_0^+\dot{\mathbf{y}}(t) \text{ – velocities}\\ \ddot{\mathbf{q}}(t) &= \mathbf{U}_0^+\ddot{\mathbf{y}}(t) \text{ – accelerations}\end{aligned} \tag{3.11}$$

The generalized system matrices are the mass matrix $\mathbf{M}_g$ describing the inertia forces, the damping matrix $\mathbf{B}_E$ describing the damping forces, and the product of $\mathbf{M}_g$ and Λ_0 describing the elastic forces. Λ_0 is the spectral matrix that contains the eigenvalues of the system. The system matrices are transferred back to the spatial space via their multiplication with the inverse of the modal matrix, as given in equation (3.10).

The PMM can be applied to non-collocated systems. Moreover, the PMM is not inherently ill-conditioned, which is mainly caused by the comprehensive set of parameters that is assumed to be known and some further requirements. So, the number of sensors needs to be greater or equal to the number of modes. At the same time, the number of modes has to be greater or equal to the number of unknown forces. The eigenvectors at all sensors need to be known. Since the complete measurement data is required for the calculation, the PMM cannot be used for real-time load calculation.

GENARO AND ALVES RADE (1998) [28] give some further insight into the PMM. They demonstrate a numerical example using a 3-DOF model, both under harmonic and transient excitation. Fairly accurate results are calculated, even when random errors contaminate the data.

3.1.2 Frequency-Domain Methods

Calculating loads inversely in frequency domain requires a transformation of the time-domain signals. Usually, a Fast Fourier Transform (FFT) is used. Converting the time-dependent system responses $\mathbf{y}(t)$ leads to the frequency-dependent responses $\mathbf{Y}(j\omega)$. The system properties are fully described by the frequency response function (FRF) matrix $\mathbf{H}(j\omega)$. To gain the unknown forces $\mathbf{F}(j\omega)$, equation (3.12) is used. This equation represents the basic principle of the frequency-domain method for the inverse load calculation.

$$\mathbf{F}(j\omega) = \mathbf{H}^{+}(j\omega) \cdot \mathbf{Y}(j\omega) \tag{3.12}$$

Mathematically, equation (3.12) is a Deconvolution in the Frequency Domain (DFD), which accounts for the naming of the method. Solving equation (3.12) requires the inversion of the FRF matrix, which is denoted by superscript +. In general, the Moore-Penrose pseudo-inverse is used. If the force vector is needed in the time domain, $\mathbf{F}(j\omega)$ can be transferred back using an inverse Fourier transformation. The response vector $\mathbf{Y}(j\omega)$ in equation (3.12) exclusively contains displacements. If displacements are not measured directly but velocities or accelerations are recorded, the measurement data have to be integrated numerically. The DFD allows the calculation of harmonic loads as well as transient loads. In addition, the underlying system has to be time-invariant, since the FRF matrix is not time-dependent.

Since Fourier transformation is an essential part of the calculation, the accuracy of the calculation strongly depends on the discretization of the time signal, i.e. the signal length and the sampling frequency. However, complete time signals are needed, which precludes real-time load calculation. However, approaches for quasi real-time calculation are developed that will be discussed later within this section.

INOUE ET AL. (2001) [42] give a brief but elaborate discussion of the DFD. In mathematical terms, the Deconvolution in Frequency Domain is relatively simple when compared to the one in time domain. In case the signal discretization is not appropriate to perform the FFT, padding the response data with zeros before the deconvolution effectively reduces the error. Applying a least-squares approach to equation (3.12) enables the enhancement of the result quality. This requires an over-determined system that is established when more sensors are applied than forces that are intended to be identified. Further regularization methods like the previously mentioned Tikhonov regularization also can be applied to improve the results.

Contrary to the time-domain approaches, there are not different approaches in the frequency domain. In fact, in the frequency domain, different ideas for solving the inverse problem from equation (3.12) exist. These ideas primarily deal with the formation of the FRF matrix. Some main ideas are presented subsequently.

- FRF matrix from modal parameters

The FRF matrix can be assembled from modal parameters, as described in López Aenlle et al. (2005) [62]. The modal parameters are obtained from vibration tests. A system identification technique is used to determine the parameters, which are the eigenfrequencies, the eigenvectors, and the damping ratios. Using only measurement data gives eigenvectors whose scaling factors are unknown. Bjerg Petersen et al. (2007) [5] describe a mass change method to solve this problem. Several vibration tests with different additionally applied masses are necessary, which probably is not applicable to every kind of structure.

Having all modal parameters, the FRF matrix can be assembled and inverted. The matrix inversion with standard procedures is only possible if the matrix has full rank, e.g. if the number of modes equals the number of sensors. In practice, measurement data often merely provide a truncated modal space. Then, the FRF becomes singular which impedes the inversion. In this case, López Aenlle et al. (2005) [62] propose a singular value decomposition (SVD).[28] For the inversion of the FRF matrix only the singular values that are considerably different from zero are taken into account.

- FRF matrix from model updating

Instead of gaining the FRF matrix by modal parameters only from measurements, López Aenlle et al. (2007) [63] describe the use of an updated model. The basic idea of this method is updating a finite element (FE) model, so that the FE model represents the measured eigenfrequencies and eigenvectors as accurately as possible. Then, the FRF matrix can be assembled by using the mass matrix and the stiffness matrix of the FE model. The damping matrix can be added e.g. by proportional damping that is based on the measurement data and the information known from the mass and stiffness matrix.

Thus, a matrix with full rank can be created which alleviate the matrix inversion. Additionally, the FE model allows the use of more modal parameters than identified from the measurements. Assuming that the first n modes are represented fairly accurately, the further n+i

---

[28] The SVD approach is an alternative to the use of the Moore-Penrose pseudo-inverse that bases on the 2-norm (see Moler (2004) [68], chapter 5.6, page 13ff.).

modes will most likely represented enhanced in the updated model as well. Evidently, the quality of the inverse load calculation strongly depends on the accuracy of the model updating process.

- Treatment of noise and quasi real-time load calculation

The ill-conditioning of the inverse problem manifests in the amplification of noise. Assuming the response vector $\mathbf{Y}(j\omega)$ in equation (3.12) is the sum of a noise-free undisturbed signal $\mathbf{Y}_U(j\omega)$ and noise term $\mathbf{Y}_N(j\omega)$, equation (3.13) occurs.

$$\mathbf{F}(j\omega) = \mathbf{H}^+(j\omega) \cdot \mathbf{Y}(j\omega) = \mathbf{H}^+(j\omega) \cdot \mathbf{Y}_U(j\omega) + \mathbf{H}^+(j\omega) \cdot \mathbf{Y}_N(j\omega) \tag{3.13}$$

If $\mathbf{Y}_U(j\omega)$ becomes very small at a certain frequency, $\mathbf{Y}_N(j\omega)$ will dominate the result of the inverse load. Additionally, $\mathbf{Y}_N(j\omega)$ is amplified by the multiplication with the inverse FRF matrix. The easiest way to deal with this characteristic is the application of a low-pass filter. INOUE ET AL. (2001) [42] suggest the use of a Wiener-Filter as an alternative. BJERG PETERSEN ET AL. (2007) [5] describe how the SVD can be used to handle noisy data.

The Fourier transformation is described by an infinite integral. Measurement data have to be formed by a finite signal length. This discrepancy causes a discontinuity at the end of the frequency-domain data. This error is called leakage. The leakage error can be minimized using an exponential window that is applied to the time-domain data.[29] LÓPEZ AENLLE ET AL. (2005) [62] propose a procedure to deal with the leakage effect and to enable a quasi real-time calculation.

3.1.3 Discussion of Inverse Load Calculation Methods

Time-domain methods and frequency-domain methods show few differences in terms of the result quality for the inverse load calculation.[30] Hence, the choice of an appropriate method does not depend on the calculation domain. The above discussed characteristics show all methods to have their limitations and drawbacks. Consequently, a decision for a certain method has to be made with regards to the specific application. In this work, the inverse load calculation is applied to wind turbines, which requires taking into account the following points:

- Application to a real-world structure: The quality of the results for the inverse calculation not only depends on the used inverse method, but also on the input parameters for the inverse calculation. For this reason, it is important, which parameters are necessary and how accurate they can be determined in case real-world structures are investigated.
- Use of measurement data: The use of measurement data always induces uncertainties. This means that random errors can occur within the inverse calculation.

---

[29] See INOUE ET AL. (2001) [42].

[30] INOUE ET AL. (2001) [42] cites: HOJO ET AL. (1989) [35].

- Ill-conditioning: Using perfect data, e.g. in numerical examples or nearly in laboratory tests, prevents a pollution of the inverse calculation results by effects caused by the ill-conditioning. The use of measurement data will cause the ill-conditioning to be present. For this reason, a reliable regularization is mandatory.
- Stochastic load: Wind and waves induce stochastic loads. Hence, an appropriate inverse method must be able to deal with stochastic loads.
- Time-invariant system and non-linearities: Based on the assumptions described in section 2.2.2, the application to wind turbines support structures can be described by a time-invariant system in which the non-linearities are treated by choosing constant operating conditions.
- Real-time load calculation: From the standpoint of this work, a real-time calculation is not seen as a mandatory condition for wind turbine support structures. Those calculations may serve condition monitoring purposes, which will most likely always allow sufficient data processing time before formulating decisions on the basis of the monitoring results.

All methods presented cope with linear, time-invariant systems. The DP is prone to errors if noise is present due to the ill-conditioning. These errors are reduced with a L-curved weighting term that has the disadvantage that it is detected visually. The PMM converts the entire problem in a way so that it is no longer ill-conditioned. Thus, the accuracy of the calculation strongly depends on the fact that the conditions of the conversion are nearly perfectly fulfilled. The literature does not reveal an application of the DP or the PMM neither under stochastic loads nor to real-world structures. The UIO mainly aims on real-time calculation. Hence, this method spends considerable numerical effort on the determination of the observer matrices. However, real-time calculation is not the scope of this work.

The ISF is already applied to real-world structures. In the course of this thesis, the ISF was applied to a laboratory structure representing a wind turbine support structure loaded with a stochastic force. Descriptions both of the model and the results are summarized in HÄCKELL (2010) [112]. Various regularization approaches are studied. The numerical effort of the regularization is high in contrast to the improvement of the result quality. Especially finding the regularization order is laborious.

The DFD seems to match best the above-given application-specific requirements. This method already was used in various research fields and was also used for stochastic loads. For the regularization, the Tikhonov[31] regularization, an SVD approach, and the use of windowing and filters are presented in the literature. The problem of ill-posedness will be handled by two assumptions. Firstly, the load location is assumed to be known.[32] And second, there are considered at least as many sensors as modes and at least as many modes as forces. The second assumption also assures a determined or an over-determined system of

---

[31] For fundamental description of the approach see TIKHONOV AND ARSENIN (1977) [98].

[32] See also section 2.2.2 Scope of the Inverse Load Calculation.

equations. In case of an over-determined system, a least-squares approach is used to solve the system of equations. In this way, random errors can be eliminated. The system matrices are determined by means of system identification. An updated FE model is used to guarantee full rank system matrices. This results in scaled eigenvectors.

For these reasons, the DFD is used for the inverse load calculation in this work. The briefly described characteristics of the DFD are explained more detailed subsequently. The theoretical fundamentals of the DFD are given in section 3.2. The calculation procedure is demonstrated at a numerical 2-DOF system in section 3.3.

3.2 Fundamentals of the Deconvolution in the Frequency Domain

The Deconvolution in the Frequency Domain is based on the solution of the forward problem. The forward problem is defined by the fundamentals of structural dynamics, which are already investigated in detail and described extensively. Thus, a discussion of the forward problem is not needed. For detailed information about the fundamentals of structural dynamics, see e.g. ROLFES ET AL. (2007) [89], NATKE (1989) [71], or GASCH AND KNOTHE (1987) [25] and GASCH AND KNOTHE (1989) [26].

3.2.1 Inverse Load Calculation using the Deconvolution in the Frequency Domain (DFD)

The Deconvolution in the Frequency Domain is based on the equation of motion (EoM) in the time domain. The EoM for a multi-degree of freedom (MDOF) system is given by the second-order ordinary differential equation for a linear, time-invariant vibrating system in equation (3.14).

$$\mathbf{M}\ddot{\mathbf{y}}(t)+\mathbf{B}\dot{\mathbf{y}}(t)+\mathbf{K}\mathbf{y}(t)=\mathbf{f}(t) \tag{3.14}$$

The equation describes the spatial space. Here, **M** is the mass matrix, **B** the damping matrix and **K** the stiffness matrix. The matrices have square dimension (n, n) and are symmetric. The vector **y**(t) contains the responses in form of displacements and the vector **f**(t) the inputs formed by forces.

The transformation to the frequency domain is done by a Fourier transformation. The response and input vectors are as shown in equation (3.15).[33]

$$\begin{aligned}\mathbf{Y}(j\omega)&=F\{\mathbf{y}(t)\}\\ \mathbf{F}(j\omega)&=F\{\mathbf{f}(t)\}\end{aligned} \tag{3.15}$$

The derivatives of the responses in the frequency domain **Y**(jω) are based on the assumption that the initial condition are set to zero, so that there are

---

[33] Further information to the mathematics of the Fourier transformation is given e.g. in ROLFES ET AL. (2007) [89] p. 36ff., NATKE (1983) [70] p. 48ff.

$$\begin{aligned}\dot{\mathbf{Y}}(j\omega) &= F\{\dot{\mathbf{y}}(t)\} = j\omega\cdot\mathbf{Y}(j\omega)\\ \ddot{\mathbf{Y}}(j\omega) &= F\{\ddot{\mathbf{y}}(t)\} = -\omega^2\cdot\mathbf{Y}(j\omega)\end{aligned}. \tag{3.16}$$

Rearranging equation (3.16) leads to

$$\mathbf{Y}(j\omega) = \frac{1}{j\omega}\dot{\mathbf{Y}}(j\omega) = -\frac{1}{\omega^2}\ddot{\mathbf{Y}}(j\omega) \quad \text{and} \quad \dot{\mathbf{Y}}(j\omega) = \frac{1}{j\omega}\ddot{\mathbf{Y}}(j\omega). \tag{3.17}$$

With the derivatives of the responses, expressions for the displacements, the velocities, and the accelerations are found. Then, the EoM given in equation (3.14) can be set up in the form

$$\mathbf{M}F\{\ddot{\mathbf{y}}(t)\} + \mathbf{B}F\{\dot{\mathbf{y}}(t)\} + \mathbf{K}F\{\mathbf{y}(t)\} = F\{\mathbf{f}(t)\}. \tag{3.18}$$

Further transformations lead to equation (3.19) that represents the EoM in the frequency domain.

$$\left(-\omega^2\mathbf{M} + j\omega\mathbf{B} + \mathbf{K}\right)\mathbf{Y}(j\omega) = \mathbf{F}(j\omega) \tag{3.19}$$

If the system responses are of interest, the EoM in the frequency domain can simply be transformed to the expression

$$\mathbf{Y}(j\omega) = \left(-\omega^2\mathbf{M} + j\omega\mathbf{B} + \mathbf{K}\right)^{-1}\mathbf{F}(j\omega). \tag{3.20}$$

Introducing the frequency response function (FRF) matrix $\mathbf{H}(j\omega)$, equation (3.20) can be written in a more compact form.

$$\mathbf{Y}(j\omega) = \mathbf{H}(j\omega)\mathbf{F}(j\omega) \tag{3.21}$$

The FRF matrix fully describes the dynamic characteristics of the spatial system. Equation (3.21) represents the solution of the forward problem in frequency domain.

The inverse calculation aims on the determination of unknown inputs. Hence, equation (3.21) has to be rearranged so that the basic formulation for the inverse problem in the frequency domain is found

$$\mathbf{F}(j\omega) = \mathbf{H}^{-1}(j\omega)\mathbf{Y}(j\omega). \tag{3.22}$$

To enable the calculation of equation (3.22) the multi-degree of freedom (MDOF) system of dimension n has to be expressed in modal space. For that purpose, a decoupling of the spatial system into n linear independent single-degree of freedom (SDOF) systems is necessary. The decoupling can be performed with a modal transformation as given in equation (3.23).

$$\mathbf{Y}(j\omega) = \mathbf{U}_0\mathbf{Q}(j\omega) = \sum_{i=1}^{n} Q_i(j\omega)\mathbf{u}_{0i} \tag{3.23}$$

The modal transformation requires the modal matrix $\mathbf{U}_0$ that contains the n orthogonal eigenvectors of the undamped system in columns. The modal matrix is known from an eigenvalue analysis of the undamped MDOF system. The displacements of the modal system are now given by the vector $\mathbf{Q}(j\omega)$, which can be expressed by

$$\mathbf{Q}(j\omega) = \mathbf{U}_0^{-1}\mathbf{Y}(j\omega)\,. \tag{3.24}$$

With the mathematical relationship for the modal transformation, equation (3.19) can be rearranged to

$$\left(-\omega^2\mathbf{M}\mathbf{U}_0 + j\omega\mathbf{B}\mathbf{U}_0 + \mathbf{K}\mathbf{U}_0\right)\mathbf{Q}(j\omega) = \mathbf{F}(j\omega)\,. \tag{3.25}$$

Applying a left multiplication with the transposed modal matrix leads to the equation

$$\left(-\omega^2\mathbf{U}_0^T\mathbf{M}\mathbf{U}_0 + j\omega\mathbf{U}_0^T\mathbf{B}\mathbf{U}_0 + \mathbf{U}_0^T\mathbf{K}\mathbf{U}_0\right)\mathbf{Q}(j\omega) = \mathbf{U}_0^T\mathbf{F}(j\omega)\,. \tag{3.26}$$

The eigenvectors are orthogonal to the mass and the stiffness matrix. This characteristic enables the transformation of both matrices to diagonal matrices.

$$\begin{aligned} \mathbf{U}_0^T\mathbf{M}\mathbf{U}_0 &= \mathbf{M}_g = \mathrm{diag}(m_{gi}) \\ \mathbf{U}_0^T\mathbf{K}\mathbf{U}_0 &= \mathbf{K}_g = \mathrm{diag}(k_{gi}) \end{aligned} \tag{3.27}$$

The scalar values m_{gi} and k_{gi} are the generalized masses and generalized stiffness, respectively. The scalars are greater or equal to zero. Subscript i indicates the i-th mode of vibration, which can be interpreted as a SDOF system. Consequently, the relationship for a SDOF system can be applied, so that the following equation is obtained.

$$-\lambda_{0i}^2 = \omega_{0i}^2 = \frac{k_{gi}}{m_{gi}} \tag{3.28}$$

Thus, the dependencies between the eigenfrequencies ω_{0i}, the eigenvalues of the undamped system $\lambda_{0i} = \pm j\omega$, and the mass properties and stiffness properties are set. These relationships allow the definition of the spectral matrix Λ_0.

$$\Lambda_0 = \mathrm{diag}\left(-\lambda_{0i}^2\right) = \mathrm{diag}\left(\omega_{0i}^2\right) \tag{3.29}$$

The spectral matrix is related to the generalized mass matrix and the generalized stiffness matrix according to equation (3.30), which is defined by the form of the eigenvalue problem.

$$-\mathbf{M}_g\Lambda_0 + \mathbf{K}_g = 0 \tag{3.30}$$

Eigenvectors can be scaled arbitrarily, which is another important characteristic of the eigenvectors, next to their orthogonality. A very common scaling is the conversion of the generalized mass matrix to the identity matrix, as given by

$$\mathrm{diag}\left(m_{gi}\right) = \mathbf{U}_0^T\mathbf{M}\mathbf{U}_0 = \mathbf{\Phi}^T\mathbf{M}\mathbf{\Phi} = \mathbf{I}\,. \tag{3.31}$$

The matrix $\mathbf{\Phi}$ now represents the modal matrix associated with this specific scaling (mass). According to equation (3.30), the generalized stiffness matrix becomes the spectral matrix. Hence, equation (3.32) is valid.

$$\mathbf{M}_g = \mathbf{I} \quad \text{and} \quad \mathbf{K}_g = \Lambda_0 \tag{3.32}$$

In accordance with the generalized description of the mass and stiffness terms, a generalized damping matrix can be defined, which is done by

$$\mathbf{B}_g = \mathbf{U}_0^T \mathbf{B} \mathbf{U}_0 \,. \tag{3.33}$$

So far, there is no reason for $\mathbf{B}_g$ to be a diagonal matrix, as it is the case for $\mathbf{M}_g$ and $\mathbf{K}_g$. $\mathbf{B}_g$ often is defined as being diagonal. This assumption is derived from practical experiences and is used within this work as well. The diagonal generalized damping matrix is denoted as $\mathbf{B}_E$.

$$\mathbf{B}_g = \mathbf{B}_E = \mathrm{diag}\left(b_{Ei}\right) \tag{3.34}$$

Additionally, the damping matrix $\mathbf{B}$ is assumed to be proportional to the stiffness matrix $\mathbf{K}$. This second assumption assures the interpretation of the entries b_{Ei} of the generalized damping matrix. Now the damping ratios can be related to the modes of vibration and the damping ratios are proportional to the undamped eigenfrequencies. The modal damping ratios are defined as follows.

$$D_i = \frac{b_{Ei}\omega_{0i}}{2} \tag{3.35}$$

Knowing the basics of the modal transformation enables the simplification of equation (3.26) that is an arranged form of the EoM in the frequency domain. Using the equations (3.27) and (3.33), assuming a diagonal generalized damping matrix and applying equation (3.30) leads to

$$\left(-\omega^2 \mathbf{M}_g + j\omega \mathbf{B}_E + \mathbf{M}_g \Lambda_0\right) \mathbf{Q}(j\omega) = \mathbf{U}_0^T \mathbf{F}(j\omega) = \mathbf{F}_g(j\omega) \,. \tag{3.36}$$

Equation (3.36) represents the description of the generalized system that now is described by generalized diagonal matrices. Thus, the force vector can be interpreted as a modal force. The relationship between the forces in spatial and modal space is now

$$\mathbf{F}(j\omega) = \left(\mathbf{U}_0^T\right)^{-1} \mathbf{F}_g(j\omega) \,. \tag{3.37}$$

Substituting equation (3.36) into equation (3.37) and considering the modal transformation of the responses from equation (3.24) gives

$$\mathbf{F}(j\omega) = \left(\mathbf{U}_0^T\right)^{-1} \left(-\omega^2 \mathbf{M}_g + j\omega \mathbf{B}_E + \mathbf{M}_g \Lambda_0\right) \mathbf{U}_0^{-1} \mathbf{Y}(j\omega) \,. \tag{3.38}$$

Equation (3.38) is of essential relevance for the inverse load calculation because it describes the relationship between the force vector $\mathbf{F}(j\omega)$ and the displacement vector $\mathbf{Y}(j\omega)$ in spatial space with the system matrices in modal space. The modal matrix $\mathbf{U}_0$ enables the transformation between both spaces. Because of the linear independence of the eigenvectors, the modal matrix $\mathbf{U}_0$ is a regular matrix, and consequently it is invertible. In practical applications, the displacements or their derivatives will be measured in spatial space. The forces are needed in spatial space as well. However, the system description usually is gained by means of system identification. Thus, modal parameters such as eigenfrequencies, eigenvectors, and damping ratios are known from measurements. Equation (3.38) combines these requirements. Furthermore, the inverse problem can be calculated solving n independent SDOF systems.

Additionally, equation (3.38) can be given in the form of a sum. This leads to equation (3.39). As it is not of major interest at this point, the detailed derivation of the mathematical steps from equation (3.38) to (3.39) is given in Appendix A.

$$\mathbf{F}(j\omega) = \sum_{i=1}^{n} \left(-\omega m_{gi} + j\omega b_{Ei} + m_{gi}\omega_{0i}^{2}\right) \left(\mathbf{u}_{0i}^{T}\right)^{-1} \mathbf{Y}(j\omega)\, \mathbf{u}_{0i}^{-1} \tag{3.39}$$

Equation (3.39) clarifies that n modal parameters are needed to assemble the FRF matrix. The n corresponding eigenvectors serve to perform the modal transformation. The responses **Y**(jω) are transformed from the spatial to the modal space. The transformation is reversed with respect to the force vector **F**(jω). All terms are still formulated in the frequency domain.

The back transformation to the time domain is obtained applying an inverse Fourier transformation, as is shown in equation (3.40) for the force vector.

$$\mathbf{f}(t) = F^{-1}\left\{\mathbf{F}(j\omega)\right\}. \tag{3.40}$$

3.2.2 Assembly of the FRF Matrix and Least-Squares Approach

The mathematical fundamentals of the inverse load calculation in the frequency domain are described in detail in the previous section. Subsequently, the assembly of the FRF matrix is discussed. First, determined systems are focused on. These are systems in which the number of unknown forces equals the number of measured responses. Subsequently, a least-squares approach is discussed. This approach enables the calculation of over-determined systems, i.e. systems with a number of measured responses that is greater than the number of the unknown forces. The descriptions are mainly based on the publications of STEVENS (1987) [96] and EWINS (2000) [18] .

<u>FRF matrix for determined systems (n = m)</u>

1. Calculation of the receptance matrix **Z**(jω) in modal space

$$\mathbf{Z}(j\omega) = \mathbf{H}_g^{-1}(j\omega) = -\omega^2\mathbf{M}_g + j\omega\mathbf{B}_E + \mathbf{M}_g\mathbf{\Lambda}_0 \tag{3.41}$$

with $\mathbf{Z}$ - Receptance matrix (n x n), diagonal
$\mathbf{H}_g^{-1}$ - inverse FRF matrix in modal space (n x n), diagonal
$\mathbf{M}_g$ - generalized mass matrix (n x n), diagonal
$\mathbf{B}_E$ - generalized damping matrix (n x n), diagonal
$\mathbf{\Lambda}_0$ - spectral matrix (n x n), diagonal

2. Inversion of the receptance matrix

   $$\mathbf{H}_g(j\omega) = \mathbf{Z}^{-1}(j\omega) \tag{3.42}$$

   All matrices used to assemble the receptance matrix are square. Consequently, the receptance matrix also has a square form. A matrix inversion requires a regular matrix of square dimension.[34] This condition is fulfilled in case of the receptance matrix of determined systems. The inversion of the receptance matrix gives the FRF matrix.

3. Modal transformation of the FRF matrix into spatial space

   $$\mathbf{H}(j\omega) = \mathbf{U}_0 \cdot \mathbf{H}_g(j\omega) \cdot \mathbf{U}_0^T \tag{3.43}$$

   Coupling is based on the modal transformation as described in equation (3.27), using the n x n modal matrix $\mathbf{U}_0$. The FRF matrix in modal space $\mathbf{H}_g(j\omega)$ is a diagonal matrix. The multiplication with the modal matrix and its transpose causes coupling of the modes. Hence, the FRF matrix in spatial space $\mathbf{H}(j\omega)$ is a fully populated matrix. (Exception: decoupled eigenvectors, i.e. each eigenvector has one entry unequal to zero and all remaining entries equal to zero.)

   As an alternative, the FRF matrix can be obtained in spatial space directly using

   $$\mathbf{H}(j\omega) = \left(-\omega^2\mathbf{M} + j\omega\mathbf{B} + \mathbf{K}\right)^{-1}. \tag{3.44}$$

   This alternative makes bullets 1 and 2 obsolete. It requires the knowledge of the system matrices in spatial space. For example, the mass matrix and stiffness matrix can be obtained from a FE model. The damping matrix can be assembled using damping ratios gained from system identification.

4. Inversion of the FRF matrix

   The inverse load calculation requires the inversion of the FRF matrix $\mathbf{H}(j\omega)$ to $\mathbf{H}^{-1}(j\omega)$.

   Note: Bullets 1-4 deal with the calculation of H_g^{-1}, which afterwards is inverted to H_g. Then, the modal transformation to H is shown, which again is inverted to H^{-1}. This procedure seems very laborious. However, it is important for over-determined systems (n > m). This case will be shown subsequently using a least-squares approach. Then, the FRF matrix H in spatial space is needed. In case only determined systems (n = m) are taken into consideration, the FRF matrix can be calculated directly using

   $$\mathbf{H}^{-1}(j\omega) = \left(\mathbf{U}_0^T\right)^{-1} \cdot \mathbf{H}_g^{-1}(j\omega) \cdot \mathbf{U}_0^{-1} = -\omega^2\mathbf{M} + j\omega\mathbf{B} + \mathbf{K}. \tag{3.45}$$

---

[34] Papula (2000) [82], p. 195.

5. Inverse calculation of the load for the determined system (n = m)

$$\mathbf{F}(j\omega) = \mathbf{H}^{-1}(j\omega) \cdot \mathbf{Y}(j\omega) \tag{3.46}$$

with $\mathbf{F}(j\omega)$ - load vector in spatial space

$\mathbf{Y}(j\omega)$ - vector of responses (displacements) in spatial space

FRF matrix for over-determined systems (n > m)

If the number of known system responses n is greater than the number of unknown forces m, the system is over-determined. In this case, the redundant system responses can be used to average the random errors in the responses.[35] A least-squares approach is applied for this purpose.

The basic problem of an over-determined system with n > m can be formulated as follows

$$\mathbf{Y}_{n \times 1}(j\omega) \approx \mathbf{H}_{n \times m}(j\omega) \cdot \mathbf{F}_{m \times 1}(j\omega). \tag{3.47}$$

The application of the least-squares approach leads to the minimizing problem

$$\min_{\mathbf{F}(j\omega)} \left\| \mathbf{H}(j\omega) \cdot \mathbf{F}(j\omega) - \mathbf{Y}(j\omega) \right\|. \tag{3.48}$$

The over-determined system from equation (3.47) can be solved by multiplying both sides with $\mathbf{H}^T$. Then, a square m x m system is obtained, which represents the so-called "normal equation"

$$\mathbf{H}^T \cdot \mathbf{H} \cdot \mathbf{F}(j\omega) = \mathbf{H}^T \cdot \mathbf{Y}(j\omega).^{36} \tag{3.49}$$

If there are independent basis functions, $\mathbf{H}^T\mathbf{H}$ is not singular, which enables the transformation of equation (3.49) to

$$\mathbf{F}_{est}(j\omega) = \left[\mathbf{H}^T\mathbf{H}\right]^{-1} \mathbf{H}^T \cdot \mathbf{Y}(j\omega) \text{ or} \tag{3.50}$$

$$\mathbf{F}_{est}(j\omega) = \mathbf{H}^{+}(j\omega) \cdot \mathbf{Y}(j\omega) \text{, respectively.} \tag{3.51}$$

Now, $\mathbf{F}_{est}(j\omega)$ is an estimate of the force vector $\mathbf{F}$ $(j\omega)$. The system is of the dimension as shown in equation (3.52). Subscripts m and n respectively denote the number of forces and the number of responses.

$$\begin{bmatrix} \mathbf{F}_{est} \end{bmatrix}_{m \times 1} = \begin{bmatrix} \quad \mathbf{H}^{+} \quad \end{bmatrix}_{m \times n} \cdot \begin{bmatrix} \\ \mathbf{Y} \\ \\ \end{bmatrix}_{n \times 1} \tag{3.52}$$

---

[35] Stevens (1987) [96].

[36] For the purpose of clarity, the frequency dependence of the FRF matrix is omitted, although **H** is still a function of $(j\omega)$.

The matrix $\mathbf{H}^+$ represents the pseudo-inverse of the matrix **H**. $\mathbf{H}^+$ can be calculated as a Moore-Penrose pseudo-inverse, so that

$$\mathbf{H}^+ = \left[\mathbf{H}^T\mathbf{H}\right]^{-1}\mathbf{H}^T. \tag{3.53}$$

The pseudo-inverse does not have exactly the same properties as $\mathbf{H}^{-1}$. $\mathbf{H}^T$ is the hermetic transpose of **H**, which means the transpose of its complex conjugate. Equation (3.54) clarifies the matrix dimension of the FRF matrix and its pseudo-inverse in case of an over-determined system (n > m).

$$\begin{aligned} &\mathbf{H}_{n\times m}\cdot\mathbf{F}_m = \mathbf{Y}_n \\ &\mathbf{F}_m = \mathbf{H}^+_{m\times n}\cdot\mathbf{Y}_n \\ &\mathbf{H}_{n\times m} \leftrightarrow \mathbf{H}^+_{m\times n} \end{aligned} \tag{3.54}$$

The FRF matrix **H** can be assembled in two ways:

I) Assembly using system matrices (in both modal and spatial space)

$$\mathbf{H}(j\omega) = \mathbf{U}_0\cdot\mathbf{H}_g(j\omega)\cdot\mathbf{U}_0^T \tag{3.55}$$

- Coupling using the modal transformation as described in equation (3.27)
- All matrices are of dimension n x n
- Truncation of the remaining columns in **H**, so that
- $$\mathbf{H}_{n\times n} = \begin{bmatrix} \qquad\qquad & \\ \\ \\ \end{bmatrix} \rightarrow \mathbf{H}_{n\times m} = \begin{bmatrix} \quad \\ \\ \\ \end{bmatrix}$$

II) Assembly using a summation of modal parameters

a) <u>in modal space</u>

$$\mathbf{H}_{g\ m\times n} = \sum_{i=1}^{N}\frac{\phi_{ni}\cdot\phi_{mi}}{\lambda_i^2-\omega^2+j\omega b_{Ei}} = \sum_{i=1}^{N}\frac{{}_iA_{nm}}{\lambda_i^2-\omega^2+j\omega b_{Ei}}\,^{37} \tag{3.56}$$

n - number of rows in the modal matrix $\mathbf{\Phi}$ (n x n)[38]

m - number of columns of the transposed modal matrix $\mathbf{\Phi}^T$

ϕ - eigenvector, column of the modal matrix $\mathbf{\Phi}$

i - vibration mode

N - number of modes

Afterwards, the modal matrix can be transformed into spatial space, see equation (3.43).

---

[37] Damping proportional to the stiffness is assumed.

[38] The scaled modal matrix $\mathbf{\Phi}$ is used. The scaling is done with respect to $\mathbf{M}_g = \mathbf{I}$, see equation (3.31).

$$\boldsymbol{\Phi} = \overbrace{\begin{bmatrix} \phi_{1,1} & & \\ \phi_{2,1} & & \\ \cdots & & \\ \phi_{n,1} & & \end{bmatrix}}^{i} \Big\downarrow n \qquad \boldsymbol{\Phi}^T = \left.\overset{\xrightarrow{\quad} m}{\begin{bmatrix} \phi_{1,1} & \phi_{2,1} & \cdots & \phi_{m,1} \\ & & & \\ & & & \\ & & & \end{bmatrix}}\right\} i$$

b) <u>in spatial space</u>

$$\mathbf{H}_{m\times n} = \sum_{i=1}^{N} \frac{u_{0,ni} \cdot u_{0,mi}}{k_i - \omega^2 m_i + j\omega b_i} = \sum_{i=1}^{N} \frac{{}_iA_{nm}}{k_i - \omega^2 m_i + j\omega b_i} {}^{37} \tag{3.57}$$

- the subscripts are in accordance with the descriptions in a)
- the modal matrix $\mathbf{U}_0$ is arbitrary scaled

Both I) and II) require knowledge of n vibration modes, which equals the number of considered responses.

Applying the least-squares approach to the inversion of the non-square FRF matrix **H**, the inverse $\mathbf{H}^+$ appears in the dimension, as given in the equations (3.58) to (3.61).[39]

$$\mathbf{H}^+ = \left[\mathbf{H}^T\mathbf{H}\right]^{-1}\mathbf{H}^T = \begin{bmatrix} \qquad\qquad\qquad \end{bmatrix}_{m\times n} \tag{3.58}$$

$$\mathbf{H} = \begin{bmatrix} \quad \\ \\ \\ \\ \end{bmatrix}_{n\times m} \quad \text{and} \quad \mathbf{H}^T = \begin{bmatrix} \qquad\qquad\qquad \end{bmatrix}_{m\times n} \tag{3.59}$$

$$\mathbf{H}^T\mathbf{H} = \begin{bmatrix} \qquad \end{bmatrix}_{m\times m} \quad \text{and} \quad \left[\mathbf{H}^T\mathbf{H}\right]^{-1} = \begin{bmatrix} \qquad \end{bmatrix}_{m\times m} \tag{3.60}$$

$$\left[\mathbf{H}^T\mathbf{H}\right]^{-1} \cdot \mathbf{H}^T = \begin{bmatrix} \qquad\qquad\qquad \end{bmatrix}_{m\times n} \tag{3.61}$$

Since the calculations in this work are done using the software MATLAB[40], some important remarks about the calculation of the FRF matrix are given in Appendix B. Additional information is presented by MOLER (2004) [68].

---

[39] Note: Only regular matrices of square dimension can be inverted, see PAPULA (2000) [82]. Otherwise, the pseudo-inverse has to be calculated, see MOLER (2004) [68].

[40] MATLAB is used to imply MATLAB®

3.3 Numerical Example using a 2-DOF System

3.3.1 Idea and Numerical System

This section presents a numerical example to demonstrate the theoretical fundamentals given above. The calculations aim to implement mathematical algorithms. For this reason, a simple 2-DOF system is chosen. The simplicity of the 2-DOF system limits the parameter that may influence the inverse calculation. In this way, a verification of the accuracy of the inverse calculation can be obtained. A reliable verification of the inverse calculation can be obtained if the corresponding forward solution is known.

In addition, the effects of data polluted with noise are studied. Noisy data are of special interest, because measured system responses are always polluted with noise. The noise represents a small disturbance in the input data. Due to the ill-conditioning of the inverse calculation, effects to the inversely calculated loads are expected.

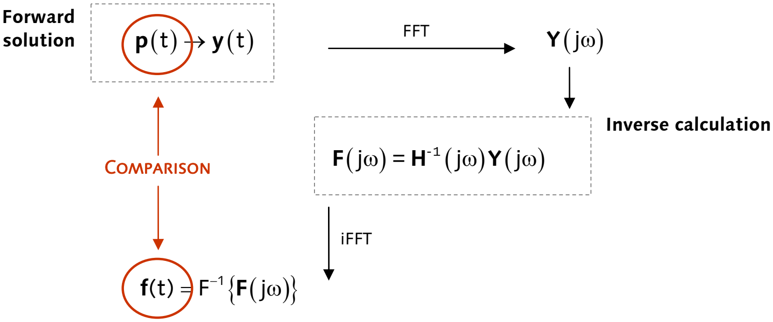

Figure 3.2: Scheme for the verification of the inverse calculation

The idea of the verification procedure is given in Figure 3.2. The basis for the description of real-world phenomena are time-dependent processes. A time-dependent load vector **p**(t) is applied to a linear vibrating system. The corresponding displacement vector **y**(t) is calculated. Because a frequency-domain method is used for the inverse calculation, the displacements have to be transferred to the frequency domain, using a FFT. The system description is known from the solution of the forward problem. Hence, the FRF matrix **H**(jω) can be assembled and inverted, which enables the inverse calculation of the force vector **F**(jω). An inverse Fast Fourier Transform (iFFT) allows the back transformation to the time domain. Now, a comparison of the initially applied load **p**(t) to the inversely calculated load **f**(t) is possible, which gives an estimate about the accuracy of the inverse calculation procedure. The chosen 2-DOF system is shown in Figure 3.3.

$$\mathbf{K} = \begin{bmatrix} 2000 & -2000 \\ -2000 & 5000 \end{bmatrix} \text{in Nm}^{-1}$$

$$\mathbf{M} = \begin{bmatrix} 1 & 0 \\ 0 & 2 \end{bmatrix} \text{in kg}$$

$$\mathbf{B}_E = \begin{bmatrix} b_{E1} & 0 \\ 0 & b_{E2} \end{bmatrix} = \begin{bmatrix} 2m_{g1}\omega_{01}D_1 & 0 \\ 0 & 2m_{g2}\omega_{02}D_2 \end{bmatrix}$$

$$D_1 = 0.0025 = 0.25\%$$

$$D_2 = \frac{D_1 \cdot \omega_{02}}{\omega_{01}} = 0{,}018925 = 1.9\%$$

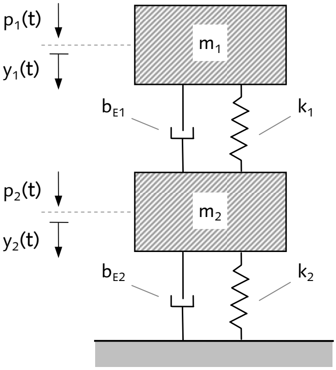

Figure 3.3: Numerical 2-DOF system

The system is described by two masses, connected with springs that represent the stiffness properties. The parameters m_i and k_i are chosen reasonably. The damping ratio $D_1 = 0.25$ % represents common values in structural dynamics. Because viscous damping is assumed, D_2 can be calculated as defined in equation (3.35). The EoM is based on the force equilibrium at each DOF, so that the system matrices can be obtained, as given below.

The eigenfrequencies and eigenvectors of the undamped system are gained from an eigenvalue analysis. The eigenfrequencies are

$$\omega_{01} = 28.53 \text{ s}^{-1} \quad \rightarrow \quad f_{01} = 4.54 \text{ Hz}$$
$$\omega_{02} = 60.71 \text{ s}^{-1} \quad \rightarrow \quad f_{02} = 9.66 \text{ Hz}$$

The graph of the applied load vector **p**(t) is shown in Figure 3.4. A stochastic load is applied to the first DOF. The second DOF is unloaded. This load model is chosen to represent the load characteristics of an onshore wind turbine in operation. The length of the time series is set to $t_{max} = 100$ s. The resolution of the time vector is $t_S = 0.01$ s.

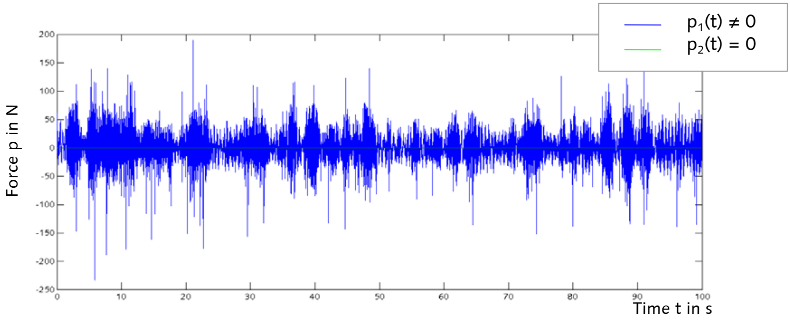

Figure 3.4: Stochastic load

3.3.2 Forward Solution

In general, the forward solution can be obtained using either a time-domain method or a frequency-domain method. Here, the frequency-domain approach that is given in equation (3.62) is used. Since the displacements are needed in the time domain, an iFFT is applied.

$$\mathbf{y}(t) = F^{-1}\left\{ \sum_{i=1}^{n} \frac{\mathbf{u}_{0i}^{T}\mathbf{p}_{0}}{-\omega^{2} m_{gi} + j\omega b_{Ei} + \omega_{0i} m_{gi}} \mathbf{u}_{0i} \right\} \tag{3.62}$$

The calculated system response is depicted in Figure 3.5. The time-dependent displacements **y**(t) are shown. In addition, the absolute value of the frequency-dependent displacements |**Y**(jω)| are given in Figure 3.6. The frequency-domain depiction, in particular, gives insight into the interaction between the load and the system. The displacements show spectral peaks at 29 s^{-1} and 61 s^{-1}, which obviously are caused by the amplification at the resonances to the system eigenfrequencies. The further spectral peaks correspond to the energy content of the stochastic load.

Since the transformation of signals from the time domain to the frequency domain and its reverse is essential not only for the forward solution but also for the inverse calculation, some important fundamentals are summarized in Appendix B.

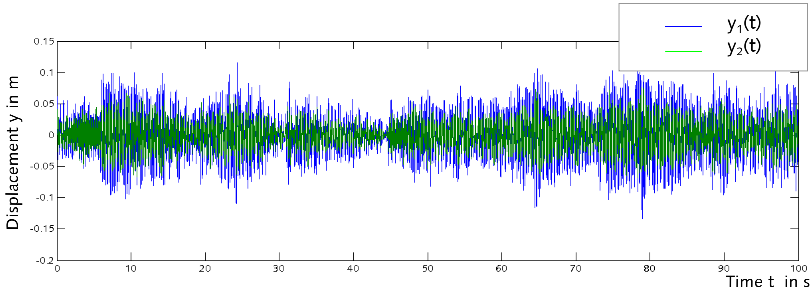

Figure 3.5: Displacements of the 2-DOF system in time domain

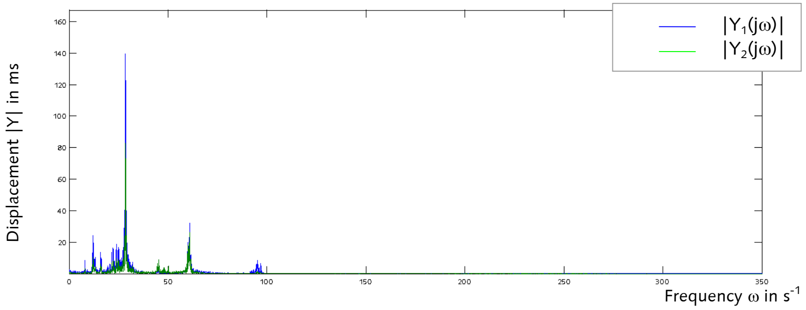

Figure 3.6: Displacements of the 2-DOF system in frequency domain

3.3.3 Inverse Calculation

The solution of the forward problem gives the displacements under the stochastic load for the chosen 2-DOF system. The displacements serve as input for the inverse calculation. In addition, the system description is known, so that the inverse calculation can be done according to the above-mentioned basic equation (3.51), which here is given again.

$$\mathbf{F}_{est}(j\omega) = \mathbf{H}^{+}(j\omega) \cdot \mathbf{Y}(j\omega) \tag{3.51}$$

Since the system is determined, the FRF matrix **H**(jω) can be inverted by an ordinary matrix inversion. A least-squares approach is not applied. For this reason, the inverse FRF matrix is gained by the receptance matrix in modal space, as shown above in equation (3.41), but now written in matrix form.

$$\mathbf{Z}(j\omega) = \mathbf{H}_g^{-1}(j\omega) = -\omega^2 \begin{bmatrix} 1 & 0 \\ 0 & 1 \end{bmatrix} + j\omega \begin{bmatrix} b_{E1} & 0 \\ 0 & b_{E2} \end{bmatrix} + \begin{bmatrix} \omega_{01}^2 & 0 \\ 0 & \omega_{02}^2 \end{bmatrix} \tag{3.63}$$

The scaling that sets the mass matrix equal to the identity matrix is applied. This decoupled system matrix that now represents two linear independent SDOF systems is depicted in Figure 3.7.

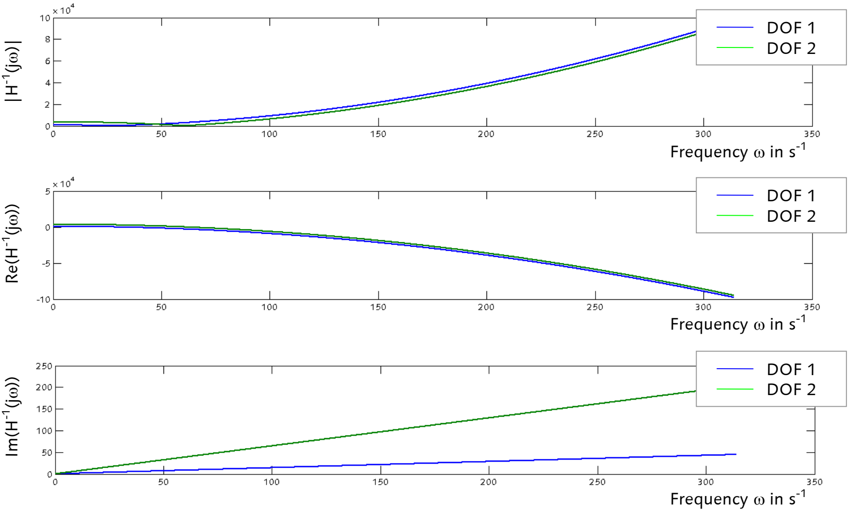

Figure 3.7: Inverse FRF matrix of the 2-DOF system – absolute value, real part, and imaginary part

The plot of the inverse FRF matrix in Figure 3.7 gives insight into the system characteristics. The real part of the inverse FRF matrix depends on the mass and stiffness properties of the system, which is in accordance with equation (3.63). The graph of the real part is a quadratic function. Even though the figure does not show the crossing points at the axis of ordinates, the real parts are equal to zero at the corresponding eigenfrequencies ω_{0i}. The imaginary part of the inverse FRF matrix is a function only of the damping. The graph shows linear behavior and equals zero at $\omega = 0$. This characteristic is due to the assumption of viscous damping. The slope of the imaginary part is defined by the viscous damping rates b_{Ei}. The comparison of the absolute values of the inverse FRF matrix to the graphs of the real parts and the imaginary parts clarifies the fact that the system behavior is dominated by the mass and stiffness properties, whereas the damping plays a secondary role. Consequently, the exact knowledge of the mass and stiffness distribution is more important for the inverse calculation than knowledge of the system damping.

The transformation of the inverse FRF matrix into the spatial space is done using the relationship known from equation (3.45).

$$\mathbf{H}^{-1}(j\omega) = \left(\mathbf{\Phi}_0^{\mathrm{T}}\right)^{-1} \cdot \mathbf{H}_g^{-1}(j\omega) \cdot \mathbf{\Phi}_0^{-1} \tag{3.64}$$

The scaled modal matrix has to be used. The eigenvectors cause the coupling of the entries of the diagonal matrix $\mathbf{H}_g^{-1}(j\omega)$ so that the spatial space form $\mathbf{H}^{-1}(j\omega)$ becomes a fully occupied matrix.

The inverse calculation gives the loads as depicted in Figure 3.8 and Figure 3.9. Both figures show a comparison of the applied load **p** to the inversely calculated load **f**, each for the first and the second DOF separately. Figure 3.8 depicts the comparison in the time-domain and Figure 3.9 gives the loads in the frequency domain.

The second DOF was initially unloaded, which can be seen both in the time-domain and the frequency-domain plots. For the inversely calculated load, the time-domain and frequency-domain results show an oscillating graph and spectral peaks, respectively. However, the order of magnitude is between 10^{-9} and 10^{-12}. The inversely calculated load at the second DOF equals zero, as expected.

The first DOF is loaded by the stochastic load. Only one graph seems to be visible in the time domain and in the frequency domain. In fact, both the applied load and the inversely calculated load match perfectly. The amplitudes clearly exceed the numerical inaccuracies. To underline this conclusion, the error in the time domain ε between the applied load vector **p**(t) and the inversely calculated load vector **f**(t) is calculated according to equation (3.65).

$$\varepsilon = \frac{\sqrt{\sum_{i=1}^{n}\left[p(t_i) - f(t_i)\right]^2}}{n \cdot \sqrt{\max\left[p(t)\right]^2}} \tag{3.65}$$

Here, the error in time is $\varepsilon = 0.00$ %. In case of a determined system with accurately known system properties and undisturbed input, the inverse load calculation in the frequency domain gives exact results.

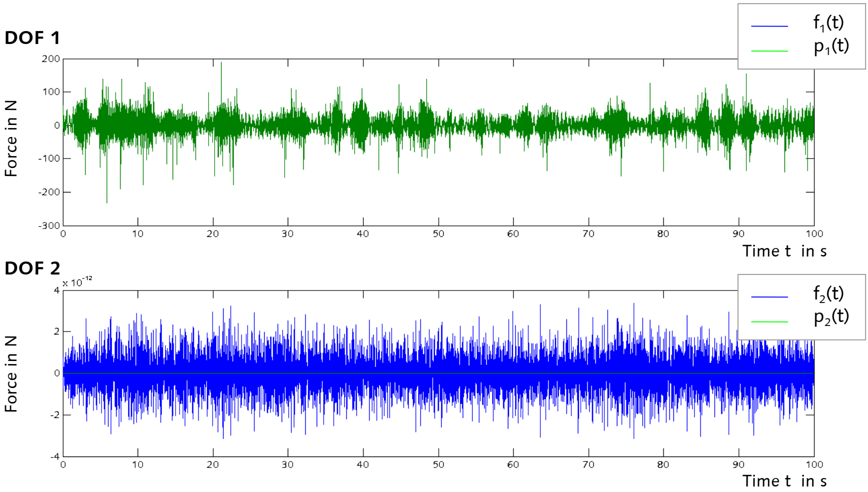

Figure 3.8: Comparison of the loads of the 2-DOF system in the time domain

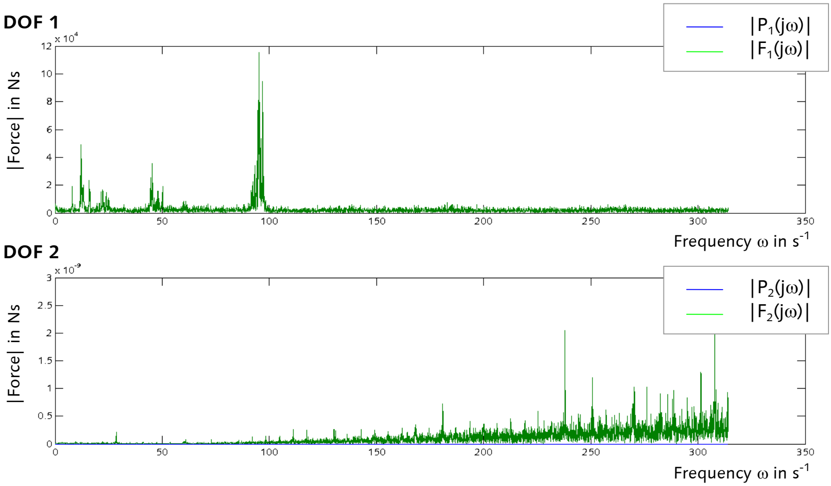

Figure 3.9: Comparison of the loads of the 2-DOF system in the frequency domain

3.3.4 Inverse Calculation with Noise – Solution of the Ill-Conditioning

As discussed previously, inverse problems are prone to be ill-conditioned. This means that small disturbances in the calculation inputs may cause large errors in the solution. Typically, dealing with measurement data that serve as calculation input for the inverse calculation automatically leads to the presence of disturbed data. The disturbance of the data is caused by noise that is part of the measured signal and does not belong to the system response.

In order to study the effects of noisy data to the solution on the inverse problem, the inverse calculation at the simple 2-DOF system is expanded. The load and the system remain in the same configuration. Again, the forward solution serves as a comparative verification. The result in form of the displacement vector **y**(t) is used as calculation input for the inverse calculation. However, in this case, the displacements vector is disturbed by a noise term **e**(t), representing white noise, so that the verification procedure is due to Figure 3.10.

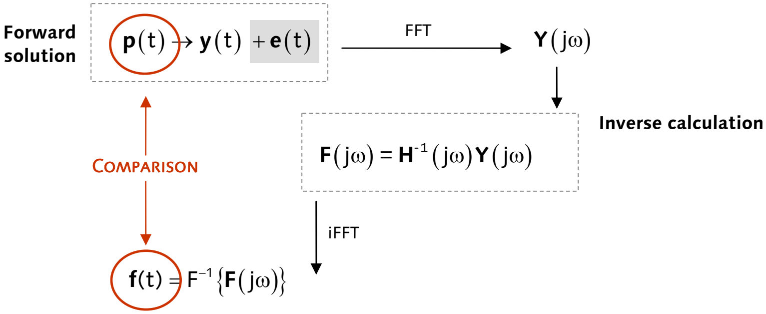

Figure 3.10: Verification of the inverse calculation with noisy data

For the inverse calculation at the 2-DOF system, a noise ratio of V_r = 3 % is chosen (see Appendix B). A comparison of the undisturbed displacement signal $y_1(t)$ at the DOF 1 to the disturbed displacement signal $y_1(t) + e(t)$ is shown in Figure 3.11. Indeed, the error can be considered small.

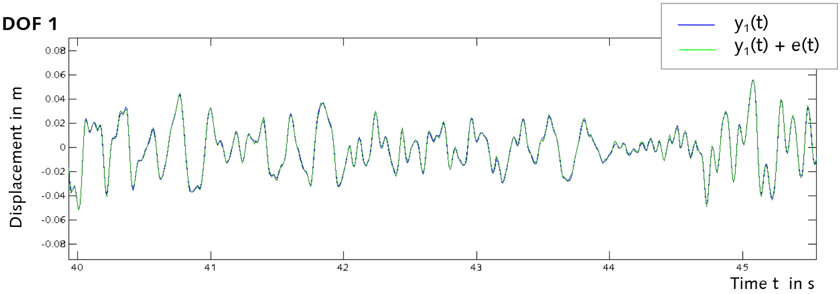

Figure 3.11: Displacement at DOF 1 with and without noise

The effects of this small disturbance in the input signal to the inversely calculated load are depicted in Figure 3.12 and Figure 3.13, at both DOFs each in time domain and frequency domain.

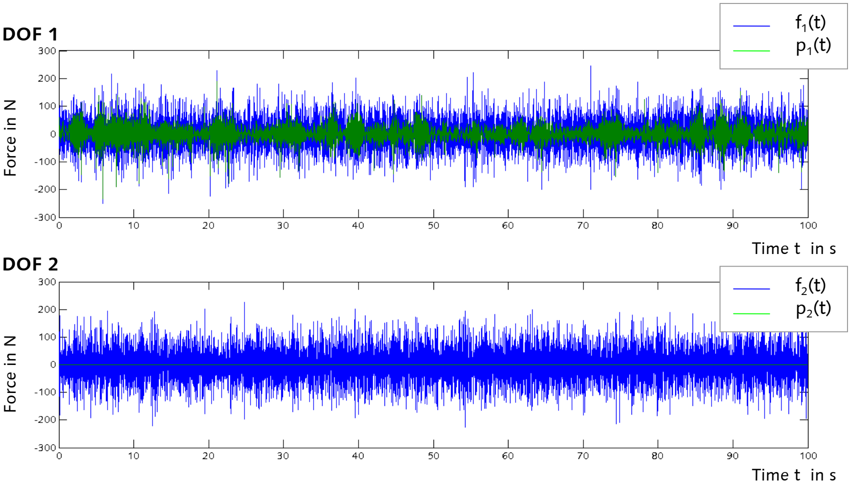

DOF 1

DOF 2

Figure 3.12: Load comparison at the 2-DOF system in the time domain with noise

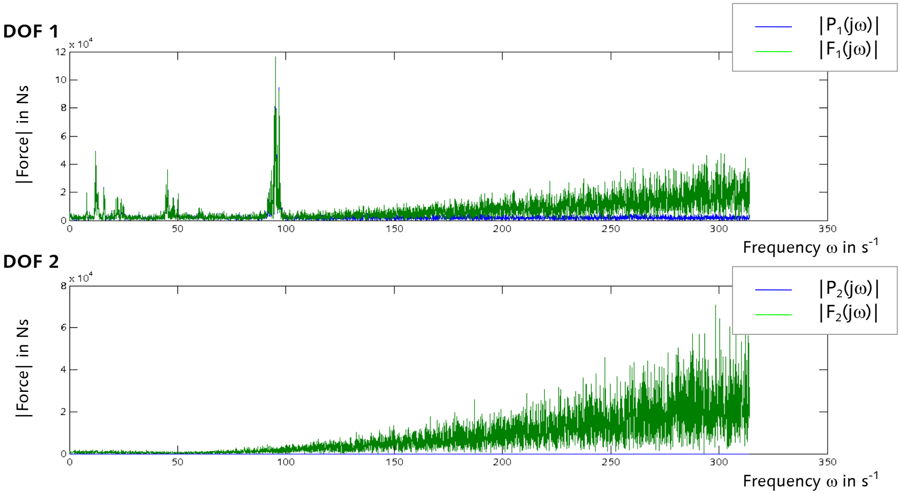

DOF 1

DOF 2

Figure 3.13: Load comparison at the 2-DOF system in the frequency domain with noise

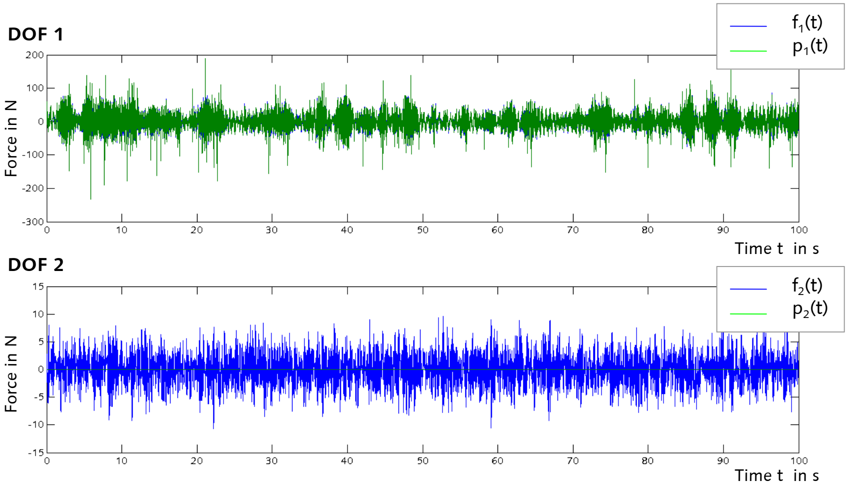

Figure 3.14: Load comparison at the 2-DOF system in the time domain – low-pass filtered noise

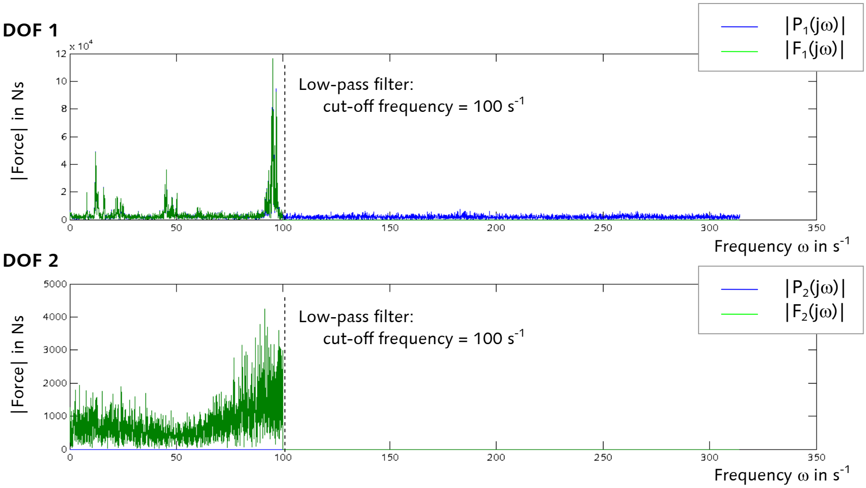

Figure 3.15: Load comparison at the 2-DOF system in the frequency domain – low-pass filtered noise

The time-domain comparison of the applied load **p**(t) to the inversely calculated load **f**(t) in Figure 3.12 clearly shows large differences between both graphs. The amplitudes of the inversely calculated load considerably exceed the amplitudes of the applied load. The reason becomes obvious by looking at the frequency-domain comparison of both loads in Figure 3.13. Up to a certain frequency, both graphs seem to match perfectly. With increasing frequency, the inverse load shows continuously rising spectral amplitudes. The inverse system amplifies the high frequency components. This behavior was already indicated by the undisturbed case – see section 3.3.3, Figure 3.9. In case of noisy data that represent small disturbances in the calculation input, these amplifications affect the solution even more strongly. This characteristic shows the ill-conditioning of the inverse problem.

Apparently, the ill-conditioning behavior affects the high frequency components of the inverse solution in particular. For this reason, a low-pass filter at the inversely calculated load is suggested to overcome the ill-conditioning. The filter has to be set in such a way that the lower frequencies that define the load are not influenced, but only the amplification of the high frequencies is eliminated.[41] In the presented case, the cut-off frequency for the low-pass filter is set to $\omega_{cut\text{-}off} = 100\ s^{-1}$.

The comparison of the filtered inverse load to the applied load is given in Figure 3.14 and Figure 3.15, again at both DOFs in time domain and frequency domain. The cut-off frequency of the low-pass filter is clearly visible in the frequency domain depicted in Figure 3.15. All frequencies above the cut-off equal zero exactly. The lower part of the frequency spectrum remains unfiltered.

It is impotant, taking into account that the inverse calculation of **f**(t) is based on noisy displacement data **y**(t) + **e**(t), whereas the applied load **p**(t) is undisturbed (Figure 3.10). For this reason, a perfect match between the applied load and the inversely calculated load is not expected.

The DOF 1 shows very good accordance between the applied and the inverse load. The accordance can be quantified by the error calculated according to equation (3.65). The error value is $\varepsilon = 4.87\ \%$. This value determines the difference between the undisturbed applied load $\mathbf{p}_1(t)$ and the inversely calculated load $\mathbf{f}_1(t)$ that is calculated with an noise ratio of $V_r = 3\ \%$. For the DOF 2, the inverse calculation determines a load $\mathbf{f}_2(t)$. A mathematical quantification of the result quality is difficult because the applied load $\mathbf{p}_2(t)$ equals zero. The amplitudes of $\mathbf{f}_2(t)$ are small if compared to the amplitudes of the DOF 1. The maximum at DOF 2 is around 5 % of the maximum at DOF 1. A mathematical comparison of the error percentage and the noise percentage is incorrect, since they do not base on the same equation. Nevertheless, the two percentage values are in the same range what allows assuming that the inverse calculation procedure interprets the noise as an applied load.

Finally, the following conclusions can be derived: 1) Adding noise to the displacement data clearly points out the ill-conditioning behavior of the inverse problem. The ill-conditioning causes an amplification of the high frequencies, which can be treated very well with a low-pass filter. 2) The added noise is interpreted as an applied load. This behavior is expected since the purpose of the inverse calculation is not eliminating errors due to wrong input data, but rather calculating reliable results even if the input data are disturbed. 3) The accordance of the inversely calculated load to the applied load is very good, especially at the

---

[41] For a more detailed discussion of filter shall be referred to Appendix E.

loaded DOF 1. And 4) The error between the undisturbed applied load $\mathbf{p}_1(t)$ and the inverse load $\mathbf{f}_1(t)$ that is based on noisy displacement data is very small if visually inspected. This means, that the error value of $\varepsilon = 4.87\ \%$ represents a small error. This statement is important, because the error value does not allow an absolute estimate of the error. The error value only can serve as reference between the error values ε calculated within this work.

3.3.5 The Least-Squares Approach

In order to demonstrate the application of the least-squares approach for the solution of the inverse problem, the following calculation is shown. The stochastic load from Figure 3.4 is applied to the 2-DOF system. The inverse FRF matrix is assembled as was mentioned above and the calculated displacements of the forward solution are not disturbed by a noise term. The solution is obtained using equation (3.51). The complete displacement vector of dimension 2x1 is used. Because the DOF 2 is unloaded, the load vector shall be reduced to the loaded DOF 1. The FRF matrix $\mathbf{H}$ is truncated, thereby eliminating the second column. Since $\mathbf{H}$ is no longer regular and in a square form, the Moore-Penrose pseudoinverse has to be calculated according to equation (3.58) to obtain the inverse FRF matrix $\mathbf{H}^+$. Consequently, the problem appears with the following dimension.

$$\left[F_{1,1}\right] = \left[H_{1,1}^{+} \quad H_{1,2}^{+}\right] \cdot \begin{bmatrix} Y_1(j\omega) \\ Y_2(j\omega) \end{bmatrix} \tag{3.66}$$

The solution of the inverse problem using the least-squares approach is given in Figure 3.16. The time-domain comparison of the inverse load $\mathbf{f}(t)$ to the applied load $\mathbf{p}(t)$ is shown for both DOFs. As expected, the inversely calculated load at the DOF 2 equals zero, because it is set to zero under constraint due to the problem definition. For this reason, a depiction of the DOF 2 in frequency domain is omitted. The frequency spectrum of the loads at the DOF 1 is shown below. The inversely calculated load matches the applied load perfectly, both in time domain and frequency domain. This statement is proved by the time-domain error of $\varepsilon = 0.00\ \%$.

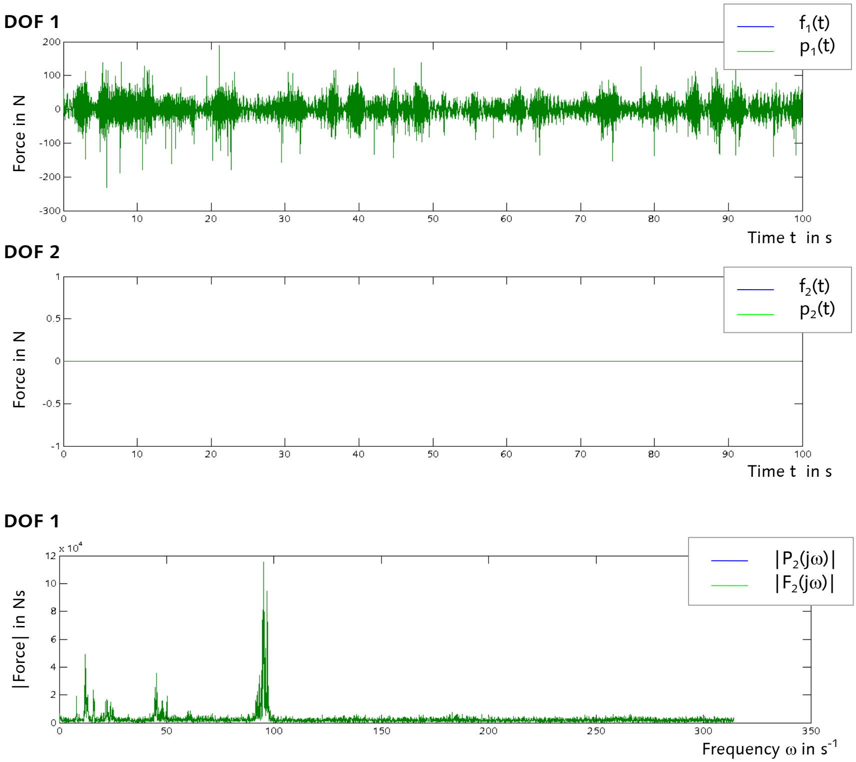

Figure 3.16: Least-squares solution for the inverse problem at the 2-DOF system

3.4 Summary

Different methods for the solution of inverse problems are discussed. The advantages and drawbacks of several methods are set into relation to the requirements of the inverse load calculation for wind turbines. The DFD – a frequency-domain based procedure – is chosen. The discussion reveals that this method matches the specific requrements best. The theoretical fundamentals of the method are presented.

Using a simple numerical 2-DOF example, the system properties are discussed by means of the inverse FRF matrix. The implementation of the mathematical procedure for the inverse calculation in the frequency domain is shown.

The ill-conditioning of the inverse problem is illustrated by adding artificial white noise to the displacement signals that serve as calculation input for the inverse calculation. The effects of the ill-conditioning become obvious by an amplification of the high frequencies in the inversely calculated load. It is shown, that the ill-conditioning can be handled very well using a low-pass filter.

Disturbing the input data by adding noise shows the inverse calculation interpreting the noise as applied load. If the ratio between the noise and the load is small, the results of the inverse calculation are very good.

An error value is introduced that allows estimating the quality of the inverse calculation if compared to a known applied load. This error value allows comparing the calculations within this work, but cannot be taken for assessing an absolute error.

Thus far, all calculations are performed at determined systems. In practice, over-determined systems are aspired to, because this approach allows for the elimination of random errors. For this reason, the results for a least-squares solution are shown.

4 Inverse Load Calculation at a 5 MW Onshore Wind Turbine Model

The previous section explained the theoretical foundations of the inverse load calculation in the frequency domain. Important characteristics such as the properties of the inverse system, the handling of the ill-conditioning in case of disturbed calculation input data, and the solution using a least-squares approach were discussed for a simple 2-DOF system.

However, this simple 2-DOF system is still far away from representing a real wind turbine. In order to approach more realistic problems, this section deals with the inverse load calculation using a model simulated with the comprehensive simulation code FAST.[42] FAST can perform simulations of both onshore and offshore wind turbines. In onshore simulations, FAST accounts for the coupled dynamics of the wind inflow, aerodynamics, elasticity, and control of the wind turbine.[43] In order to permit fast simulation runs, FAST is limited to the essential number of DOFs. Thus, on one hand, FAST is able to model realistic wind turbine characteristics with an appropriate quality. On the other hand, the amount of system information that has to be considered and interpreted within the inverse calculation is limited. The combination of both features is advantageous for verifying the inverse load calculation procedure. The model chosen is a 5 MW onshore wind turbine with a tubular steel tower.[44] This wind turbine size represents the current state of technology. The FAST simulation calculates structural dynamic responses that can be output both as accelerations and as displacements. Since measurements usually record acceleration data and the chosen inverse calculation procedure demands for displacements, the simulation results are used to show the integration process. The accuracy of the integration is assessed.

Hence, in contrast to the simple 2-DOF system the following additional effects are taken into account and studied in this section.

- Loads from defined wind-inflow conditions
- Coupled dynamics of the wind inflow, aerodynamics, elasticity, and control of the wind turbine
- Nonlinearities in the system model (particularly in the rotor aero/structure/control)
- Integration of acceleration signals to displacements

The verification procedure of the inverse calculation basically follows the same steps as the procedure introduced in section 3.3.1, Figure 3.2. The solution of the forward problem is

---

[42] See JONKMAN AND BUHL (2005) [45].

[43] See JONKMAN ET AL. (2008) [47].

[44] See JONKMAN ET AL. (2009) [49].

used as calculation input for the inverse load calculation. The calculation input is either given by displacement data **y**(t) or by acceleration data **a**(t). The model is defined by the system matrices and the applied load serves as a reference for the inversely calculated load, which is again illustrated in Figure 4.1. Under onshore conditions, the scope of the inverse load calculation is the determination of a rotor thrust force (see section 2.2.2 and Figure 2.9), which is denoted as **f**(t) in Figure 4.1. For reasons of comparability, the applied load **p**(t) is not the wind field, but the rotor thrust force of the FAST simulation. The simulated rotor thrust force is considered a reasonable approximation of the applied load. The rotor thrust output from FAST does not represent the applied aerodynamic thrust, but the force transmitted between the rotor and the low-speed shaft. This force includes both the applied aerodynamic thrust as well as the rotor inertia forces from the turbine vibration.

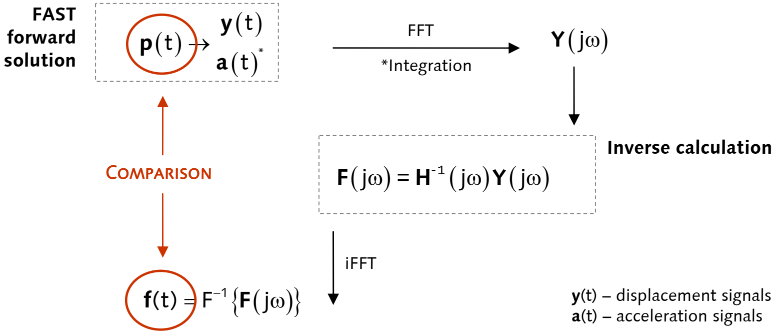

Figure 4.1: Scheme for the verification of the inverse calculation using FAST

In this chapter, the theoretical basics of the simulation environment are first given in section 4.1. Thereafter, the analysis in FAST is described, including the chosen model (section 4.2). Additionally, the linearization is discussed, which is needed to obtain the system matrices of the wind turbine model. The model description includes a description of the settings chosen for the FAST simulation. Section 4.3 presents the results of the inverse load calculation. The inverse load calculation requires the integration and the filtering of signals. Appendix E summarizes the methods and assumptions made.

4.1 Theoretical Fundamentals of FAST and AeroDyn

FAST, which stands for "Fatigue, Aerodynamics, Structures, and Turbulence", is a comprehensive aeroelastic simulator. FAST is developed for computing the extreme and fatigue loads of two- and three-bladed horizontal-axis wind turbines (HAWTs). FAST is able to predict loads for both onshore and offshore wind turbines. This section does not give a complete overview of all the capabilities of FAST. Since this section focuses on the simulation of a three-bladed horizontal-axis onshore wind turbine, the given description of the theoretical foundations is limited to those conditions. The described theory is basically taken from the FAST User's Guide[45], unless further references are cited. Subsequently, the theory for the comprehensive simulation code FAST and for the subroutine AeroDyn[46] is given. AeroDyn accounts for the calculation of the aerodynamics of a HAWT.[47] In this work, the FAST version v7.00.01 [116] is used.

4.1.1 FAST

In general, FAST enables an aero-hydro-servo-elastic simulation for horizontal-axis wind turbines. Several turbine configurations can be modeled. They can be categorized as follows:

- Number of rotor blades - two-bladed or three-bladed
- Wind direction - upwind or downwind
- Hub configuration - rigid or teetering
- Yaw system - control driven or rotor- and/or tail-furling
- Site condition - land-based or sea-based
- Foundation type - rigid or flexible
- Offshore foundation - monopile or floating

Basically, the system model is a combination of multi-body and modal dynamics formulations. Structural components such as the platform, the nacelle, the generator, the gears, the hub, and the tail are modeled as multi-bodies. The blades and the tower are described by a modal-dynamics formulation. A three-bladed HAWT is modeled by a total of 24 DOFs. The number of DOFs result from 6 DOFs for the translational and rotational motions of the foundation relative to the inertial frame, 4 DOFs for the tower motions, 1 DOF for the yawing motion of the nacelle, 1 DOF for the generator azimuth angle, 1 DOF for the rotational flexibility of the drivetrain, 3 DOFs for the 1st flapwise tip motion at each blade, 3 DOFs for the 2nd flapwise tip motion at each blade, 3 DOFs for the 1st edgewise tip motion at each blade, 1 DOF for rotor-tail and 1 DOF for rotor-furl. Any combination of the DOFs can be enabled.

The structural dynamics model is based on the solution of the kinematics expressions for the positions, velocities, and accelerations at all appropriate DOFs. Using Kane's dynamics enables establishing the partial velocity vectors. The combination with the generalized active and inertia forces leads to the complete non-linear time-domain equation of motions in general form[48]

$$\boldsymbol{M}(\mathbf{q},\mathbf{u},t)\ddot{\mathbf{q}} + f(\mathbf{q},\dot{\mathbf{q}},\mathbf{u},\mathbf{u}_d,t) = \mathbf{0} \tag{4.1}$$

---

[45] See Jonkman and Buhl (2005) [45].

[46] The version AeroDyn v13.00.00 [115] is used.

[47] For a discussion regarding the calculation of the hydrodynamics in case of an offshore wind turbine shall be referred to section 6.1.1.

[48] See Jonkman (2007) [46].

with the inertia mass matrix $\mathbf{M}$, the non-linear forcing function $f(\ )$, the vector of displacements $\mathbf{q}$, its derivatives in time $\dot{\mathbf{q}}$ (vector of velocities) and $\ddot{\mathbf{q}}$ (vector of accelerations), the vector of control inputs $\mathbf{u}$, the vector of wind input disturbances $\mathbf{u}_d$, and the time t.

In equation (4.1)[49], the inertia mass matrix $\mathbf{M}$ has dimensions n x n, with n representing the number of DOFs. The time-dependent inertia mass matrix depends non-linearly on the displacement vector $\mathbf{q}$ at the DOFs and the control inputs $\mathbf{u}$. The vector $\ddot{\mathbf{q}}$ is the second-order time derivative of the displacement vector $\mathbf{q}$, presenting the accelerations. The forcing function f is time-dependent as well and depends non-linearly on the displacements $\mathbf{q}$ at the DOFs, their first-order time derivative $\dot{\mathbf{q}}$ (velocities), and the input vectors for the controls $\mathbf{u}$ and the wind disturbances $\mathbf{u}_d$. The system of equations can be solved for each time step for the accelerations. FAST uses a matrix inversion method based on the Gauss elimination. To solve the resulting differential equations a fourth-order Adams-Bashforth predictor and Adams-Moulton corrector is applied. Since the method is not self-starting, a fourth-order Runga-Kutta method is used for the first four steps.[50]

To set up the structural dynamics model, the foundation pitch, roll, and yaw rotations employ small angle approximations with correction of orthogonality. The motions of the blades and the tower are limited to moderate deflections. All other DOFs may exhibit large displacements without loss of accuracy.

The blades and tower in FAST are modeled with a nonlinear Bernoulli-Euler beam formulation, but using a linear superposition of shape functions derived from a linear modal analysis. To ensure coordinate system orthogonality, small angle approximations with correction are employed, which includes correction for radial shortening. The beam elements are straight with linear isotropic material and no mass or elastic offset. The description of the tower is initially limited to four different mode shapes, two in fore-aft and two in side-side direction. The mode shapes take the form of a sixth-order polynomial, cantilevered at the base. This assumption requires zero deflection and slope at the base, whereas the tower top deflection is normalized to 1. The blade mode shapes are defined similar to the tower mode shapes. The two flapwise modes and the edgewise mode are defined with respect to the local structural twist that is three-dimensional since the shape twists with the blade. The tip of a twisted blade will deflect in both the in-plane and out-of-plane directions due to a pure flapwise deflection – the edgewise mode works similar. The mode shapes are input parameter to FAST.

The drivetrain is modeled as an equivalent shaft separating the generator from the hub. The shaft is represented by a linear torsional spring and a linear torsional damper. The generator defines the rotational speed at the generator side of the shaft. Several generator models for control purposes are available (see JONKMAN AND BUHL (2005) [45], p.11). The nacelle yaw is modeled using a yaw spring and a yaw damping. Both parameters can be set in a way so

---

[49] See JONKMAN (2011) [50].

[50] See WILSON ET AL. (1999) [102].

that either a perfect hinge with no resistance forces, a free-yaw machine with yaw damping, or the flexibility and the damping of a yaw-driven turbine whose commanded yaw position is held constant can be modeled. Additionally, the nacelle yaw motion can be controlled actively during simulation.

Since rotor-furl, tail-furl, and consequently tail-fin aerodynamics represent unusual turbine configurations that are not discussed in this work, these aspects are not described.

For the foundation, FAST provides the modeling of either an onshore foundation, a fixed-bottom offshore foundation, or floating offshore configurations. Disabling all three options results in a rigid cantilever connection of the tower to the inertia frame (ground).

During time-marching analysis five basic methods of control are available: pitching the blades, controlling the generator torque, applying the high-speed shaft (HSS) brake, deploying the tip brakes, and yawing the nacelle.

The time-marching simulation allows the computation of special events such as turbine startup, normal pitch-to-feather shutdown, one blade feather accidentally, HSS brake shutdown after loss of grid, HSS brake shutdown with generator brake, normal tip brake shutdown, tip brake shutdown after loss of grid, accidental deployment of tip brake, idling turbine, parked turbine.

FAST generates different output files depending on the settings in the input files. For time-marching analysis various output parameters are defined. The output files contain columns of time series of each requested output variable. The output variables can be summarized into the following categories[51]: wind motions, blade tip motions, blade local span motions, blade pitch motions, shaft motions, nacelle inertial measurement unit motions, nacelle yaw motions, tower-top/yaw-bearing motions, local tower motions, platform motions, blade root loads, blade local span loads, hub and rotor loads, shaft strain gage loads, generator and HSS loads, tower-top/yaw-bearing loads, tower base loads, local tower loads, platform loads.

Beyond that, FAST provides interfaces to other software packages. Thus, FAST can be used as a preprocessor for generating ADAMS[52] datasets of wind turbine models. Additionally, a FAST to master controller is implemented as a dynamic-link-library (DLL) in the style of Garrad Hassan's Bladed wind turbine software package. And finally, the interface between FAST and Simulink[53] with MATLAB enables advanced turbine controls in Simulinks convenient block diagram form. The software tool FAST is certified by Germanischer Lloyd Wind Energie for "the calculation of onshore wind turbine loads for design and certification".

---

[51] All output categories regarding teeter, rotor-tail, and rotor-furl are omitted. For more details see JONKMAN AND BUHL (2005) [45].

[52] ADAMS is used to imply ADAMS®

[53] Simulink is used to imply Simulink®

4.1.2 AeroDyn

AeroDyn is a set of routines for predicting the aerodynamics of horizontal-axis wind turbines. AeroDyn is proposed for usage in conjunction with an aeroelastic simulation tool. Running FAST inherently implies the use of AeroDyn as subroutine to predict the aerodynamics.

AeroDyn can calculate wind turbine wake. One of the two models can be used: the blade element momentum (BEM) theory and the generalized dynamic wake (GDW) theory. The blade element momentum theory is the classical standard. BEM allows various corrections such as incorporating the aerodynamic effects of tip losses, hub losses and skewed wakes. The generalized dynamic wake theory is a more recent model. All of the effects described for the BEM are automatically included in the GDW. Beyond that, the generalized dynamic wake theory is useful for modeling non-stationary wake dynamics. Both theories are used to calculate the axial induced velocities from the wake in the rotor plane. Additionally, AeroDyn has the option of calculating the rotational induced velocities.

Particularly for yawed wind turbines, a dynamic stall model based on the semi-empirical Beddeos-Leishman model is available. The tower shadow and upwind tower-influences are calculated as well. These aerodynamic models are based on potential flow around a cylinder and an expanding wake. A detailed discussion of the underlying assumptions and equations is given in MORIARTY AND HANSEN (2005) [69].

The communication between FAST and AeroDyn is defined by input and output files. AeroDyn uses the inputs from the main FAST input file. Additionally, a simple text file is needed that defines hub-height wind data, including wind shears and gusts.

Moreover, full-field wind data are required. In this work, TurbSim[54] is used whose theoretical foundations are thoroughly described in JONKMAN (2009) [44]. TurbSim is a stochastic, full-field, turbulent-wind simulator. TurbSim describes the full-field wind data by two-dimensional vertical rectangular grids of three-component wind-speed vectors fixed in space that march past the turbine at mean wind speed. Taylor's frozen turbulence hypothesis is used to obtain local wind speeds by interpolating the TurbSim-generated wind fields in both time and space. Spectra of velocity components and spatial coherence are defined in the frequency domain. An inverse Fourier transformation produces time series. This procedure demands a stationary process. The simulation of non-stationary components is done by superimposing coherent turbulent structures onto the generated time series or by running separate simulations with different wind inputs.

4.2 Analysis in FAST

Subsequently, the chosen wind turbine model will be described in detail. FAST has two different analysis modes – simulation and linearization. Both are used in this work. The objectives as well as the input and output parameters are described.

---

[54] The version TurbSim v1.50 [117] is used.

4.2.1 Description of the 5 MW Wind Turbine Model

The scope of the study using FAST is to investigate the effects of coupled dynamics of the wind inflow, aerodynamics, elasticity, and control of the wind turbine. In order to use a wind turbine type that represents the current state of technology, the NREL 5 MW reference wind turbine model is chosen. The structural properties of this model are described in JONKMAN ET AL. (2009) [49]. A brief summary is given in Table 4.1.

The NREL 5 MW reference wind turbine model is a conventional three-bladed upwind variable-speed variable pitch-to-feather-controlled turbine. An illustration of the wind turbine model is given in Figure 4.2, right. The turbine has a hub height of 90 m and rotor-blade lengths of 63 m. A scheme of the variable definition as used in FAST is shown in Figure 4.2, left. To focus exclusively on the aeroelastic interaction and turbine control influences, a simple structure is desired. For this reason, the tubular tower structure with a rigid foundation is preferred. Any combination of the available DOFs can be enabled. Here, 16 DOFs are enabled so that the dynamics of the following components are represented:

• 1st and 2nd flapwise blade modes (3 blades)	_ 6 DOFs
• 1st edgewise blade modes (3 blades)	_ 3 DOFs
• Drivetrain rotational flexibility, generator, yaw	_ 3 DOFs
• 1st and 2nd tower bending modes in fore-aft and side-side direction	_ 4 DOFs

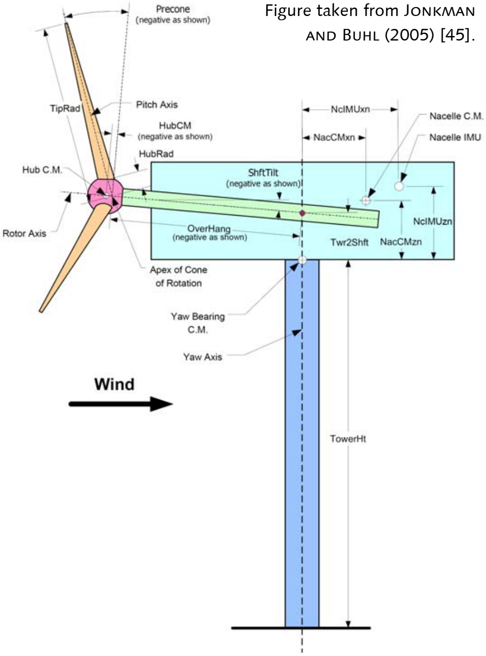

Figure taken from JONKMAN AND BUHL (2005) [45].

Figure 4.2: Variable definition in FAST

Table 4.1: Summary of the NREL 5 MW reference wind turbine model properties

Tower properties		
Material	steel	
Shape	tubular	
Discretization 1)	10	segments
Height of tower	87.60	m
Base diameter	6.00	m
Thickness of base tower section	0.027	m
Top diameter	3.87	m
Thickness of top tower section	0.019	m
Young's modulus	$2.10 \cdot 10^5$	N/mm^2
Shear modulus	$8.08 \cdot 10^4$	N/mm^2
Effective density of the steel 2)	8,500	kg/m^3
Overall integrated mass	347,460	kg
Structural damping ratio 3)	1	%
Rotor blade structural properties		
Number of blades	3	
Material	glass fiber	
Discretization	17	elements
Rotor radius	63	m
Overall integrated blade mass	17,740	kg
Nominal second mass moment of inertia 4)	11,776,047	$kg \cdot m^2$
Nominal first mass moment of inertia 4)	363,231	$kg \cdot m$
Nominal radial CM location 4)	20.047	m
Structural damping ratio 5)	0.477465	%
Hub and nacelle properties		
Hub height	90	m
Horizontal upwind location w.r.t. tower center line	5.00	m
Vertical distance from tower top	2.40	m
Shaft tilt	5	°
Hub mass	56,780	kg
Hub inertia about the shaft	115,926	$kg \cdot m^2$
Nacelle mass	240,000	kg
Nacelle inertia about yaw axis	2,607,890	$kg \cdot m^2$
Drivetrain properties		
Rated rotor speed	12.1	rpm
Generator inertia about high-speed shaft	534.116	$kg \cdot m^2$

1) The radius and thickness is assumed to be linearly tapered from the tower base to the tower top.

2) The density of 8,500 kg/m^3 is meant to be an increase above steel's typical value of 7,850 kg/m^3 to account for paint, bolts, welds, and flanges that are not accounted for in the tower thickness data.

3) The structural damping ratio is the percentage of critical damping in all tower modes of the isolated tower, without the rotor-nacelle assembly mass presented.

4) With respect to the blade root.

5) The structural damping ratio is the percentage of critical damping in all modes of the isolated blade.

The NREL 5 MW reference wind turbine model is created with a heavy emphasis on the public information of the REpower 5M machine. For this reason, this verification study will also gain useful predictions for the investigation presented in section 5, since section 5 will deal with the inverse load calculation at a wind turbine support structure carrying a REpower 5M machine.

4.2.2 Time-Marching Simulation

Simulation is time-marching of the non-linear equations of motion. During simulation, the wind turbine aerodynamics and the structural response to wind-inflow conditions are determined in time. Output data include time series of the aerodynamic loads as well as the loads and deflections of the structural members of the wind turbine.

Using TurbSim [44], stochastic turbulent wind fields are generated as input for the simulations. Three load cases (LC) are defined according to IEC 61400-1 Ed. 3: 2005 [107]. Normal wind conditions for power production conditions are chosen. Such load conditions are dominant contributions to fatigue, which the inverse load calculation aims to predict.

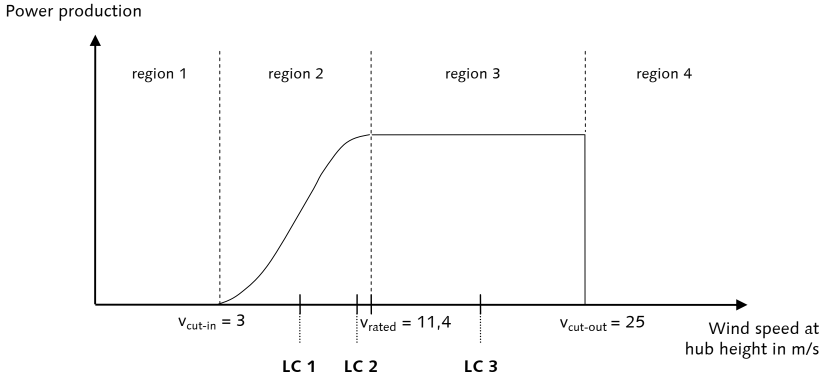

Figure 4.3: Qualitative power curve of a wind turbine and chosen load cases (LC)

In order to study the influences of turbine control, load cases with mean wind speeds at hub height between cut-in and rated wind speed (middle of region 2), near rated wind speed and between rated and cut-out wind speed (middle of region 3) are chosen. The qualitative relation between the power curve of a wind turbine and the wind speed is given in Figure 4.3. Thus, conditions with little expected control activity (load case 1) and high expected control activity (load case 3) are generated. In addition, load case 2 represents the transition between controllers where maximum thrust occurs. An overview of the load cases is given in Table 4.2.

Table 4.2: Load cases for the FAST verification study

Load case	**Mean wind speed** [1]	**Turbulence type**	**Turbulence characteristic**
1	7 m/s	NTM [2]	B [3]
2	12 m/s		
3	18 m/s		

[1] At hub height, power law exponent 0.20. No horizontal shear about rotor disk is considered.
[2] Normal turbulence model [107].
[3] Medium turbulence characteristic – 14 % turbulence intensity at 15 m/s [107].

Table 4.3: Output signals for the FAST verification study

Turbine signals	
WindVxi	Normal downwind component of the hub-height wind velocity (m/s)
HorWndDir	Horizontal hub height wind direction (deg)
PtchPMzc1 to ~3	Blade pitch angle (deg)
LSSTipVxa	Rotor azimuth angular speed (rpm)
YawPzn	Nacelle yaw angle (deg)
GenTq	Electrical generator torque (kNm)
Motions of the structure	
YawBrTDxt	**Tower top fore-aft deflection (m)**
YawBrTAxp	**Tower top fore-aft acceleration (m/s^2)**
TwHt$_i$TDxt [1]	**Local tower fore-aft displacements at the i-th tower gage (m)**
TwHt$_i$ALxt	**Local tower fore-aft accelerations at the i-th tower gage (m/s^2)**
PtfmTDxt	horizontal surge displacement (m)
PtfmTAxt	horizontal surge acceleration (m/s^2)
Force signals	
LSShftFxa / RotThrust	**LSS[2] thrust force, constant along shaft and equivalent to rotor thrust force (kN)**
YawBrFxn	Rotating (with nacelle) tower top / yaw bearing shear force (kN)

[1] The output of the local tower displacements is not an available option of the current FAST version v7.00.01. For this reason, the FAST source code was adjusted so that the output of the local tower displacements is enabled.
[2] LSS – low-speed shaft.

The simulation settings are run in a way that closely meets the requirements from the design stage and from practical field test conditions. The simulation time is set to 600 s. Also, the time- to frequency-domain transforms are sufficiently accurate for this simulation length. The simulation time steps are set to dt = 0.0125 s. Output data are stored every 0.05 s.

Full-span collective blade-pitch control and variable-speed generator-torque control are enabled for the turbine control. FAST also provides nacelle yaw control, which is not used in this study because the influence of a changing yaw angle is not of high interest in the verification of the inverse load calculation. Only an additional coordinate transformation would be required.

The output signals, requested from the FAST analysis, are summarized in Table 4.3. The turbine signals are principally chosen for a plausibility check of the FAST analysis and visualization of the turbine control. The motions of the structure and the force signals serve as input signals for the inverse load calculation. The input signals also include the rotor thrust force computed by FAST, which is used as a comparative signal for the inversely calculated load. The signals used for the inverse calculation are bold.

The results of the simulation are presented in connection with the inverse load calculation, which are part of section 4.3. A brief summary of the results is also given in PAHN ET AL. (2012) [80] and in PAHN AND ROLFES (2012) [81].

4.2.3 Linearization

FAST can extract linearized representations of the complete non-linear aeroelastic wind turbine, as described in the FAST user's guide [45]. This capability is used for developing state matrices and is useful for determining the full system modes of an operating stationary HAWT through the use of an eigenanalysis. The linearization process consists of two steps: computing a periodic steady state operating point condition for the DOFs, and numerically linearizing the FAST model about the operating point to form periodic state matrices. Then, the output state matrices can be azimuth-averaged for non-periodic or time-invariant controls development.

To obtain the periodic steady state solution, determining an operating point to linearize the model about is the first step in the linearization process. An operating point is a set of values of the system DOF displacements, DOF velocities, DOF accelerations, control inputs, and wind inputs that characterize a stationary condition of the wind turbine. For a wind turbine operating in stationary winds, this operating point is periodic. This periodicity is driven by aerodynamic loads, which depend on the rotor azimuth position, caused by shaft tilt (which leads to gravitational loads), wind shear, yaw error, tower shadow, and further gravitational loads if the tower is deflected to the thrust loading considerably. The computation of the steady state solution is done iteratively. FAST integrates the non-linear equation of motions in time until the solution converges. Convergence is defined by the 2-norm of the differences between conditions at the beginning and the end of each period of rotor revolution of the rotor. The 2-norm is computed for the angular displacement vector differences and the angular velocity vector differences.

Once a periodic steady state solution is found, the linearization step follows. FAST numerically linearizes the complete non-linear aeroelastic model about the operating point. The linearized representation of the model is periodic, because the operating point is periodic with the rotor azimuth position. The output of FAST is given at a number of equally spaced rotor azimuth steps. The resulting matrices can be averaged over the different steps. The FAST linearization routine can be used to develop both first-order and second-order linearized representation of the non-linear aeroelastic model.

A description of the system is needed to calculate loads inversely. For the FAST verification study, the linearization is used to obtain the second-order system matrices of the 5 MW reference wind turbine model.

The calculation of an operating point depends on whether the rotor is 'stationary' or 'spinning'. In case of a spinning rotor, FAST allows the differentiation between a 'constant-speed turbine' and a 'variable-speed turbine'. The determination of the operating point for a variable speed turbine can be done by a trim analysis. A trim analysis is the process of trimming a control input in order to reach a desired azimuth-averaged rotor speed while holding all other inputs constant. Three cases are available that allow trimming the 1) nacelle yaw control input, 2) electrical generator torque that is recommended for variable speed turbines in region 2, and 3) rotor collective blade pitch that is recommended for variable-speed turbines in region 3. An illustration of the different options for the calculation of the operating point is given in Figure 4.4.

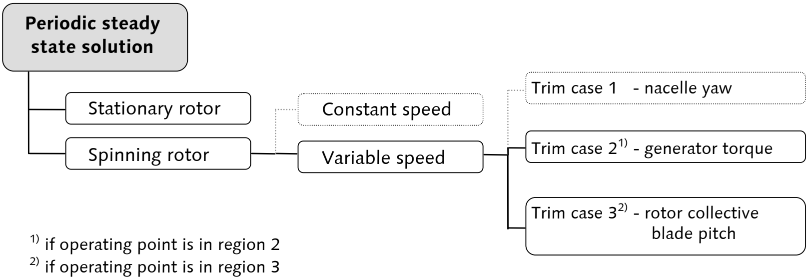

Figure 4.4: Options to calculate the operating point for the linearization in FAST

4.2.4 System Matrices and Modal Reduction

The results of the linearization, which are the system matrices, amongst others, are gained by a post-processing step that is carried out after the linearization in FAST. With the FAST package a MATLAB routine is available that allows the linearization results to be output in MATLAB format.

- Full-system eigenfrequencies

In case of a stationary rotor, the steady state solution is not periodic because the rotor is not spinning. Thus, the turbine is represented in standstill, which could be used as an approximation for the wind turbine in operation. In order to determine if this approximation is appropriate or if the system matrices need to be calculated under spinning rotor conditions for a variable-speed turbine, a short case study is presented. The three following settings are calculated.

- Setting i) A stationary rotor.
- Setting ii) A variable-speed wind turbine with a spinning rotor and a constant wind speed in region 2 that implies trim case 2, which is regulated by the generator torque.
- Setting iii) A variable-speed wind turbine with a spinning rotor and a constant wind speed in region 3 that implies trim case 3, which is regulated by the rotor collective blade pitch.

The chosen linearization paths are marked by the solid lines in Figure 4.4. The setting i) requires disabling the generator DOF; the initial conditions of the linearization are set to zero. Brief summaries of the setting ii) and iii) are given in Appendix C.

The case study of the linearization is based on the comparison of the eigenfrequencies. The eigenfrequencies of the NREL 5 MW reference wind turbine model are already known from its documentation.[55] The full-system eigenfrequencies are calculated by FAST and in addition by ADAMS, whereas FAST was used to build up the model. Comparing the eigenfrequencies that result from the three settings to the given eigenfrequencies allows demonstrating the accuracy of the calculated linearization.

Table 4.4: Full-system eigenfrequencies of the NREL 5 MW reference wind turbine model in Hz

	Reference values		Calculated eigenfrequencies		
Mode	**FAST**	**ADAMS**	**Setting i)**	**Setting ii)**	**Setting iii)**
1st Tower fore-aft	0.3240	0.3195	0.3243	0.3263	0.3297
1st Tower side-side	0.3120	0.3164	0.3137	0.3208	0.3211
1st Drivetrain Torsion	0.6205	0.6094	0.6199	1.6990	1.6354
1st Blade Assym. Flap. Yaw	0.6664	0.6296	0.6673	0.5645	0.5762
1st Blade Assym. Flap. Pitch	0.6675	0.6686	0.6756	0.7133	0.7315
1st Blade Collective Flap.	0.6993	0.7019	0.6988	0.8216	0.8500
1st Blade Assym. Edge. Pitch	1.0793	1.0740	1.0796	0.9560	0.9163
1st Blade Assym. Edge. Yaw	1.0898	1.0877	1.0911	1.2261	1.2514
2nd Blade Assym. Flap. Yaw	1.9337	1.6507	1.9209	1.8408	1.8210
2nd Blade Assym. Flap. Pitch	1.9223	1.8558	1.9963	2.0357	2.0169
2nd Blade Collective Flap.	2.0205	1.9601	2.0201	2.1066	2.1470
2nd Tower fore-aft	2.9003	2.8590	2.9188	2.9204	2.9061
2nd Tower side-side	2.9361	2.9408	2.9530	2.9538	2.9733

---

[55] See JONKMAN ET AL. (2009) [49], p. 30.

Table 4.4 shows the full-system eigenfrequencies. The columns labeled with FAST and ADAMS give the eigenfrequencies published in the documentation[55], which serve as reference values. The columns superscribed by the three settings contain the calculated eigenfrequencies[56] gained by the linearizations according to the described input variables. An emphasis is laid on the tower bending modes because they are of special interest for the inverse load calculation. The calculated eigenfrequencies of the tower bending modes match very well, which is true for all three settings. The modes for the drivetrain and the blades of setting i) are in particularly good accordance with the reference values. The blade modes of the settings ii) and iii) vary slightly in comparison to those given by the reference values. The drivetrain natural frequency changes dramatically between setting i) and ii) because the generator is locked in the former (giving a fixed-free mode) and free in the later (giving a free-free mode).

In this work, only the tower bending modes of the system are used for the inverse load calculation, as pointed out in section 2.2.2. As long as the tower bending modes are needed, each of the three presented settings i), ii), and iii) might be used.

- Reduction of the system

As a matter of fact, the system matrices, which lead to the eigenfrequencies and the corresponding modes (see Table 4.4), are based on the full system. Since the chosen approach for the inverse calculation[57] requires the fore-aft modes, the system has to be reduced to these modes.

The system is reduced according to an algorithm that is described, for example, in GASCH AND KNOTHE (1989) [26] and is summarized briefly in Appendix D. The reduction is based on the linear time-invariant equation of motion with n DOFs, as given previously in equation (3.14). By the means of a transformation matrix **T** that is left-multiplied to the system matrices of the EoM, the reduced system is created. Three system reduction methods exist that differ in the way in which they compose the transformation matrix. A brief discussion of these methods is given in Appendix D.

In this work, the dynamic characteristics of the system are decisive for the system reduction. Additionally, the chosen approach aims to reduce the system to a small number of DOFs. This requirement is particularly important if an updated FE model is used, which initially is described by a huge number of DOFs. For these reasons, the so-called modal reduction is chosen.

---

[56] The relation between the eigenfrequencies and the mode shapes is obtained by the use of an EXCEL sheet that requires the results of the post-processing MATLAB routine. The EXCEL sheet is part of the FAST package.

[57] See section „2.2.2 Scope of the Inverse Load Calculation“, page 24.

- System matrices for the inverse load calculation

FAST gives the square full-system matrices depending on the settings for the linearization (see section 4.2.3). The full-system matrices can be post-processed e.g. with MATLAB. The setting i) represents a stationary rotor, which requires disabling the generator and yaw DOF. For this reason, the system matrices are 14 x 14 in dimension. Since the rotor is not spinning, the rotor azimuth position is not changing and consequently, the system matrices are constant as well. The settings ii) and iii) consider a variable-speed turbine with a spinning rotor. A periodic steady state solution is found by trimming in ii) the generator torque and in iii) the rotor collective blade pitch. The generator DOF is enabled. Additionally, the system matrices are periodic about the rotor azimuth position. For the linearization, the system matrices are calculated at 36 rotor azimuth steps. For this reason, the matrices are 15 x 15 x 36 in dimension. In further calculations, these system matrices are azimuth-averaged, which leads to matrices of dimension 15 x 15.

Once the matrices are derived, the modal reduction can be performed. The post-processing with MATLAB allows for relating the vibration modes to the entries in the system matrices. An eigenvalue analysis gives the modal matrix. Since the system shall be reduced to the fore-aft tower bending modes,[58] the transformation matrix is composed of the eigenvectors of the 1st fore-aft tower bending mode and the 2nd fore-aft tower-bending mode. The transformation matrix is of dimension n x 2, with n = 14, 15.

$$\mathbf{T} = \begin{bmatrix} \mathbf{u}_{01}^{\text{fore-aft}} & \mathbf{u}_{02}^{\text{fore-aft}} \end{bmatrix}_{n,2} \tag{4.2}$$

Reducing the system matrices according to the theory of the modal reduction[59] gives the reduced mass and stiffness matrix, both of dimension 2 x 2.

$$\mathbf{K}^{\text{red}} = \mathbf{T}^{\mathrm{T}}\mathbf{K}\mathbf{T} \qquad \mathbf{M}^{\text{red}} = \mathbf{T}^{\mathrm{T}}\mathbf{M}\mathbf{T} \tag{4.3}$$

The reduced mass and stiffness matrices are diagonal and contain generalized entries due to the orthogonality of the eigenvectors. The comparison of the eigenfrequencies of the full system to the eigenfrequencies of the reduced system gives information about the quality of the system reduction. The comparison is shown in Table 4.5.

Table 4.5: Comparison of the full-system eigenfrequencies to the reduced-system eigenfrequencies

	Setting i)		**Setting ii)**		**Setting iii)**	
Mode	full	reduced	full	reduced	full	reduced
1st fore-aft tower bending	0.32 Hz	0.32 Hz	0.33 Hz	0.33 Hz	0.33 Hz	0.33 Hz
2nd fore-aft tower bending	2.92 Hz	2.92 Hz	2.92 Hz	2.94 Hz	2.91 Hz	2.96 Hz

---

[58] An explanation of the scope of the inverse calculation is given in section 2.2.2.

[59] See Appendix D

The comparison in Table 4.5 shows a nearly perfect match between the full-system eigenfrequencies of the fore-aft tower bending modes and those from the reduced system. Especially for setting i), the reduced system represents the full-system eigenfrequencies exactly. The differences that occur for setting ii) and iii) can be neglected.

The different settings only show negligible variances regarding their eigenfrequencies if they are compared to each other. Hence, the choice of the linearization setting is not a decisive factor. For this reason, the system description derived from the setting i) that represented the stationary rotor are chosen for the inverse load calculation. Consequently, the mass and stiffness matrix are as follows.

$$\mathbf{K}^{red} = \begin{bmatrix} 1.06 \cdot 10^6 & 0 \\ 0 & 0.92 \cdot 10^6 \end{bmatrix} \text{ in Nm}^{-1} \tag{4.4}$$

$$\mathbf{M}^{red} = \begin{bmatrix} 2.56 \cdot 10^5 & 0 \\ 0 & 2.73 \cdot 10^3 \end{bmatrix} \text{ in kg} \tag{4.5}$$

Additionally, the FAST post-processing calculates modal damping ratios for each mode of vibration. The damping ratios[60] vary slightly between the three different settings. For this reason, averaged damping ratios D_1 and D_2 are used. The source of damping is structural damping. D_1 additionally contains aerodynamic damping. The calculation of the damping matrix $\mathbf{B}_E$ is done according to the descriptions given in section 3.2.1.

$$D_1 = 0.04 \quad \text{and} \quad D_2 = 0.01 \tag{4.6}$$

4.3 Results of the Inverse Load Calculation at a 5 MW Onshore Wind Turbine Model

The inverse load calculation procedure is verified according to the scheme given in Figure 4.1. For the FAST simulation, the 5 MW reference wind turbine model that was described in section 4.2.1 is used. The result of the inverse load calculation is an equivalent rotor thrust force. For verification purposes, this force will be compared to the rotor thrust force known from the FAST simulation (see Figure 4.5). The FRF matrix is assembled using the information of the eigenvalue analysis and the system matrices given in section 4.2.4.

Additionally, system responses are needed as calculation input. As depicted in Figure 4.5, acceleration time series at the tower top (maximum amplitude of 1st tower bending mode) and at nearly half of tower height (maximum amplitude of 2nd tower bending mode) are chosen. Generally, the acceleration signals are purely dynamic system responses – the signals oscillating around a mean of zero. The chosen inverse load calculation approach requires displacements that are obtained by double-integrating the accelerations as explained in Appendix E. The integration process is not able to generate the integration constants. In the strict sense, this means that the inverse load calculation based on the Deconvolution in

---

[60] As a percentage of critical damping.

the Frequency Domain (see section 3.2) solely calculates a dynamic part of the rotor thrust force. Since a complete representation of the rotor thrust is desired, the remaining force component is superimposed linearly. This assumption is in accordance with the load characteristics that are discussed in section 2.2.1, Table 2.1. In addition, displacements at the tower top in combination with known stiffness properties from the matrix **K** are used to calculate a static/quasi-static component of the force.

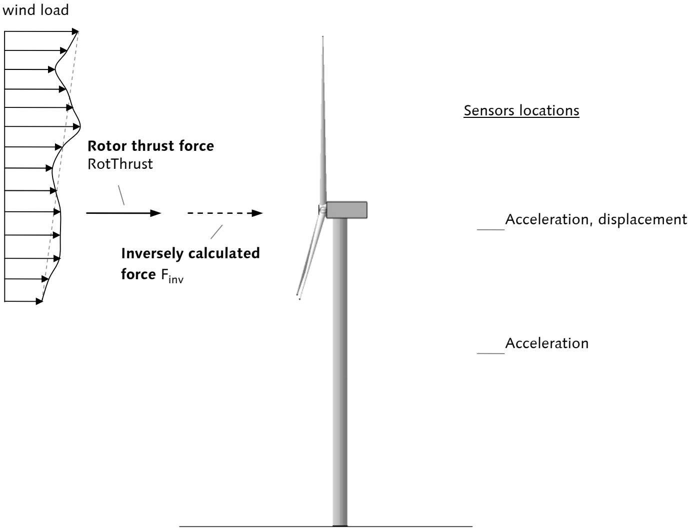

Figure 4.5: Assumptions for the verification study using FAST

The force components are depicted in Figure 4.6. To distinguish between the force components, a cut-off frequency has to be chosen. This frequency is chosen at a spectral gap of the force, so that neither exciting frequencies nor eigenfrequencies are influenced. These simulations are run with a cut-off frequency of 0.15 Hz, which is approximately half the 1st tower fore-aft eigenfrequency. Accelerations are used for the dynamic force components and the static/quasi-static force components are derived from displacements at tower top.[61]

Since a single load shall be calculated and at the same time, all available tower modes shall be considered, an over-determined system of equations is set up. The system of equations is solved using the least-squares approach as described in equations (3.63) and (3.64).[62] Three load cases under normal wind conditions for power production conditions are calculated. An overview of the load cases is given in Table 4.2.

---

[61] The calculation of the static/quasi-static force component using measured strains is decribed in section 5.

[62] See also section "3.2.2 Assembly of the FRF Matrix and Least-Squares Approach".

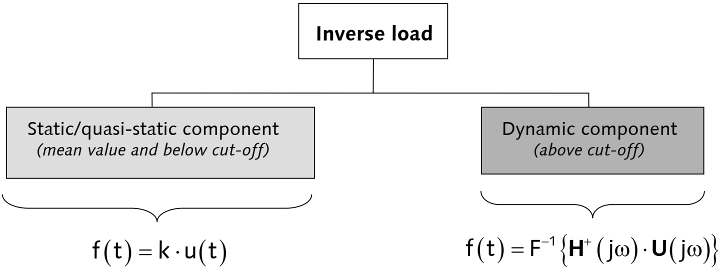

Figure 4.6: Force components

4.3.1 Inverse Load Calculation for LC 1 to LC 3

- Load case 1

Load case 1 (see Table 4.2) represents a mean wind speed at hub height between cut-in and rated wind speed. The mean wind speed is 6.94 m/s, which results in a mean rotor speed of 8.46 rpm. LC 1 is chosen because little control activity is expected, because the variable-speed controller operates in region 2. The nacelle yaw holds a constant position. The blade-pitch angle is constant at zero, which means that all three blades do not show blade-pitch control activity. The generator-torque is proportional to the square of the rotor speed in the active region.[63]

Figure 4.7 shows the inversely calculated load. For verification purposes, the rotor thrust force that is computed by FAST is also displayed. Figure 4.8 depicts a comparison between the quasi-static force components in the time domain and the frequency domain. The static component (mean value) and the quasi-static component (below cut-off) of the inversely calculated force are derived from the displacement-to-stiffness relation at the tower top. To gain better insight into the pure dynamic force component, Figure 4.9 shows a comparison of these components in the time domain and the frequency domain. The inverse force component is calculated using the equations presented in section 3.2.

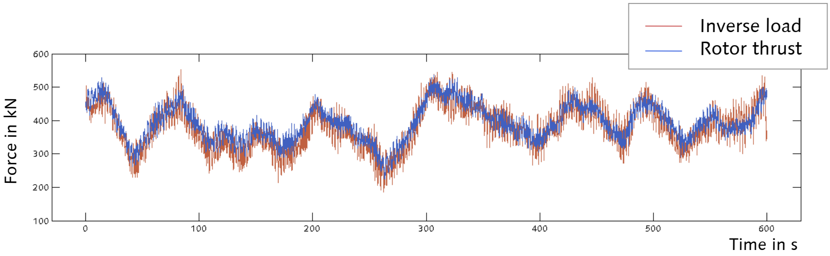

Figure 4.7: Rotor thrust and inversely calculated force – LC 1

---

[63] A depiction of the control outputs of FAST is given in Appendix F.

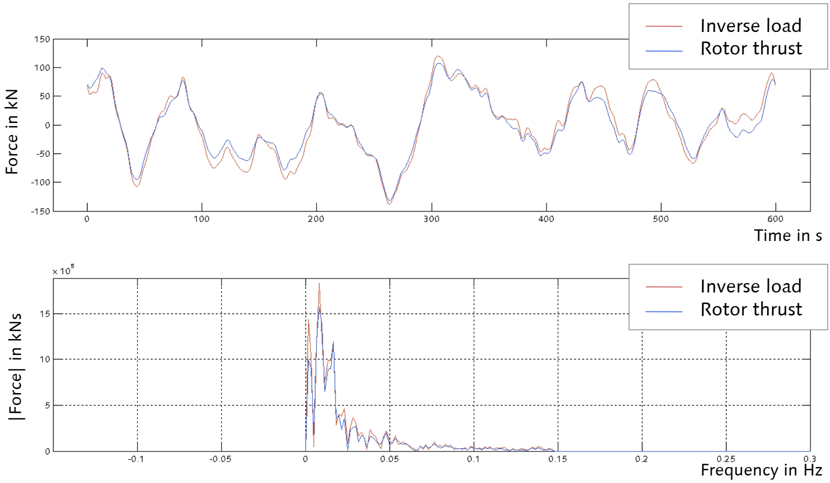

Figure 4.8: Quasi-static components – LC 1

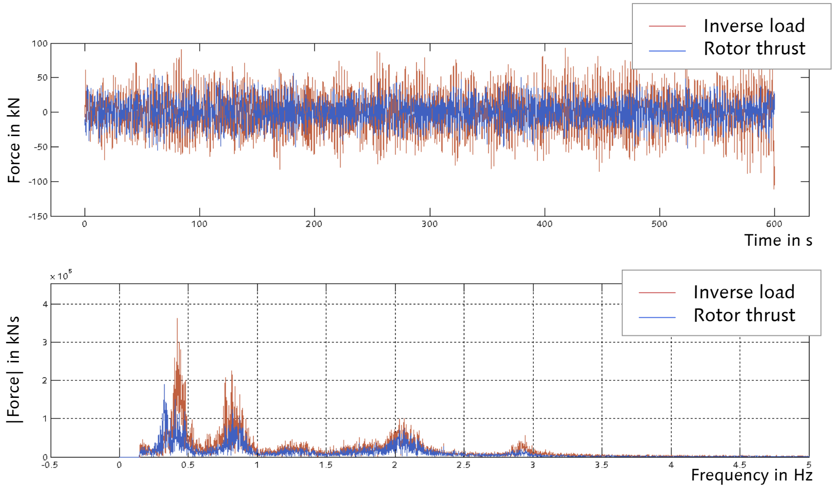

Figure 4.9: Dynamic components – LC 1

- Load case 2

Load case 2 (see Table 4.2) has a mean wind speed of 12.00 m/s (rated wind speed) with a mean rotor speed of 12.00 rpm, which represents the rated conditions of the wind turbine. This load case represents the transition between controllers at the point where maximal thrust occurs. The generator torque is no longer proportional to the rotor speed. Again, the nacelle position is constant, near zero. Furthermore, blade-pitch control shows activity during the simulation. Since collective blade pitch control is enabled, all three blades follow exactly the same control algorithm. The blade pitch angle varies between 0° and 10°.[64]

Figure 4.10 shows the result of the inverse calculation. As done for LC 1, the inversely calculated load and the rotor thrust are compared. The quasi-static components are depicted in Figure 4.11, both in the time domain and the frequency domain. An analog depiction for the dynamic components is given in Figure 4.12.

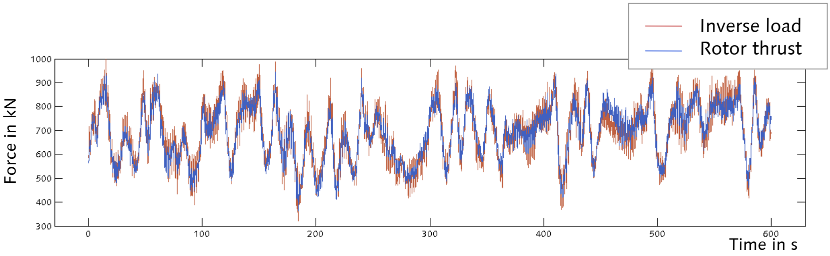

Figure 4.10: Rotor thrust and inversely calculated force – LC 2

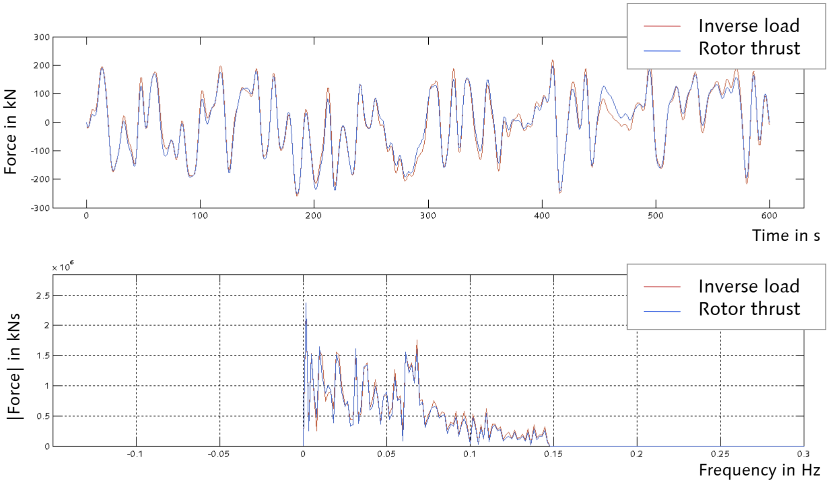

Figure 4.11: Quasi-static components – LC 2

---

[64] A depiction of the control outputs of FAST is given in Appendix F.

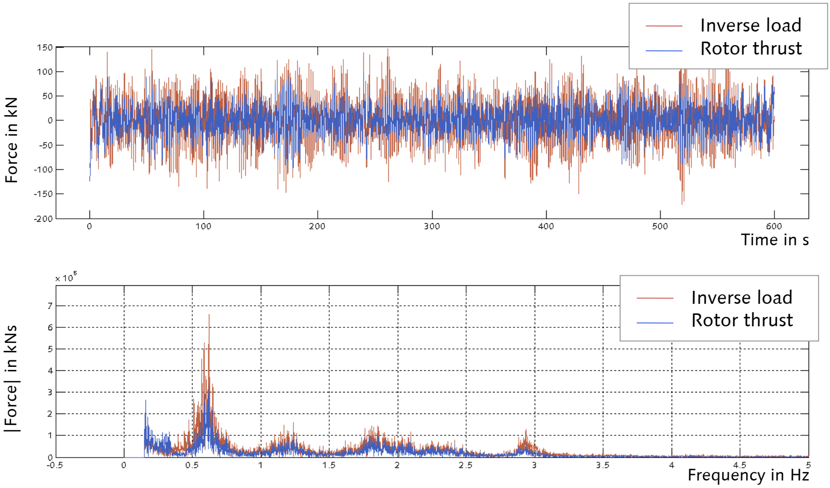

Figure 4.12: Dynamic components – LC 2

- Load case 3

The load case 3 (see Table 4.2) has a mean wind speed of 18.19 m/s, which represents a mean wind speed at hub height between rated and cut-out wind speed (middle of region 3). LC 3 is chosen because high control activity is expected. As for the LCs 1 and 2, the yaw position is constant at zero. The collective blade pitch ranges between pitch angles of 10° to 20°. While the torque controller operates in region 3, relative to region 2, the control strategy has changed from “optimal power” in region 2 to “constant power” in region 3.[65] The mean rotor speed is 12.10 rpm.

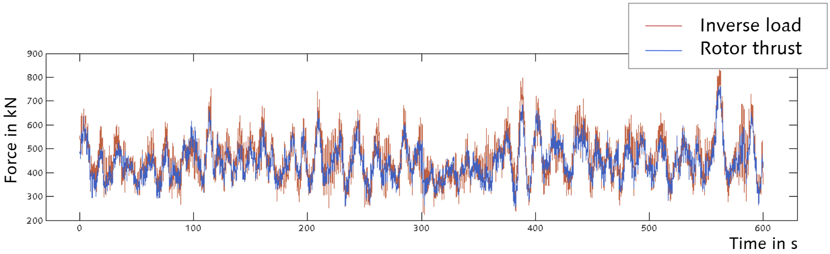

Figure 4.13: Rotor thrust and inversely calculated force – LC 3

---

[65] A depiction of the control outputs of FAST is given in Appendix F.

Figure 4.13 shows an illustration of the result of the inverse load calculation for LC 3. The inversely calculated load and the rotor thrust of the FAST simulation are depicted. The quasi-static components are depicted in Figure 4.14, both in the time domain and the frequency domain. Figure 4.15 shows the time-domain and frequency-domain depiction of the dynamic component.

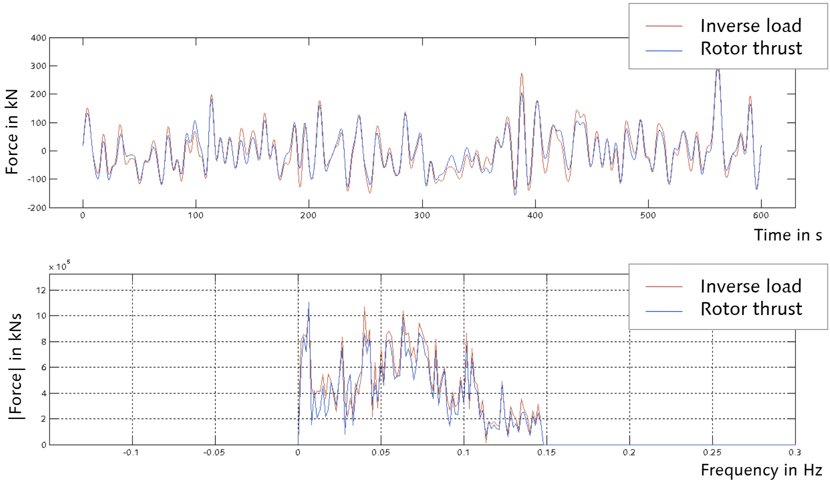

Figure 4.14: Quasi-static components – LC 3

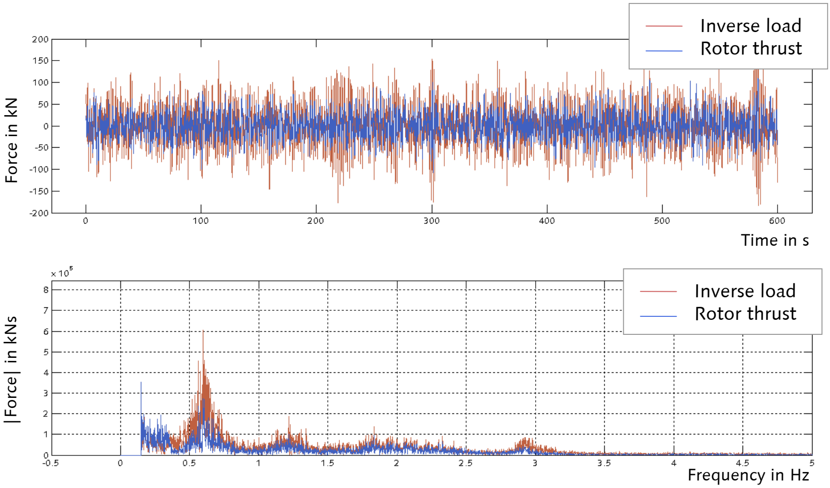

Figure 4.15: Dynamic components – LC 3

4.3.2 Summary of the Results for LC 1 to LC 3

In general, the verification study of the three load cases shows that the inverse load calculation produces reasonable results. A good match can be seen between the rotor thrust of the simulation and the inversely calculated load. This statement is true for all three load cases, as visualized by Figure 4.7, Figure 4.10, and Figure 4.13.

A more detailed assessment of the results is done by separating the forces into their static, quasi-static, and dynamic components and comparing these components. The separation is done according to the scheme given in Figure 4.6. With this, the following conclusions can be deduced from the verification study:

- To get a more detailed picture of the accuracy of the inverse calculation, the mean value and the standard deviation of the forces are calculated. They are summarized in Table 4.6 for all three load cases. The mean value is a measure of the static component of each force signal. Comparing the inversely calculated forces with the rotor thrust forces from FAST reveals that the pure static components of the forces have a high level of agreement, which is true for all three load cases.
- The standard deviation (see also Table 4.6) is assumed to be a measure for the time-dependent part of the force signals. The standard deviations show a good level of agreement for all load cases. The one for the inverse load is slightly higher than the one for the rotor thrust.
- The time-dependent parts of the force signal can be separated into their quasi-static components and their dynamic components. A closer look to the quasi-static components of the force signals is depicted in Figure 4.8, Figure 4.11, and Figure 4.14. It becomes apparent for all three load cases that the quasi-static components are calculated inversely with high accuracy.
- Both the static and the quasi-static components depend on the displacement-to-stiffness relation that is derived from the FAST displacement output at the tower-top and the corresponding entries in the stiffness matrix **K** that is known from the linearization.

Table 4.6: Comparison of mean value and standard deviation

		Rotor thrust	**Inverse load**
LC 1	Mean value ∅	392.38 kN	379.88 kN
	Standard deviation σ	53.78 kN	62.60 kN
LC 2	Mean value ∅	690.40 kN	693.43 kN
	Standard deviation σ	108.75 kN	116.66 kN
LC 3	Mean value ∅	443.96 kN	458.56 kN
	Standard deviation σ	74.34 kN	89.07 kN

- The dynamic components also show similar behavior for all three load cases; see Figure 4.9, Figure 4.12, and Figure 4.15. The comparison in the frequency domain shows that the inverse calculation is able to reproduce the frequencies of the rotor thrust. However, amplified peaks in the spectra occur at ca. 0.6 Hz to 0.7 Hz. For LC 1, a second peak at around 0.4 Hz is clearly visible. The corresponding time-domain depictions show inversely calculated loads with higher amplitudes than the rotor thrust.

- The dynamic components contribute most to the observed differences. Since the calculation of the numerical 2-DOF example showed the underlying equations to produce exact results, the mathematics do not seem to be the problem. However, the inverse calculation is based on an important assumption: the system used for the inverse calculation is a reduced system. The reasons for the reduction are described in section 2.2.2. Thus, the rotor thrust force is derived from the full-system description, whereas the inverse load is calculated with a reduced system.
- The dynamic force components have peaks at ca. 0.6 Hz to 0.7 Hz (see Table 4.4), which correspond to the rotor-blade eigenfrequencies. The reason is the system reduction. Because the rotor blade eigenfrequencies are not part of the dynamic system description used for the inverse calculation, their vibrations are interpreted as external loads.
- The peak at ca. 0.42 Hz for LC 1 seems to be caused by the 3P-excitation at 8.46 rpm. The occurrence in the spectra follows the same mechanism as observed at the 2-DOF example with noisy input data in section 3.3.4. The P-excitation is not part of the externally applied load but is inherent in the response data of the wind turbine.
- The reduction only affects the inverse calculation of the dynamic components. Therefore, the system reduction is assumed to be the main reason for the observed differences. Nevertheless, the results regarding the dynamic components have a good level of agreement. The dynamic component is calculated using the equations from the Deconvolution in the Frequency Domain (see section 3.2).

For each load case, the error between the time signals of the rotor thrust and the inverse load is calculated according to equation (3.65). The error values of the full signals, the quasi-static components, and the dynamic components are summarized in Table 4.7. The error values of the full-load signals range from 11 % to 16 %. These values have to be set into relation to the error value of $\varepsilon = 4.87$ % that is calculated in section 3.3.4. This previous calculation deals with a numerical 2-DOF system. The verification study of the 5 MW wind turbine with FAST is a more complex problem, e.g. due to presence of the wind turbine control and the more detailed model formulation. Thus, gaining higher error values for the inverse load meets the expectation. The quasi-static components show a very good accordance if expected visually. The corresponding error values are in the range of 8 % to 11 %. The dynamic components show the highest differences between the inverse load and the rotor thrust, with ε lying between 20 % and 27 %. The inverse calculation overestimates the force amplitudes, which is true for all three load cases.

The error values in Table 4.7 seem to imply a tendency to reach smaller error values with increasing load case numbers. This suggested tendency occurs not only for the full load signals, but also for the quasi-static and the dynamic components. Therefore, the suggested tendency cannot be caused by the mean values of the signals, which are equal to the static components. This conclusion is confirmed by the fact that the maximal rotor thrust occurs for LC 2, which does not correspond with the suggested tendency. This leads to the conclusion that all three calculated error values lie in a similar range.

Table 4.7: Error values for the time signals of the inverse loads

Error in time ε	**LC 1**	**LC 2**	**LC 3**
Full load signal	16.08 %	11.34 %	10.81 %
Quasi-static component	9.90 %	8.13 %	10.81 %
Dynamic component	27.05 %	20.22 %	19.53 %

The calculated error values are similar, which leads to the next conclusion. The inverse calculation does not depend on the control activities of the wind turbine. The three load cases are set up in order to represent different operating conditions with different control activities. Since the error values do not vary significantly between the three load cases, no tendency is observable.

The frequency-domain graphs do not show any effects caused by the ill-conditioning. In section 3.3.4, the ill-conditioning becomes obvious by the amplification of the high-frequent content. Here, no significant frequencies occur above 5 Hz. For testing purposes, the inverse loads can be low-pass filtered at 5 Hz, which does not change the results for the inverse load calculation. This means that the ill-conditioning does not affect the inverse solution. This is probably caused by the integration of the used acceleration signals. As stated in Appendix E, the integration process shows low-pass characteristics, even better than a filter. And a low-pass filter is suggested to eliminate the effects of ill-conditioning – see section 3.3.4.

Additionally, the integration of the acceleration signals might induce errors. The influence of the integration process is studied in detail in Appendix G. A comparative study that uses tower deflections as input parameters is presented. The study results in exactly the same inverse loads, which leads to the conclusion that the integration process does not cause errors. Additionally, a method for treating the effects caused by the ill-conditioning is shown. The use of filters and windowing leads to adequate results. The guess that the integration process affects the inverse calculation positively in terms of treating the ill-conditioning is demonstrated.

4.4 Summary

The comprehensive simulation code FAST is used for verification studies of the inverse load calculation method presented in section 3. The use of FAST allows loads to be applied from a defined stochastic wind field and enables the interacting dynamics of the wind inflow, aerodynamics, elasticity, and the control of the wind turbine to be considered. The simulations are run for a 5 MW onshore wind turbine. Three load cases are calculated with representative operating conditions. With the system matrices from the FAST model and the simulated accelerations along the tower, inverse loads are calculated. The accuracy of the inverse load calculation is estimated by comparing the inversely calculated load with the rotor thrust from FAST.

The main conclusion of the verification study is that the inverse load calculation is capable of generating good estimates of the applied load. An approach is chosen that calculates a static/quasi-static and a dynamic component. The full inverse load is obtained by superimposing these components. The static/quasi-static load component is calculated inversely with very good accuracy. The dynamic component shows higher differences, which is caused by the system reduction. These uncertainties cause an overestimation of the amplitudes, visible both in the depictions of the time domain and the frequency domain.

Theoretically, the system reduction can be avoided. This would require including the blade modes to the system that is used for the inverse calculation. In a first step, the fore-aft modes of a fixed rotor system could be added. A further step could consider the fore-aft blade modes for a spinning rotor system. An even more enhanced step should taking into account the aerodynamic interaction between the blades and the wind loads. In fact, expanding the system to the rotor blade dynamics is a complex problem. The accuracy of the single steps needs to be assessed. This problem will not be discussed in detail in this work.

The inverse calculation does not depend on the wind turbine control, which is studied comparing the results of three load cases.

Additionally, the effects caused by the integration of acceleration signals to displacement signals are studied. The study shows that the integration does not imply errors for the inverse calculation. The integration even affects the inverse calculation positively in terms of the ill-conditioning of the inverse problem, which allows omitting further regularization.

The inverse load calculation is intended to eventually be used for lifetime predictions using measurement data of offshore wind turbines. The fatigue-strength analysis mainly depends on the range of stresses. Assuming a linear dependency between the loads and the stresses, as is done for steel under normal operational conditions, the quasi-static and the dynamic component of the inverse load will be used for the fatigue analysis. The quasi-static component shows an excellent agreement and the dynamic component contains amplified amplitudes. Consequently, using inversely calculated loads for fatigue analysis is a safe assumption. This conclusion is also valid in the case of non-linear load-to-stress relations, as occurs e.g. for reinforced concrete. Then, the mean values of the stresses, which depend on the static component that also shows high accuracy, have to be taken into account additionally.

The entire section contributes new information to the research field of calculating loads inversely at wind turbine support structures. As described in the literature research in section 1.2.3 an appraisal of the results qualities is missing, if coupled dynamics of stochastic wind inflow, aerodynamics, elasticity of the structure, and the turbine control is considered.

5 Inverse Load Calculation at a 5 MW Onshore Wind Turbine using Measurement Data

The numerical study, presented in section 4, shows the ability of the inverse load calculation to deal with aerodynamic coupling effects and with wind turbine control. This numerical verification was done at an onshore wind turbine model loaded by stochastic wind inflow. The system description was known from the used FAST model. The simulated system responses were used as input parameters for the inverse calculation. On this basis, the following section will demonstrate the application of the inverse load calculation to a real wind turbine structure. The structure investigated is a lattice offshore sub-structure carrying a 5 MW wind turbine. The investigations are part of the collaborative research project OGOWin, whose complete results are documented in the corresponding final report [74]. The structure is erected onshore as a prototype.

As known from the preliminary thoughts given in section 1.2.2,[66] an accurate system description is decisive for the quality of the inverse load calculation. For the numerical study, the linearization in FAST gave the system matrices. Real structures are usually modeled e.g. using a FE representation that allows predicting the dynamic structural behavior. However, models always contain assumptions and simplifications, which may lead to differences between the simulated dynamical behavior and the real dynamical behavior. In contrast to static calculations, dynamic calculations hardly allow conservative calculations. For this reason, the determination of the real dynamic behavior by means of structural measurements is a common approach. Using a system identification technique enables gaining the dynamic characteristics of a structure from measurement data. These measured dynamic characteristics can be used to adjust a FE model, so that the model represents best the dynamics of the real structure. This process is called model updating and results in a realistic mathematical representation of the structure, which was previously referred to as system description.

First, section 5.1 gives a description of the structure investigated. The corresponding FE model and the concept for measuring the structure are presented. Section 5.2 summarizes the results of the system identification, including dynamic parameters of important local structural components and for the global structure respectively. Finally, section 5.3 describes the application of the inverse load calculation procedure.

---

[66] See description of the “inverse calculation of applied loading”.

5.1 Investigated Structure

5.1.1 Description of the Structure

The structure investigated is an onshore prototype of a support structure for a 5-MW-class wind turbine. The prototype, which is shown in Figure 5.1, is erected in Bremerhaven (Germany) and is based on a lattice sub-structure that consists of tubular steel pipes and cast-steel nodes. The lattice structure is connected to the tubular steel tower via a special transition piece, made of steel as well. The entire support structure carries a REpower 5M wind turbine, which is a 5 MW, three-bladed, horizontal-axis, upwind wind turbine.

Top left:	REpower 5M with tubular tower
Bottom left:	lattice sub-structure
Bottom center:	onshore foundation bodies
Bottom right:	transition piece
Top right:	upwards view support structure

Figure 5.1: Offshore support structure with the REpower 5M in Bremerhaven, Germany [67]

The support structure is developed for water depths of approximately 30 m. Thus, the hub height of the wind turbine is located at 120 m. The rotor-blade lengths are 61.5 m. The design of this innovative structure follows the concept: standard components such as equal

---

[67] Picture at bottom center is taken by Weserwind GmbH.

pipes and connecting nodes of equal size are used to achieve cost-efficient fabrication and time-saving assembly.

The REpower 5M machine incorporates a control system that consists of a variable-speed generator-torque controller and an electrical blade-pitch controller. A complete summary of all technical data is given in the official brochure of the REpower 5M [85].

The foundation of the onshore prototype is a site-specific construction. The layer succession of the soil consists of three main layers.[68] The upper layer with a depth of approximately 15.50 m contains clay that shows a very low load-bearing capacity. Subsequently, a sand layer of circa 6.50 m occurs, followed by a silt layer. Due to the specific soil layer stiffness, the sand layer essentially contributes to the load transfer into the ground in both horizontal and vertical direction. For this reason, each of the four legs of the lattice structure is supported by a cylindrical reinforced concrete structure that each are founded on 14 reinforced concrete piles with a length of approximately 26 m and an inclination ratio of 8:1. A scheme of one foundation body and the genuine soil layers is given in Figure 5.2.

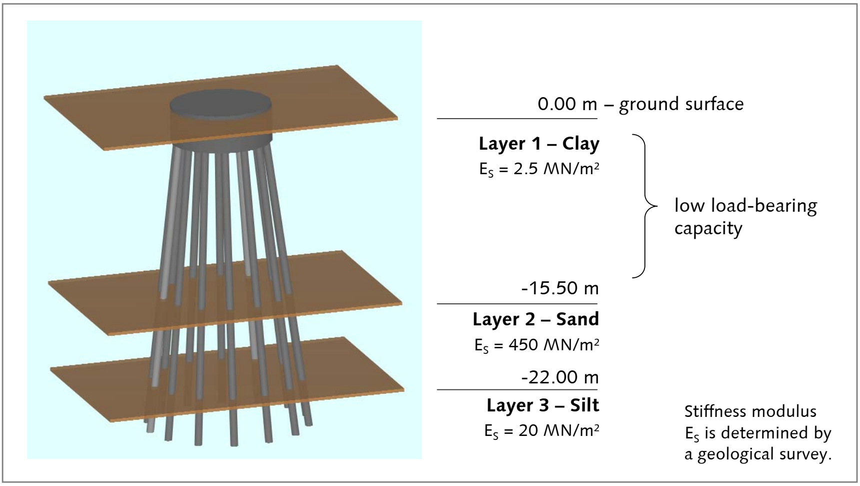

Figure 5.2: Foundation body and soil layers at the onshore site in Bremerhaven

5.1.2 Finite-Element Model and Modal Analysis

- Finite-Element model

The structure described in section 5.1.1 is modeled using the FE software ANSYS. This model is built up for the following reasons:

---

[68] See summary of the geological survey [33].

- Determining the effects of different modeling strategies in terms of the dynamic behavior of the structure
- Calculation of the dynamic characteristics by means of a modal analysis
- Setting up a measurement concept
- Defining excitation forces for the measurement campaigns

The several structural components can be modeled using different levels of detail, such as modeling the tubular tower by beam elements or creating a spatial representation using shell elements. Comparing different modeling variants allows finding a model that has a fast calculation time with the fewest modeling effort, without losing accuracy with regards to the eigenfrequencies of the entire structure. The comparative study of the modeling variants is described in Pahn and Rolfes (2011) [78]. The final modeling variant is shown in Figure 5.3. The modeling of the several structural components is described in Appendix H.

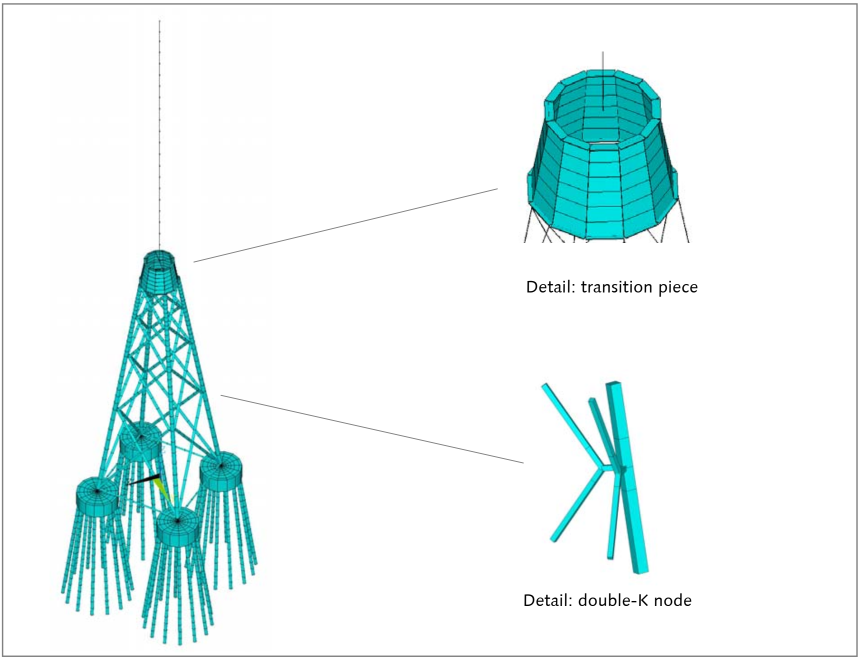

Detail: transition piece

Detail: double-K node

Figure 5.3: FE model – onshore foundation, lattice structure, transition piece, and tubular tower

By means of the FE model, the eigenfrequencies and mode shapes of the structure can be calculated by a modal analysis. Knowledge of these dynamic characteristics enables setting up a measurement concept, which is described in section 5.1.3 and section 5.2.1.

- Modal analysis

The results of the modal analysis are the mode shapes and the eigenfrequencies of the main global modes and of important local modes.

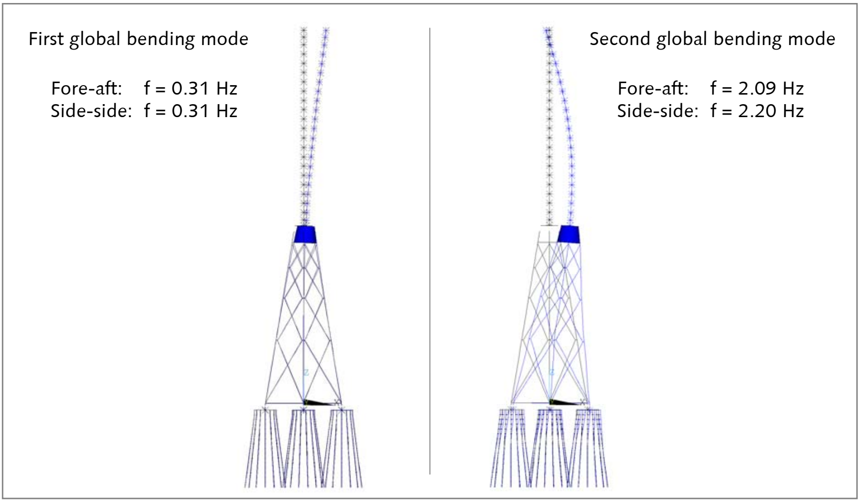

Figure 5.4: First and second global bending mode

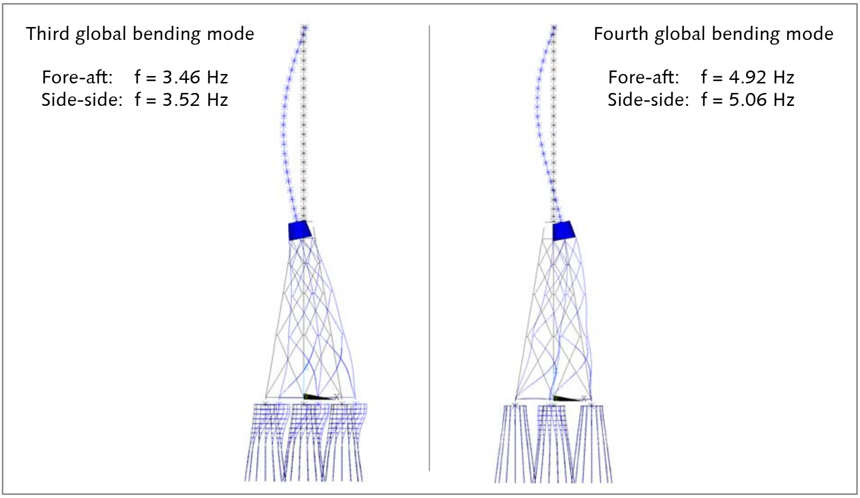

Figure 5.5: Third and fourth global bending mode

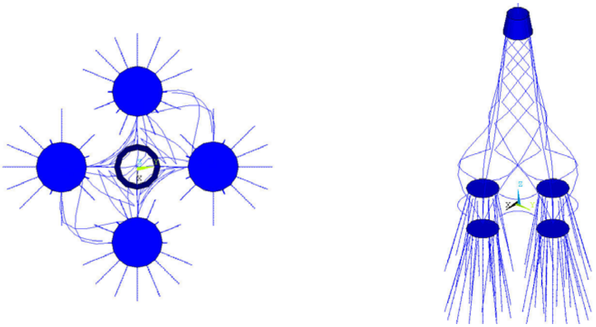

Figure 5.6: Local mode shape bay 5 – f = 5.14 Hz

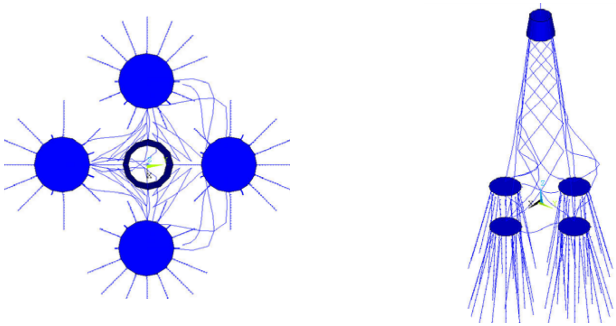

Figure 5.7: Local mode shape bay 5 – f = 5.38 Hz

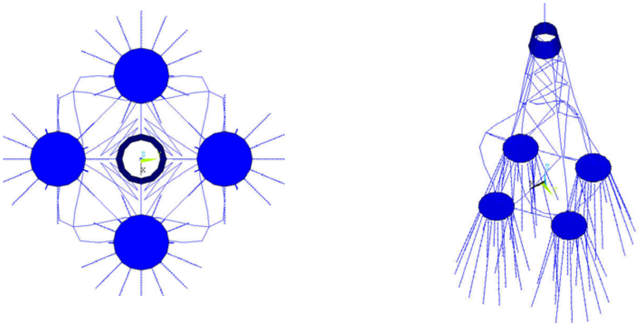

Figure 5.8: Local mode shape bay 5 – f = 5.47 Hz

The modal analysis focuses on those eigenfrequencies that are potentially determinable with system identification. This assumption applies for the first four eigenmodes of the global structure that are depicted in Figure 5.4 and Figure 5.5. Each global bending mode occurs both for the fore-aft and for the side-side direction. Comparing each fore-aft mode shape with its corresponding side-side mode shape gives qualitatively similar deflections for which reason only one mode shape is depicted per global bending mode. The figures additionally contain the eigenfrequencies. As visible, the eigenfrequencies of the second, third, and fourth mode shape differ between the fore-aft and the side-side direction. The reason is the mass and inertia distribution of the rotor-nacelle-assembly (RNA). The rotor blades cause different tower-top rotation in fore-aft and side-side direction. The mode shapes of the second to fourth modes depend on the tower-top rotation. Whereas the first mode shapes are dominated by the tower-top deflection with minor importance of the tower-top rotation. Consequently, the first mode shapes are unaffected. Further, it can be seen that especially the third but also the second and the fourth mode shapes contain deflections from the foundation bodies. This is due to the low stiffness of the upper soil layer. The chosen stiffness value is based on a geological survey. In general, stiffness values from geological surveys are prone to uncertainties. Thus, a special part of the measurements aims on deriving the soil stiffness that has to be used for an updated model.

Aside from the global mode shapes, the modal analysis gives local mode shapes that are depicted in Figure 5.6, Figure 5.7, and Figure 5.8. These mode shapes are considered local mode shapes because the vibrations are almost exclusively dominated by bay 5, whereas the remaining structure is nearly unaffected. Bay 5 is the denotation for the lowest cross of the lattice structure. The corresponding eigenfrequencies are of interest because excitation frequencies from wind and from operation of the wind turbine might be in resonance. For this reason, the local frequencies are identified in the measurement concept. As shown, the three local modes lie within a small frequency range of only 0.30 Hz, which might cause interaction in the form of beat frequencies. The different local mode shapes are characterized by in-phase vibrations of opposing crosses (Figure 5.6), by in-phase vibrations of neighboring crosses (Figure 5.7), and by in-phase vibrations of all crosses (Figure 5.8).

The presented eigenfrequencies serve as expectancy values for the system identification.

5.1.3 Sensors and Sensor Locations

The setup of the sensor types and the sensor locations is part of the collaborative research project OGOWin. A full description is given in the final report of OGOWin (2011) [74]. The system identification aims to determine the dynamic characteristics of the structure, which are the eigenfrequencies, the mode shapes, and the damping ratios. For this purpose, accelerometers distributed along the structure's height are used. The locations of the accelerometers are indicated by green dots in Figure 5.9. As depicted by the top view of the tower-top cross-section (top left), the accelerometers are spatially arranged to gain three-dimensional representations of the vibrations. Strain measurement devices such as strain gages and fiber-optic sensors, are used additionally for verification purposes.

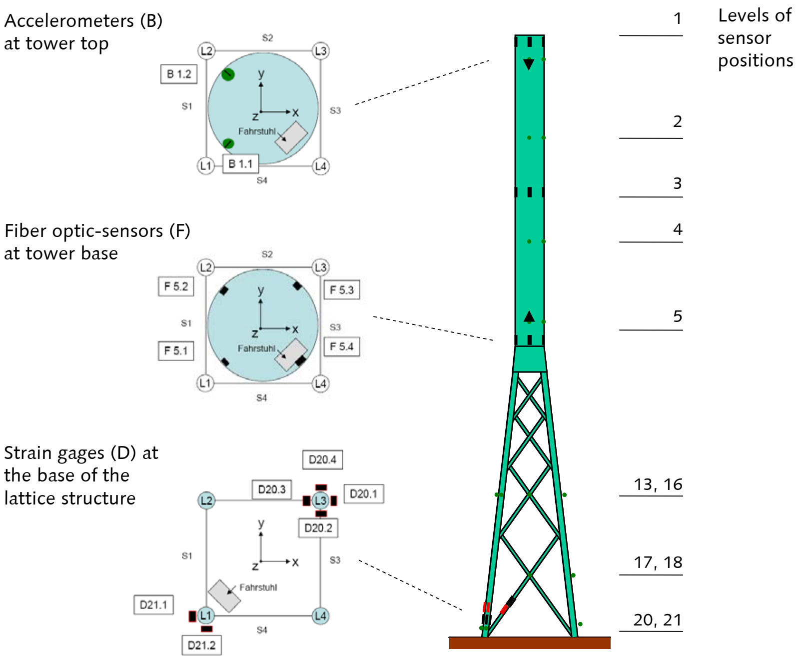

Figure 5.9: Sensor locations[69]

5.2 Output-Only System Identification

5.2.1 Measurement Concept

The objective of the measurement is to determine the eigenfrequencies and the damping ratios of the modes in order to compare with the values calculated by modal analysis (section 5.1.2). The identification of modal parameters via measurements essentially depends on the excitation of the structure. The sources of excitation can be divided into two main categories – ambient excitations and artificial excitations.

Ambient excitation may be induced by wind, (water, earthquake, acoustic) waves, currents, or operation of machines. This type of excitation is present naturally. However, the occurrence and the value of the excitation force are not controllable. Furthermore, the excited frequency range cannot be influenced. Alternatively, artificial excitations can be used in order to produce defined vibration amplitudes of the structure that allows for indentifying

---

[69] Drawings are taken from Fraunhofer IWES, Bremerhaven.

the modal parameters. The artificial excitation is generated by applying a test function. Test functions are advantageous, because

- the occurrence of the test function is known,
- the excitation force is defined so that a clear response signal is generated, which exceeds the noise in the measurement data,
- by means of the type of the test function, the excited frequency range can be controlled.

Theoretical basics of different test functions are presented in Natke (1983) [70]. Felber (1993) [21] gives an overview oriented on practical issues. In terms of the investigated wind turbine support structure, three types of test functions are chosen for assessment: the sine sweep, the impact test, and the pullback test.

The different test functions are simulated using the FE model. The objective of the simulations is determining the locations and the values of the excitation forces. The simulations focus on the eigenfrequencies that result from the modal analysis presented in section 5.1.2. Detailed results of these simulations are presented in Pahn and Rolfes (2011) [78]. On the basis of the simulation results, a measurement concept is set up. Additionally, practical constraints are considered, such as the technical effort and preventing the structure from damage. The final measurement concept is given in Table 5.1.

Table 5.1: Measurement concept

Global modes		
	Modes	First to fourth global bending modes, each in fore-aft and side-side direction
	Excitation	Ambient excitation from wind and operation of the wind turbine
	Objectives	Eigenfrequencies, mode shapes, and damping ratios in standstill and various operation states
Local modes of the lower crosses of the lattice structure (bay 5)		
	Modes	Local modes of the bay 5, depending on the phase relation of adjacent crosses
	Excitation	Artificial excitation using a pullback test, excitation forces 5,000 N and 8,000 N
	Objectives	Eigenfrequencies, mode shapes, and damping ratios
Local modes of a single foundation body		
	Modes	Horizontal deflection and torsional mode of a single foundation body 1)
	Excitation	Artificial excitation using a sweep excitation 2), excitation force max. 1,000 N
	Objectives	Eigenfrequency
1) Before erecting the structure, no interaction between foundation bodies. 2) Realized by a mobile device that is property of the Institute for Structural Analysis of Leibniz Universität Hannover		

The excitation of the global modes is realized using ambient excitation from wind and operation of the wind turbine. Adequate artificial excitations could not be determined. Main restrictions are the required forces, the accessibility of the wind turbine (locating the mobile sweep exciter), and the required space in the surrounding area of the wind turbine (pullback test). The excitation of the global modes is of stochastic nature. For this reason, a series of measurement data should be used in order to gain reliable results. Stochastic data have the disadvantage that the force value and the excited frequency content are not predictable.

A pullback test is used for the measurement of bay 5. The chosen force values are derived from a FE simulation. Thus, free vibrations of the crosses with adequate amplitudes are ensured. The tests are conducted at standstill.

Additionally, one of the four foundation bodies is investigated. The test is done before the erection of the wind turbine support structure. A sine sweep is applied using the mobile exciter. This procedure allows determining the eigenfrequency of the separate structure. Comparing the measurement results to the modal analysis allows for verifying the modeling of the soil stiffness. A similar approach is described in IBSEN AND LIINGAARD (2006) [39] at a prototype for a wind turbine foundation structure with a bucket foundation.

The results of the identification of the local components are given in section 5.2.3. The global dynamics of the structure are presented in section 5.2.5.

An important aspect that is decisive for the quality of the identification results is the system identification method. The main part of the measurements is based on ambient excitation, where the excitation forces are unknown. For this reason, an output-only system identification method has to be used. Since output-only methods are capable to deal with artificial excitations, an appropriate method is chosen in this work that is applied to all measurements. The chosen method is presented subsequently in section 5.2.2.

5.2.2 Frequency Domain Decomposition

The publications of PEETERS AND DE ROECK (2001) [83] and of ANDERSEN ET AL. (1999) [1] are helpful in choosing an appropriate system identification method. Both publications discuss different methods and compare the accuracy of the methods using a FE model of a frame structure and bridge test data respectively. All methods give reasonable estimates for the eigenfrequencies, the mode shapes, and the damping ratios. Hence, the preferable method depends on the specific application.

A discussion of output-only system identification techniques is given in Appendix I. The discussion focuses on those methods that already have been applied to wind turbine structures under stochastic excitation. Thus, the three methods Autoregressive Model (AR), Stochastic Subspace Identification (SSI) and Frequency Domain Decomposition (FDD) are reviewed.

This research literature reveals a successful application of the Frequency Domain Decomposition to wind turbines in operation. This approach is described to give reliable estimates of the eigenfrequencies, the mode shapes, and the damping ratios. Additionally, the FDD is promising in terms of handling large amounts of data that shall handled automatically, as it is intended in this work. The FDD is also able to identify closely spaced modes, which occur in the modal analysis (see section 5.1.2). For these reasons, the FDD is chosen.

The theoretical fundamentals of the Frequency Domain Decomposition are explained in Brincker et al. (2000) [7] and Brincker et al. (2001) [9] in detail. The essential steps of the FDD and important information in terms of its practical application are given subsequently.

Considering an output-only system, the mathematical description between the unknown inputs $\mathbf{x}(t)$ and the measured responses $\mathbf{y}(t)$ is set by

$$\mathbf{G}_{yy}(j\omega) = \bar{\mathbf{H}}(j\omega) \cdot \mathbf{G}_{xx}(j\omega) \cdot \mathbf{H}^T(j\omega). \tag{5.1}$$

In equation (5.1) $\mathbf{G}_{yy}(j\omega)$ denotes the m x m power spectral density matrix (PSD) of the responses, with m being the number of responses. Accordingly, $\mathbf{G}_{xx}(j\omega)$ is the r x r PSD of the inputs, where r is the number of inputs. $\mathbf{H}(j\omega)$ represents the frequency response function matrix (FRF) of the size m x r. Overbar represents complex conjugate and superscript T symbolizes the transpose.

When transforming the FRF by means of partial fraction using pole and residue, one attains the following equation.

$$\mathbf{H}(j\omega) = \sum_{k=1}^{n} \frac{\mathbf{R}_k}{j\omega - \lambda_k} + \frac{\bar{\mathbf{R}}_k}{j\omega - \bar{\lambda}_k} \tag{5.2}$$

Here, n is the number of modes, λ_k is the pole and $\mathbf{R}_k$ is the residue expressed by

$$\mathbf{R}_k = \phi_k \cdot \gamma_k^T \tag{5.3}$$

as the product of the mode shape vector ϕ_k and the modal participation vector γ_k. The input is assumed to be white noise. Then, $\mathbf{G}_{xx}(j\omega)$ becomes a constant PSD matrix.

$$\mathbf{G}_{xx}(j\omega) = \mathbf{C} \tag{5.4}$$

Substituting equation (5.1) with equations (5.2) and (5.4) leads to a description of the response PSD in partial fraction form. After using some mathematical transformation,[70] equation (5.1) can be written in a reduced pole-residue-form

$$\mathbf{G}_{yy}(j\omega) = \sum_{k=1}^{n} \frac{\mathbf{A}_k}{j\omega - \lambda_k} + \frac{\bar{\mathbf{A}}_k}{j\omega - \bar{\lambda}_k} + \frac{\mathbf{B}_k}{-j\omega - \lambda_k} + \frac{\bar{\mathbf{B}}_k}{-j\omega - \bar{\lambda}_k}. \tag{5.5}$$

Now, $\mathbf{A}_k$ represents the k-th residue matrix of the output PSD, containing the inputs defined in equation (5.4). For light damping the residue becomes proportional to the mode shape vector. The response at a certain frequency ω will be dominated only by a few num-

---

[70] For more detailed information see Brincker et al. (2000) [8].

ber of modes, usually one or two modes. Denoting this subset of modes by $\mathrm{Sub}(\omega)$ with d_k as a scalar constant, the response PSD matrix results in

$$\mathbf{G}_{yy}(j\omega) = \sum_{k \in \mathrm{Sub}(\omega)} \frac{d_k \phi_k \phi_k^T}{j\omega - \lambda_k} + \frac{\bar{d}_k \bar{\phi}_k \bar{\phi}_k^T}{j\omega - \bar{\lambda}_k}\,. \tag{5.6}$$

Equation (5.6) describes a modal decomposition of the spectral matrix introduced in equation (5.1).

Regarding the practical identification process, the estimate of the response PSD $\hat{\mathbf{G}}_{yy}(j\omega)$ can be assembled by using the recorded sensor data. The response PSD is calculated by means of the Fourier transformation of the acceleration response $\ddot{Y}(j\omega)$ multiplied by its complex conjugate $\ddot{Y}^*(j\omega)$.[71]

$$\hat{\mathbf{G}}_{yy}(j\omega) = \ddot{Y}_p(j\omega) \cdot \ddot{Y}_q^*(j\omega) \tag{5.7}$$

Applying equation (5.7) gives a square PSD matrix of dimension m x m with p and q as coordinates of the sensor locations, whereas p, q = 1…m and $m \in N$. Because the acceleration responses are discrete data, the PSD estimation exists for discrete known frequencies $\omega = \omega_i$. The decomposition is done by applying a singular value decomposition (SVD) so that

$$\hat{\mathbf{G}}_{yy}(j\omega_i) = \mathbf{U}_i \cdot \mathbf{S}_i \cdot \mathbf{U}_i^H\,. \tag{5.8}$$

$\hat{\mathbf{G}}_{yy}(j\omega_i)$ is split into a unitary matrix $\mathbf{U}_i$ containing the singular vectors $\mathbf{u}_{ij}$ and the diagonal matrix $\mathbf{S}_i$ filled with the scalar singular values s_{ij}, see equations (5.9) and (5.10). Superscript H denotes complex conjugate and transpose.

$$\mathbf{S}_i = \begin{bmatrix} s_{i1} & & & & \\ & s_{i2} & & & \\ & & s_{i3} & & \\ & & & \cdots & \\ & & & & s_{im} \end{bmatrix} \tag{5.9}$$

$$\mathbf{U}_i = \begin{bmatrix} \mathbf{u}_{i1} & \mathbf{u}_{i2} & \mathbf{u}_{i3} & \cdots & \mathbf{u}_{i1} \end{bmatrix} = \begin{bmatrix} u_{i11} & u_{i21} & u_{i31} & \cdots & u_{im1} \\ u_{i12} & u_{i22} & u_{i32} & \cdots & u_{im2} \\ \cdots & \cdots & \cdots & \cdots & \cdots \\ u_{i1n} & u_{i2n} & u_{i3n} & \cdots & u_{imn} \end{bmatrix} \tag{5.10}$$

Generally, the spectrum near a peak is dominated by only one k-th mode, so that equation (5.6) reduces to one term. Then, the first singular vector $\mathbf{u}_{i1}$ becomes an estimate of the

---

[71] See e.g. FELBER (1993) [21], page 26.

mode shape $\hat{\phi}$. The corresponding singular value describes the auto-PSD function of the related SDOF system.

To determine the PSD function of the SDOF system, the peak at ω_i in the first singular value s_{i1} has to be detected. The corresponding mode shape estimate $\hat{\phi} = \mathbf{u}_{i1}$ is compared to the singular vectors of the neighboring singular values s_{j1} ($j \neq i$). As long as the singular vectors – representing the mode shape estimates – have a high value of the modal assurance criterion (MAC), the corresponding singular value is part of the PSD function of the SDOF system. The MAC value Ω quantifies the geometrical similarity of two mode shapes $\mathbf{u}_{i1}$ and $\mathbf{u}_{j1}$.[72]

$$\Omega = \frac{\left|\mathbf{u}_{i1}^T \cdot \mathbf{u}_{j1}\right|^2}{\left[\mathbf{u}_{i1}^T \cdot \mathbf{u}_{j1}\right]\left[\mathbf{u}_{j1}^T \cdot \mathbf{u}_{i1}\right]} \tag{5.11}$$

Andersen et al. (2007) [2] recommends a MAC value of $\Omega \geq 0.8$ to select the piece of the PSD function that corresponds to the SDOF system. Once the auto PSD function of the SDOF system is determined, all remaining frequency lines of the spectrum are set to zero. Applying an inverse Fourier transformation gives the autocorrelation function of the SDOF system, which appears as a decaying function in the time domain. According to the properties of the autocorrelation[73], the autocorrelation function does not allow the reconstruction of the underlying time-domain signal. However, the autocorrelation function contains the same periodicity, which enables the determination of the frequency and an estimation of the damping.

A qualitative example of a decaying time-domain function that depicts the variables necessary to calculate the damping ratio D and the eigenfrequency is shown in Figure 5.10.

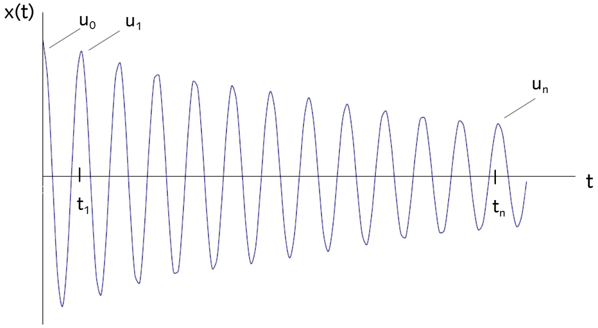

Figure 5.10: Decaying time-domain function

---

[72] Further properties of the MAC value are described in Ewins (2000) [18].

[73] See e.g. Natke (1983) [70], page 93ff.

Counting the maxima enables the calculation of the damping. The damping ratio D can be determined both via the logarithmic decrement ϑ and via the decay constant δ. Because the decaying function is usually built by more than one time period, a regression analysis using a least-squares approach can be used, which allows for eliminating stochastic errors. The application of the regression analysis is explained in detail in Appendix J.

$$D = \frac{\vartheta}{2\pi} \qquad \text{or} \qquad D = \frac{\delta}{2\pi f_0} \tag{5.12}$$

The eigenfrequency f_0 of the SDOF system results from counting the crossing times of the time-domain function. The arithmetic mean value of the frequency $\bar{f}_0$ is calculated according to

$$\bar{f}_0 = \frac{1}{n}\sum_{i=1}^{n} f_{0i} = \frac{1}{n}\sum_{i=1}^{n} \frac{1}{T_{0i}} = \frac{1}{n}\sum_{i=1}^{n} \frac{1}{t_{i+1} - t_i}\,. \tag{5.13}$$

In fact, equation (5.13) gives a damped eigenfrequency that now shall be denoted as f_D. Since the damping ratio D is known, the undamped eigenfrequency f can be obtained.

$$f = \frac{f_D}{\sqrt{1 - D^2}} \tag{5.14}$$

The influence of the damping on the eigenfrequency is negligible for damping ratios of approximately $D < 5\%$. For this reason, the assumption of $f = f_D$ is applied in this work.

A further insight into the damping calculation is given in BRINCKER ET AL. (2001) [10], demonstrated at measurement data of a bridge.

In case a series of measurement data are available, an averaged PSD can be calculated that eliminates random errors. Figure 5.11 qualitatively shows an averaged singular value decomposition of a response PSD matrix.

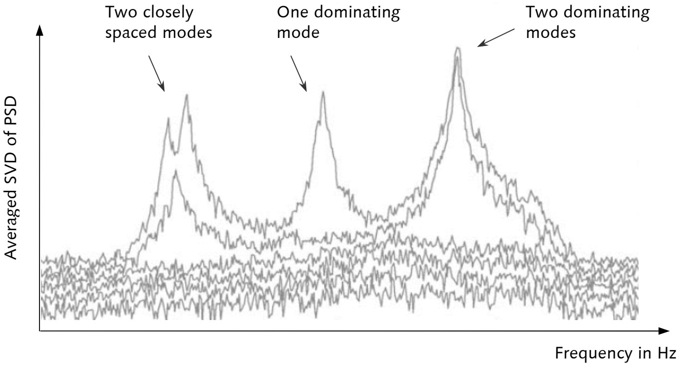

Figure 5.11: Qualitative characteristics of an averaged SVD (taken from BRINCKER ET AL. *(2001) [9])*

In general, one mode is dominating the PSD described in equation (5.6). If two modes are present in the PSD at the same frequency, the first singular vector is a good estimate for the mode shape of the strongest mode. Typically, the bias at the strong mode shape is very small, whereas the bias at the weak mode shape is strong. In case the two modes are orthogonal, their two singular vectors are unbiased estimates of the related mode shapes.[74] The FDD is also able to identify closely spaced modes.[75] The described characteristics are depicted in Figure 5.11.

In Andersen et al. (2007) [2], further practical hints such as indicators that help to distinguish between physical modes, harmonics and noise are given. The FDD is valid for lightly damped structures. However, even if higher damping ratios occur – as it is expected for operating wind turbines due to aerodynamic damping effects – results are supposed to be still a good estimate.

5.2.3 Local Measurements

Measurements have been carried out at two local structural components, which are a single foundation body and the lower crosses of the lattice structure (see Figure 5.1). The reasons for these measurements are pointed out in section 5.1.2. The results of the measurements are published in Pahn and Rolfes (2011) [79]. The objectives of the measurements, the measurement setups, and the results are given in Appendix L. The conclusions that are derived from the measurements are briefly summarized subsequently.

- Measurement of a single foundation body

The first bending mode of the structure is measured in a frequency range of 4.0 Hz to 4.5 Hz. This measured eigenfrequency is higher than the eigenfrequency from the modal analysis (circa 3.5 Hz). The modal analysis is based on the soil stiffness values given in the geological survey [33]. The soil stiffness of the upper layer is suggested to $E_S = 2.5$ MN/m^2 (see Figure 5.2).

The comparison of the modeled eigenfrequency to the measured eigenfrequency reveals that the spring stiffness in the FE model that represent the stiffness of the upper soil layer should be increased in contrast to the soil stiffness of the upper layer proposed by the geological survey. The model updating process will account for this result.

- Lower crosses of the lattice structure

The eigenfrequencies, the mode shapes, and the damping ratios for the lower crosses of the lattice structure are determined by an artificial excitation. Three closely spaced eigenfrequencies are detected, as it is predicted by the modal analysis. Using the phase-angle rela-

---

[74] See Brincker et al. (2001) [9].

[75] See Brincker et al. (2001) [10].

tionships between the two sensors, an unequivocal correlation of the frequencies to the mode shapes is possible. Comparing the mode shapes gained by the modal analysis (see Figure 5.6 to Figure 5.8) to the identified mode shapes (Table 5.2) shows that there is a mode shape shift between the simulation and the measurement. Both in the simulation and the measurement the mode shape with the smallest frequency is described by an in-phase vibration of opposing crosses. However, the second and third mode shape are shifted. The main reason is seen in the modeling of the connecting-node stiffness, which contains simplifications in the FE model.[76] This conclusion will be taken into consideration in the model updating process.

Table 5.2: Summary of the identified modes of bay 5

No.	Eigenfrequency	Damping ratio	Mode shape
1	5.09 Hz	0.37 %	Opposing crosses in phase
2	5.26 Hz	0.38 %	All crosses in phase
3	5.33 Hz	0.22 %	Neighboring crosses in phase

5.2.4 Expectations for the Global System Identification

Before handling measurement data, it is always useful to have expectation values in terms of the results that shall be derived from the measured signals. In section 5.1.2, predictions are already made about the eigenfrequencies and the mode shapes by means of the modal analysis. However, the modal analysis cannot answer two further important questions. How many frequencies are usually detectable in measurement data obtained at running wind turbines? And, which damping ratios can be identified, especially if aerodynamic damping effects are taken into account? To answer these two questions a survey through the corresponding literature is given subsequently.

- Expectation for the number of eigenfrequencies

SCHAUMANN AND SEIDEL (2000) [92] present measurement results gained at several onshore wind turbines with a tubular steel tower. The turbines have rated power of 500 kW to 1 MW. The first and the second fore-aft tower bending modes are derived from the free vibrations of the turbines after shutdown.

IBSEN AND LIINGAARD (2005) [38] conduct tests at a 3 MW onshore wind turbine with a tubular steel tower and a bucket foundation. The first and the second fore-aft tower modes are presented for standstill conditions. In operation, the first fore-aft tower mode as well as the 1P and 3P excitations are detected.

---

[76] See the descriptions in section 5.1.2.

Rebelo et al. (2008) [84] describe measurements at an onshore wind turbine with an eighty-meter tubular steel tower. The first and second tower modes, each in fore-aft and side-side direction, are determined for the operating wind turbine.

A recent publication of Kraemer (2011) [57] investigates an onshore wind turbine of the 5 MW class carried by a tripod structure. This work presents a detailed system identification. For the operating turbine, the first and second tower modes in fore-aft and side-side direction are determined. Additionally, the third tower mode in side-side direction could be identified. The system identification is completed by blade modes in flap- and edgewise direction.

The short survey clarifies that the first and second mode of a wind turbine seems to be detectable for sure, which is true both for the fore-aft and the side-side direction, as well as in standstill and in operation of the turbine. With enhanced effort, further tower modes may be detected, which most likely depends on the dynamics of the structure. Additionally, blade modes can be added.

- Predictions of the damping ratios

The sources of damping that have to be taken into account for offshore wind turbines are summarized by Kühn (2001) [58] in descending order by its importance as follows:

- Aerodynamic damping
- Structural damping
- Soil damping
- Hydrodynamic damping

Aerodynamic damping is caused by an interaction of the combined system of the rotor and the support structure with the aerodynamic wind forces acting on the blades. Aerodynamic effects are always present during the operation of the wind turbine. The first fore-aft mode of the operating wind turbine is primarily affected. Structural damping depends on the material of the structure and friction between the connecting parts. Thus, this source is always present. Soil damping describes the energy dissipation into the soil. Generally, this source of damping is always present at the points where the structure is connected to the ground. But, the effect of the soil damping to the structure highly depends on the type of the foundation and the respective mode shape. Since the measurement and the estimation of soil damping is very difficult and most of the mode shapes taken into account are not affected by soil damping, this damping source is not considered separately. Soil damping is assumed to be a part of the structural damping. Hydrodynamic damping is a result of moving structural parts surrounded by water. Here, an onshore wind turbine is investigated, for which reason hydrodynamic effects do not occur. Consequently, the main sources of damping that are expected for the investigated structure are structural damping in standstill conditions and a combination of structural damping and aerodynamic damping in operation, whereas the aerodynamic damping is supposed to mainly affect the first fore-aft mode.

Predictions of the structural damping with an emphasis on steel lattice structures can be derived from the literature. Table 5.3 gives a summary that contains damping values from selected wind turbine related standards and technical publications. The damping ratios are a combination of structural damping and soil damping. The damping ratio represents the modal damping of the first fore-aft bending mode and is the percentage of critical damping. The overall range of the summarized damping ratios is 0.2 % to 1.0 %. The upper limit mainly relies on the recommendations given by the standards. On the bases of experiences gained from measurements of civil engineering structures, structural damping ratios near the lower limit are expected for the investigated structure.

Table 5.3: Summary of estimations for structural damping ratios

Reference	**Material**	**Structure**	**Damping ratio**[1]
DIBt Richtlinie (2004) [104]	Steel	Tubular tower	0.24 % [2]
DNV-OS-J101 (2004) [105]	Steel	Lattice structure	1.00 %
GL guideline (2004) [106]	Steel	Any	1.00 %
KÜHN (2001) [58]	Steel	Lattice structure	0.2 % - 1.0 %
SCHAUMANN AND SEIDEL (2000) [92]	Steel	Tubular tower	0.2 % - 0.5 % [3]
		Overall range	**0.2 % - 1.0 %**

[1] Modal damping as percentage of critical damping, valid for the first fore-aft bending mode.
[2] Originally given as logarithmic decrement.
[3] Derived by measurements.

As stated by KÜHN (2001) [58], the aerodynamic damping absolutely dominates all further damping sources during operation. The aerodynamic damping is caused by the spinning rotor that is pushed into the direction of the wind. This motion is the reason for a decreasing angle of attack α at the rotor blades. The angle α is defined as the angle between the vector of the wind force and the vector of the reacting forces in the rotor plane. The decrease occurs because the apparent out-of-plane velocity vector is reduced by the tower-top velocity. The smaller angle of attack leads to a reduction of the aerodynamic drag and lift forces and consequently, to a reduction of the thrust force. In the same way, a movement of the tower top against the wind direction results in an increase of α and thus an increase of the thrust force. In both cases, the motion in and against the wind direction, the rotor thrust force is oriented opposite to the motion. This effect is called aerodynamic damping. For higher angles of attack, the aerodynamic damping is lower.

LANGE (2002) [59] presents a numerical estimation of the aerodynamic damping derived from the aeroelastic simulation of a 750 kW onshore wind turbine with a tubular steel tower. Eight simulations are run, each with a mean wind speed equally spaced between the cut-in and the cut-out wind speed of the turbine. The derived modal damping ratios are a combination of structural and aerodynamic damping, whereas the structural damping is a constant value of D = 0.7 %. The damping values are gained for the first fore-aft mode of the wind turbine. The simulation results are depicted in Figure 5.12 (blue graph).

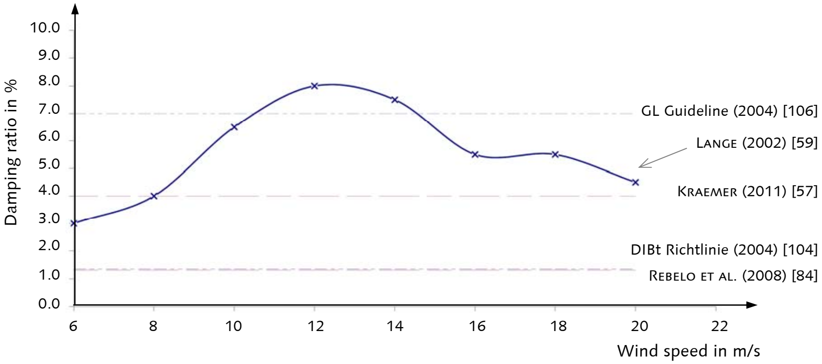

Figure 5.12: Estimation of combined aerodynamic and structural damping

LANGE (2002) [59] points out that the aerodynamic damping increases up to the rated wind speed of 13 m/s. Above rated wind speed, the pitch-angle control is active so that the effects of the aerodynamic damping decrease. Additionally, recommendations from selected wind turbine standards as well as results from measurements are added to Figure 5.12. Again, the damping ratios consider structural and aerodynamic damping for the first fore-aft mode. None of the cited references present wind-speed dependent results, for what reason the given values are depicted as constant functions in Figure 5.12. The given values in the two standards, GL guideline (2004) [106] and DIBt Richtlinie (2004) [104], can be seen as rough approximation in case no other information is available. REBELO ET AL. (2008) [84] neither describe the wind turbine type nor present the operating conditions of the wind turbine during the tests. Their study mainly aims to identify the eigenfrequencies and therefore does not treat the damping ratios in depth. KRAEMER (2011) [57] mainly uses the damping ratios to distinguish between the first fore-aft and side-side mode. For this reason, no detailed discussion of the wind speed dependency is given.

The data in Figure 5.12 give a good idea about the wind-speed dependent development of the aerodynamic damping. All presented damping ratios can be considered as useful expectation, even though the several values show broad variations. According to LANGE (2002) [59], this uncertainty is expected for the identification of aerodynamic damping. KRAEMER (2011) [57] investigates a 5 MW onshore wind turbine, which most likely matches best the structure investigated in this study.

In order to get an estimate of the investigated REpower 5M wind turbine, an analytical approach for estimating the aerodynamic damping is used, that is presented in KÜHN (2001) [58].[77] This approach is based on stationary rotor aerodynamics. It is valid for wind turbines operating with a high tip-speed ratio and near rated wind speed. Applying this approach to the data of the REpower 5M at rated wind speed gives the aerodynamic

---

[77] See page 105.

damping[78] D_{aero} calculated in equation (5.15). D_{aero} is a purely aerodynamic damping so that the structural damping has to be added. The parameters used are described in Appendix M.

$$D_{aero} = 1.59\ \% \tag{5.15}$$

The result in equation (5.15) is based on a constant slope of the lift coefficient, since the pitch-angle control is assumed to be inactive. The slope of the lift coefficient affects the damping ratio considerably. For this reason, a mean value of the slope is taken. Additionally, a lower and upper limit of the aerodynamic damping can be estimated by varying the slope of the lift coefficient, as done in equation (5.16). This estimation lies in the range gained from the literature study that is illustrated in Figure 5.12.

$$\hat{D}_{aero} = 0.98 \ldots 2.24\ \%\,. \tag{5.16}$$

Generally, there are only few results published that refer to measurements of the aerodynamic damping. For this reason, SCHAUMANN AND SEIDEL (2000) [92] mention the demand for further investigations, especially at large wind turbines that are turbines in the upper megawatt class. In the following section 5.2.5, a detailed study of the damping ratios for a 5 MW wind turbine in standstill and in operation is given, next to the determination of the structural eigenfrequencies.

5.2.5 Global Eigenfrequencies and Damping Ratios

- Measurement data

Measurement data of the structure were collected in the time period between June 2009 and March 2010. Recording the data during several months ensures the occurrence of different load conditions and operating states, each in a sufficient number of time series. The recorded sensor signals are split into 10-min time series with a sampling rate of 50 Hz. For the identification, the accelerometers, located along the height of the structure are used (Figure 5.9). Next to the structural responses, wind turbine signals such as

- wind speed (in m/s)
- pitch angle (in °)
- generator speed (in rpm)
- power production (in kW)
- nacelle yaw position (in °)
- rotor speed (in rpm)

are available. In order to select the data that are used for the system identification a statistical analysis is done. For each wind turbine signal the mean values ∅ and the maximal variation Δ (difference of the maximum and the minimum within one 10-min time series) are calculated.

---

[78] Aerodynamic damping is given as a percentage of critical damping.

A preparation of the measurement data is necessary before determining the modal parameters of the global structure. This preparation includes transforming all sensors in a consistent coordinate system. The single steps of this preparation are presented in Appendix K.

- Identification of global eigenfrequencies

The data selected for the identification of the global eigenfrequencies and mode shapes are listed in Appendix N. The separation of the data follows the principle to create comparable operation states. Two main categories are differentiated: standstill and power production.

All data sets are selected so that certain signals are constant in order to gain consistent and comparable results. Thus, only time series with a fixed nacelle position during the 10-min record are chosen. As a result, a constant coordinate system during the complete series is obtained. Additionally, the correlation between the sensor orientation and the fore-aft and side-side orientation of the structure, which is defined by the nacelle yaw position, is assured.

Standstill conditions are detected by a rotor speed of nearly 0 rpm. The blade-pitch angles equal 90°, which represents rotor blades twisted out of the wind. Only data with a considerable wind speed are used, so that a sufficient excitation of the structure can be expected. In terms of the standstill data, the wind direction does not necessarily coincide with the fore-aft and side-side orientation of the wind turbine.

Power production conditions are separated in operation states, with rotor speeds from 7 rpm to 12 rpm, with an increment of one. This range represents rotor speeds from cut-in wind speed to rated wind speed. The range is chosen in order to determine a possible rotor-speed dependency of the eigenfrequencies and to study the effects of the harmonic P-excitations due to rotor-blade passing. Each operation state allows a range of rotor speeds. To minimize a spread in the harmonic excitation due to blade passing, data sets with a small rotor speed variation are chosen. Constant blade-pitch angles are assured by selecting those data with a mean blade-pitch angle of circa 0° and a pitch angle variance that is nearly zero. The pitch angle of 0° represents rotor blades fully twisted into the wind.

Limiting the data both in standstill and power production to constant pitch angles allows omitting a spread of rotor blade eigenfrequencies. The number of data sets that are gained by the described selection is given in Appendix N for each operation state. In total, a number of 307 10-min time series are considered. Each data set contains all acceleration signals that are recorded along the height of the structure.

According to the FDD, the power spectral density matrix is calculated and contains the accelerations of each data set. Applying the SVD reveals the singular vectors $\mathbf{u}_{i1}$ and the singular values s_{i1}. The use of several data sets allows averaging the singular values. Calculating the average is done for each operation state. By means of the average, random errors in the data can be smoothed. In total, seven averaged singular value functions are calculated so that each corresponds to one of the defined operation states. The singular value functions need to be interpreted in order to identify the eigenfrequencies. This interpretation is done using the eigenvectors that are gained from the modal analysis. The simulated eigenvectors are compared to the first singular vector. The singular vectors of each operation state are averaged over the used data sets, as is done for the singular values. If a high accordance is detected, an eigenfrequency is identified in the singular value function. The geometrical accordance is assessed by the MAC value.

Using the MAC values reveals interpreted singular value functions. Subsequently, the singular value function in standstill (0 rpm, Figure 5.13) and for the operation states of 7 rpm, 10 rpm, and 12 rpm (Figure 5.14 to Figure 5.16) are depicted. The depictions of the remaining operation states are given in Appendix N. Next to the eigenfrequencies, the harmonic P-excitations and the local eigenfrequencies of bay 5 (see section 5.2.3) are marked.

The depictions of the averaged singular values clearly show the first and second modes. The MAC values are always high, in the range of 0.8 to 1.0. That means an unequivocal identification of these modes is possible. The third modes are less clear in the spectrum. The identification is only possible by means of the MAC comparison. The MAC values are smaller and occur in the range of 0.6 to 0.8. The third modes were predicted differently by the FE simulation, mainly due to the imprecise assumptions about the stiffness of the upper soil layer. After correcting this soil stiffness according to the local measurement (section 5.2.3), better predictions simplify the identification. Because the identification of the third modes shows uncertainties, the identification of further global modes is omitted. Most of the further peaks that occur in the presented singular values are related to rotor blade modes or to vibrations of single structural components. The identification of further single components is not of interest in this work.

Additionally, the influence of the P-excitation is clearly visible. The operation states in power production (Figure 5.14 to Figure 5.16 and Appendix O) always show the 1P and the 3P-excitation and how they march through the spectrum. In Figure 5.14 the first mode and the 3P-excitation at 7 rpm are closely spaced so that even the amplitude of the 3P-excitation dominates. The same characteristic is visible in Figure 5.16 which reflects a rotor speed of 12 rpm, but there for the interaction of the second side-side mode with the 12P-excitation. This fact points out that even high multiples of 1P may influence the response in case it resonates with an eigenfrequency.

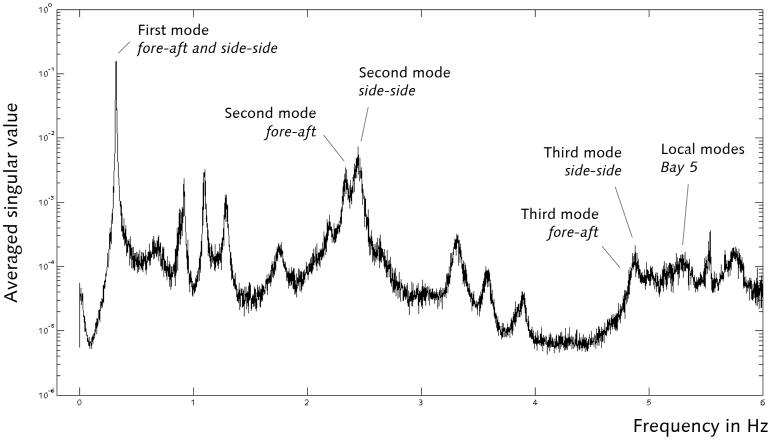

Figure 5.13: Averaged singular value – 0 rpm

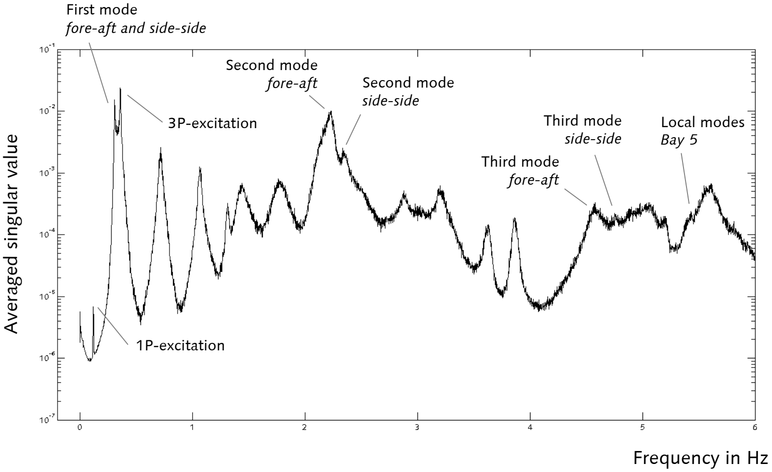

Figure 5.14: Averaged singular value – 7 rpm

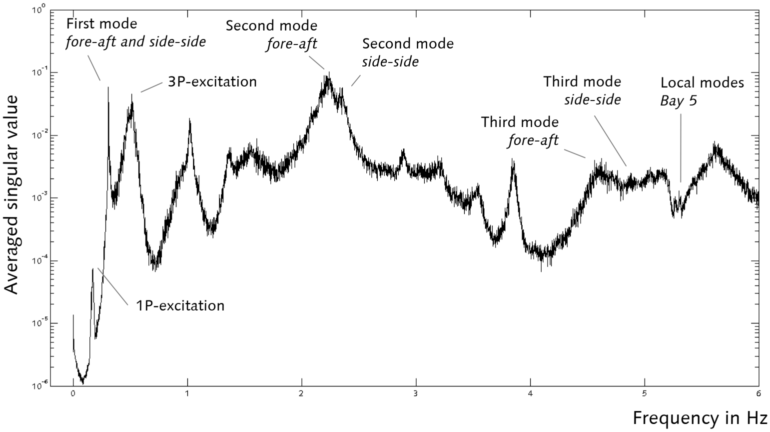

Figure 5.15: Averaged singular value – 10 rpm

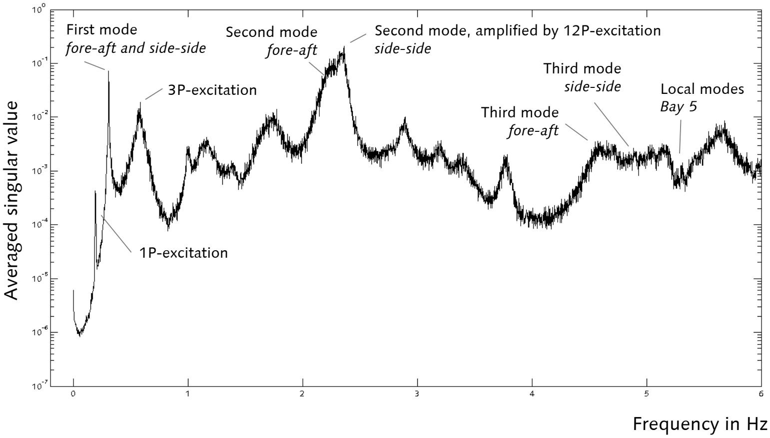

Figure 5.16: Averaged singular value – 12 rpm

A brief summary of the identified frequencies is possible by means of the Campbell diagram that depicts the frequencies with respect to the rotor speed (Figure 5.17). The eigenfrequencies are identified with an accuracy of two positions after the decimal point, which is considered sufficient. The variations of the frequencies in the first and second modes are ±0.1 Hz. The third fore-aft modes have variations of ±0.2 Hz and the side-side modes of ±0.9 Hz. Especially the third side-side mode shows uncertainties, which are most likely caused by a poor excitation of this mode. The predominant small variations indicate that there is no rotor-speed dependency. Therefore, the frequencies are averaged over the operation states. Consequently, the frequencies appear as a constant function in the Campbell diagram. The crossing points of the P-excitations with the eigenfrequencies mark points of possible resonance.

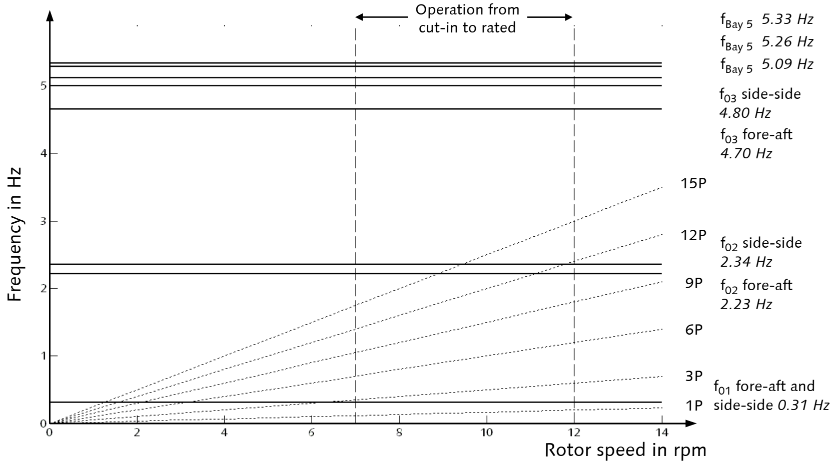

Figure 5.17: Campbell diagram with system identification results

- Identification of damping ratios

Estimating damping ratios is the next step after identifying the eigenfrequencies. Subsequently, modal damping ratios as percentage of critical damping are calculated. An emphasis is laid on the first fore-aft mode of the structure with respect to different operation states, because this mode is affected by aerodynamic damping that shall be determined. As done for the identification of the eigenfrequencies, the available measurement data are divided into different operation states. The damping ratios are also estimated both for standstill and power production. For the operation states in power production, two further states are added that are located above rated wind speed, as depicted in Figure 5.18. These states serve to determine the wind-speed dependency of the aerodynamic damping that is discussed in Figure 5.12. The available measurement data does not contain sufficient data sets above wind speeds at hub height of 19 m/s, which thus represents the upper limit for the definition of operation states.

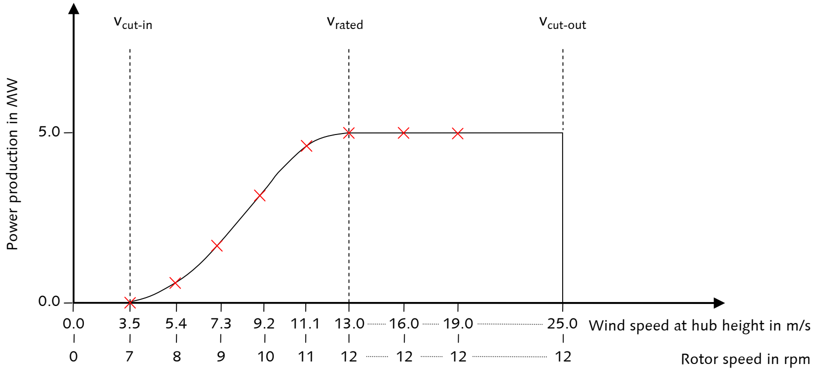

Figure 5.18: Operation states for damping estimation

The summary of the data selection is given in Appendix N. Again, the data are selected so that each operation state contains several data sets that produce comparable results. All chosen data have a fixed nacelle position during the recorded 10-min time series, which ensures a constant coordinate system and a defined correlation between the sensor orientations and the fore-aft and side-side orientation of the structure. A total number of 229 10-min time series are considered.

The standstill conditions are detected by a rotor speed nearly 0 rpm and blade-pitch angles of 90°, which represents rotor blades twisted out of the wind. In terms of the standstill data, the wind direction does not necessarily coincide with the fore-aft and side-side orientation of the wind turbine. Aerodynamic effects are not expected in standstill conditions.

The power production conditions are defined by the wind speeds at hub height. In order to keep the relation to the operation-states definition for the frequency identification, the rotor speeds are given next to the wind speeds in Figure 5.18. The operation states between cut-in and rated wind speed are defined by a limitation of rotor-speed ranges in combination with small variances of the rotor speeds. Additionally, the blade-pitch angles are restricted to a constant value of 0°, which means that the blades are twisted into the wind. Only small variations of the blade-pitch angles are allowed. The operation states between rated and cut-out wind speeds are defined by limited wind speed ranges, whereas the rotor speeds are constant at 12 rpm.

Each data set is analyzed separately using the algorithm of the FDD as described in section 5.2.2. To determine the damping ratio of a certain eigenfrequency, the corresponding SDOF system has to be detected. A MAC value of $\Omega \geq 0.9$ is used to find the frequency lines of the auto-PSD function. If all further lines are set to zero, the PSD of the autocorrelation can be transformed into the time domain, applying an iFFT. This decaying time-domain signal enables the estimation of the damping ratio, which is here calculated using two methods. Both the decay constant δ and the logarithmic decrement ϑ is determined by a least-squares approach that is applied to the maxima of the time-domain function.[79] An example of a detected autocorrelation function that represents the first fore-aft mode is depicted in Figure 5.19.

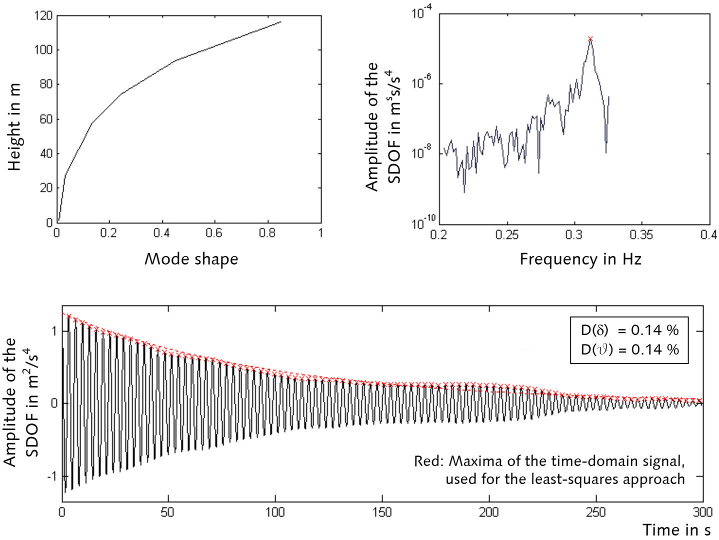

Figure 5.19: Detected autocorrelation function in the frequency- and the time domain

The data sets in standstill conditions (see Appendix N) are used to determine the structural damping without aerodynamic effects. The results are summarized in Table 5.4. The given damping ratios are based on stochastic wind excitations at rotor speeds of nearly 0 rpm and blade-pitch angles of 90°.

Table 5.4: Damping ratios in standstill

Mode shape	**Fore-Aft**		**Side-Side**	
	Frequency	D (1)	Frequency	D (1)
1st global bending (2)	0.31 Hz	0.3 %	0.31 Hz	0.3 %
2nd global bending	2.23 Hz	0.5 %	2.34 Hz	0.4 %

(1) Damping ratio D as percentage of critical damping.
(2) See Appendix O.

---

[79] See Appendix J.

Figure 5.20 presents damping ratios for the wind turbine in power production. Both the logarithmic decrement ϑ and the decay constant δ are calculated. Thus, two damping ratios are available for each data set. Appendix O contains the distributions of the estimated damping ratios for each operation state.[80] A comprehensive summary of these results reveals the depiction in Figure 5.20. The red curve represents the mean values of the damping ratios and show how they develop over the operation states, mainly caused by aerodynamic effects. The operation states are those that were presented in Figure 5.18. As pointed out in section 5.2.4, damping estimation always underlies uncertainties in the identification process. For this reason, the standard deviations (yellow area) that correspond to the mean values are given additionally, which clarifies the range in which the damping ratios vary.

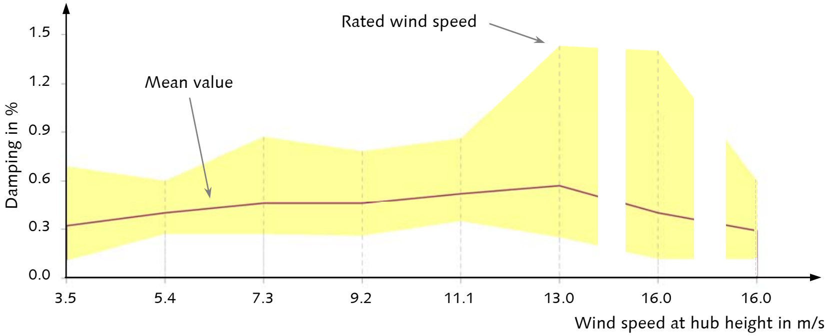

Figure 5.20: Estimated damping ratios over wind speeds at hub height

.. ..

- Conclusion

The identification of global eigenfrequencies reveals values for the 1st, the 2nd, and the 3rd global bending modes, each in fore-aft and in side-side directions. These results are summarized in Figure 5.17. Further global modes, such as the 4th bending mode, could not be identified with reliable accuracy due to the poor excitation of these modes. Hence, not all eigenfrequencies that were predicted in the modal analysis are derived from the measurement data. However, the expectation in terms of the number of detectable eigenfrequencies – see the literature research given in section 5.2.4 – is slightly exceeded with the three global bending modes. The gained eigenfrequencies serve as reference values for the modal updating process. Additionally, the P-excitations with its higher harmonics appear in the spectra. The resonance with the eigenfrequencies is clearly visible.

Structural damping ratios are estimated for the 1st and the 2nd global bending modes, each in fore-aft and side-side directions. The damping ratio of the first fore-aft mode (Table 5.4)

---

[80] As average of the mean values of δ and ϑ, calculated for each operation state.

results in a value of 0.3 %. The comparison to the literature (Table 5.3) shows the identified damping ratios to be at the lower edge of the expected range. Thus, the investigated support structure with its main parts, the lattice tower and the tubular tower, is a lightly damped steel structure.

Effects of the aerodynamic damping are studied looking at different power production conditions. The development of the damping ratios of the first global fore-aft mode with respect to different wind speeds is shown in Figure 5.20. As expected (see Figure 5.12), the damping ratios increase up to rated wind speed at 13 m/s. Above rated wind speed, the damping ratios decrease. This effect is caused by the aerodynamic forces acting at the rotor blades due to the moving tower top. The mean of the damping ratios at rated wind speed is 0.6 %. Single data set even produce damping ratios that exceed 1 %. Consequently, the identified damping ratios are smaller than the prediction derived from equation (5.16).[81] The identified operation-state dependent damping ratios from Figure 5.20 can be compared to the damping ratios given in the literature (Figure 5.12). This comparison shows the identified damping ratios lying at the lower edge of the expected damping-ratio range.

As a general conclusion, it can be stated that the identification of the eigenfrequencies and mode shapes give reasonable results. The damping estimation contains uncertainties, which is indicated by higher standard deviations of the damping ratio results. The statement is true both for the identification of the global structure and the local structural components. The presence of uncertainties is in accordance with the statements derived by ANDERSEN ET AL. (1999) [1] and PEETERS AND DE ROECK (2001) [83].

Further information that describes the above-given system identification results in detail is presented in PAHN AND ROLFES (2011) [79]. Additional related publications are PAHN ET AL. (2010) [77] and RAABA (2010) [113].

5.3 Inverse Load Calculation using Measurement Data

5.3.1 Model Updating

The objective of the model updating is to adjust the FE model (see section 5.1.2) so that its undamped eigenfrequencies match the measured eigenfrequencies (see sections 5.2.3 and 5.2.5) best. Thus, a realistic dynamical model of the structure is gained. As a matter of fact, model updating is a research field of its own. Even though the model updating is important for the inverse load calculation, a detailed theoretical discussion is not given in this work. For further information, it shall be referred to the excellent publications of EWINS (2000) [18] and FRISWELL AND MOTTERSHEAD (1995) [22].

Choosing appropriate parameters is essential for the accuracy of the model updating. This means that the model updating parameters need to fulfill two conditions: 1) they should be based on physically meaningful uncertainties such as modeling simplifications and 2) they should be sensitive to the eigenfrequencies. With respect to these conditions, the model

---

[81] Equation (5.16) calculates a purely aerodynamic damping. Structural damping has to be added.

updating parameters depicted in Figure 5.21 are chosen. This choice is based on sensitivity analysis for the structural components of the tower and the lattice structure that are presented in Pahn and Rolfes (2011) [79]. A sensitivity analysis of the soil parameters is given in Appendix P. Appendix P also contains a discussion that outlines how the chosen parameters fulfill the two above-mentioned conditions.

The masses of the structural components lattice structure, foundations, transition piece, tower, and rotor-nacelle assembly (RNA) are determined using the engineering drawings and, when possible, completed by weighing results (e.g. nodes, transition piece). The masses are compared to the FE modeling. All structural components show deviations of less than 3 %, which guarantees the accuracy of the masses in the updated FE model.

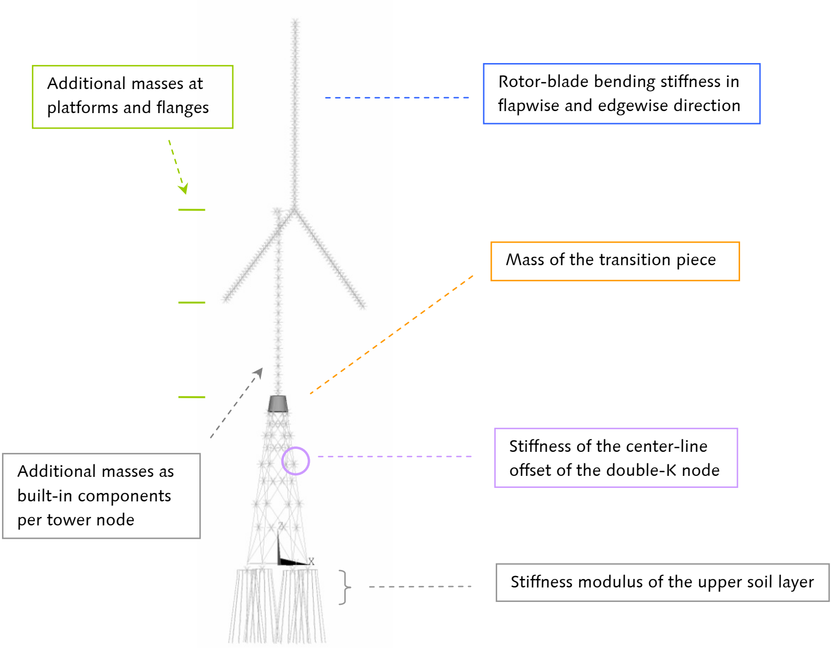

Figure 5.21: Parameters chosen for the model updating process

The FE model in Figure 5.21 shows an enhanced modeling of the RNA, with the rotor blades represented by flapwise and edgewise stiffness and mass elements distributed along the rotor-blade length. Since accurate structural data are not available, these data are estimated.[82] The need to enhance the model is caused by the interaction of the RNA with higher bending modes, which, in this particular case, are the third global bending modes.

---

[82] The structural properties are similar to the NREL 5 MW Baseline. See Jonkman et al. (2009) [49].

The so-far used simplified RNA (see section 5.1.2) does not allow a satisfactory model updating of the offshore support structure. Due to the complexity of the structure, a stepwise model updating process turns out to be advantageous, in which initially the first and second global bending modes are adjusted. Before continuing the model updating, the new FE model is assessed using a modal analysis. This procedure concentrates on a limited number of model updating parameters. In case the number of parameters that need to be updated in one step increases, an automated model-updating tool can be used such as introduced in HAAKE (2010) [31].

The results of the model updating are summarized in Table 5.5. The eigenfrequencies of the updated FE model are shown in combination with the differences to the frequencies gained by the measurements. As visible, the first and second global bending modes have a very high accuracy. The maximal error is 0.03 Hz, which is in the range of measurement uncertainties. The differences that occur for the third global bending modes and the local modes of bay 5 are higher. The reason is that they interact with the RNA, whose modeling is based on estimated structural data that induce uncertainties. Nevertheless, the differences are between 2 % and 6 %, which is still satisfactorily.

Table 5.5: Eigenfrequencies of the updated FE model

Mode shape	**Frequency**	**Difference to the measured frequency**	
1st global bending fore-aft	0.31 Hz	0.00 Hz	0.0 %
1st global bending side-side	0.31 Hz	0.00 Hz	0.0 %
2nd global bending fore-aft	2.26 Hz	0.03 Hz	1.3 %
2nd global bending side-side	2.37 Hz	0.03 Hz	1.3 %
3rd global bending fore-aft	4.42 Hz	0.28 Hz	6.0 %
3rd global bending side-side	4.69 Hz	0.11 Hz	2.3 %
Bay 5 – mode 1 } see Table 5.2	4.91 Hz	0.18 Hz	3.5 %
Bay 5 – mode 2 } see Table 5.2	5.36 Hz	0.10 Hz	1.9 %
Bay 5 – mode 3 } see Table 5.2	5.47 Hz	0.14 Hz	2.6 %

5.3.2 Results of the Inverse Load Calculation

The inverse load calculation follows the steps described in the previous sections. The objective of the calculation is to determine the rotor thrust force acting at hub height, as depicted in Figure 5.22. The inverse load results from superimposing the static/quasi-static component and the dynamic component (Figure 4.6). The dynamic component is derived from applying the Deconvolution in the Frequency Domain using the least-squares approach (section 3.2).

The first step is deriving the system matrices from the updated FE model. ANSYS provides the possibility to read out the stiffness and the mass matrices. Both matrices are given in Harwell-Boeing format and come together with a so-called mapping file that assigns the node numbers to the degrees of freedom. The complex FE description of the structure contains a huge number of DOFs. For this reason, the system matrices need to be reduced to those modes that are decisive for the inverse calculation. As a reduction method, the modal reduction that is introduced in equation (4.3) is used. First of all, the decisive modes are the global fore-aft modes of the structure because the unknown force is acting in the fore-aft direction. In terms of the mode number, there is no exact conclusion so far. The verification study in section 4 did not allow for varying the number of DOFs, since by default, FAST has a maximum of two tower-bending modes. For the real-world wind turbine investigated in this section, a "true" rotor thrust force that could be used as a reference is not known. Hence, assessing the dependency of the used mode number to the accuracy of the inverse load calculation is impossible. In order to stay close to the verification study in section 4 and with respect to the system identification results from section 5.2.5, the first and the second global bending modes of the updated FE model are chosen.

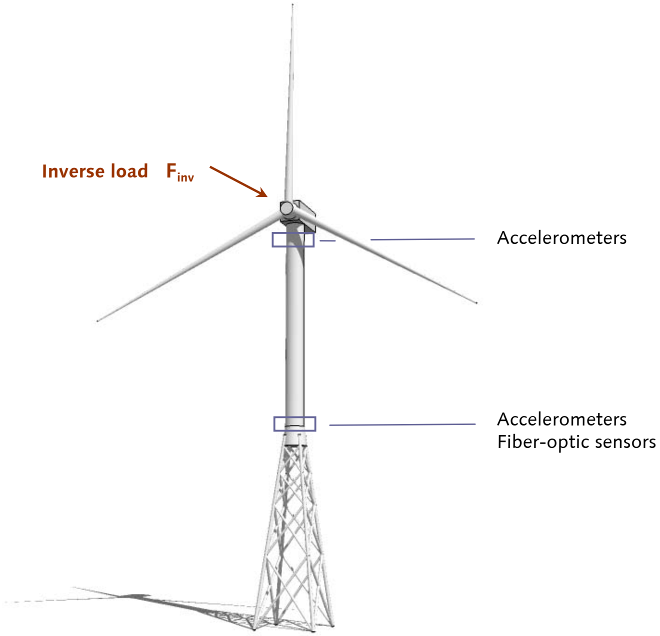

Figure 5.22: Sensor positions for the inverse load calculation

Figure 5.22 depicts the sensors needed for the inverse calculation. The static/quasi-static component is gained from strain sensors (fiber optic) at the tower bottom. The signals are low-pass filtered[83] at the chosen cut-off frequency of 0.15 Hz. The static/quasi-static load component is calculated using a strain-force relationship that is derived from the updated

---

[83] See Appendix E.

FE model. The calculation of the dynamic component is based on acceleration signals that are double integrated to displacements. The integration can be done both in the time domain and in the frequency domain. Based on the discussion in Appendix E, the frequency-domain based Omega Arithmetic is used in this work.

The inverse calculation is done for the wind turbine in operation. The calculation accounts for the damping ratios given in Table 5.4. Additionally, the aerodynamic damping presented in Figure 5.20 is taken into consideration. The identification of the damping ratios shows uncertainties. A variation of the damping ratios within the identified range does not affect the inverse calculation result considerably. For this reason, the mean values of the damping ratios are used. The result of the inverse load calculation is depicted in Figure 5.23.

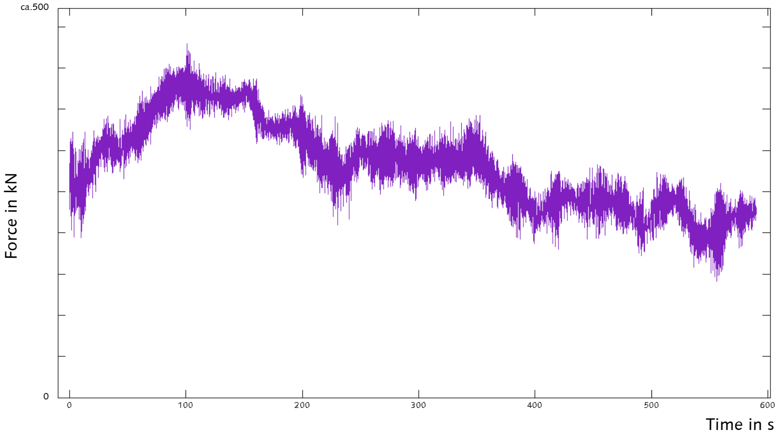

Figure 5.23: Inversely calculated load

As previously mentioned, an exact verification of the inverse load is not possible, due to a lacking reference or a “true” rotor thrust force. Nevertheless, a rough appraisal of the resulting quality reveals the comparison of the inversely calculated load with a simple rotor thrust force estimation that is given by the GL guideline (2004) [106].[84] The product of the swept rotor area A and the pressure p_N gives an approximation of the rotor thrust force F_{xN}. The pressure p_N in equation (5.17) depends on the wind speed v. The estimation is based on the Betz law and is described by the quantity equation

$$\frac{F_{xN}}{(kN)} = \frac{v^2/(m/s^2)}{1800} \cdot \frac{A}{(m^2)} . \tag{5.17}$$

---

[84] See chapter 4, Appendix B, part C.

Figure 5.24 depicts the comparison of the inversely calculated load F_{inv} to the estimation F_{xN}. The comparison shows obvious differences between both graphs, which meets the expectation. The estimate directly depends on the wind speed containing short-period wind-speed changes with high amplitudes. In addition, the estimate does not account for the structural dynamics of the wind turbine and its support structure. Consequently, the interaction between the structural dynamics and the load is not considered. Above all, the estimate does not cover the wind turbine control. All these aspects explain the differences in Figure 5.24. But nevertheless, Figure 5.24 gives important information. The comparison shows that the inversely calculated load lies within a reasonable range, which at least allows excluding gross calculation errors.

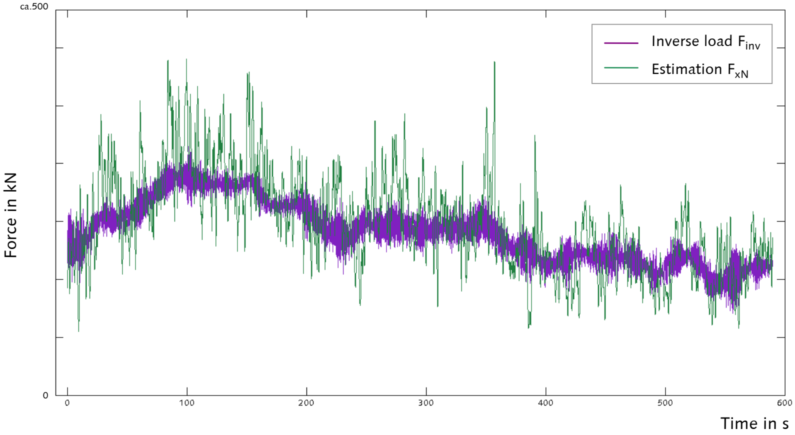

Figure 5.24: Comparison of the inverse load to estimated rotor thrust

Figure 5.25 gives a further verification of the inverse load calculation. The Figure compares the measured strains to strains gained from the FE simulation, each at the tower bottom of the structure and the updated FE model, respectively. The simulated strains result from a time-marching dynamic analysis of the FE model, with the above-calculated inverse load F_{inv} as the applied load. F_{inv} is derived from the same measurement data as the measured strains are taken from. The comparison in Figure 5.25 shows a good accordance between the measured and the simulated strains. The simulation is able to reproduce the vibrations of the structure, which is especially visible for the high-frequent content of the strain signals. A static offset between the simulation results and the measurement data occurs. However, this offset is part of the measured fiber-optic signals, because of the difficulty in calibrating sensors for the strain measurement.[85]

---

[85] A discussion of this problem with focus on the investigated structure is given in the final report of the OGOWin research project [74].

An estimate for the accuracy is gained by calculating the error between the simulated and the measuremd strain data in Figure 5.25. Therefore, equation (3.65) is applied to the upwind strain data, which are modified by substracting their mean values. The result is $\varepsilon = 29\ \%$.

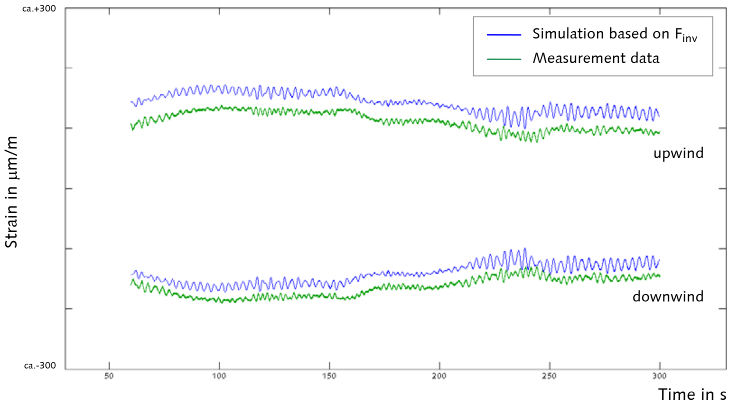

Figure 5.25: Strain at tower bottom

As a final conclusion, the calculated inverse load, in combination with the updated FE model, is able to generate realistic strain values at certain cross-sections. Even though the shown verification only considers a single cross-section, the results are promising in terms of using the inverse load for the calculation of stresses at arbitrary cross-sections, which could be used for fatigue-strength analysis and lifetime predictions.

5.4 Summary

This section describes the inverse load calculation for a 5 MW wind turbine with an offshore support structure that is erected onshore as a prototype. The previous section 4 dealt with a virtual wind turbine, generated and calculated with FAST. In contrast, this section investigates a real-world wind turbine. Thus, this section focuses on aspects that additionally have to be solved, while representing the real-world structure as a numerical model. In particular, the identification of structural dynamic parameters and the model updating are discussed.

A high effort is made to the system identification. With the Frequency Domain Decomposition, an adequate method for determining eigenfrequencies and damping ratios from measurement data is described. Measurements are analyzed for local structural components and for the dynamics of the entire structure. Standstill and various operation states are investigated, with a special focus on the wind-speed dependency of the eigenfrequencies and the damping ratios. For the eigenfrequencies no rotor-speed dependency is observed, whereas the influence of aerodynamic effects is clearly shown within the identified damping ratios. The influences of high multiples of the P-excitation that resonate with eigenfrequencies are also shown.

Additionally, this section shows how the structural description and the results of the system identification are used to create a mathematical model of the structure. This process is called model updating. The model updating is done with very high accuracy. Thus, a FE model is created that represents the measured eigenfrequencies, which is an important precondition for the inverse load calculation. In the model updating process, it turned out that the RNA modeling simplification needs to be enhanced. Distributed mass and stiffness representation of the rotor blades are necessary in order to cover the interactions that occur between the rotor blades and global bending modes or local modes respectively.

The result for the inverse load calculation is shown, which is the rotor thrust force caused by a load case representing the operating wind turbine. Detailed descriptions are omitted because of proprietary information. A verification study shows the plausibility and the accuracy of the inversely calculated load. The accuracy is determined by comparing measured strains to simulated strains that are derived from the updated FE model, with the inverse load as applied load.

In conclusion, the outcomes of this section are 1) the methodical approach for the inverse load calculation at a wind turbine using measurement data, 2) a contribution to the system identification of wind turbines under operation, especially in terms of aerodynamic damping, and 3) a selective assessment of the quality of the inverse load calculation results.

6 Inverse Load Calculation at a 5 MW Offshore Wind Turbine Model

The previous sections discussed the inverse load calculation of aerodynamic loads in steps. These were chosen in order of increasing complexity. Based on studying basic characteristics of the inverse load calculation (section 3), specific characteristics of wind turbines – such as coupled dynamics and the control of the wind turbine – were additionally taken into account. These specific characteristics are investigated in section 4 using the simulation code FAST. In section 5, the requirements are discussed that occur while applying the developed calculation procedure to a real-world wind turbine with measured data. The so-far developed procedure with the according results and conclusions are now used in order to apply the inverse load calculation to offshore conditions.

In order to investigate the ability of the inverse load calculation to cope with combined wind and wave loads, the simulation code FAST is used. FAST accounts for the coupled dynamics of the wind inflow, aerodynamics, elasticity, and control of the wind turbine. Additionally, FAST considers incident waves, sea currents, hydrodynamics, and foundation dynamics of the support structure.[86] A 5 MW wind turbine model with a monopile foundation is used. Hence, the description of the structure is known. FAST simulates the corresponding system response due to defined loads. Using the simulated system response and the known system descriptions allows calculating the applied wind and wave loads inversely. The inversely calculated wind load is based on the previously discussed procedures, results, and conclusions. This section investigates the capability of calculating the wave load additionally. Comparing the inversely calculated loads to the loads defined for the simulation serves as a verification study in order to assess the accuracy of the inverse load calculation procedure.

For this verification study, section 6.1 first gives an overview of the calculation of hydrodynamic loads with FAST and discusses the approach for the inverse load calculation with respect to the simulation. Section 6.2 describes the chosen wind turbine model and summarizes the simulation steps, including the necessary post-processing. The results of the inverse load calculation and the verification of the result accuracy is presented in section 6.3.

---

[86] See JONKMAN ET AL. (2008) [47].

6.1 Hydrodynamic Loads in FAST with HydroDyn

6.1.1 Theoretical Basics of FAST with HydroDyn

FAST calculates hydrodynamic loads using the built-in routine HydroDyn.[87] At the moment, a user's guide for HydroDyn is not available. The theoretical basics of HydroDyn are documented in Jonkman (2007) [46] and in Jonkman (2009) [48]. HydroDyn is able to handle two different support-structure types: monopiles and floating platforms. The entire section 6 is limited to a monopile structure, thus, the theoretical basics of HydroDyn given below are summarized for the monopile-related modeling and calculation of waves, currents, and hydrodynamic loads. Floating-platform specific theory, such as the calculation of mooring system reactions, is omitted.

The modeling of monopile structures is defined by the tower parameters of the FAST input file. The foundation modeling of the monopile is possible through user-defined routines,[88] with options for apparent fixity, coupled springs, and distributed springs (Figure 6.3, right). The springs can be defined either linearly or non-linearly, whereas the non-linearity can be taken from p-y-curves. Simple models are typically suitable for a full-system analysis.[89]

The theoretical fundamentals and some basic assumptions about FAST are already described in section 4.1. For monopiles, the wave kinematics (linear or non-linear) are solved in the absence of the structure and hydrodynamic loads are applied using Morrisons' equation, which includes non-linear viscous-drag terms. The wave kinematics are calculated with the Airy wave theory, which enables the modeling of the most waves in deep water and small-amplitude waves in shallow water. Stochastic waves are described by the Pierson-Moskowitz spectrum[90], the JONSWAP spectrum[90], or a user-defined spectrum. Three stretching methods are available: vertical, extrapolation, and Wheeler. Arbitrary wave directions are possible, but without spreading. Optionally, non-linear waves are available that have to be read in from externally generated wave data. Steady sea currents are calculated as IEC-style sub-surface currents, near-surface currents, and depth-dependent currents. Additionally, user-defined currents can be considered.

The hydrodynamic loads are calculated using the relative form of the Morison equation. The linearization of the hydrodynamic problem usually does not account for non-linear second- or higher-order hydrodynamic effects. But, the linearized hydrodynamic problem that is solved in HydroDyn includes the non-linear viscous-drag term from the Morison equation. The total hydrodynamic loads at the monopile structure F_{ik}^{Hydro} are calculated at each structural node along the tower as

$$F_{ik}^{Hydro} = F_{ik}^{prtHyd} - A_{ijk} \cdot \ddot{q}_{jk} \qquad (6.1)$$

---

[87] HydroDyn is part of FAST version v7.00.01a-bjj and newer.

[88] Currently, built-in foundation models are not available.

[89] See Jonkman (2011) [51].

[90] See Figure 2.5, page 18.

with the node number k, the force component i and the acceleration component j. The subscripts i and j range from 1 to 6, representing the displacement and rotational DOFs of the tower nodes. The accelerations in the spatial coordinate system are represented by $\ddot{q}$. The term F_{ik}^{prtHyd} represents the portion of the hydrodynamic force that does not depend on accelerations,[91] including inertia and viscous drag loads. The product of the hydrodynamic added-mass matrix A_{ijk} with the accelerations gives the hydrodynamic impulsive-added-mass. Composing equation (6.1) in form of a difference[92] avoids an implicit EoM, with a forcing function[93] that depends on the accelerations.

6.1.2 Source-Code Modification in FAST

The approach for the inverse load calculation for combined wind and wave loads is theoretically discussed in section 2.2.2. In order to use FAST for the verification study, the hydrodynamic forces that are applied to the FAST model have to be known. But, the hydrodynamic forces are not output parameters by default. For this reason, the source code of FAST is modified. This modification and some further preliminary thoughts about the inverse calculation are given subsequently.

By default, FAST accounts for two tower bending modes in the fore-aft direction. Hence, for the time being, using FAST allows for the inverse calculation of two loads. These two loads are the aerodynamic wind load – simplified to the rotor thrust – and the hydrodynamic wave load[94] – simplified to the resulting wave load – as depicted in Figure 6.1 (left). The inverse calculation of the wind load follows the procedure described in the previous sections. The use of a small number of DOFs is a reasonable approach. This statement is e.g. confirmed by Jensen et al. (2007) [43]. They use an ARMA approach in order to gain load information for a pile with a top mass put into a basin and loaded with stochastic waves. One DOF is used in order to gain good results. Nevertheless, further research should investigate the effects of using a higher number of DOF.

In terms of the hydrodynamics, FAST calculates loads for the fixed-bottom monopile structure from mudline to the current wave surface. The hydrodynamic loads are described by equation (6.1). The inverse load calculation needs the hydrodynamic loads as output parameters because they are needed as a reference value that can be compared to the inversely calculated wave load. In order to make the hydrodynamic loads from FAST available, the FAST output routine is rewritten as described in Appendix Q.

---

[91] This portion of the hydrodynamic force can depend on displacements and velocities.

[92] In case of floating platforms, equation (6.1) contains an additional forcing term that describes the mooring lines.

[93] See equation (4.1).

[94] See section 2.2.2, which discusses the neglect of the sea currents contribution to the hydrodynamic loading in terms of the inverse load calculation.

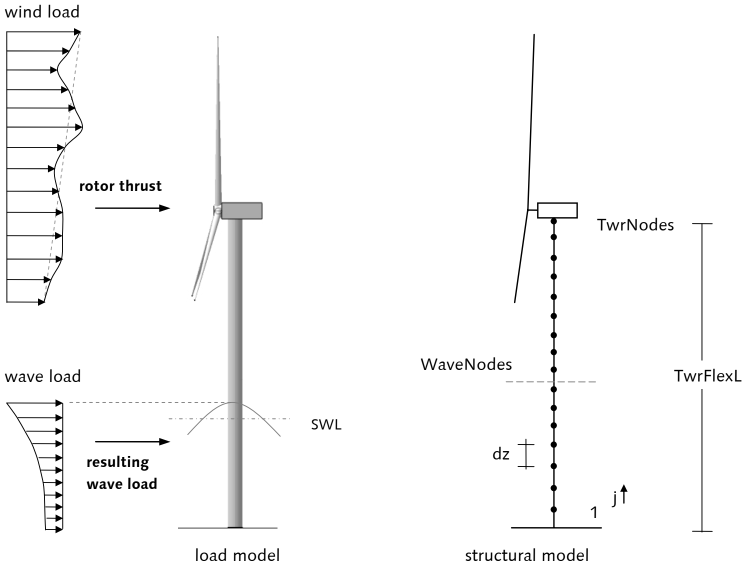

Figure 6.1: Structural nodes with hydrodynamic loading

According Airy wave theory, the wave load is non-linearly distributed along the tower's height. In order to capture the gradient of the wave load, a sufficient number of nodes has to be defined below the wave surface, which is assured by choosing a sufficient number of tower nodes. But only a limited number of nodes are loaded with hydrodynamic forces. The rewritten FAST output only considers the loaded nodes.

The total number of tower nodes TwrNodes is defined in the FAST input file. The coordinates of the elements h_k and the element length dz depend on the height of the structure TwrFlexL, which is the sum of the distance from mudline to SWL and the distance from SWL to tower top (Figure 6.1). The indexed variable $k \in N$ ranges from 1 to (TwrNodes + 1). The nodes are located in the center of the elements.

$$h_k = (k-1) \cdot \left(\frac{\text{TwrFlexL}}{\text{TwrNodes}} \right) \tag{6.2}$$

$$dz = \left(\frac{\text{TwrFlexL}}{\text{TwrNodes}} \right) \tag{6.3}$$

The number of nodes that are loaded with hydrodynamic forces is denoted with the variable WaveNodes. An approximation of WaveNodes gives equation (6.4), which calculates the nodes up to the elevation of the SWL plus three times H_S.

$$\text{WaveNodes} = \frac{\left(\text{SWL} + 3 \cdot \text{H}_\text{S}\right) + 0.5 \cdot \left(\dfrac{\text{TwrFlexL}}{\text{TwrNodes}}\right)}{\left(\dfrac{\text{TwrFlexL}}{\text{TwrNodes}}\right)} \tag{6.4}$$

The rewritten FAST output contains the matrix of the hydrodynamic forces $\mathbf{F}^{\text{Hydro}}$ in the fore-aft direction for the nodes for the node numbers 1 (mudline) to WaveNodes, for each time step t. Within a post-processing step the resulting wave load F^R and its points of application h^R can be calculated using equations (6.5) and (6.6).

$$F^R = \sum_{k=1}^{n} F_k^{\text{Hydro}} \cdot dz \tag{6.5}$$

$$h^R = \frac{\sum_{k=1}^{n} h_k \cdot \left(F_k^{\text{Hydro}} \cdot dz\right)}{F^R} \tag{6.6}$$

F^R and h^R have to be calculated for each time step t. The utilized variables and indices are explained in Figure 6.2.

F^R – resulting wave load $^{(1)}$
F_k^{Hydro} – hydrodynamic force at node k $^{(1)}$
h^R – point of application of $F^{R\,(1)}$
h_k – point of application of $F_k^{\text{Hydro}\,(1)}$
dz – element length
k – node number $^{(1)}$
n – maximal number of nodes $^{(1)}$

$^{(1)}$ at every time step

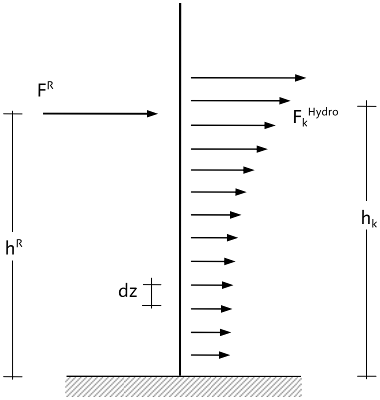

Figure 6.2: Calculation of the resulting wave load

6.2 Analysis in FAST

In what follows, the defined wind turbine model that is used for the analysis is described. Additionally, the settings for the linearization and for the time-marching simulation are summarized.

6.2.1 Description of the 5 MW Offshore Wind Turbine Model

The previously described NREL 5 MW reference wind turbine is used.[95] Now, the properties in Table 4.1 describe the structure from still water level (SWL) upwards. Thus, the three-bladed upwind variable-speed variable pitch-to-feather controlled turbine has a hub height of 90 m above SWL. The rotor blade lengths are 63 m. A total number of 16 DOFs are enabled. The number of DOFs result from the 1st and 2nd flapwise blade modes (3 blades – 6 DOFs), the 1st edgewise blade modes (3 DOFs), the drivetrain rotational flexibility, generator, and yaw (3 DOFs), and the 1st and 2nd tower bending modes in fore-aft and in side-side direction (4 DOFs). The wind turbine is carried by a tubular steel tower. Below SWL, the tower is supported by a fixed-bottom (apparent fixity) monopile substructure. The water depth is set to 20 m, which equals the height of the substructure. Thus, the height of the entire structure from mudline to hub height is 110 m. The diameter of the steel monopile is 6 m. Figure 6.3 depicts the model. The number of tower nodes is chosen to 175.[96] Thus, the element length between the tower nodes is dz = 0.63 m, which gives a number of 31 nodes under SLW. This number is sufficient in order to represent the non-linear distribution of the hydrodynamic load. All offshore-related hydrodynamic inputs are defined in the platform input file that has to be read into the FAST input file.

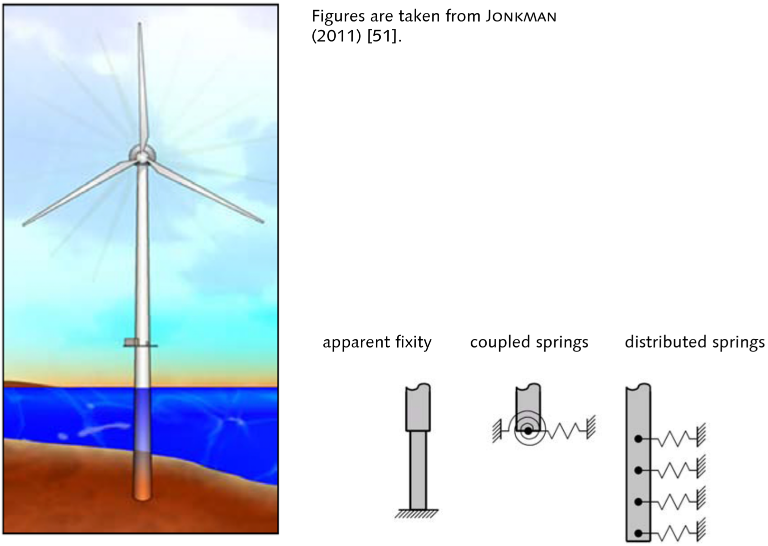
Figures are taken from JONKMAN (2011) [51].

Figure 6.3: Offshore monopile model and simplified monopile foundation models

---

[95] See JONKMAN ET AL. (2009) [49] and section 4.2.1.

[96] FAST allows an arbitrary number of tower nodes. In case the number of tower nodes exceeds 99, the ADAMS preprocessor mode has to be set to ADAMSPrep = 1 in the FAST input file.

In fact, the model described above is an extended offshore version of the 5 MW onshore wind turbine model that was used in section 4. This close structural affinity directly allows applying the conclusions from the onshore simulations. Consequently, the offshore simulations – both the linearization and the time-marching simulation – follow the already described algorithms from section 4.2.2 and 4.2.3. The new offshore-related simulation settings are discussed subsequently.

6.2.2 Linearization and System Matrices

The objective of the linearization is the determination of the full-system eigenfrequencies of the FAST model used. The way in which FAST linearizes the complete non-linear aeroelastic model is described in detail in section 4.2.3. The same simulation setup (see Figure 4.4 – stationary rotor)[97] is used in order to calculate the periodic steady state solution.

FAST cannot linearize a model with incident wave kinematics. For this reason, the 110 m tower structure with the spinning blades is only loaded with aerodynamic loads. The linearization results in the full-system matrices that generate the full-system eigenfrequencies presented in Table 6.1.

Table 6.1: Full-system eigenfrequencies for the Offshore Wind Turbine Model

No.	Frequency	DOF
1	0.28 Hz	1st Tower side-side bending
2	0.29 Hz	1st Tower fore-aft bending
3	0.56 Hz	1st Blade flapwise bending
4	0.74 Hz	1st Blade flapwise bending
5	0.89 Hz	1st Blade edgewise bending
6	0.91 Hz	1st Blade flapwise bending
7	1.29 Hz	1st Blade edgewise bending
8	1.67 Hz	1st Blade edgewise bending
9	1.79 Hz	2nd Blade flapwise bending
10	2.05 Hz	2nd Blade flapwise bending
11	2.17 Hz	2nd Blade flapwise bending
12	2.38 Hz	2nd Tower side-side bending
13	2.39 Hz	2nd Tower fore-aft bending
14	3.90 Hz	Drivetrain rotational flexibility

Based on the full-system matrices and the eigenfrequency information, the reduced system matrices needed for the inverse calculation are generated. The reduction of the system matrices follows the procedure described in section 4.2.4. With the transformation matrix

---

[97] See also the descriptions in section 4.2.4.

composed of the tower fore-aft modes, the modal reduction gives the following reduced stiffness and mass matrices.

$$\mathbf{K}^{red} = \begin{bmatrix} 1.3384 \cdot 10^6 & 0 \\ 0 & 2.1868 \cdot 10^6 \end{bmatrix} \text{ in } Nm^{-1} \tag{6.7}$$

$$\mathbf{M}^{red} = \begin{bmatrix} 4.2695 \cdot 10^5 & 0 \\ 0 & 9.8095 \cdot 10^3 \end{bmatrix} \text{ in } kg \tag{6.8}$$

Applying an eigenvalue analysis to the reduced system matrices allows calculating the eigenfrequencies of the reduced system. Table 6.2 summarizes these eigenfrequencies. The comparison to the full-system eigenfrequencies shows the accuracy of the reduced system in terms of representing the fore-aft tower bending modes. Additionally, Table 6.2 contains the damping ratios that are used for the inverse calculation. Again, the damping ratio of the first mode is the sum of structural and aerodynamic damping, whereas the damping ratio of the second mode represents structural damping.

Table 6.2: Reduced-system eigenfrequencies for the Offshore Wind Turbine Model

Mode	**Frequency**	**Damping ratio** 1)
1st fore-aft tower bending	0.28 Hz	0.07
2nd fore-aft tower bending	2.38 Hz	0.04
1) As percentage of critical damping.		

6.2.3 Time-Marching Simulation

Simulation is time-marching of the non-linear equations of motion. During simulation, the aerodynamics, the hydrodynamics, and the structural response of the wind turbine to these conditions are determined in time. Output data includes time series of the aerodynamic loads as well as the loads and deflections of the structural members of the wind turbine. Additionally, the hydrodynamic loads are part of the output data, as described in section 6.1.2.

In order to perform the time-marching simulation, loads that take into account combined wind and wave loads have to be defined. Wind loads are usually described by the mean wind speed at hub height v_{Hub}.[98] Wave loads result from incident waves that form a sea state. The sea state is usually defined by a wave spectrum.[99] For the mathematical description of the typical wave spectra, the significant wave height H_S and the peak spectral period T_P are needed. The mean wind speed and the significant wave height are strictly corre-

---

[98] See section 2.1.1 and section 4.2.2.

[99] See section 2.1.2.

lated,[100] which has to be considered in the load case definition. GRÜNBERG AND GÖHLMANN (2011) [29][101] present several JONSWAP spectra with their corresponding wind speeds.

With TurbSim [44], stochastic turbulent wind fields are generated that are the aerodynamic input for the simulations. For the offshore verification study here presented, the load case 3 from section 4.2.2 is used. This load case is in the middle of region 3, with a mean wind speed of 18 m/s, which is between rated wind speed and cut-out wind speed (Figure 4.3). The ability of the inverse load calculation to handle different turbine control configurations is already discussed in section 4.3.2. Considering one of the previously defined LCs has the advantage that there is already an expectation in terms of the aerodynamic inverse load and its accuracy.

This section mainly focuses on studying the ability and the accuracy of the inverse load calculation with respect to the hydrodynamic loads. A stochastic sea state that is described by the JONSWAP spectrum is chosen. The JONSWAP spectrum is based on extensive measurements at the German North Sea cost. In order to fulfill the correlation with the chosen wind speed, a significant wave height of $H_S = 5$ m and a peak spectral period $T_P = 12.4$ s is used. Further parameters needed are the peak shape parameter γ and the scaling factor σ. Both parameters are derived from the pair of values H_S/T_P, as recommended by the design standard IEC 61400-3 (2009) [108].[102] Wheeler stretching is applied. Consequently, a load case as summarized in Table 6.3 is defined.

Table 6.3: Load case for the FAST offshore verification study

Wind	
Mean wind speed [1)]	$v_{Hub} = 18$ m/s
Turbulence mode [2)]	NTM
Turbulence characteristic [2)]	B
Wave	
Significant wave height	$H_S = 5$ m
Peak spectral period	$T_P = 12.4$ s
Wave model [3)]	JONSWAP (irregular)
Stretching	Wheeler

[1)] At hub height, mean vertical shear about rotor disk is 0.03 m/s. Horizontal shear is not considered.
[2)] IEC 61400-1 (2005) [107].
[3)] Peak shape parameter γ and scaling factor σ calculated according to IEC 61400-3 (2009) [108].

In general, combined wind and wave loads are simulated for 1 hour, which is a compromise between 10 min wind simulations and 3 hours wave simulations. The simulation of waves

---

[100] See GRÜNBERG (2011) [30], page 53.

[101] See GRÜNBERG AND GÖHLMANN (2011) [29], page 51.

[102] See also JONKMAN (2007) [46], page 23.

requires a larger time window in order to cover a sufficient number of significant incidents, since wave data contain more low-frequent content than wind data.[103] For that reason, a simulation time of 3,600 s is used. The FAST simulation time steps are dt = 0.0125 s. In order to limit the amount of data, a decimation factor of 4 is applied to the output data, so that a time increment of 0.05 s and a Nyquist frequency of 10 Hz are produced. Both values guarantee sufficient accuracy for the frequency-domain transformations.

Full-span collective blade-pitch control and variable-speed generator-torque control are enabled for the turbine control, whereas the yaw control mode is disabled.

Table 6.4: Output signals for the FAST offshore verification study

Turbine signals	
WindVxi	Normal downwind component of the hub-height wind velocity (m/s)
HorWndDir	Horizontal hub height wind direction (deg)
PtchPMzc1 to ~3	Blade pitch angle (deg)
LSSTipVxa	Rotor azimuth angular speed (rpm)
YawPzn	Nacelle yaw angle (deg)
HSShftV	Angular speed of the HSS and generator (rpm)
GenTq	Electrical generator torque (kNm)
Motions of the structure	
YawBrTDxt	**Tower top fore-aft deflection (m)**
YawBrTAxp	**Tower top fore-aft acceleration (m/s^2)**
TwHt$_i$TDxt 1)	**Local tower fore-aft displacements at the i-th tower gage (m)**
TwHt$_i$ALxt	**Local tower fore-aft accelerations at the i-th tower gage (m/s^2)**
Force signals	
LSShftFxa / RotThrust	**LSS**2) **thrust force, constant along shaft and equivalent to rotor thrust force (kN)**
YawBrFxn	Rotating (with nacelle) tower top / yaw bearing shear force (kN)
TwHt$_i$FLyt	Local tower fore-aft shear force at the i-th tower gage (kN)
FTHydro 3)	**Hydrodynamic force from Morison equation (kN)**

1) The output of the local tower displacements is not an available option of the current FAST version v7.00.01. For this reason, the FAST source code was adjusted so that the output of the local tower displacements is enabled.
2) LSS – low-speed shaft.
3) Gained from the source code modification described in section 6.1.2.

The requested output signals are summarized in Table 6.4. The turbine signals serve as plausibility checks of the FAST analysis and visualization of the turbine control. The motions of the structure and the force signals are used as input signals for the inverse load calcula-

---

[103] See Figure 2.7 and Figure 2.8.

tion. The input signals also include the rotor thrust force computed by FAST, which is required as a comparative signal for the inversely calculated aerodynamic load. The applied hydrodynamic load that is part of the rewritten FAST output is used as comparative signal for the inversely calculated hydrodynamic load. The signals used for the inverse calculation are bold.

In case the substructure is very stiff with respect to the tower, the aerodynamic and the hydrodynamic loads will be uncorrelated. This would be true, for example, for the lattice structure described in section 5 and the here investigated monopile substructure. The results of the simulation and of the inverse load calculation are presented in section 6.3.

6.3 Results of the Inverse Load Calculation at a 5 MW Offshore Wind Turbine Model

The verification of the inverse load calculation follows the scheme depicted in Figure 4.1. The inversely calculated aerodynamic and hydrodynamic load will be compared to the FAST rotor thrust and to the resulting hydrodynamic force from FAST, respectively (Figure 6.4). The FRF matrix is assembled using the information from the eigenvalue analysis and the system matrices given in section 6.2.2.

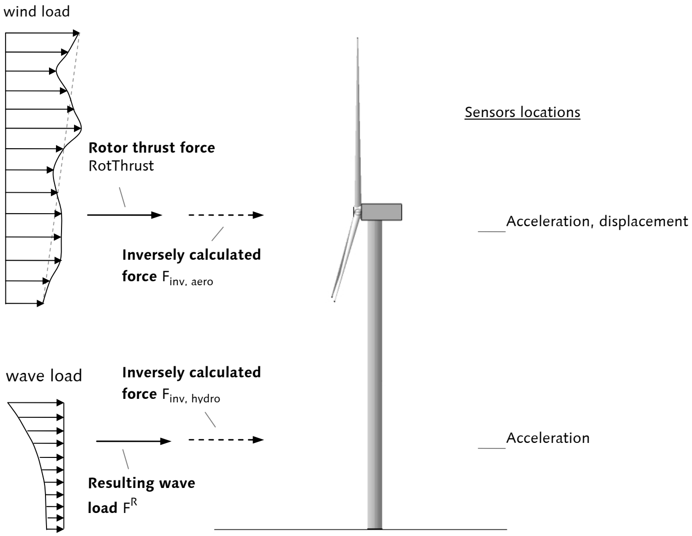

Figure 6.4: Assumptions for the offshore verification study using FAST

Additionally, system responses are needed as calculation input. As depicted in Figure 6.4, acceleration time series at the tower top (maximal amplitude of 1st tower bending mode) and at the point where the resulting wave load is located are chosen. Because the location of the resulting wave load does not necessarily coincide with the maximal amplitude of 2nd tower-bending mode, the second row of the reduced modal matrix has to be scaled. The tower-bending mode shapes are known from the linearization described in section 6.2.2. A depiction of the calculated mode shapes is given in Figure 6.5. The scaling factor results from the ratio of the maximal amplitude to the amplitude at the sensor location, denoted as $\overline{h}^R$.

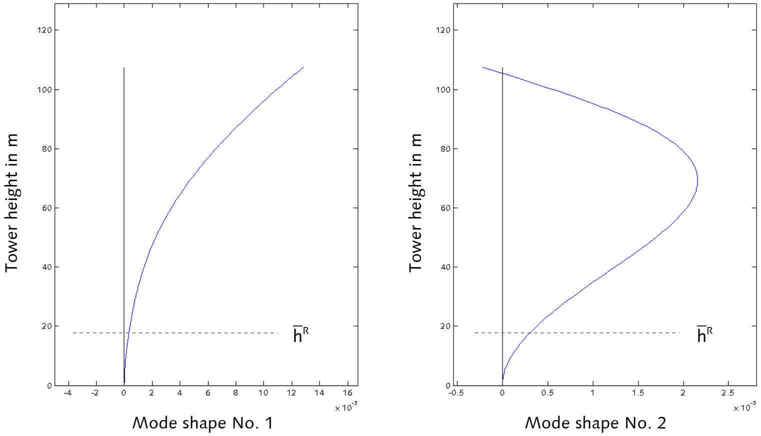

Figure 6.5: Tower bending modes shapes

The inversely calculated wind load results from superimposing the static/quasi-static and the dynamic component, seperated by a cut-off frequency of 0.07 Hz. The static/quasi-static component is derived from displacement signals at tower top (Figure 6.4). The calculation of the dynamic component is based on the Deconvolution in the Frequency Domain.[104] The corresponding procedure is described in detail in section 4.3. The hydrodynamic load is assumed to be purely dynamic. Thus, the inverse hydrodynamic load is calculated using the Deconvolution in the Frequency Domain.[104] The underlying system of equations is now a determined system. Two tower bending modes are used in order to calculate two unknown forces.[105] The results for the inverse load calculation with combined aerodynamic and hydrodynamic loads are subsequently shown.

---

[104] See section 3.2.

[105] See also section "3.2.2 Assembly of the FRF Matrix and Least-Squares Approach".

6.3.1 Calculation of the Resulting Wave Load

The sensor location at the level of the resulting wave load is not known prior to the simulation. For this reason, a simulation run has to be performed in order to make the applied hydrodynamic force FTHydro available. Figure 6.6 shows a time range of 100 s of the FAST output variable FTHydro. Applying equations (6.5) and (6.6) gives the time-dependent resulting wave load $F^R(t)$ and its points of application $h^R(t)$. The sensor location $\overline{h}^R$ is found by averaging the points of application over the entire simulation time.

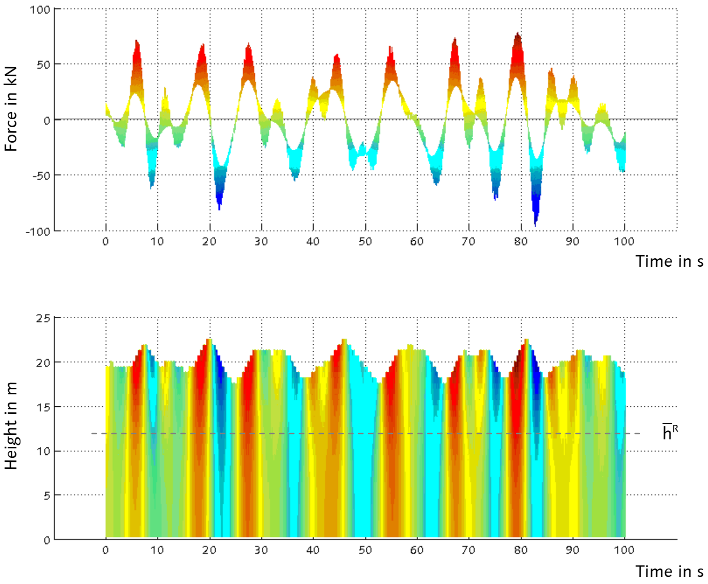

Figure 6.6: Hydrodynamic load derived from the FAST offshore simulation

6.3.2 Load Case – Stochastic Wind and Irregular Waves

Once the sensor location $\overline{h}^R$ is known, the simulation for the load case described in Table 6.3 can be performed. The description of the reduced system (section 6.2.2) completes the input parameters for the inverse calculation.

The simulated mean wind speed at hub height is 17.99 m/s. Hence, the load case represents the middle of region 3, between rated and cut-out wind speed. In this region, high control activity is observed. The yaw position is constant at zero. However, the collective blade pitch ranges between pitch angles of 0° to 20°. While the torque controller operates in region 3, the control strategy aims on generating "constant power". The mean rotor speed is 12.10 rpm. Figure 6.7 gives an overview about the wind turbine control.

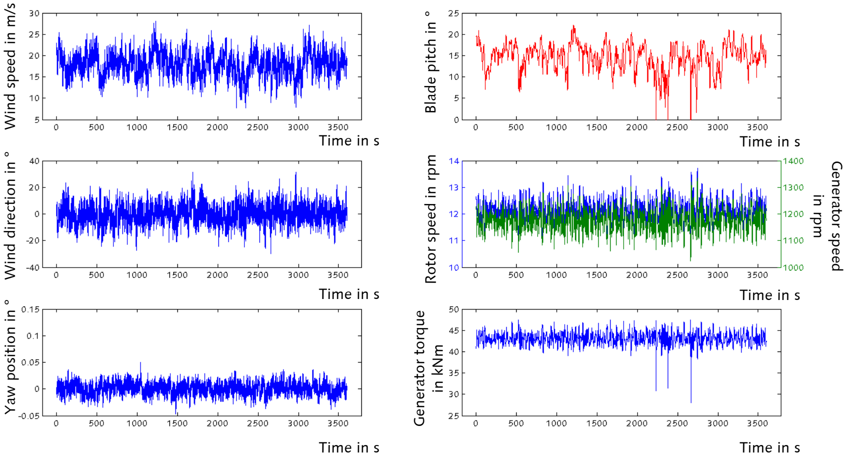

Figure 6.7: Wind turbine control

Figure 6.8 shows the inversely calculated aerodynamic load, both in the time and in the frequency domain. For verification purposes, the rotor thrust force that is computed by FAST is also displayed. The differences to the results in section 4, Figure 4.13 are the extended simulation time, the tower height that exceeds the SWL down to mudline and the simultaneously occurring hydrodynamic load.

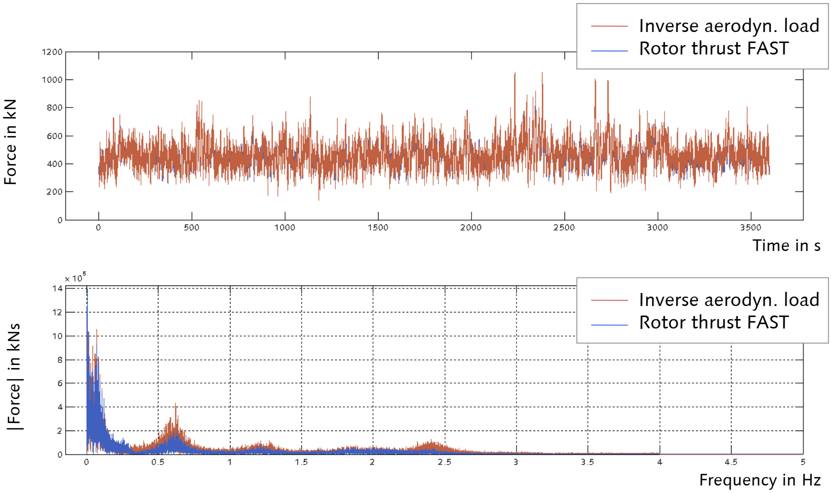

Figure 6.8: Rotor thrust and inverse aerodynamic load

Figure 6.9 shows the inversely calculated hydrodynamic load, also in the time and in the frequency domain. Now, the verification is done by comparing the inversely calculated load to the resulting wave load that is based on the hydrodynamic forces calculated by FAST. The resulting wave load results from applying equation (6.5).

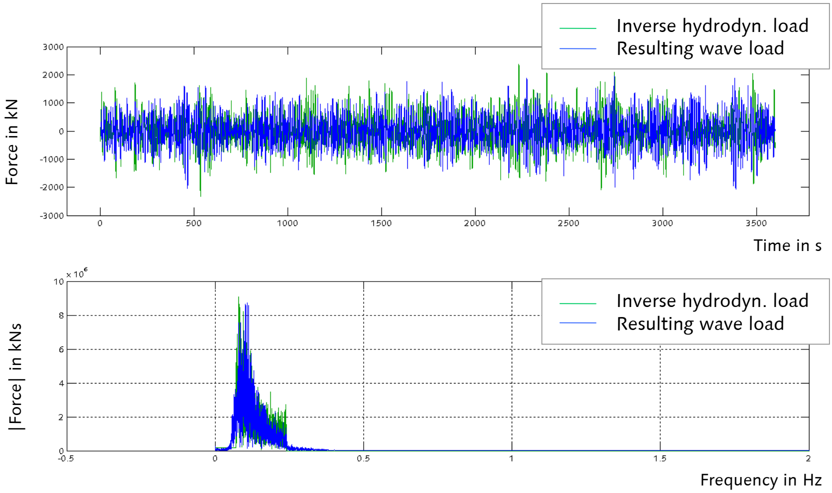

Figure 6.9: Resulting wave load and hydrodynamic inverse load

6.3.3 Discussion of the Results

A visual inspection of the results in Figure 6.8 and Figure 6.9 leads to the first conclusion that the inverse load calculation procedure produces reasonable results. This statement is true both for the inversely calculated aerodynamic and hydrodynamic loads when compared to the FAST reference loads.

Table 6.5 presents the error values of the inversely calculated loads, each derived from equation (3.65). The error value of the aerodynamic load $\varepsilon_{Aero} = 7.4\ \%$ is smaller than the error values that were calculated for the inverse loads in section 4.3.2 that are based on pure aerodynamic loadings. In contrast to the former calculation, the verification study here presented is based on a larger simulation time, a modified structural description, and additional hydrodynamic loads. The variation of these conditions does not downgrade the accuracy of the inversely calculated aerodynamic load. This second conclusion is a sign of the reliability of the inverse load calculation procedure in terms of aerodynamic loads.

Figure 6.9 shows the inversely calculated hydrodynamic load compared to the resulting wave load that is based on the rewritten FAST output. The wave load in FAST is generated using a JONSWAP spectrum with a peak spectral period of $T_P = 12.4$ s. As a consequence, a peak occurs at 0.08 Hz in the resulting wave load (blue signal in Figure 6.9). Additionally, the spectrum of the resulting wave load contains energy in a narrow frequency band that ranges from ca. 0.06 Hz to 0.25 Hz. This frequency band shows a steep slope left to the maximum and a flat slop right to the maximum, which also fulfills the expectations on the JONSWAP spectrum.[106] The inversely calculated hydrodynamic load (green signal in Figure 6.9) reproduces these described characteristics. The same narrow frequency band is visible, with a maximum at approximately the spectral peak and the characteristic slops left and right to the maximum, which constitutes the third conclusion.

Table 6.5: Error values from the offshore verification study

Error in time ε	**Aerodynamic load**	**Hydrodynamic load** 1)
Full load signal	7.4 %	26.8 %
Quasi-static component	6.3 %	---
Dynamic component	11.5 %	26.8 %

1) In terms of the hydrodynamic load the dynamic component equals the full load signal because the hydrodynamic load does not contain static and quasi-static components.

The error value of the hydrodynamic load is $\varepsilon_{\text{Hydro}}$ = 26.8 % (Table 6.5). Again, it should be mentioned that the chosen error estimation is not intended to give absolute quantifications of the accuracy of the inverse calculation results, but it is rather used to compare results within this work. The inversely calculated hydrodynamic load is a purely dynamic load, derived from the relations of the Deconvolution in the Frequency Domain. As pointed out in section 4.3.2, the dynamic load components show higher uncertainties than the static/quasi-static components and consequently the full load signals. The main reason is seen in the system reduction from the full system to the tower bending modes, which is also part of the inversely calculated hydrodynamic load. This means that the acceleration signals that serve as input for the inverse calculation are based on a full-system calculation. Whereas the inverse load is calculated using the reduced system. This fact causes the uncertainties in the results. The reason for the system reduction is discussed in section 2.2.2.

The comparison between the dynamic force components obtained by the offshore load case (Table 6.5) shows the aerodynamic load to be more accurate than the hydrodynamic load. This leads to the fourth conclusion: The aerodynamic load can be calculated inversely with a higher accuracy than the hydrodynamic load.

The fifth conclusion is derived by having a look at previous inverse calculation results. The error value of the hydrodynamic load lies on the upper edge of the accuracy range if compared to the error values of the dynamic load components for the wind loads in section 4.3.2 and the strain comparison in section 5.3.2. All conclusions need to be verified by further calculations.

There are further influences that contribute to the differences between the inversely calculated hydrodynamic load and the resulting wave load (Figure 6.9). First of all, the linearization that gives the system matrices is calculated without hydrodynamic loads. As described

---

[106] See for example Figure 2.5, page 18.

in section 6.2.2, FAST cannot consider incident wave kinematics within the linearization. A second simplification concerns the sensor location $\overline{h}^R$ of the lower accelerometer to be a constant value. In fact, it is an average of the time-dependently varying points of application $h^R(t)$ of the resulting wave load. This assumption is made because the accelerometer has a fixed location during the entire simulation time. In addition, the inversely calculated hydrodynamic load is high pass filtered at the cut-off frequency of 0.07 Hz, which is caused by the double-integration of the acceleration signals to velocity signals.[107] Applying this filter does not violate the inverse calculation, because it is located at the upper edge of the expected frequency band that results from the applied JONSWAP spectrum. In addition, the inversely calculated load is treated with a high pass filter that cuts off the frequencies above the energy-containing frequency band. In this way, high frequent content that may result from rotor blades (that are not covered in the reduced system) is suppressed.

As is true for the already discussed inverse calculations in sections 3 to 5, the quality of the mode shapes is important for the accuracy of the results.

6.4 Summary

This section aims at investigating the inverse load calculation that considers combined wind and wave loads. The investigation is based on the previous gained results (section 3 to 5). The comprehensive simulation code FAST is used for a verification study of the inverse load calculation. FAST allows loads to be applied from a defined stochastic wind field and enables the interacting dynamics of the wind inflow, aerodynamics, elasticity, and the control of the wind turbine to be considered. Additionally, FAST considers incident waves, sea currents, hydrodynamics, and foundation dynamics of the support structure. A three-bladed 5 MW offshore wind turbine model is used. The structure of the model consists of a tubular steel tower with a monopile foundation. A still water level of 20 m is chosen. One representative load case is defined. With the system matrices from the FAST model and the simulated accelerations along the tower, inverse loads are calculated. An approach is introduced in which the wind load is reduced to the rotor thrust and the wave load is represented by a resulting wave load (see also section 2.2.2). The accuracy of the inverse load calculation is estimated by comparing the inversely calculated loads with the applied loads from FAST.

Summarizing the main conclusions of the presented verification study leads to the following statements: The inverse load calculation is capable of generating good estimates of the applied wind and wave loads. The accuracy of the inversely calculated wind load is not disturbed by the additionally occurring wave load. The inversely calculated hydrodynamic load reproduces the same frequency-domain characteristics as there are for the applied hydrodynamic load. The aerodynamic load can be calculated inversely with a higher accuracy than the hydrodynamic load. The error value of the hydrodynamic load lies on the upper edge of the accuracy range if compared to all previously gained error values.

---

[107] See Appendix E „Integration in the Frequency Domain“.

The conclusions are derived from only one representative load case. Thus, their general validity has to be confirmed by further verifications. A wind turbine model is used for the presented verification. In case, a real-world offshore wind turbine is used, the additional necessary steps are presented in section 5. In general, they are also valid in case of an application to a real-world offshore wind turbine. However, further questions have to be answered. For example, how the sensor location of the lower accelerometer can be estimated or how the resulting wave load can be used for continuing investigations, such as the calculation of strains – as presented in section 5.3.2 – that may allow lifetime predictions.

The calculations presented are maybe the first application of an inverse load calculation procedure to a wind turbine model under combined wind and wave loads and with the consideration of the dynamic coupling effects. An application to a real-world offshore wind turbine is also not observed in the analyzed literature in section 1.2.3.

7 Conclusions and Outlook

7.1 Conclusions

This work presents the inverse load calculation at offshore wind turbines. The literature review of related research publications shows a lack of information, especially when investigating the effects of wind turbine specific characteristics to the results of the inverse calculation. Consequently, the ill-conditioning of the inverse calculation procedure, dynamic coupling effects, wind turbine control, the occurrence of combined wind and wave loads, and the application of the inverse load calculation procedure to a real-world wind turbine, are studied. There are no publications that describe the application of the inverse load calculation for combined wind and wave loads. In addition, a verification of the result accuracy is poorly discussed so far. This work is intended to fill this gap. In fact, the value of this work is

- suggesting an approach to the inverse load calculation procedure that is appropriate for wind turbines and that is based on known mathematical relations,
- giving verifications of the results for the inverse load calculation at onshore and offshore wind turbines that consider wind turbine specific characteristics, and
- applying the inverse load calculation to a real-world structure, including a verification of the gained results.

Approach to the inverse load calculation

The suggested procedure for the inverse load calculation is the following: First, dynamic system responses and a system description are needed. The responses are measured acceleration signals. The system description results from the FRF matrix that contains the modal information of the fore-aft modes of the structure. The inverse problem is solved using the Deconvolution in the Frequency Domain and results in the externally acting aerodynamic and hydrodynamic loads. The aerodynamic loads of interest are caused by a stochastic wind field. These loads are represented by the rotor thrust. The unknown hydrodynamic loads result from incident waves and are represented by the resulting wave load.

The mathematics of the Deconvolution in the Frequency Domain are illustrated using a simple numerical example. The procedure for assembling the FRF matrix is shown. In addition, a least-squares approach is introduced that allows the consideration of a larger number of system responses than the number of unknown forces. This approach allows for the elimination of random errors that are inherent parts of measurement data. Finally, the numerical example is used to outline the effects of the ill-conditioning of the inverse problem to the calculation results. Digital filters are used to cope with the ill-conditioning.

Verification of the results for the inverse load calculation

The comprehensive simulation code FAST is used for verification studies of the inverse load calculation method. FAST allows loads to be applied from a defined stochastic wind field and enables a consideration of the interacting dynamics of the wind inflow, aerodynamics, elasticity, and the control of the wind turbine. Additionally, FAST considers incident waves, hydrodynamics, and foundation dynamics of the support structure. Thus, using FAST allows the study of the effects of all of these wind turbine specific characteristics.

The simulation is verified by comparing the inversely calculated loads to the loads applied to the FAST model. The inverse calculation is based on the simulated dynamic responses of the structure and the system description of the model that is also an output of the FAST simulation. Representative load cases are investigated at a 5 MW wind turbine model with a tubular steel tower, both at onshore and offshore conditions.

The Deconvolution in the Frequency Domain is used for the inverse calculation. The calculation is based on acceleration signals and gives dynamic force components. Aerodynamic loads have considerable static/quasi-static components. These components are calculated from tower deflections. The full inverse load is obtained by superimposing the components.

The main conclusion of the verification study is that the inverse load calculation is capable of generating reasonable estimates of the applied load. A good result quality is obtained for aerodynamic and combined aerodynamic/hydrodynamic loads.

The inverse calculation does not depend on the wind turbine control.

The verification of the aerodynamic loads shows that the static/quasi static load components are calculated inversely with high accuracy. The dynamic components show uncertainties. The simplification of the RNA and the system reduction to the fore-aft modes is seen as the main reason for the observed differences. The uncertainties cause an overestimation of the load amplitudes.

The verification of the combined aerodynamic and hydrodynamic loads shows that the inverse load calculation is capable of generating good estimates of the applied wind and wave loads. The calculation of the inversely calculated wind load is not disturbed by an additional wave load. The inverse calculation reproduces the frequency-domain characteristics of the applied hydrodynamic load. The aerodynamic load can be calculated inversely with a higher accuracy than the hydrodynamic load.

The integration of acceleration signals to displacement signals does not cause errors to the inverse calculation. The integration even affects the inverse calculation positively in terms of the ill-conditioning of the inverse problem.

Application to a real-world wind turbine

If the inverse load calculation is applied to a real-world wind turbine, additional aspects have to be considered. For this reason, a 5 MW wind turbine with an offshore support structure is investigated. The structure is erected as an onshore prototype. Now, the system responses are measured signals and a realistic system description has to be derived from the real-world structure.

The chosen approach for deriving the realistic system description is using an output-only system identification method. The system identification gives the modal information of the structure. A finite-element model of the structure is updated so that this model represents the identified modal information. Now, the realistic system description is gained from the updated finite-element model.

A large effort is allocated to the system identification procedure. The Frequency Domain Decomposition is chosen. The system identification determines the eigenfrequencies, mode shapes, and the damping ratios from measurement data. In order to get a comprehensive and accurate system description, measurements are analyzed for local structural components and for the dynamics of the entire structure. Standstill and various operation states are investigated, with a special focus on the wind-speed dependency of the eigenfrequencies and the damping ratios. For the eigenfrequencies no wind-speed dependency is observed, whereas the influence of aerodynamic effects is clearly shown within the identified damping ratios. The influences of high multiples of the P-excitation resonate with eigenfrequencies are also shown. The determination of eigenfrequencies and mode shapes from measurement data show a very high accuracy, whereas the damping ratios are identified with acceptable uncertainties.

A finite-element model is adjusted to measured modal information, which is called model updating. The model updating is done with very high accuracy. Thus, a realistic system description is generated, which is an important precondition for the inverse load calculation. The representation of eigenfrequencies and mode shapes is of particular importance for the inverse load calculation. The damping ratios are of minor importance. During the model updating process, it turned out that distributed mass and stiffness representation of the rotor blades are necessary in order to cover the interactions that occur between the rotor blades and global bending modes or local modes, respectively.

The result for the inverse load calculation is the rotor thrust force due to a load case representing the wind turbine in operation. The verification is done by comparing measured strains to simulated strains that are derived from the updated FE model with the inverse load as applied load. This verification shows a high level of agreement between the strain signals.

The inverse load calculation presented is an alternative to the direct determination of structural loads. The direct determination uses strain gauges applied to a limited number of crucial cross-sections. This method is easy in its application and therefore, the method is well suited for the monitoring of specific structural components. But there are also a few drawbacks. The loads exclusively depend on the measurement data at one certain cross-section. If this cross-section does not have a linear stress-to-load relationship, e.g. near the flanges of tubular steel towers, incorrect results are gained. If there is dynamic interaction between the loads and the structure, as it is for wind turbines, the strain gauges give internal structural loads. These structural loads cannot be related to externally applied loads due to the dynamic amplification of system responses.

The inverse load calculation requires much more mathematical effort. This effort includes setting up the system matrices, which requires system identification of real-world wind turbines. Additionally, the inverse calculation procedure itself is laborious and strongly depends on the quality of the input data. However, this work shows the inverse load calculation to be able to reproduce realistic estimates of applied loads. It is also shown that the applied loads can be used for simulations that result in a good estimate of realistic strains. With the knowledge of applied loads, strains can be determined at arbitrary cross-sections. For this reason, a promising field of application of the inverse load calculation is seen in the calculation of lifetime predictions, where information about the entire structure is needed.

7.2 Outlook

The main field of application of the inverse load calculation is for monitoring purposes or remaining lifetime predictions.

Onshore wind turbines – aerodynamic loads

In this work, the inverse load calculation procedure and its good results when aerodynamic loads are calculated are discussed in detail. The resulting accuracy is promising. This work shows how the inverse load can be used to simulate strains that have a good level of agreement with measured strains.

Further investigations are necessary in order to assure that the accuracy of the compared strain signals can be reproduced at arbitrary cross-sections and for different operation states of wind turbines with arbitrary support structures. The simulated strains can be used for lifetime predictions.

An absolute quantification of the result quality could be made by a comparison of fatigue calculations that base on strains from inversely calculated loads to strains measured with strain gauges.

Offshore wind turbines – aerodynamic and hydrodynamic loads

Essentially, all conclusions derived for onshore wind turbines are also crucial for offshore wind turbines. The presented investigation of combined wind and wave loads is only based on one representative load case. Hence, there is a demand for further verification studies.

The investigation of combined wind and wave loads is done using a model simulated with FAST. Consequently, the application of the described procedures to a real-world offshore wind turbine is not yet discussed. Although many of the aspects described for the application under onshore conditions can be used, the application to offshore conditions will produce further questions. Some of these questions are subsequently summarized.

- How does one find the sensor position which equals the location of the resulting wave load? Several sensors (e.g. 3) can be located at the height of the structure, where the resulting wave load is expected to occur. A hypothesis might be derived from simulations.

- Is it necessary to increase the number of vibration modes when assembling the system description? Does this influence the accuracy of the inverse calculation?
- How does one cope with wind and wave loads coming from different directions? The system description used for the inverse calculation needs to be extended to the side-side modes. The assumption that the sum of the fore-aft and the side-side load vectors gives the inverse load has to be verified.
- For what purpose can the resulting wave load be used? In the first instance, the resulting wave load can be applied as a single load to the structure in order to calculate structural strains. An enhanced approach may expand the resulting wave load to their non-linear distribution along the structure. This expansion might be based on the mathematical description of the wave kinematics and may require further sensors along the height of the structure.
- How can the inverse load calculation for combined wind and wave loads be realized if there are other types of offshore support structures?

All of these questions should lead to the final goal, which is to use the inverse load calculation for lifetime predictions at real-world offshore wind turbines.

References

Literature

[1] Andersen, P; Brincker, R.; Peeters, B.; De Roeck, G.; Hermans, L.; Krämer, C. (1999): *Comparison of system identification methods using ambient bridge test data*. In Proceedings of IMAC 17, International Modal Analysis Conference, Kissimmee (FL), USA, pp. 1035-1041.

[2] Andersen, P.; Brincker, R.; Goursat, M.; Mevel, L. (2007): *Automated Modal Parameter Estimation for Operational Modal Analysis of Large Systems*. In Proceedings of the 2nd International Operational Modal Analysis Conference (IOMAC), Copenhagen, Denmark. Vol. 1, pp. 299-308.

[3] Bader, G.; Schenk, K. (2001): *Skriptum zur Vorlesung Ingenieurmathematik*. Brandenburgische Technische Universität Cottbus, Lehrstuhl Numerische Mathematik und Wissenschaftliches Rechnen.

[4] Bartlett, F. D. Jr.; Flanelli, W. G. (1979): *Model Verification of Force Determination for Measuring Vibratory Loads*. J. American Helicopter Soc, Vol. 24, 1979, pp. 10-18.

[5] Bjerg Petersen, I.C.; Mosegaard Hansen, S.; Brincker, R.; López Aenlle, M. (2007): *Load estimation by Frequency Domain Decomposition*. Proc. of the 2nd International Operational Modal Analysis Conference in Copenhagen, Denmark. Vol. 2, p. 669-676. ISBN 8791606144.

[6] Böker, C. (2009): *Load simulation and local dynamics of support structures for offshore wind turbines*. Dissertation. Schriftenreihe des Institutes für Stahlbau der Gottfried Wilhelm Leibniz Universität Hannover, 26. Shaker Verlag, Aachen. ISBN 978-3-8322-8850-1.

[7] Brincker, R.; Zhang, L.; Andersen, P. (2000): *Output-Only Modal Analysis by Frequency Domain Decomposition*. In Proceedings of ISMA25, International Conference on Noise and Vibration Engineering, Vol. 2. Leuven, Belgium.

[8] Brincker, R.; Zhang, L.; Andersen, P. (2000): *Modal Identification from Ambient Responses using Frequency Domain Decomposition*. In Proceedings of SPIE, the International Society for Optical Engineering. http://www.svibs.com/solutions/literature/2000_2.pdf. Accessed 25.04.2013.

[9] Brincker, R.; Zhang, L.; Andersen, P. (2001): *Modal identification of output-only systems using frequency domain decomposition*. Journal of Smart Materials and Structures. Vol. 10, pp. 441-445.

[10] Brincker, R.; Ventura, C. E.; Andersen, P. (2001): *Damping Estimation by Frequency Domain Decomposition*. In Proceedings of SPIE, the International Society for Optical Engineering. Vol. 4359 (1), pp. 698-703. ISSN 0277-786X.

[11] Brincker, R.; Andersen, P. (2006): *Understanding Stochastic Subspace Identification*. Proceedings of the 24th International Modal Analysis Conference (IMAC), St. Louis, Missouri. http://www.svibs.com/solutions/ literature/2006_2.pdf. Accessed 25.04.2013.

[12] Bundesministerium für Wirtschaft und Technologie (2011): *Forschung für eine umweltschonende, zuverlässige und bezahlbare Energieversorgung – Das 6. Energieforschungsprogramm der Bundesregierung*. http://www.bmwi.de/BMWi/Redaktion/ PDF/E/6-energieforschungsprogramm-der-bundesregierung,property=pdf,bereich= bmwi2012,sprache=de,rwb=true.pdf. Accessed 05.12.2012.

[13] Camp, T. R.; Grainger, W.; Henderson, A.; Argyriadis, K.; Lauritsen, P. H.; Weighill, V. (2002): *Load Measurement on a 2 MW Wind Turbine in the North Sea*. http://130.226.17.201/extra/web_doc/blyth/doc_01.pdf. Accessed 02.11.2011.

[14] Chauhan, S.; Hansen, M. H.; Tcherniak, D. (2009): *Application of Operational Modal Analysis and Blind Source Separation / Independent Component Analysis Techniques to Wind Turbines*. In Proceedings of the IMAC-XXVII in Orlando, Florida, USA. http://sem-proceedings.com/27i/sem.org-IMAC-XXVII-Conf-s22p004-Application-Operational-Modal-Analysis-Blind-Source-Separation.pdf. Accessed 05.04.2012.

[15] Cosack, N. (2010): *Fatigue Load Monitoring with Standard Wind Turbine Signals*. Dissertation, Endowed Chair of Wind Energy at the Institute of Aircraft Design, Universität Stuttgart. Shaker Verlag, Aachen. ISBN 978-3-8322-9605-6.

[16] Doyle, J. F. (1984): *Further development in determining the dynamic contact law*. Journal of Experimental Mechanics, Vol. 27, pp. 68-72.

[17] EWEA European Wind Energy Association (2009): *Wind Energy – The Facts*. Routledge. ISBN 978-1-84407-710-6.

[18] Ewins, D. J. (2000): *Modal Testing – theory, practice and application*. Second edition. Research Study Press Ltd. Baldock, England. ISBN 978-0-86380-218-8.

[19] Faber, T. (2008): *Windenergieanlagen – ein dynamisch belastetes Bauteil*. 12. Dresdner Baustatik-Seminar. Dresden. ISSN 1615-9705.

[20] Federal Ministry for the Environment, Nature Conservation and Nuclear Safety (2010): *Energy Concept for an Environmentally Sound, Reliable and Affordable Energy Supply*. www.bmu.de. Accessed 28.10.2011.

[21] Felber, A. J. (1993): *Development of a Hybrid Bridge Evaluation System*. Dissertation. Department of Civil Engineering, University of British Columbia. https://circle.ubc.ca/bitstream/handle/2429/6869/ubc_1994893516.pdf?sequence= 1. Accessed 30.03.2012.

[22] Friswell, M. I.; Mottershead, J. E. (1995): *Finite Model Updating in Structural Dynamics*. Solid Mechanics and its Applications, Vol. 38. Kluwer Academic Publisher, Dordrecht. ISBN 0-7923-3431-0.

[23] Fritzen, C.-P.; Klinkov, M. (2006): *Online Force Identification with Robust Observer*. VDI Tagung Baudynamik. Kassel, Germany. VDI-Berichte Nr. 1941.

[24] Fritzen, C.-P.; Klinkov, M. (2007): *Online Wind Load Estimation for Offshore Wind Energy Plants*. Proc. of the 6. Intl. Workshop on Structural Health Monitoring, Stanford, CA, pp. 1905-1912.

[25] Gasch, R.; Knothe, K. (1987): *Strukturdynamik – Band 1: Diskrete Systeme*. Springer Verlag, Berlin Heidelberg. ISBN 3-540-16849-4.

[26] Gasch, R.; Knothe, K. (1989): *Strukturdynamik – Band 2: Kontinua und ihre Diskretisierung*. Springer Verlag, Berlin Heidelberg. ISBN 3-540-50771-X.

[27] Gasch, R.; Twele, J. (2005): *Windkraftanlagen – Grundlagen, Entwurf, Planung und Betrieb*. 4. vollständig überarbeitete und erweiterte Auflage. Teubner Verlag, Wiesbaden. ISBN 3-519-36334-8.

[28] Genaro, G; Alves Rade, D. (1998): *Input Force Identification in the Time Domain*. Proceedings of the 16th International Modal Analysis Conference. Santa Barbara, California, USA. Vol. I, p. 124-129.

[29] Grünberg, J.; Göhlmann, J. (2011): *Windenergieanlagen in Stahl- und Spannbetonbauweise*. In Betonkalender 2011 *Kraftwerke, Faserbeton*. Hrsg. Bergmeister, Fingerloos, Wörner. Ernst & Sohn, Berlin. ISBN 978-3-433-02954-1.

[30] Grünberg, J. (2011): *Stahl- und Spannbetonkonstruktionen für Offshore Windenergieanlagen*. Der Prüfingenieur, Vol. 39, Seite 45-63. Hrsg. Bundesvereinigung der Prüfingenieure für Bautechnik e.V. ISSN 1430-9084.

[31] Haake, G. (2010): *Systemidentifikation mit Autoregressiven Modellen und Validierung numerischer Strukturmodelle bei Offshore-Windenergieanlagen*. Dissertation. Mitteilungen des Instituts für Statik und Dynamik der Leibniz Universität Hannover. 11/2010. ISSN 1862-4650.

[32] Hansen, P. C. (1992): *Analysis of discrete ill-posed problems by means of the L-curve*. SIAM Review, Volume 34, Issue 4, pp. 561-580. ISSN 0036-1445 (print), ISSN 1095-7200 (online).

[33] Harder, Harry (2006): *Windenergieanlage REpower 5M in Bremerhaven-Weddewarden. Baugrundbeurteilung und Gründungsberatung*. Gutachterliche Stellungsnahme des Instituts für Geotechnik der Hochschule Bremen vom 22.06.2006.

[34] Hau, E. (2000): *Wind turbines – fundamentals, technologies, application, economics*. Springer, Berlin Heidelberg. ISBN 3-540-57064-0.

[35] Hojo, A.; Chatani, A.; Uemura, F. (1989): *An estimation of impact force by convolution integral*. Trans. Jpn. Soc. Mech. Eng., Ser. A 55A, 447-482. (in Japanese)

[36] Holthuijzen, L. H. (1992): *Wind en Golven*. Proc. Symposium Wind Technology Buitengaads, 18 November 1992. Apeldoorn, KIVI and NEWIN.

[37] Hoven, I. van der (1957): *Power Spectrum of Horizontal Wind Speed in a Frequency Range from 0.0007 to 90 Hz*. Jour Meteorology, 14, 160-164.

[38] Ibsen, L. B.; Liingaard, M. (2005): *Output-Only Modal Analysis used on new Foundation Concept for Offshore Wind Turbine*. In Proceedings of the 1st International Operational Modal Analysis Conference, Copenhagen, Denmark. ISBN 9788791606021.

[39] Ibsen, L. B.; Liingaard, M. (2006): *Prototype bucket foundation for wind turbines – natural frequency estimation*. DCE Technical Report No. 9, Department of Civil Engineering, Aalborg University. ISSN 1901-726X.

[40] Ibsen, L. B.; Liingaard, M. (2006): *Experimental Modal Analysis*. DCE Technical Report No. 10, Department of Civil Engineering, Aalborg University. ISSN 1901-726X.

[41] IMO-Wind (2010): *Integrales Monitoring- und Bewertungssystem für Offshore-Windenergieanlagen*. Kapitel 5. Abschlussbericht zu den InnoNet-Projekten 16INO326 und 16INO327. Erschienen: Technische Informationsbibliothek, Berlin, Germany.

[42] Inoue, H.; Harrigan, J. J.; Reid, S. R. (2001): *Review of inverse analysis for indirect measurement of impact force*. Journal of Applied Mechanics, Vol. 54, No. 6. p. 503-524.

[43] Jensen, J. K.; Kirkegaard, P. H.; Brincker, R. (2007): *Modal and Wave Load Identification by ARMA Calibration*. J. Eng. Mech., 118(6), 1268–1273. doi: 10.1061/(ASCE)0733-9399(1992)118:6(1268).

[44] Jonkman, B. (2009): *TurbSim User's Guide: Version 1.50*. Technical Report NREL/TP-500-46198. http://wind.nrel.gov/designcodes/preprocessors/turbsim/TurbSim.pdf. Accessed 12.01.2012.

[45] Jonkman, J.; Buhl, M. (2005): *FAST User's Guide*. Technical Report NREL/EL-500-38230. http://wind.nrel.gov/designcodes/simulators/fast/FAST.pdf. Accessed 10.01.2012.

[46] Jonkman, J. (2007): *Dynamics Modeling and Loads Analysis of an Offshore Floating Wind Turbine*. PhD work. Technical Report NREL/TP-500-41958. http://www.nrel.gov /docs/fy08osti/41958.pdf. Accessed 12.01.2012.

[47] Jonkman, J.; Butterfield, S.; Passon, P.; Larsen, T.; Camp, T.; Nichols, J.; Azcona, J.; Martinez, A. (2008): *Offshore Code Comparison Collaboration within the IEA Wind Annex XXIII: Phase II Results Regarding Monopile Foundation Modelling*. Conference paper at the IEA Offshore Wind Conference in Berlin, Germany, December 2007. NREL/CP-500-42471. http://www.nrel.gov/wind/pdfs/42471.pdf. Accessed 10.01.2012.

[48] Jonkman, J. (2009): *Dynamics of Offshore Floating Wind Turbines – Model Development and Verification*. In Wind Energy 12, page 459-492. Published online 26 June 2009 in Wiley Interscience. http://wind.nrel.gov/public/jjonkman/FloatingWind-Papers/Jonkman_DynamicsOfOffshoreFloatingWindTurbines-ModelDevelopment AndVerification_WindEnergy_2009.pdf. Accessed 16.01.2013.

[49] Jonkman, J.; Butterfield, S.; Musial, W.; Scott, G. (2009): *Definition of a 5-MW Reference Wind Turbine for Offshore System Development*. NREL/TP-500-38060. https://ceprofs.civil.tamu.edu/jzhang/ocen407/5MW%20Reference%20Turbine.pdf. Accessed 10.01.2012.

[50] Jonkman, J. (2011): *Overview over the FAST Servo-Elastic Module*. Presentation for the CREW/NREL Wind Turbine Design Code Workshop. Boulder, CO, USA. http://wind.nrel.gov/public/jjonkman/Presentations/DesignCodesWorkshop_110304 _CREW_BoulderCO/. Accessed 16.01.2012.

[51] Jonkman, J. (2011): *Overview of the HydroDyn Hydrodynamic Module*. Presentation for the CREW/NREL Wind Turbine Design Code Workshop. March 2011, CU Campus, Boulder CO, USA. http://wind.nrel.gov/public/jjonkman/Presentations/Design CodesWorkshop_110304_CREW_BoulderCO/. Accessed 16.01.2013.

[52] Kammeyer, K.-D. (2006): *Digitale Signalverarbeitung – Filterung und Spektralanalyse mit MATLAB-Übungen*. Teubner Verlag, Wiesbaden. ISBN 3-8351-0072-6.

[53] Karrenberg, U. (2010): *Signale – Prozesse – Systeme. Eine multimediale und Interaktive Einführung in die Signalverarbeitung*. 5. Auflage. Springer Verlag Berlin Heidelberg. ISBN 978-3-642-01863-3.

[54] Klinkov, M.; Fritzen, C.-P. (2006): *Online estimation of external loads from dynamic measurement*. Proceedings of ISMA 2006, pp 3957-3968.

[55] Klinkov, M.; Fritzen, C.-P. (2007): *An Updated Comparison of the Force Reconstruction Methods*. Key Engineering Materials, Vol. 347, pp 461-466.

[56] Klinkov, M.; Fritzen, C.-P. (2010): *Wind Load Observer for a 5MW Wind Energy plant*. Proceedings of IMAC-XXVIII 2010, Jacksonville, Florida USA.

[57] Kraemer, P. (2011): *Schadensdiagnoseverfahren für die Zustandsüberwachung von Offshore-Windenergieanlagen*. Dissertation. Band 3 der Schriftenreihe der Arbeitsgruppe für Technische Mechanik im Institut für Mechanik und Regelungstechnik - Mechatronik der Universität Siegen. Hrsg. Fritzen, C.-P. ISSN 2191-5601.

[58] Kühn, M. (2001): *Dynamics and Design Optimization of Offshore Wind Energy Conversion Systems*. Dissertation. DUWIND Delft University Wind Energy Research Institute, Report 2001.002. ISBN 90-76466-07-9.

[59] Lange, H. (2002): *Ermüdungsbeanspruchungen stählerner Rohrtürme für Windenergieanlagen im Binnenland*. Dissertation. Fachbereich Bauwesen der Universität Essen. Cuvillier Verlag, Göttingen. ISBN 3-89873-364-5.

[60] Lange, H. (2010): *Condition Monitoring für Windenergieanlagen*. VDI-Tagung Schwingungen von Windenergieanlagen. Hannover, Germany. ISSN 0083-5560

[61] Lincoln, A. (2007): *Calculating Velocity or Displacement from Acceleration Time Histories*. Prosig Signal Processing Tutorials. http://blog.prosig.com/2007/10/05/ calculating-velocity-or-displacement-from-acceleration-time-histories/. Accessed 15.01.2012.

[62] López Aenlle, M.; Brincker, R; Fernández Fernández, P.; Fernández Canteli, A. (2005): *Load estimation from Natural Input Modal Analyis*. Proc. of IMAC-XXIII, A Conference and Exposition on Structural Dynamics, in Orlando, USA. ISBN 0912053895.

[63] López Aenlle, M.; Brincker, R; Fernández Canteli, A. (2007): *Load estimation from modal parameters*. Proc. of the 2nd International Operational Modal Analysis Conference in Copenhagen, Denmark. Vol. 1, p. 39-50. ISBN 8791606136.

[64] Menke, W. (1984): *Geophysical Data Analysis: Discrete Inverse Theory*. Academic Press Inc. San Diego, USA. 1984. ISBN 0-12-490921-3.

[65] Mercer, C. (2001): *Differentiation and Integrating Numerically*. Prosig Signal Processing Tutorials. http://blog.prosig.com/2001/06/06/differentiating-and-integrating-signals-numerically/. Accessed 15.01.2012.

[66] Mercer, C. (2001): *Data Decimation. What Do I Do?* Prosig Signal Processing Tutorials. http://blog.prosig.com/2001/06/06/data-decimation-what-do-i-do/. Accessed 15.01.2012.

[67] Mercer, C. (2006): *Acceleration, Velocity and Displacement Spectra – Omega Arithmetic*. Prosig Signal Processing Tutorials. http://blog.prosig.com/2006/12/07/ acceleration-velocity-displacement-spectra-%E2%80%93-omega-arithmetic/. Accessed 15.01.2012.

[68] Moler, C. (2004): *Numerical Computation with MATLAB*. Society of Industrial Mechanics SIAM. ISBN 978-0898715606.

[69] Moriarty, P.; Hansen, C. (2005): *AeroDyn Theory Manual*. Technical Report NREL/EL-500-36881. http://www.nrel.gov/docs/fy05osti/36881.pdf. Accessed 12.01.2012.

[70] Natke, H. G. (1983): *Einführung in die Theorie und Praxis der Zeitreihen- und Modalanalyse*. Vieweg & Sohn, Braunschweig/Wiesbaden. ISBN 3-528-08145-7.

[71] Natke, H. G. (1989): *Baudynamik - Einführung in die Dynamik mit Anwendungen im Bauwesen*. B. G. Teubner, Stuttgart. ISBN 3-519-02368-7.

[72] Nordberg, Patrik L. (2004): *Time-domain Methods for Load Identification of Linear and Non-linear Systems*. Doctor Thesis. Chalmers University of Technology. Department of Applied Mechanics. Göteborg, Sweden. 2004. ISBN 91-7291-489-0.

[73] Nordström, Lars J. L. (2005): *Input Estimation in Structural Dynamics*. Doctor Thesis. Chalmers University of Technology. Department of Applied Mechanics. Göteborg, Sweden. 2005. ISBN 91-7291-668-0.

[74] OGOWin (2011): *Optimierung aufgelöster Gründungsstrukturen für Offshore Windenergieanlagen*. Schlussbericht zum Verbundprojekt. Laufzeit des Vorhabens: 01.08.2006 - 31.07.2010. http://edok01.tib.uni-hannover.de/edoks/e01fb11/ 668288175.pdf. Accessed 15.03.2012.

[75] Okubo, N.; Tanabe, S., Tatsuno, T. (1985): *Identification of Forces Generated by Machine under Operating Conditions*. Proc. 3rd International Modal Analysis Conference, Orlando, USA, pp. 920-927.

[76] Overschee, P. van; De Moor, B. (1996): *Subspace Identification for linear Systems – Theory-Implementation-Applications*. Kluwer Academic Publishers. Boston, London, Dordrecht. http://www.shadmehrlab.org/Courses/learningtheory_files/subspace _book_96.pdf. Accessed 05.04.2012.

[77] Pahn, T.; Rolfes, R; Kohlmeier, M. (2010): *System identification of a jacket support structure for a 5 MW offshore wind turbine due to artificial and ambient excitation*. Proceedings of Torque 2010 in Crete, Greece. Pg 769-780.

[78] Pahn, T.; Rolfes, R. (2011): *Abschlussbericht OGOWin – Kapitel 2.2 Schwingungsverhalten*. In: Optimierung aufgelöster Gründungsstrukturen für Offshore Windenergieanlagen. Schlussbericht zum Verbundprojekt OGOWin. Laufzeit des Vorhabens: 01.08.2006 - 31.07.2010. http://edok01.tib.uni-hannover.de/edoks/e01fb11/ 668288175.pdf. Accessed 15.03.2012.

[79] Pahn, T.; Rolfes, R. (2011): *Abschlussbericht OGOWin – Kapitel 6.2 Anpassung des Rechenmodells mit Hilfe von Messwerten an die Wirklichkeit*. In: Optimierung aufgelöster Gründungsstrukturen für Offshore Windenergieanlagen. Schlussbericht zum Verbundprojekt OGOWin. Laufzeit des Vorhabens: 01.08.2006 - 31.07.2010. http://edok01.tib.uni-hannover.de/edoks/e01fb11/ 668288175.pdf. Accessed 15.03.2012.

[80] Pahn, T.; Jonkman, J.; Rolfes, R.; Robertson, A. (2012): *Inverse load calculation of wind turbine support structures – a numerical verification using the comprehensive simulation code FAST*. Proceedings of the 53rd AIAA/ASME/ASCE/AHS/ASC Structures, Structural Dynamics and Material Conference. 23-26 April 2012, Honolulu, Hawaii, USA. AIAA 2012-1735. Also available at: http://www.nrel.gov/docs/ fy13osti/54675.pdf.

[81] Pahn, T.; Rolfes, R. (2012): *Inverse Lastermittlung zur Restlebensdauerprognose von Tragstrukturen für Windenergieanlagen*. 4. VDI-Fachtagung Baudynamik. Kassel, 2012. VDI-Berichte 2160. ISBN 978-3-18-092160-0.

[82] Papula, L. (2000): *Mathematische Formelsammlung für Ingenieure und Naturwissenschaftler*. 6. Auflage. Vieweg & Sohn, Wiesbaden. ISBN 3-528-54442-2.

[83] Peeters, B.; De Roeck, G. (2001): *Stochastic System Identification for Operational Modal Analysis: A Review*. Journal of Dynamic Systems, Measurement, and Control. Vol. 123, pp. 659-667.

[84] Rebelo, C.; Henriques, J.; Simoes, R.; Simoes da Silva, L. (2008): *Long-term monitoring of an eighty meters high wind turbine steel tower*. IABSE Conference, Helsinki 2008, pp. 24-30(7).

[85] REpower Systems SE (2010): *The 5-megawatt power plant with 126 metre rotor diameter*. http://www.repower.de/fileadmin/download/produkte/ RE_PP_5M_uk.pdf. Accessed 18.01.2012.

[86] Reuter, A.; Busmann, H.-G. (2010): *Forschung für das Zeitalter der erneuerbaren Energien*. FVEE Forschungsverbund Erneuerbare Energien, Tagungsband zur Jubiläumstagung des FVEE 11. und 12. Oktober 2010, Umweltforum Berlin. ISSN 0939-7582. www.fvee.de/fileadmin/publikationen/Themenhefte/th2010-2/th2010.pdf. Accessed 20.03.2013.

[87] Reuter, A. (2013): *Zukunftsfeld Windenergie*. In IWES Jahresbericht 12/13, Seite 10-13. www.iwes.fraunhofer.de/content/dam/iwes/de/documents/2012_2013_IWES_Jahresbericht_web.pdf. Accessed 20.03.2013.

[88] Rolfes, R.; Gerasch, W.-J.; Haake, G. (2006): *Validierte Strukturmodelle*. Kapitel 4 des GIGAWINDplus Jahresbericht 2005: Validierung bautechnischer Bemessungsmethoden für Offshore-Windenergieanlagen anhand der Messdaten der Messplattform FINO 1 und FINO 2. www.gigawind.de. Accessed 15.03.2012.

[89] Rolfes, R.; Gerasch, W.-J-; Rotert, D. (2007): *Vorlesung Tragwerksdynamik*. 2. Auflage. Mitteilungen des Instituts für Statik und Dynamik der Leibniz Universität Hannover. ISSN 1862-4650.

[90] Romppannen, A.-J. (2008): *Inverse Load Sensing Method for Line load Determination of Beam-Like Structures*. Doctor Thesis. Tampere University of Technology, Finland. 2008. ISBN 987-952-15-2053-2.

[91] Rosenow, S.-E.; Andersen, P. (2010): *Operational Modal Analysis of a Wind Turbine Mainframe using Cristal Clear SSI*. Proceedings of the the 28th International Modal Analysis Conference (IMAC) Jacksonville, Florida USA. http://www.svibs.com/solutions/literature/2010_3.pdf. Accessed 24.04.2013.

[92] Schaumann, P.; Seidel, M. (2000): *Eigenschwingverhalten von Windenergieanlagen - Berechnungen und Messungen*. Conference DEWEK, Wilhelmshaven, Germany. http://www.marc-seidel.de/English/publications.html. Accessed 30.03.2012.

[93] Seidel, M. (2001): *Zur Bemessung geschraubter Ringflanschverbindungen von Windenergieanlagen*. Dissertation. Schriftenreihe des Institutes für Stahlbau der Universität Hannover, Heft 20. Shaker Verlag. Aachen, Germany. ISBN 3-8265-8911-4.

[94] Sharpe, W. N. (2008); Editor of: *Handbook of Experimental Solid Mechanics*. Springer Science+Business Media, New York. ISBN 978-0-387-26883-5.

[95] Steltzner, A. D; Kammer, D. C. (1999): *Input Force Estimation Using an Inverse Structural Filter*. Proc. of the 17th International Modal Analysis Conference, Kissimmee, Florida, USA, p. 954-960.

[96] Stevens, K. (1987): *Force Identification Problems – an overview*. Proceedings of SEM, Spring Meeting, Houston, pp. 838-844.

[97] Swartz, R. A.; Zimmermann, A. T.; Lynch, J. P. (2010): *Automated Wind Load Characterization of Wind Turbine Structures by Embedded Model Updating*. Proceedings of SPIE 7647, 76470J.

[98] Tikhonov, N. A.; Arsenin, V. Y. (1977): *Solution of Ill-Posed Problems*. Translated English version. V. H. Winston & Sons, Washington D.C. ISBN 0-470-99124-0.

[99] Ungrad, A. K. (2004): *Zusammenstellung der Beanspruchungen auf Offshore-Windenergieanlagen*. Projektarbeit am Lehrstuhl für Massivbau der Gottfried Wilhelm Leibniz Universität Hannover.

[100] Verbruggen, T. M. (2009): *Load monitoring for wind turbines – Fibre optic sensing and data processing*. Report of the Energy Research Center of the Netherlands ECN. ECN-E-09-071.

[101] Williams, D.; Jones, R. P. N. (1948): *Dynamic Loads in Aeroplanes under given Impulsive Loads with Particular Reference to Landing and Gust Loads on a large Flying Boat*. Aeronautical Research Council Tech Report No. 2221, 1948.

[102] Wilson, R.; Walker, S.; Heh, P. (1999): *Technical and User's Manual for the FAST_AD Advanced Dynamic Code – Two-bladed Tilting and Teetering Hub Version, three-bladed Rigid Hub Version*. OSU/NREL Report 99-01. http://wind.nrel.gov/designcodes/ papers/FAST_AD.pdf. Accessed 12.01.2012.

Design codes, standards, and guidelines

[103] BSH standard (2007): *Design of Offshore Wind Turbines*. Bundesamt für Seeschifffahrt und Hydrographie (Federal Maritime and Hydrographic Agency). BSh-No. 7005. Hamburg and Rostock, Germany. http://www.bsh.de/en/Products/Books/ Standard/index.jsp. Accessed 25.04.2013.

[104] DIBt Richtlinie (2004): *Richtlinie für Windenergieanlagen. Einwirkungen und Standsicherheitsnachweise für Turm und Gründung*. Schriftenreihe des Deutschen Instituts für Bautechnik, Reihe B, Heft 8. Berlin, Germany.

[105] DNV-OS-J101 (2004): *Design of Offshore Wind Turbine Structures*. Offshore Standard. Det Norske Veritas. Norway.

[106] GL guideline (2004): *Guideline for the Certification of Offshore Wind Turbines*. Germanischer Lloyd WindEnergie, Rules and Guidelines – IV Industrial Services. Hamburg, Germany.

[107] IEC 61400-1 (2005): *Wind turbines – part 1: Design requirements*. Final Draft International Standard. Edition 3. International Electrotechnical Commission. Geneva, Switzerland.

[108] IEC 61400-3 (2009): *Wind turbines – part 3: Design requirements for offshore wind turbines*. International Standard. Edition 1. International Electrotechnical Commission. Geneva, Switzerland.

[109] IEC TS 61400-13 (2001): *Wind turbine generator systems – Part 13: Measurement of mechanical loads*. International Standard. Edition 1. International Electrotechnical Commission. Geneva, Switzerland.

[110] VDI 3834 (2009): *Measurement and evaluation of the mechanical vibration of wind energy turbines and their components – Onshore wind energy turbines with gears*. Richtlinie Verein Deutscher Ingenieure. Düsseldorf, Germany.

Supervised student mid-study theses and diploma theses

[111] Häckell, M. (2009): *Systemidentifikation einer aufgelösten Offshore-Gründungsstruktur mittels MATLAB*. Studienarbeit. Institut für Statik und Dynamik, Leibniz Universität Hannover.

[112] Häckell, M. (2010): *Application of an Inverse Load Identification Procedure at a Wind Turbine Model*. Diploma thesis. Institut für Statik und Dynamik, Leibniz Universität Hannover and Department of Civil and Environmental Engineering, University of Michigan.

[113] Raaba, A. (2010): *Damping estimation for a 5 megawatt offshore support structure using measurement data in standstill and operation*. Studienarbeit. Institut für Statik und Dynamik, Leibniz Universität Hannover.

[114] Wigger, M. (2009): *Schwingungstechnische Untersuchung der Gründungskonstruktion eines Rotorblattprüfstandes*. Studienarbeit. Institut für Statik und Dynamik, Leibniz Universität Hannover.

Software used with free download

[115] NWTC Design Codes (AeroDyn by Dr. David J. Laino), version v13.00.00. http://wind.nrel.gov/designcodes/simulators/aerodyn/. Last modified 03-February-2011. Accessed 24.01.2012.

[116] NWTC Design Codes (FAST by Jason Jonkman, Ph.D.) version v7.00.01a-bj. http://wind.nrel.gov/designcodes/simulators/fast/. Last modified 05-November-2010. Accessed 24.01.2012.

[117] NWTC Design Codes (TurbSim by Neil Kelley, Bonnie Jonkman), version v1.50. http://wind.nrel.gov/designcodes/preprocessors/turbsim/. Last modified 03-February-2011. Accessed 24.01.2012.

Appendix A – Inverse Load in Sum Form

Mathematical derivation of the frequency-domain expression for the inverse load calculation from matrix form into sum form

The frequency-domain expression for the inverse load calculation in matrix form is given by the equation

$$\mathbf{F}(j\omega)=\left(\mathbf{U}_0^{\mathrm{T}}\right)^{-1}\left(-\omega^2\mathbf{M}_g+j\omega\mathbf{B}_E+\mathbf{M}_g\Lambda_0\right)\mathbf{U}_0^{-1}\mathbf{Y}(j\omega)\,.$$

The matrix form can also be expressed in the form of a sum. For the mathematical derivation of the problem, a simplification of the variable denotation is done first, which results in

$$\mathbf{F}_{(m,1)}=\mathbf{V}_{(m,n)}^{\mathrm{T}}\cdot\mathbf{H}_{(n,n)}\cdot\mathbf{V}_{(n,m)}\cdot\mathbf{Y}_{(m,1)}$$

The terms that indicate the frequency dependency ($j\omega$) are omitted. The matrix **V** represents the inverse modal matrix $\mathbf{U}_0^{-1}$. The force vector **F** and the vector of displacements **Y** are given in spatial space. The FRF matrix **H** represents a modal space description. Additionally, subscripts n and m indicate the dimensions of the vectors and matrices, with n as the number of columns and m as the number of rows. The matrix form can be converted to an index form. Now, j is the index for the rows and k the index for the columns, resulting in

$$\begin{aligned}\mathbf{F}_{(m,1)}&=\left(v_{j,k}\right)_{(m,n)}^{\mathrm{T}}\cdot\left(h_{k,k}\right)_{(n,n)}\cdot\left(v_{j,k}\right)_{(n,m)}\cdot\left(y_{j,1}\right)_{(m,1)}\\&=\left(v_{k,j}\right)_{(n,m)}\cdot\left(h_{k,k}\right)_{(n,n)}\cdot\left(v_{j,k}\right)_{(n,m)}\cdot\left(y_{j,1}\right)_{(m,1)}\\&=\sum_{p=1}^{m}v_{k,p}\cdot h_{p,p}\cdot\sum_{q=1}^{n}v_{j,q}\cdot y_{q,1}\,.\end{aligned}$$

The two sums can be written more compactly as the matrices $\left(a_{k,p}\right)_{(n,n)}$ and $\left(b_{j,1}\right)_{(m,1)}$. The product of both matrices can be expressed in the form of a sum, which leads to

$$\begin{aligned}&=\left(a_{k,p}\right)_{(n,n)}\cdot\left(b_{j,1}\right)_{(m,1)}\\&=\sum_{i=1}^{n}a_{k,i}\cdot b_{i,1}\,.\end{aligned}$$

The back transformation to the initial term gives the following equation.

$$= \sum_{i=1}^{n} \left(v_{k,i} \cdot h_{i,i} \cdot \sum_{q=1}^{n} v_{i,q} \cdot y_{q,1} \right)$$

Now, the vector $\mathbf{v}_i$ is the i-th column of the inverse modal matrix that has k entries per row. In addition, the vector $\mathbf{v}^i$ describes the i-th row, now with k entries per column.

$$= \sum_{i=1}^{n} \left(\mathbf{v}_i \cdot h_{i,i} \cdot \mathbf{v}^i \cdot \mathbf{y} \right)$$

With the relationship $\mathbf{v}_i = \left(\mathbf{v}^i\right)^T$ a new form can be written as

$$= \sum_{i=1}^{n} \left(\mathbf{v}_i \cdot \mathbf{H}_i \cdot \mathbf{v}_i^T \cdot \mathbf{y} \right).$$

Finally, the back substitution of the variable gives the frequency-domain expression for the inverse load calculation in sum form.

$$\mathbf{F}(j\omega) = \sum_{i=1}^{n} \left(-\omega m_{gi} + j\omega b_{Ei} + m_{gi}\omega_{0i}^2 \right) \left(u_{0i}^T \right)^{-1} \mathbf{Y}(j\omega)\, u_{0i}^{-1}$$

Appendix B – Inversion in MATLAB, Signal Transformation, and Calculation of Noise

Remarks about the calculation of the FRF matrix in MATLAB

1. When compared to a solution using the Gaussian elimination, solving a system of equations by means of an inverse matrix means more computational effort and less accuracy in the solution.

   In addition, the normal equation is worse conditioned than the original over-determined system. The condition number even is squared.

   $$\kappa\left(\mathbf{H}^T\mathbf{H}\right) = \kappa\left(\mathbf{H}\right)^2$$

   Numerical computation is of finite precision. For this reason, the normal equation can become singular. In this case, an inverse $(\mathbf{H}^T\mathbf{H})^{-1}$ does not exist, although the columns of **H** are independent.
2. MATLAB is able to perform the calculation of the normal equation using the backslash operator. The backslash operator solves square, non-singular systems, but it also computes the least-squares solution of rectangular, over-determined systems. The solution bases on a QR factorization.

   $$\mathbf{F}(j\omega) = \mathbf{H}(j\omega) \setminus \mathbf{Y}(j\omega)$$
3. Pseudo-inverse (Moore-Penrose)

   The pseudo-inverse is used if the matrix **H** is not of square dimension.
4. Rank deficiency

   If the matrix **H** is rank deficient or if there are more columns than rows, the least-squares solution with the backslash operator is no longer unique.

   The pseudo-inverse has to be computed via the minimum norm solution, which gives a unique solution. The corresponding MATLAB command is pinv().
5. MATLAB is also capable of computing non-linear least-squares problems.

Transformation from time domain to frequency domain and vice versa

The following mathematical relationships transform a signal from the time domain to the frequency domain and vice versa. The length of the time signal t_{max} is computed from the multiplication of the resolution in time t_S and the number of samples in the signal N.

$$t_{max} = t_S \cdot N$$

Usually, the time signal is given. Consequently, t_{max}, $t_{S,}$ and N are known. The reciprocal of the resolution in time t_S is the so-called sampling frequency f_{Sample}. According to the time-domain description, the length of the signal in the frequency domain f_{max} is gained from the multiplication of the resolution in the frequency domain f_S and the number of samples N.

$$f_{max} = f_S \cdot N = f_{Sample}$$

The resolution in the frequency domain depends on the length of the time signal. In fact, the resolution is equal to the reciprocal of t_{max}. The reverse transformation follows the same algorithm.

$$f_S = \frac{1}{t_{max}} \quad \text{and} \quad t_S = \frac{1}{f_{max}}$$

This means that a large signal length leads to the required, fine resolution. For this reason, frequency-domain approaches are not optimal for real-time calculations. The corresponding time scale and frequency scale are computed as follows.

$$t = 0 : t_S : t_{max} - t_S \quad \text{and} \quad f = 0 : f_S : f_{max} - f_S$$

Furthermore, the maximal frequency of a signal is limited by the Nyquist frequency. The Nyquist frequency is based on the Nyquist-Shannon sampling theorem and ensures an accurate reconstruction of an arbitrary signal.

$$f_{Nyquist} = \frac{1}{2} \cdot f_{Sample}$$

In practice, the sampling frequency has to be chosen to allow for a sufficient range of frequencies to be covered.

Finally, the FFT of a discrete time signal leads to a frequency-domain signal that is its complex conjugate. Due to the sampling of discrete data points, the so-called Alias effect occurs (HAAKE (2010) [31], p. 30-31). This effect causes a duplication of the frequency spectrum, mirrored at the Nyquist frequency. Because of the mirroring, the peaks in the frequency spectrum only show the half amplitude. To countervail the Alias effect, the following procedure is chosen. After applying the FFT, the frequencies above the Nyquist frequency are eliminated using a low-pass filter. The amplitudes of the remaining frequencies (frequencies below the Nyquist frequency) are doubled. Now the transformation to the frequency domain is equal to the time-domain description of the signal. This truncated frequency spectrum is used for the inverse calculation. For the back transformation, first the frequency spectrum has to be mirrored at the Nyquist frequency. However, the part above the Nyquist frequency needs to be equal to the complex conjugate of the frequencies below $f_{Nyquist}$. After reducing the amplitudes by half and applying an iFFT, a time signal is obtained that exclusively contains real values.

Calculation of the noise ratio V_r

The noise is added to the displacement vector in form of white noise. A signal-to-noise ratio (SNR) is used to determine the magnitude of the noise. The SNR defines the relationship of the effective values of the displacement vector **y**(t) and the noise term **e**(t). The effective value of a signal x(t) is calculated by

$$x_{\mathrm{eff}} = \frac{1}{T}\sqrt{\int_T x^2(t)\,dt}\ .$$

The SNR is calculated according to the formula

$$\mathrm{SNR} = 10 \cdot \log_{10}\left(\frac{x_{S,\mathrm{eff}}^2}{x_{N,\mathrm{eff}}^2}\right)$$

with $x_{S,\mathrm{eff}}$ - effective value of the signal

$x_{N,\mathrm{eff}}$ - effective value of the noise

The percentage ratio of both effective values is of interest. This ratio can be described by the noise ratio V_r.

$$V_r = \frac{x_{N,\mathrm{eff}}}{x_{S,\mathrm{eff}}} \cdot 100 \quad \text{in } \%$$

Hence, the SNR can be expressed depending on V_r.

$$x_{N,\mathrm{eff}} = \frac{V_r \cdot x_{S,\mathrm{eff}}}{100}$$

$$\frac{x_{S,\mathrm{eff}}^2}{x_{N,\mathrm{eff}}^2} = \frac{x_{S,\mathrm{eff}}^2 \cdot 100^2}{V_r^2 \cdot x_{S,\mathrm{eff}}^2} = \frac{100^2}{V_r^2}$$

$$\mathrm{SNR} = 10 \cdot \log_{10}\left(\frac{100^2}{V_r^2}\right)$$

Appendix C – Linearization in FAST

Trim case setting for the linearization in FAST

Setting ii) representing a linearization for trim case 2

FAST primary input file (*.fst)		
AnalMode	2	Analysis Mode: creates a periodic linearized model
YCMode	0	Yaw control disabled [1]
PCMode	0	Pitch control disabled [1]
VSContrl	**0**	**Variable-speed control disabled**
BlPitch$_i$	0	Initial blade pitch of blade i (deg)
FlapDOF1	True	First flapwise blade mode enabled
FlapDOF1	True	Second flapwise blade mode enabled
EdgeDOF	True	First edgewise blade mode enabled
DrTrDOF	True	Drivetrain rotational-flexibility DOF enabled
GenDOF	True	Generator DOF enabled
YawDOF	False	Yaw DOF disabled
TwFADOF1	True	First fore-aft tower bending-mode DOF enabled
TwFADOF2	True	Second fore-aft tower bending-mode DOF enabled
TwSSDOF1	True	First side-side tower bending-mode DOF enabled
TwSSDOF2	True	Second side-side tower bending-mode DOF enabled
CompAero	True	Compute aerodynamic forces enabled
CompNoise	False	Compute aerodynamic noise disabled
RotSpeed	**8**	**Initial rotor speed (rpm)**
AeroDyn input file (*.ipt)		
StallMod	STEADY	Dynamic stall mode set to steady
InfModel	EQUIL	Inflow model set to equilibrium
WindFile		**File containing a constant wind speed of 7 m/s**
Linearization control file		
CalcStdy	True	Calculate periodic steady state condition [2]
TrimCase	**2**	**Trim case: electric generator torque**
DispTol	0.0001	Convergence tolerance for the 2-norm of displacements in the steady state calculation (rad)
VelTol	0.0010	Convergence tolerance for the 2-norm of velocities in the steady state calculation (rad/s)
NAzimStep	36	Number of equally-spaced azimuth steps in the periodic linearized model
MdlOrder	2	Order of output linearized model [3]

[1] Mandatory settings required by FAST in order to run the linearization.

[2] Set CalcStdy to False would start a linearization about the initial condition.

[3] The second order model gives amongst others the mass, damping and stiffness matrices **M**, **C**, and **K**, respectively. Setting MdlOrder = 1 gives the first order state space matrices **A**, **B**, **C**, and **D**.

Setting iii) representing a linearization for trim case 3

FAST primary input file (*.fst)		
AnalMode	2	Analysis Mode: creates a periodic linearized model
YCMode	0	Yaw control disabled [1]
PCMode	0	Pitch control disabled [1]
VSContrl	**1**	**Variable-speed control enabled**
BlPitch$_i$	0	Initial blade pitch of blade i (deg)
FlapDOF1	True	First flapwise blade mode enabled
FlapDOF1	True	Second flapwise blade mode enabled
EdgeDOF	True	First edgewise blade mode enabled
DrTrDOF	True	Drivetrain rotational-flexibility DOF enabled
GenDOF	True	Generator DOF enabled
YawDOF	False	Yaw DOF disabled
TwFADOF1	True	First fore-aft tower bending-mode DOF enabled
TwFADOF2	True	Second fore-aft tower bending-mode DOF enabled
TwSSDOF1	True	First side-side tower bending-mode DOF enabled
TwSSDOF2	True	Second side-side tower bending-mode DOF enabled
CompAero	True	Compute aerodynamic forces enabled
CompNoise	False	Compute aerodynamic noise disabled
RotSpeed	**10** [2]	**Initial rotor speed (rpm)**
VS_RtTq	**25,000** [3]	**Rated generator torque/constant generator torque in region 3 for simple variable-speed generator control (HSS side) (Nm)** [4]
AeroDyn input file (*.ipt)		
StallMod	STEADY	Dynamic stall mode set to steady
InfModel	EQUIL	Inflow model set to equilibrium
WindFile		**File containing a constant wind speed of 20 m/s** [5]
Linearization control file		
CalcStdy	True	Calculate periodic steady state condition [6]
TrimCase	**3**	**Trim case: find rotor collective blade pitch**
DispTol	0.0001	Convergence tolerance for the 2-norm of displacements in the steady state calculation (rad)
VelTol	0.0010	Convergence tolerance for the 2-norm of velocities in the steady state calculation (rad/s)
NAzimStep	36	Number of equally-spaced azimuth steps in the periodic linearized model
MdlOrder	2	Order of output linearized model [7]

[1] Mandatory settings required by FAST in order to run the linearization.

[2] Estimate for middle of region 3.

[3] Estimate for middle of region 3. See Baseline Documentation [49], p. 20 Figure 7-2.

[4] In addition, Vs_RtGnSp, VS_Rgn2K, and VS_SlPc are set to very small non-zero values.

[5] Estimate for middle of region 3.

[6] Set CalcStdy to False would start a linearization about the initial condition.

[7] The second order model gives amongst others the mass, damping and stiffness matrices **M**, **C**, and **K**, respectively. Setting MdlOrder = 1 gives the first order state space matrices **A**, **B**, **C**, and **D**.

The trim case decisive parameters are marked bold.

Appendix D – Modal Reduction of System Matrices

Discussion of system reduction methods

The reduction is based on the linear time-invariant equation of motion with n DOFs, as given previously in equation (3.14).

$$\begin{bmatrix} & & \\ & \mathbf{M} & \\ & & \end{bmatrix}_{n,n} \begin{bmatrix} \\ \ddot{\mathbf{y}} \\ \\ \end{bmatrix}_{n} + \begin{bmatrix} & & \\ & \mathbf{B} & \\ & & \end{bmatrix}_{n,n} \begin{bmatrix} \\ \dot{\mathbf{y}} \\ \\ \end{bmatrix}_{n} + \begin{bmatrix} & & \\ & \mathbf{K} & \\ & & \end{bmatrix}_{n,n} \begin{bmatrix} \\ \mathbf{y} \\ \\ \end{bmatrix}_{n} = \begin{bmatrix} \\ \mathbf{f} \\ \\ \end{bmatrix}_{n}$$

A transformation matrix **T** has to be found that reduces the n DOFs in the vector of the displacements **y** to a less number of DOFs denoted by r so that the vector **v** is obtained.

$$\begin{bmatrix} \\ \mathbf{y} \\ \\ \end{bmatrix}_{n} = \begin{bmatrix} & & \\ & \mathbf{T} & \\ & & \end{bmatrix}_{n,r} \begin{bmatrix} \mathbf{v} \\ \end{bmatrix}_{r}$$

The transformation is assumed to be time-independent. Then the following relationships are valid.

$$\mathbf{y} = \mathbf{T}\mathbf{v} \qquad \dot{\mathbf{y}} = \mathbf{T}\dot{\mathbf{v}} \qquad \ddot{\mathbf{y}} = \mathbf{T}\ddot{\mathbf{v}}$$

Combining the two above-given equations and applying a left-multiplication with the transposed transformation matrix $\mathbf{T}^{\mathrm{T}}$ leads to the reduced equation of motion

$$\mathbf{T}^{\mathrm{T}}\mathbf{M}\mathbf{T}\ddot{\mathbf{v}}(t) + \mathbf{T}^{\mathrm{T}}\mathbf{B}\mathbf{T}\dot{\mathbf{v}}(t) + \mathbf{T}^{\mathrm{T}}\mathbf{K}\mathbf{T}\mathbf{v}(t) = \mathbf{T}^{\mathrm{T}}\mathbf{f}(t)$$

, which can be also written in the form

$$\mathbf{M}^{\mathrm{red}}\ddot{\mathbf{v}}(t) + \mathbf{B}^{\mathrm{red}}\dot{\mathbf{v}}(t) + \mathbf{K}^{\mathrm{red}}\mathbf{v}(t) = \mathbf{f}^{\mathrm{red}}(t).$$

The reduced EoM now has r DOFs, with r < n.

$$\begin{bmatrix} & & \\ & \mathbf{M}^{\mathrm{red}} & \\ & & \end{bmatrix}_{r,r} \begin{bmatrix} \\ \ddot{\mathbf{v}} \\ \\ \end{bmatrix}_{r} + \begin{bmatrix} & & \\ & \mathbf{B}^{\mathrm{red}} & \\ & & \end{bmatrix}_{r,r} \begin{bmatrix} \\ \dot{\mathbf{v}} \\ \\ \end{bmatrix}_{r} + \begin{bmatrix} & & \\ & \mathbf{K}^{\mathrm{red}} & \\ & & \end{bmatrix}_{r,r} \begin{bmatrix} \\ \mathbf{v} \\ \\ \end{bmatrix}_{r} = \begin{bmatrix} \\ \mathbf{f}^{\mathrm{red}} \\ \\ \end{bmatrix}_{r}$$

In case the initial system matrices are symmetric, the reduced-system matrices will remain symmetric as well. The reduced system can then be treated similar to the descriptions of section 3.2.1.

The crucial aim of the system reduction is to find an appropriate transformation matrix **T**. An appropriate transformation matrix is found if the system can be reduced to the smaller amount r of DOFs without loosing the exact representation of the r remaining DOFs. This means that the reduction of the system does not change the eigenfrequencies and mode shapes, but that the reduction only cuts unnecessary DOFs.

In general, there are three kinds of system reduction methods that differ in the way in which they find the transformation matrix.

- Static reduction
- Modal reduction
- Combined static and modal reduction

For the static reduction – also-called Guyan reduction – the EoM has to be rearranged. The system needs to be divided into main DOFs and auxiliary DOFs. The number of main DOFs r defines the dimension of the reduced system. The rearranged EoM gives a static relationship for the stiffness of the main DOFs and the auxiliary DOFs. This relationship is used to create the transformation matrix. The reduction using the static approach is an approximation of the solution of the full system.

The modal reduction starts with an eigenvalue analysis of the full system using the undamped EoM. Eigenfrequencies and eigenvectors are obtained, as results. The modal matrix contains the eigenvectors column-wise. The transformation matrix is now gained by a truncation of the modal matrix. The truncated matrix consists of the eigenvectors whose corresponding eigenfrequencies will be part of the reduced system.

The quality of the resulting static reduction depends on the appropriate choice of the main DOFs. The system reduction cannot be done to an arbitrary small number of DOFs. However, the static reduction keeps those physical DOFs of the full system that are defined as main DOFs. The modal reduction involves much less mathematically effort in comparison to the static reduction. The system dynamics in from of the eigenfrequencies are kept exactly. Additionally, the modal reduction is useful if the full system shall be reduced to only a small number of DOFs.

The combined static and modal reduction combines the advantages of both methods. The physical meaning of some main DOFs are kept while the system can be reduced to a small number of DOFs. This characteristic is particularly important if parameter studies are intended. With a good choice of the main DOFs, parameter changes can be considered without a recalculation of the complete reduction. Parameter changes might occur due to rotation-speed-dependent stiffness or damping. The steps of the combined reduction are as follows: 1) Defining main DOFs and auxiliary DOFs and rearrangement of the EoM, 2) Creating a manipulated system by setting the main DOFs to zero, 3) Calculating the eigenvalue analysis of the manipulated system that gives the eigenfrequencies and eigenvectors, 4) Composing the modal part of the transformation matrix from the modal matrix, 5) Completing the transformation matrix by adding the static relationship of the stiffness of the main DOFs and the auxiliary DOFs, 6) Reducting the system using the transformation matrix.

Appendix E – Integration of Signals

Preliminary Thoughts

The inverse load calculation using measurement data usually requires an integration of numerical signals. In general, accelerations are recorded in order to measure the dynamic response of a structure. The structural acceleration is sampled at discrete time steps, which causes a numerical signal.

The chosen inverse load calculation method is based on the frequency-domain formulation of the second-order ordinary differential equation for a linear, time-invariant vibrating system. For this reason, the inverse load calculation demands displacement signals as input data. To approximate reality, the verification with the FAST simulation uses structural accelerations as input data. Consequently, the accelerations need to be integrated twice to obtain displacement data.

The integration of numerical signals can be done both in the time domain and in the frequency domain. In order to decide on one option, the characteristics of both approaches are subsequently described briefly.

- Integration in the time domain

The standard method for the integration of a recorded time history signal is calculating the area under the curve of the approximate trace. An approximate solution can be found by using numerical integration techniques such as rectangular or trapezoidal integration. A further technique is the finite differences integration that can be calculated as a central, backward, or forward difference. The finite differences integration also allows for a better approximation of the trace considering a higher order shape function.

Lincoln (2007) [61] presents a study that shows an important effect connected with the numerical integration. The study deals with the calculation of velocities or displacements from acceleration time histories. In particular, the effects of small frequency contents in the acceleration signals are discussed. A characteristic of an integrated signal is that its amplitudes are inversely proportional to the frequency. Although the integration is done numerically correct, this effect often leads to misleading results. An example is given in the Figure below. Part a) of the figure shows a measured acceleration signal recorded at a wind turbine support structure. The signal has zero mean and a low frequency content between 0 Hz and 5 Hz with spectral peaks around 2 Hz. The sampling frequency is 50 Hz. In b), the corresponding velocity signal is shown, which is obtained by numerical integration in the time domain. The oscillating behavior of the signal seems to have disappeared. That is because the very low frequencies with its very large time periods dominate the velocity signal. To solve this problem, a high-pass filter can be applied to the signal, as done in part c) with

f_{cut} = 0.15 Hz. Thus, the velocity signal looks more reasonable. Then, the frequencies below the chosen cut-off frequency of the filter are not existent anymore, which equals a loss of information.

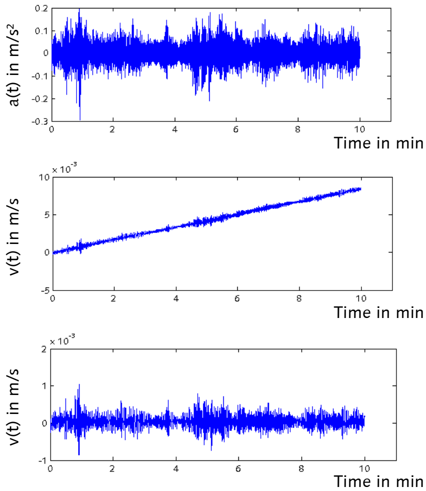

a) **acceleration signal**

b) **velocity signal**
obtained by numerical integration of the acceleration signal

c) **velocity signal**
obtained by numerical integration of the acceleration signal
5th order Butterworth filter applied

Effects of low frequencies on the integration of time history signals – time domain

Mercer (2001) [65] gives a further insight into the characteristics of the numerical integration in the time domain. Studying the frequency response function of the integration process allows an estimation of the accuracy. The study concludes that the low frequency range of the integrated signal is disturbed by a gain, whereas the high frequency range (near the Nyquist frequency) has attenuation. Only the frequency range between

$$0.02 * f_{sample} < f < 0.1 * f_{sample}$$

with f_{sample} as the sampling frequency are represented accurately. Hence, integrating a signal and then differentiating it does not give the original signal, which is not a welcome result. An approach that promises better results is the integration in the frequency domain.

- Integration in the frequency domain

Integration in the frequency domain is obtained by dividing the FFT of the signal by $j\omega$. This procedure is referred to as Omega Arithmetic (Mercer (2001) [65]). Applying the Omega Arithmetic to a Fourier transformed signal and converting the integrated signal back to the time domain using an iFFT gives a correct result. To do so, the signal has to have a mean of zero. The division by $\omega = 2\pi f$ causes an angular phase shift of $\pi/2$ or 90°, respectively. Therefore, the integration of a cosine gives a sine. Due to the division by ω, a mathematical singularity occurs around $\omega = 0$. These frequencies need to be eliminated. The elimination of the low frequencies can be done by a high-pass filter. The affected frequency range occurs at

$$0.001 * f_{sample} < f.$$

Both the time-domain and the frequency-domain approach have a limitation regarding the frequency range that can be represented accurately by the integration process. However, the frequency range that gives correct values is much bigger if the Omega Arithmetic is used.

Another characteristic that both approaches have in common is the need for filters. Whereas the time-domain approach uses filters to treat misleading results, the frequency-domain approach eliminates effects of a singularity. For the example in above-mentioned example, a 5th order Butterworth filter is used. Since filters are necessary to gain good integration results, the following section discusses different types of filter and estimates their effects on the signals.

The frequency limits depend on the sampling frequency. Beyond the given limits, the integrated signal does not contain usable frequencies. If an integration at very low frequencies is necessary, e.g. if eigenfrequencies are below the limit, Data Decimation (MERCER (2001) [66]) is recommended.

The reviewed literature clearly points out that the time-domain integration is not reversible without loss of information, which is not desirable. In contrast, the reversion of the frequency-domain integration gives correct results. In this case, the complete signal needs to be known.

A further characteristic of the integration process is stated by KARRENBERG (2010) [53]. The integration process has a low-pass characteristic, which means that high frequencies are suppressed. Thus, the integration eliminates noise in the signal – even better than a filter. This characteristic is of interest for the inverse load calculation, which is an ill-conditioned problem. Initial errors caused by noise might disturb the results, which is probably diminished using integrated signals.

Based on the given review of time-domain and frequency-domain integration, the Omega Arithmetic is chosen in this work. The mathematical calculations and an example of the Omega Arithmetic are given afterwards the discussion of the signal filtering.

Filtering of Signals

Filters divide signals into a filter passband and a filter attenuation band. The filter attenuation band is the range of frequencies that is supposed to be suppressed by the filter. Consequently, the filter passband is the frequency content that shall remain in the signal. Usually, both are divided by a blurred region called the transition band. Filters can be classified into the basic categories low-pass, high-pass, band-pass, and band-stop filter. The low-pass filter suppresses the frequencies above a defined cut-off frequency and the high-pass filter below the cut-off frequency. A band-pass filter remains a central part of the frequency range and cuts below and above the defined cut-off frequencies. The band-stop filter is the reverse of a band-pass filter. In general, filters are designed by means of three basic linear processes: phase lag, addition, and multiplication of a signal with a constant value – all in the time domain.

KARRENBERG (2010) [53][108] summarizes the most common filter types that are the Bessel filter, the Chebyshev filter, and the Butterworth filter. The several filter types differ in their slope of the gain in the frequency response that either defines a narrow or a wide transition band. Further, they show different phase delay. Depending on the filter, the phase delay can range from absolutely flat to irregular. Finally, the gain ripple in the pass band and the attenuation band is a distinctive feature. Generally, none of the filter types combines all positive characteristics. Hence, an appropriate filter has to be found for the specific problem.

The mentioned filters are analog filters. A much better performance is gained using digital filters. A simple approach for a digital filter that is defined in the frequency domain is described for a low-pass filter in the table below.

Description of the frequency-domain low-pass filter

1. The time signal is transformed into the frequency domain applying a FFT.
2. A cut-off frequency has to be chosen, so that pass band and attenuation band is defined.
3. The amplitudes and phase angles of all frequencies in the attenuation band – above the cut-off frequency – have to be set to zero.
4. Back transformation of the signal into the time domain using an iFFT.[109]

High-pass, band-pass, or stop-pass filters work in a similar way. Thus, a nearly ideal filter is realized. In contrast to the above-mentioned analog filters, this frequency-domain digital filter shows a much better performance. However, there is one drawback. The digital filter is not able to perform real-time calculation, as whereas analog filters can. Since the Fourier transformation is calculated, time-limited signals with a sufficient signal length are needed. Because this work does not focus on real-time calculation, the digital frequency-domain filter is used for signal filtering purposes. Additionally, most of the signals are needed in the frequency domain.

---

[108] For more detailed information and illustration of the filter designs, see KARRENBERG (2010) [53] chapter 7, page 213ff.

[109] In case the back transformation is done without special software that computes the FFT, the filtered frequency-domain signal has to be completed with its complex conjugate part before applying the iFFT.

Integration in the Frequency Domain

The integration in the frequency domain is done using the Omega Arithmetic, the calculations of which are explained in MERCER (2006) [67].

For a given acceleration signal $\ddot{x}(t)$, the Omega Arithmetic integrates the velocity signal $\dot{x}(t)$ as well as the displacement signal $x(t)$. Since the Omega Arithmetic is a frequency-domain approach, the acceleration signal needs to be transformed into the frequency domain, which gives the Fourier transformation of the acceleration $\ddot{X}(j\omega)$. Applying the FFT does not add or eliminate any signal information. The FFT is reversible. To denote these facts, the relationship between the time domain and the frequency domain is often written as

$$\ddot{x}(t) \Leftrightarrow \ddot{X}(j\omega).$$

The inverse transformation from frequency to time is defined by:

Acceleration $$\ddot{x}(t) = \frac{1}{2\pi}\int_{-\infty}^{\infty} \ddot{X}(j\omega)\cdot e^{j\omega t}d\omega$$

Velocity $$\dot{x}(t) = \frac{1}{2\pi}\int_{-\infty}^{\infty} \dot{X}(j\omega)\cdot e^{j\omega t}d\omega$$

Displacement $$x(t) = \frac{1}{2\pi}\int_{-\infty}^{\infty} X(j\omega)\cdot e^{j\omega t}d\omega$$

The acceleration is defined as the rate of change of the velocity.

$$\ddot{x}(t) = \frac{d}{dt}\dot{x}(t)$$

Then, inserting the equation of the velocity into the above-given equation reveals

$$\begin{aligned}\ddot{x}(t) &= \frac{d}{dt}\left[\frac{1}{2\pi}\int_{-\infty}^{\infty} \dot{X}(j\omega)\cdot e^{j\omega t}d\omega\right]\\ &= \frac{1}{2\pi}\int_{-\infty}^{\infty} \dot{X}(j\omega)\cdot \frac{d}{dt}e^{j\omega t}d\omega\\ &= \frac{j\omega}{2\pi}\int_{-\infty}^{\infty} \dot{X}(j\omega)\cdot e^{j\omega t}d\omega\end{aligned}$$

Comparing this expression for the acceleration with the Fourier transformation of the acceleration immediately makes clear that

$$\ddot{X}(j\omega) = j\omega\cdot\dot{X}(j\omega)$$

and consequently

$$\dot{X}(j\omega) = \frac{1}{j\omega}\ddot{X}(j\omega).$$

The relationship between accelerations and velocities is transferable to the relationship between velocities and displacements. The following equation which defines the Omega Arithmetic occurs.

$$X(j\omega) = \frac{1}{j\omega}\dot{X}(j\omega) = -\frac{1}{\omega^2}\ddot{X}(j\omega)$$

This means that if one of the three signals $X(j\omega)$, $\dot{X}(j\omega)$, or $\ddot{X}(j\omega)$ is known, the remaining signals can be calculated by multiplying or dividing by $j\omega$, respectively.

Applying the equation of the Omega Arithmetic leads to infinite amplitudes in the frequency spectrum at $\omega = 0$, which is caused by the division by ω. This singularity influences the neighboring frequency range. For this reason, the very low part of the frequency range cannot be used, because it produces distortion in the time signal that results from the back-transformed (iFFT) integrated signal. The singularity is of pure mathematical nature and has no physical meaning. To solve this problem, a high-pass filter is applied to the integrated frequency-domain signal. Then the frequencies in the attenuation band of the filter are cut off completely. For a one-time integration, e.g. from accelerations to velocities, the cut-off region is up to the 1,000th part of the sampling frequency. In case a double-integration from accelerations to displacements is calculated the cut-off range increases. This increase is caused by the division by $-\omega^2$. The cut-off range depends on the sampling frequency. For practical applications, one important condition has to be assured – the eigenfrequencies have to be located in the passband of the filter. If this condition is not fulfilled, the cut-off range might be reduced by applying Data Decimation, as introduced by MERCER (2001) [66].

The figure "Integration using Omega Arithmetic" gives an example of the double-integration using the Omega Arithmetic. Part a) of the figure shows an acceleration signal that is computed by FAST.[110] The signal is computed for the above-mentioned 5 MW reference wind turbine under rated wind speed. The signal is recorded at tower top. Part b) depicts the corresponding frequency-domain signal. The Omega Arithmetic is applied so that the frequency-domain displacement signal occurs, as shown in part c). Comparing both frequency-domain signals shows that the division by $-\omega^2$ emphasizes the low frequencies. The displacement signal is high-pass filtered at a cut-off frequency of 0.15 Hz to eliminate the mathematical singularity. Computing the iFFT gives the time-domain signal of the displacement, which is depicted in part d).

---

[110] It should be noted that FAST outputs the absolute acceleration, but that the acceleration is output in a body-fixed coordinate system that deflects with the wind turbine. Thus, the integration of this acceleration to get velocity or displacement leads to an error, unless the orientation of the body is taken into account. The presented results show small tower deflections so that the error is small.

Acceleration signal

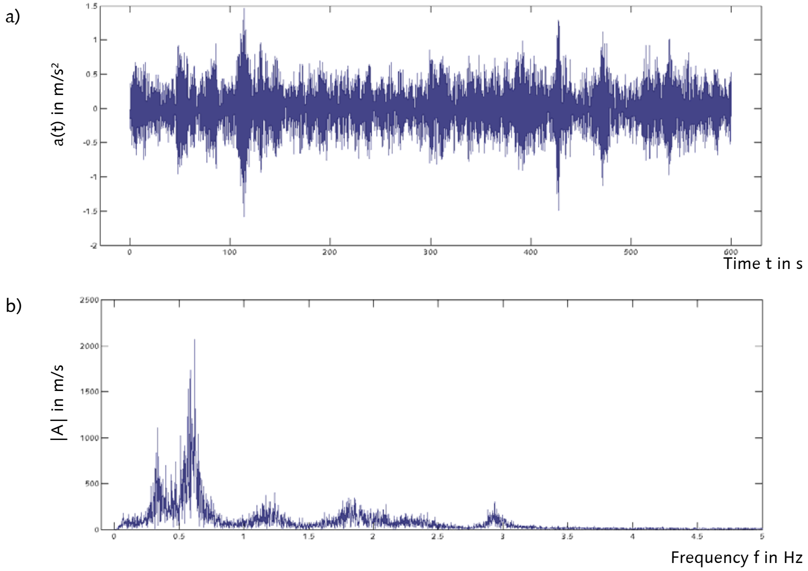

Displacement signal

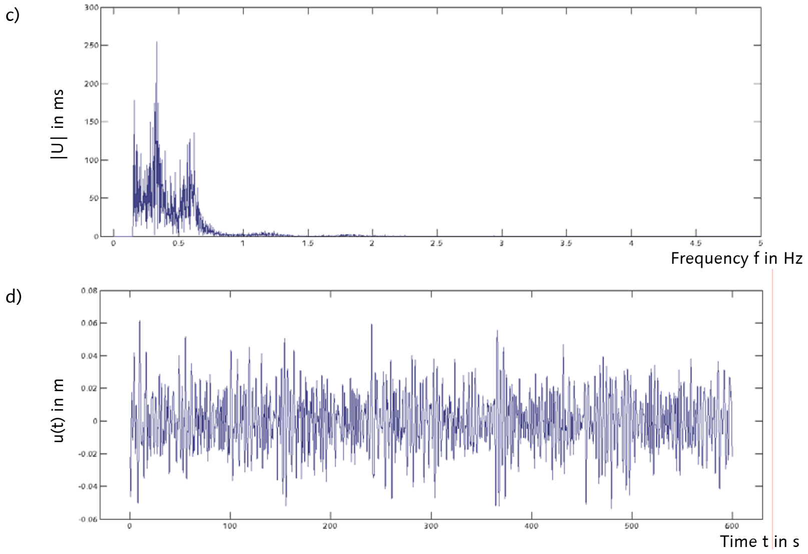

Integration using Omega Arithmetic

In order to guess the accuracy of the integration process, the time-domain signal of the displacement from part d) is compared to a displacement output of FAST, which is recorded at the same tower location. The comparison is illustrated in the figure "Comparison of displacement to twice-integrated accelerations". Both the time domain and the frequency domain are given. The signals nearly match perfectly. The Omega Arithmetic produces accurate results.

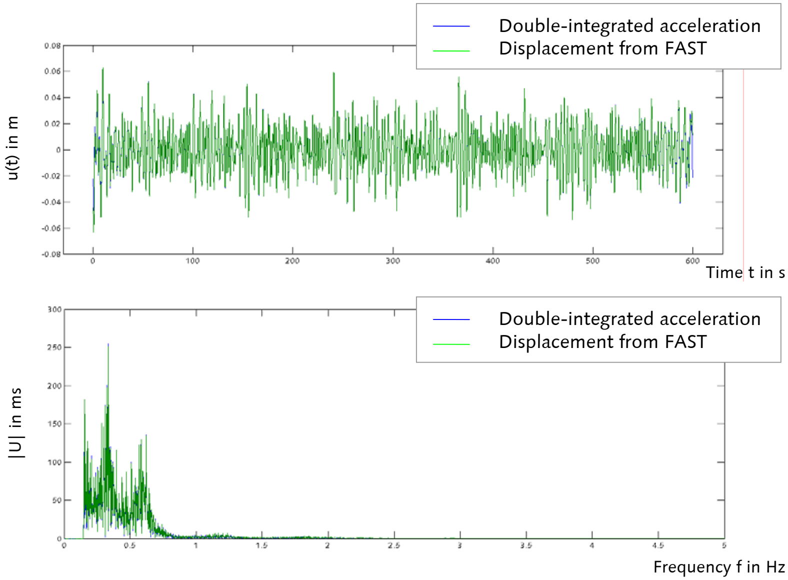

Comparison of displacement to double-integrated acceleration

For comparability, the displacement output of FAST (figure above) is also high-pass filtered at 0.15 Hz. Applying the filter is necessary because the FAST displacement output does not have a mean of zero, which equals the static displacement component. Since the integration process is not capable of generating the integration constant, the integration only accounts for purely dynamic signal components oscillating around a mean of zero. Additionally, the low-frequency content is cut off. This part of the frequency range can be considered the quasi-static part of the signal. In case the static and the quasi-static parts of the integrated signal are needed, they have to be added using additional information, such as that obtained from strain measurements.

In sum, the results of the Omega Arithmetic have very good qualitaties. In contrast to time-domain integration methods, displacements can be obtained via a double-integration, but only doing one calculation step. The calculation speed is high, especially in comparison to higher order time-domain integration methods. The effort concerning the application of the required high-pass filter is low. The integrated signal is calculated in the frequency domain, which is an advantage for this work. The back transformation to the time domain using an iFFT does not induce errors.

Appendix F – Control Outputs of FAST

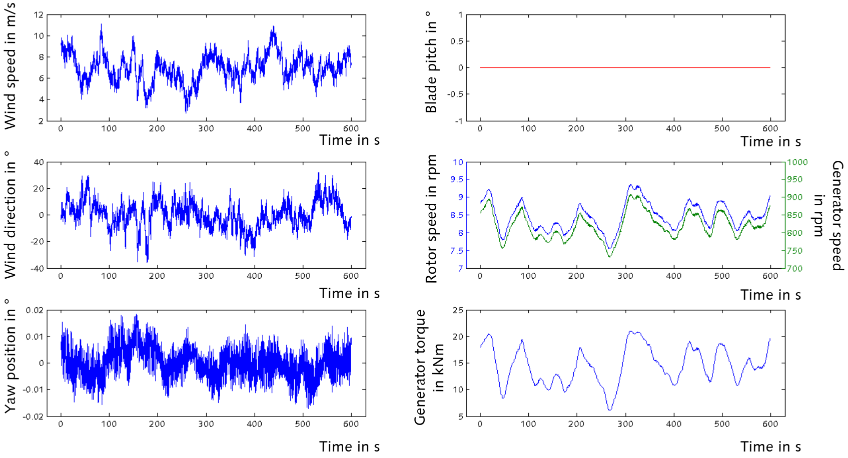

Controls – LC 1

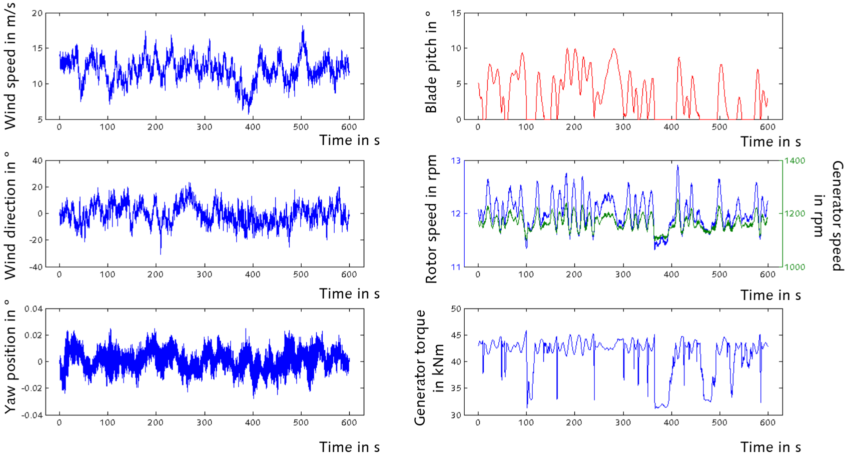

Controls – LC 2

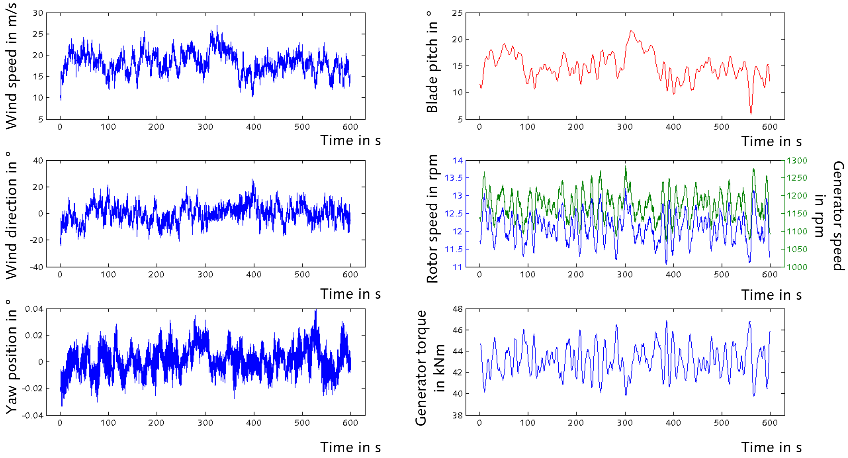

Controls – LC 3

Appendix G – Inverse Load Calculation using Displacement Signals

In order to study the influence of the integration of the acceleration signals, additional simulations are presented. Thus far, acceleration signals of the FAST output are used, as depicted in Figure 4.5. The acceleration signals at tower top and at half tower height are doubly integrated to displacements, which then served as input parameters for the inverse calculation. The integration process itself is discussed in detail in Appendix E.

Now, tower deflections at tower top and at half tower height are used directly. In this way, the integration process is omitted. Actually, the currently public available version of FAST does not allow outputting the tower deflections over the tower height. These simulations are run in collaboration with the NREL[111] that developed the FAST software. The NREL provided a version that is capable of outputing the tower deflections over the tower height.

The simulations are based on the following assumptions. Again, the NREL 5 MW onshore wind turbine model is used (see section 4.2.1). The FRF matrix that describes the system is gained by a linearization (see section 4.2.4). The inverse load is assembled by their different load components. Figure 4.6 depicts the corresponding scheme. The three load cases presented in Table 4.2 are calculated. The over-determined approach for the inverse calculation is used according to equations (3.63) and (3.64). To make sure that the tower deflection signals match to the previously used acceleration signals, both types of signals are compared to each other. To do so, the acceleration signals are integrated twice. The comparison of the displacement gained by double-integration of the acceleration to the tower deflection at tower top is shown in Appendix E.

The following figure depicts the result of the inverse calculation on the basis of tower deflections. The simulation of load case 2 is shown. The figure contains the dynamic component of the force that is calculated inversely using the Deconvolution in the Frequency Domain. Again, the inversely calculated load is intended to represent the aerodynamic rotor thrust. The inverse load is depicted in the time domain and the frequency domain. Both depictions show highly distorted graphs. The time-domain depiction seems to be a straight line that is limited by two sharp peaks at the beginning and at the end. These two sharp peaks exceed the rest of the signal by three decimal orders of magnitude. For this reason, the oscillating graph in between appears as a straight line. The frequency-domain depiction is characterized by an amplification of the high frequency content, which was already observable for the numerical 2-DOF example under noise (section 3.3.4). The distortions are

---

[111] National Renewable Energy Laboratory, Golden, USA

caused by the ill-conditioning of the inverse problem, as previously observed at the numerical 2-DOF example.

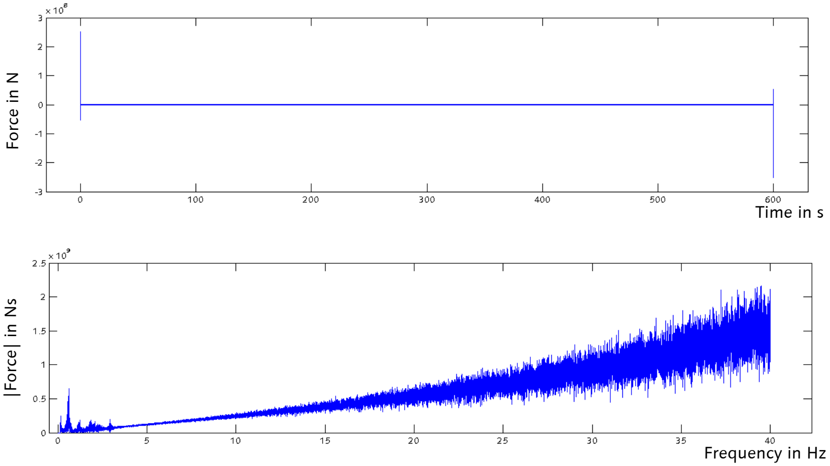

Inverse load on the basis of tower deflections

Of course, this result is not satisfying at all. As learned from the preliminary thoughts in section 3.1.2, the ill-conditioning can be treated while applying regularization. Amongst others, the application of filters and windowing are mentioned as appropriate instruments. Windowing describes a time-domain process that is similar to the filtering of signals, which is done in the frequency domain. A discrete time-domain signal of finite length is multiplied with a window function. Usually, a window function causes a fading in of the signal at the beginning and a fading out at the end. The fading occurs in a defined interval and weighs the signal from 0 to 1. In between, the signal remains undisturbed. Several window functions exist that differ in complexity. More detailed information in terms of windowing is given for example in KAMMEYER (2006) [52]. Here, a Hann window is applied to the time-domain signal of the inversely calculated load, which results in the upper graph in the figure below. Each the first 50 and last 50 data points of the time signal with a data length of 48,001 are weighed. Additionally, a low-pass filter is applied to the frequency-domain representation of the signal, which is shown in the lower graph. The cut-off frequency is set to 4 Hz. The figure still contains the results of load case 2 and depicts the dynamic component.

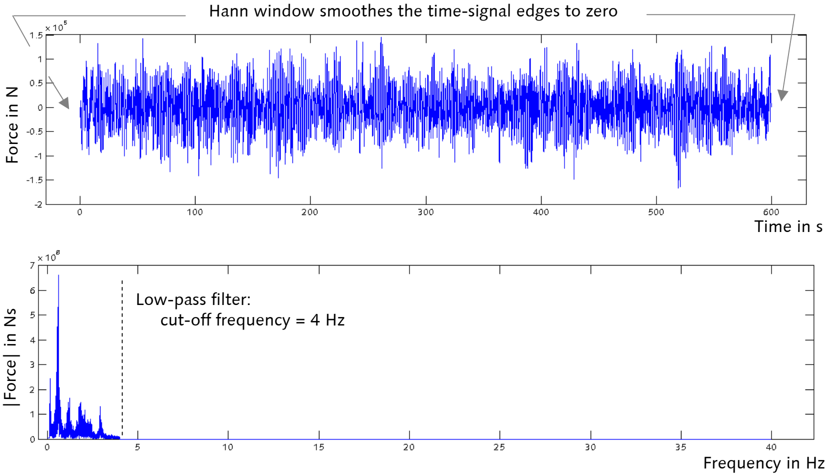

Regularization of the inversely calculated load

Using the described regularization and adding the static/quasi-static components lead to the inverse load as depicted in below. The result of the inverse load calculation is compared to the rotor thrust that is output by FAST in order to estimate the accuracy of the inverse calculation.

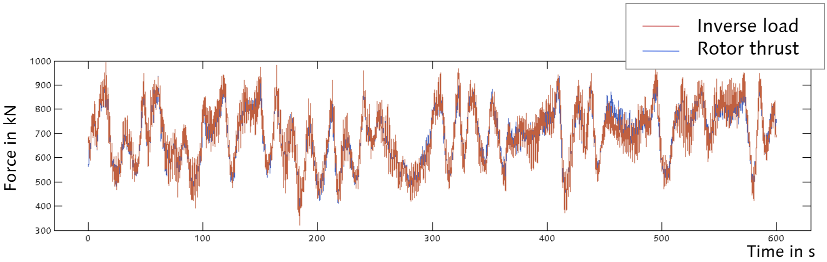

Rotor thrust and inversely calculated force after regularization

The comparison between the inverse load and the reference rotor thrust for load case 2 (figure above) has a very high agreement. To gain an idea about the calculation accuracy in relation to the results using the acceleration signals, the following table is set up. The table summarizes mean values and standard deviations of the reference rotor thrust, the inverse load basing on accelerations, and the inverse load basing on tower deflections – each for the full loads containing all components. All three load cases are calculated. As mentioned beforehand, the mean value serves as an estimate for the static component and the standard deviations as an estimate for the dynamic characteristic. The point of interest is the comparison of the values of the inverse loads. Both the mean values and the standard deviations match nearly perfectly. That means that the inverse calculation using the accelerations and the inverse calculation using the tower deflections produce exactly the same results.

Comparison of mean value and standard deviation

		Rotor thrust	**Inverse load**	
			Accelerations	**Deflections**
LC 1	Mean value ∅	392.38 kN	379.88 kN	380.04 kN
	Standard deviation σ	53.78 kN	62.60 kN	62.59 kN
LC 2	Mean value ∅	690.40 kN	693.43 kN	693.48 kN
	Standard deviation σ	108.75 kN	116.66 kN	116.65 kN
LC 3	Mean value ∅	443.96 kN	458.56 kN	458.57 kN
	Standard deviation σ	74.34 kN	89.07 kN	88.98 kN

This conclusion is underlined by the comparison of the errors in time between the rotor thrust and both the inverse load based on acceleration signals and the inverse load based on tower deflections (table below). The error values are calculated for the full loads containing all load components and are given for the three load cases. It can be seen that, there are no differences between the error values.

Comparison of the errors in time

	LC 1	**LC 2**	**LC 3**
Acceleration signals	16.08 %	11.34 %	10.81 %
Displacement signals	16.27 %	11.58 %	10.88 %

This section determines whether the integration process implies any errors to the inverse calculation or not. As revealed by the results of shown in the two tables above, the conclusion arises that the integration process does not. The comparative study that uses tower deflections as input parameters results in exactly the same inverse loads.

Additionally, the guess that the integration process affects the inverse calculation positively in terms of treating the ill-conditioning is demonstrated.

And thirdly, a method for treating the effects caused by the ill-conditioning is shown. The use of filters and windowing leads to adequate results.

Appendix H – Description of the Finite Element Model

The modeling of the structural components of the 5 MW wind turbine with an offshore support structure is done subsequently. Pictures of the structure and the FE model are given in Figure 5.1 and Figure 5.3.

- Soil

The soil is modeled using linear-elastic spring-damper elements representing the bedding characteristics. The spring-damper elements are applied at each node along the pile heights in two orthogonal horizontal directions. The stiffness properties correspond to the stiffness moduli of the genuine soil layer. The calculation of the spring constants with respect to the soil layer stiffness is explained in ROLFES ET AL. (2006) [88] (page 53). The soil damping is set to zero in order to calculate undamped eigenfrequencies. Because of the length of the piles, skin friction and tip pressure are omitted. The vertical support is realized by vertically rigid-based piles activating their axial rigidity.

- Foundation

The massive cylindrical reinforced concrete foundations are modeled by shell elements located at the vertical center of the foundation bodies. The material properties are set infinitely rigid, assuming no bending in the massive bodies. The site-mixed concrete driven piles are modeled with beam elements representing the true mass and stiffness properties. The offset between the foundation bodies and the lattice structure is modeled by rigid links transmitting the forces and the displacements. An alternative model variant of the foundation bodies using rigid beam elements can be used either. This conclusion results from the above-mentioned comparative study.

- Sub-structure

The sub-structure is a lattice structure that consists of steel pipes connected by cast-steel nodes. Beam elements are used that represent the true mass and stiffness properties. Special focus lies on the connecting nodes. The used beam elements represent the center lines of the pipes. Thus, an offset occurs for the nodes, where the vertical pipe has to be connected to the pipes that define the crosses of the structure. This offsets are modeled with extra beam elements, which represent the flexibility of the nodes (see Figure 5.3, Detail: double-K node). The flexibility value is gained by detailed FE simulations (see chapter 2.5

of the final report OGOWin (2011) [74]). Additional point masses are used to model the correct node masses.

- Transition piece

The transition piece is modeled by shell elements. The lower and upper edge is stiffened additionally as it is in the design of the transition piece. Modeling the circular cross-section with a finite number of shell elements leads to small errors in the representation of the mass (see Figure 5.3, Detail: transition piece). This error is compensated by factorizing the density of the material. This assumption also covers additional masses of built-in components. A simplification of the transition piece using an alternative beam element construction is not recommended. The above-mentioned comparative study showed that beam elements are not able to represent the spatial geometry of the transition piece in terms of calculating the eigenfrequencies of the entire structure.

- Tower

The tubular tower is approximated by beam elements. The beam elements represent the properties of the cylindrical cross-sections of the tower. Built-in components, platforms, and flanges are taken into account by additional masses distributed over the tower's height.

- Rotor-nacelle-system

Basically, the rotor-nacelle-system is reduced to a single mass with inertias. This assumption is appropriate since the effects of the spinning rotor are neglected for the calculation of the dynamic behavior of the support structure. This modeling strategy is also used by IBSEN AND LIINGAARD (2006) [39] and SCHAUMANN AND SEIDEL (2000) [92] in order to simulate the dynamics of wind turbine support structures. This approach ignores coupling between the vibrations of the blades and the support structure. These couplings can have impact on the eigenfrequencies of the support structure for all but not the first bending mode.

Appendix I – Discussion of Output-Only System Identification Methods

The discussion of output-only system identification techniques focuses on those methods that already have been applied to wind turbine structures under stochastic excitation. So, the three methods Autoregressive Model (AR), Stochastic Subspace Identification (SSI) and Frequency Domain Decomposition (FDD) are reviewed.

- Autoregressive Model (AR)

KRAEMER (2011) [57] uses the AR approach in order to determine modal parameters of an onshore prototype structure for a 5 MW offshore wind turbine, aiming on detecting structural damages. HAAKE (2010) [31] applies the AR approach to a 5 MW offshore wind turbine that is located in the first German offshore wind park 'Alpha Ventus', with the objective of updating a corresponding structural model of a wind turbine. Both authors use stochastic excitation from wind, operation, and waves respectively.

Both references give a detailed description of the underlying theoretical basics, which are briefly summarized here. The AR approach is a time-domain based system identification method, formulated in the state space. The measured time series of a structural response can be described by a summation of its N predecessor values multiplied with a coefficient matrix of the order p, which is called the AR model. The difference to the initial system response is described by a zero-mean model error. The coefficient matrices are obtained by minimizing the model error using a least-squares approach, so that all coefficients stay constant over the time series. Using the coefficients of the AR model, eigenvalues, mode shapes, and damping ratios can be calculated.

The eigenfrequencies can be calculated analytically, which is an advantage, especially if automated system identification is intended. A linear vibrating structure with pl modes is represented by a p-th order AR model, which adds spurious modes to the physical modes. In order to differentiate between physical and spurious mode, the calculation of stability diagrams is necessary. In comparison to common system identification methods, the AR approach also can be applied to data of short length such as generated by gusts. This use of only few data points produces reliable results in terms of eigenfrequencies and mode shapes, but the accuracy regarding damping ratios may decrease (see HAAKE (2010) [31]).

- Stochastic Subspace Identification (SSI)

ROSENOW AND ANDERSEN (2010) [91] demonstrate the system identification of the main frame of a 2.5 MW onshore wind turbine nacelle using the SSI. Tests are performed in standstill conditions. The study focuses on the dynamic interaction with the tower and the turbine blades.

The fundamentals of the SSI are firstly described in Overschee and De Moor (1996) [76] and are summarized briefly in Brincker and Andersen (2006) [11]. The SSI is also a time-domain approach. The SSI addresses the stochastic realization problem, i.e. the problem of identifying a stochastic state-space model from output-only data. Firstly, the state space matrices are identified from the measurements using numerical techniques such as QR factorization or singular value decomposition (SVD). The QR factorization results in a significant data reduction, whereas the SVD eliminates noise that is assumed to be part of higher singular values. Once the state space is set up, a mathematical description of the structure is found. Applying an eigenvalue decomposition to the discrete state matrix gives the eigenvalues, which enables extracting the eigenfrequencies and the damping ratios.

In fact, no literature can be found that presents the application of the SSI to a running wind turbine. Hence, no experiences how the SSI deals with wind turbine specific characteristics are published. Chauhan et al. (2009) [14] merely demonstrate the application of the SSI to a wind turbine model, simulated using HAWC2. The wind turbine is in standstill and eigenfrequencies, mode shapes, and damping ratios are obtained. The study presents promising results. However, the step to a real wind turbine in operation is not done yet.

- Frequency Domain Decomposition (FDD)

In Ibsen and Liingaard (2005) [38] and Ibsen and Liingaard (2006) [39] the system identification of an offshore wind turbine with a bucket foundation is presented. The FDD is used to determine the eigenfrequencies in standstill and operation for the first and second fore-aft mode of the turbine. Additionally, the harmonic 1P and 3P excitation are detected. Rebelo et al. (2008) [84] also use the FDD at a running wind turbine. For an onshore wind turbine, the first and second mode – each in fore-aft and side-side direction – are determined.

In contrast to the AR models and the SSI, the FDD is a frequency-domain approach. The FDD is explained briefly in Ibsen and Liingaard (2006) [40]. This approach estimates the modes from the power spectral density (PSD) matrix that is computed using the recorded response signals. The PSD matrix is split into their singular values and singular vectors by applying a singular value decomposition (SVD). The singular vectors are an estimate of the mode shapes. Using the singular vectors, a piece of the singular value function can be determined that represents a free vibrating SDOF system, which corresponds to a certain eigenmode. The obtained SDOF system allows the calculation of the eigenfrequencies and the damping ratios.

The FDD is described to be simple in terms of its application. The method is robust in finding the modal parameters, even if noise is present in the signals or two modes appear closely spaced. Andersen et al. (2007) [2] describes how the FDD has to be implemented in order to perform an automated identification.

Appendix J – Decay Constant and Logarithmic Decrement

Calculation of the damping ratio D via the decay constant δ and the logarithmic decrement ϑ using a regression analysis on the basis of a least-squares approach

As stated e.g. in Natke (1983) [70] or Gasch and Knothe (1987) [25], the damped vibration is described by

$$x(t) = \mathrm{Re}\left\{x_0 \cdot e^{-\delta t} \cdot e^{j\omega t}\right\} = \mathrm{Re}\left\{x_0 \cdot e^{(-\delta + j\omega)t}\right\}$$

with ω as the angular frequency and δ as the decay constant. The term

$$y = x_M(t) = x_0 \cdot e^{-\delta t}$$

describes the decay of a vibration and consequently, the damping of the corresponding system, as depicted below.

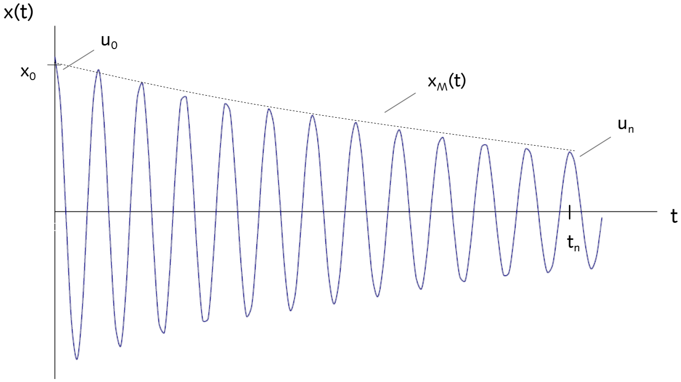

The enveloping function y can be obtained using the maxima in x(t). Exactly two maxima are required to determine the two unknown variables that are the decay constant δ and the value x_0. Additionally, x(t) contains all information to calculate the logarithmic decrement ϑ. By means of two neighboring maximal amplitudes u_n and u_{n+1}, ϑ can be calculated.

$$\vartheta = \ln\frac{u_n}{u_{n+1}}$$

Often, the logarithmic decrement is averaged over a number of periods n. Then, the first maximum u_0 and the maximum at the n-th period u_n are usually used.

$$\vartheta = \frac{1}{n}\cdot\ln\frac{u_0}{u_n}$$

The calculation of both D and ϑ depends on only two maxima, although usually more maxima occur. To enhance the accuracy of the damping calculation, more maxima or all maxima can be taken into account. Doing so creates an over-determined system of equations, which can be solved using the normal equation that is based on a least-squares approach, see e.g. BADER AND SCHENK (2001) [3].

$$f(x) = \left\|\mathbf{A}\cdot\mathbf{x}-\mathbf{b}\right\|_2^2$$

The normal equation is restricted to linear problems, which is not the case in terms of the decay constant. For this reason, the problem regarding the decay constant has to be first linearized, which follows the equations

$$\frac{y}{x_0} = e^{-\delta t} \qquad \rightarrow \qquad \ln\left(\frac{y}{x_0}\right) = -\delta t$$

$$\ln(y) - \ln(x_0) = -\delta t$$

$$\ln(y) = \ln(x_0) - \delta t\,.$$

In this way, x_0 und δ have a linear dependency. Inserting the substitutions

$$\begin{aligned} b_i &= \ln(y_i) \\ x_1 &= \ln(x_0) \\ x_2 &= -\delta \end{aligned}$$

in the normal equation enables the calculation of the minimizing problem. The corresponding system of equations has the following form.

$$\mathbf{A}\cdot\mathbf{x} = \mathbf{b}$$

$$\begin{bmatrix} 1 & t_i \end{bmatrix}\cdot\begin{bmatrix} x_1 \\ x_2 \end{bmatrix} = \begin{bmatrix} b_i \end{bmatrix}$$

Solving the normal equation is done with

$$\mathbf{A}^T\mathbf{A}\cdot\mathbf{x} = \mathbf{A}^T\mathbf{b}\,,$$

so that the vector **x** is obtained by

$$\mathbf{x} = \left(\mathbf{A}^T\mathbf{A}\right)^{-1}\cdot\mathbf{A}^T\mathbf{b}\,.$$

The back substitution gives the unknown variables.

$$x_0 = e^{x_1}$$
$$\delta = -x_2$$

With the eigenfrequency $\omega_0 = 2\pi f_0$, the damping ratio D can be calculated according to

$$D = \frac{\delta}{\omega_0} = \frac{\delta \cdot 2\pi}{f_0}.$$

In terms of calculating the logarithmic decrement ϑ, the initial equation

$$\vartheta = \frac{1}{n} \cdot \ln \frac{u_0}{u_n}$$

needs to be transformed to

$$\ln(u_n) = \ln(u_0) - \vartheta n.$$

Now the relationships

$$b_i = \ln(u_n)$$
$$x_1 = \ln(u_0)$$
$$x_2 = -\vartheta$$
$$t_i = n$$

can be derived, which enables the use of the normal equation described above. The logarithmic decrement ϑ is calculated directly. The damping ratio D is obtained by

$$D = \frac{\vartheta}{2\pi}.$$

Both approaches are based on the assumption of light damping.

Appendix K – Preparation of the Measurement Data

Before using the measurement data, all sensors have to be transformed into one consistent coordinate system. A depiction of the sensors can be found in Figure 5.9. The reasons for the coordinate system transformation are the following.

- The sensors have different orientations depending on the structural part where they are applied. That means e.g. the sensors at the tower are oriented differently to those applied at the lattice structure.
- The sensors are located in a fixed coordinate system that does not necessarily coincide with the nacelle position. But, as learned from the modal analysis (see section 5.1.2) the modal parameters depend on the nacelle position, since they are different in fore-aft and side-side direction respectively.

To gain consistency, firstly all sensors are transformed into a fixed coordinate system that is defined for the lattice structure. The north orientation of the lattice structure is known. Thus, the relation to the nacelle position is obtained, since the nacelle position is measured to its north orientation as well. In this way, the sensors can be oriented according to the rotating coordinate system of the nacelle, which allows distinguishing between their fore-aft and their side-side components. Fore-aft represents the system response along the rotor axis, positively defined in the direction of the wind, and side-side is orthogonal to the rotor axis assuming a right-handed coordinate system (figure below). Applying the described transformation enables detecting the system responses in fore-aft and side-side direction separately, which is necessary because they depend on the mass and stiffness distribution of the rotor-nacelle-system.

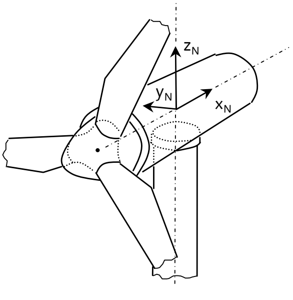

x_N – horizontal in direction of rotor axis (fore-aft)
y_N – horizontal to x in lateral direction (side-side)
z_N – vertically upward

Definition of the nacelle coordinate system

The steps of the coordinate transformation are:

1) Rotating the sensor orientation of each sensor position level into the fixed coordinate system of the lattice structure

The fixed coordinate system of the lattice structure is depicted below, inserted in a top view of the support structure. The abbreviations L1 to L4 denote the legs of the lattice structure. Additionally, the circular cross-section of the tower is depicted. As an example, the accelerometers at the tower-top level (B 1.1 and B 1.2) are shown, each with its positive sensor orientation. The lift (Fahrstuhl – equals the lift inside the tower) allows an unequivocally correlation between the coordinate system orientation and the north direction.

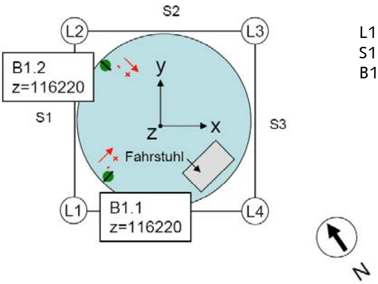

L1 to L4 – legs of the lattice structure
S1 to S4 – sides of the lattice structure
B1.1/B1.2 – accelerometers at the tower-top level

(Drawings are taken from Fraunhofer IWES, Bremerhaven)

Fixed coordinate system of the lattice structure

The sensor orientations of each sensor position level (compare to Figure 5.9) are summarized in the table below. The orientation angles are denoted by δ, which represents the rotation angle with respect to the coordinate system of the lattice structure. The angle δ rotates positively counter-clockwise.

Sensor orientations

Fore-aft	**Side-side**	δ	**Height**	**Location**
BS 1.2	BS 1.1	45°	116.220 m	Tower top
BS 2.1	BS 2.2	-135°	93.859 m	Two-third of tower height
BS 4.1	BS 4.2	-135°	74.280 m	One-third of tower height
BS 5.2	BS 5.1	45°	57.830 m	Tower base
BS 13.1	BS 13.2	0°	27.400 m	Half height of lattice structure
BS 16.2	BS 16.1	-180°	27.400 m	Half height of lattice structure
BS 20.1	BS 20.2	0°	0.736 m	Lattice structure base
BS 21.1	BS 21.2	-180°	0.736 m	Lattice structure base

2) Rotation of the nacelle

The yaw angle β represents the position of the nacelle with respect to north. A yaw angle of β = 0° results from a wind turbine heading north, i.e. the x_N-direction of the nacelle coordinate system introduced in the figure "Definition of the nacelle coordinate system" is positively oriented in southern direction. The yaw angle is a measurement signal that is recorded continuously. The rotation of the nacelle position is positively defined clockwise. The definition of the nacelle orientation in comparison to the fixed coordinate system of the lattice structure is depicted susequently.

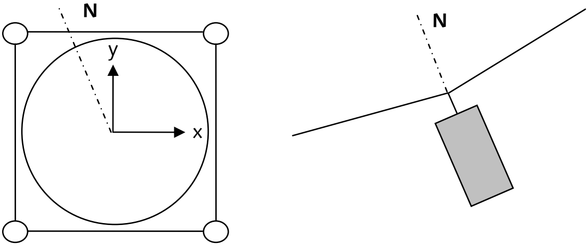

β = 0°
Nacelle heading north

β positive clockwise

Definition of the nacelle orientation

3) Relating the lattice structure coordinate system to the north direction

The orientation of the lattice structure with respect to the north direction is defined by the angle $\gamma' = 33{,}845°$, as shown in the following figure. In order to rotate the coordinate system of the lattice structure so that the nacelle position of β = 0° is reached, an angle of $\gamma = -56{,}155°$ has to be applied. The angle γ rotates positively counter-clockwise.

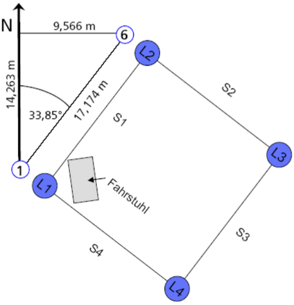

L1 to L4 – legs of the lattice structure
S1 to S4 – sides of the lattice structure

Fahrstuhl – the lift of the lattice structure

(Drawings are taken from Fraunhofer
IWES, Bremerhaven)

Orientation of the lattice structure with respect to north

4) Coordinate transformation

Considering the transformation steps 1) to 3) results in the transformation rule

$$\begin{bmatrix} x_{N,\text{fore-aft}} \\ y_{N,\text{side-side}} \end{bmatrix} = \begin{bmatrix} \cos\alpha & \sin\alpha \\ -\sin\alpha & \cos\alpha \end{bmatrix} \begin{bmatrix} BS_{\text{fore-aft}} \\ BS_{\text{side-side}} \end{bmatrix}$$

with

$x_{N,\text{fore-aft}}$ -	acceleration in fore-aft direction transformed into the rotating coordinate system of the nacelle,
$y_{N,\text{side-side}}$ -	acceleration in side-side direction transformed into the rotating coordinate system of the nacelle,
$BS_{\text{fore-aft}}$ -	accelerometer with fixed initial orientation, according to the table above, and
$BS_{\text{side-side}}$ -	accelerometer with fixed initial orientation, according to the table above.

The transformation rule is calculated at each sensor position level. The transformation angle α is defined positively counter-clockwise and is a sum of the above-mentioned transformation angles, with respect to the positive defined rotation of each angle.

$$\alpha = -\beta + \gamma + \delta$$

5) Verification of the coordinate transformation

A verification of the coordinate transformation is presented in Häckell (2009) [111], which is a student mid-study thesis that was supervised within this work. A depictive example of the transformation is given below, where the initial and the transformed acceleration signals at tower top and tower base are shown.

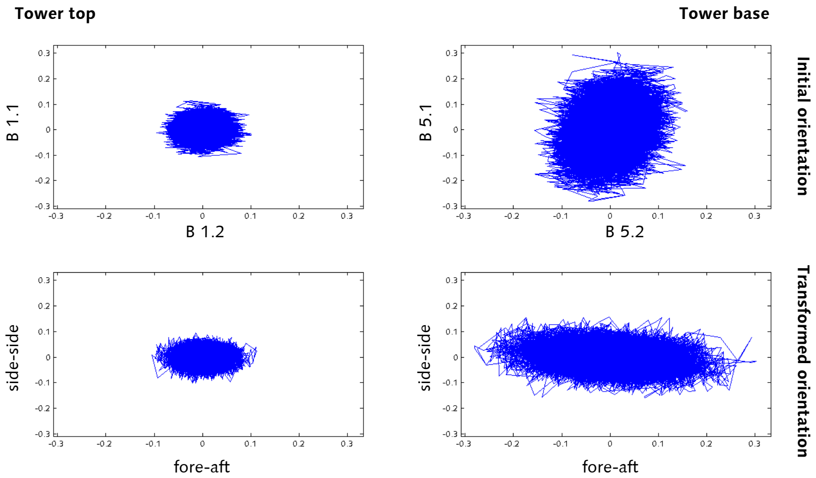

Initial and transformed acceleration signals at tower top and tower base

The acceleration sensors in its initial orientation are depicted at tower top (top left) and at tower base (top right) in the figure above. The initial accelerations are plotted as orbit plots giving the relation between the two accelerometers at each level. In comparison, the transformed signals are depicted for the same tower locations, each below its corresponding initial signal. Now, the orbit plots depict the fore-aft orientation to the side-side orientation. As visible, the transformed signals show a clear fore-aft orientation both for the tower top (bottom left) and for the tower base (bottom right). This characteristic is expected, because the used data are from operating conditions of the wind turbine. The mean wind speed of approximately 8 m/s causes higher acceleration amplitudes in fore-aft direction than there are in side-side direction.

As a further example, the two following figures depict measurement data in standstill. In each figure the absolute values of the accelerations are shown, converted into the frequency domain using a FFT. The spectra are given for different sensor location levels over the height of the structure. The upper figure contains the transformed accelerations in fore-aft direction and lower figure the corresponding transformed accelerations in side-side direction. A range from 0 Hz to 3 Hz is shown, because this range contains the first and the second global bending modes.

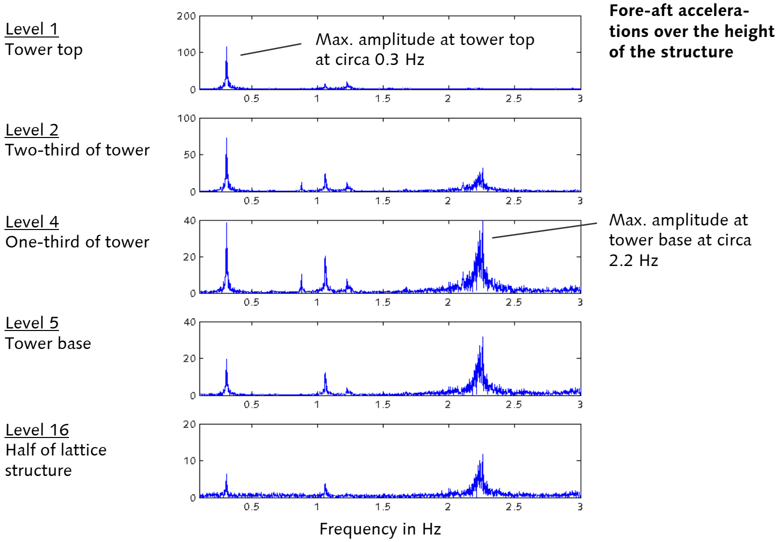

FFT of accelerometers along the height of the structure – fore-aft

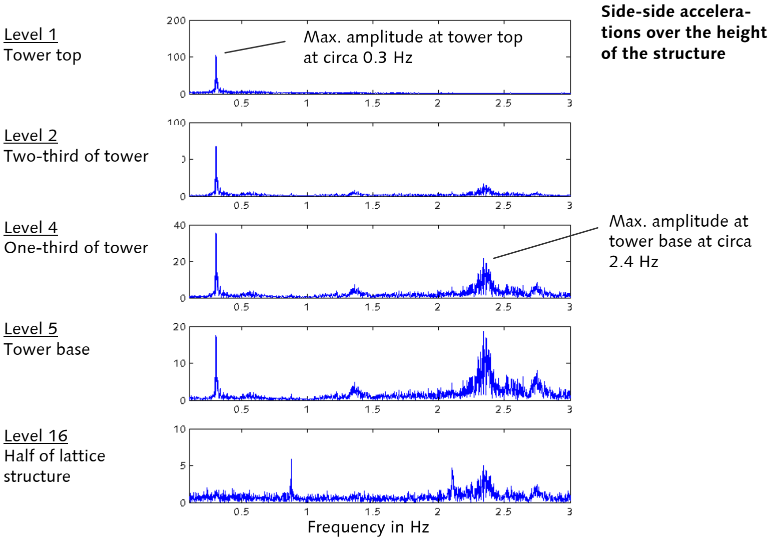

FFT of accelerometers along the height of the structure – side-side

This random inside into the measurement data, given by the frequency-domain depictions in the above-shown figures, allows deriving first conclusions. Clearly visible peaks occur at around 0.3 Hz, both in fore-aft and side-side direction. Their amplitudes are maximal at the tower top, which obviously indicates the first global bending modes.

Another two peaks are between 2.0 Hz and 3.0 Hz. They have their maxima at the tower base, whereas the corresponding amplitudes at the tower top are small. Most likely, these peaks are the second global bending modes of the structure. This interpretation is underlined by the fact that there is a difference in the frequencies for the fore-aft and the side-side direction. The peaks in the fore-aft directions (upper figure) are at circa 2.2 Hz and the peaks in the side-side direction (lower figure) at about 2.4 Hz. This characteristic confirms the prediction from the modal analysis presented in section 5.1.2. In addition, this separation indicates the successful coordinate transformation.

Appendix L – Results of the Local Measurements

Subsequently, measurements that have been carried out at local structural components of the 5 MW wind turbine, described in section 5, are explained. The measurements of a single foundation body and the measurements of the lower crosses of the lattice sub-structure are described.

Measurements of a Single Foundation Body

- Objective of the measurements

Objective of the measurement of a single foundation body is the determination of the eigenfrequency of the first bending mode, defined by the horizontal movement of the concrete body (see figure below). The tests are conducted before the erection of the lattice structure. This study allows obtaining the dynamic characteristics of one separated foundation. Thus, conclusions can be derived concerning the modeling of the stiffness of the upper soil layer that dominates the dynamics of the foundation and the dynamics of certain global bending modes of the structure (see sections 5.1.1 and 5.1.2.).

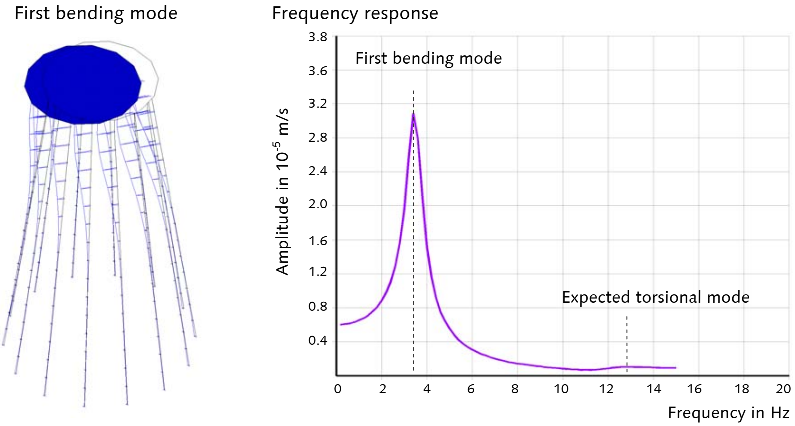
First bending mode

Frequency response

Eigenmode and simulated frequency response of a single foundation body

■ Measurement setup

The excitation of the foundation is realized using the mobile exciter depicted below. The foundation is excited by a sweep function. The excitation is done eccentrically in horizontal direction so that the first bending mode and the first torsional mode can be excited. The horizontal velocity responses are recorded at the center of the structure and at four sides, located by a 90° shift to each other. The measurement setup is shown in the figures below.

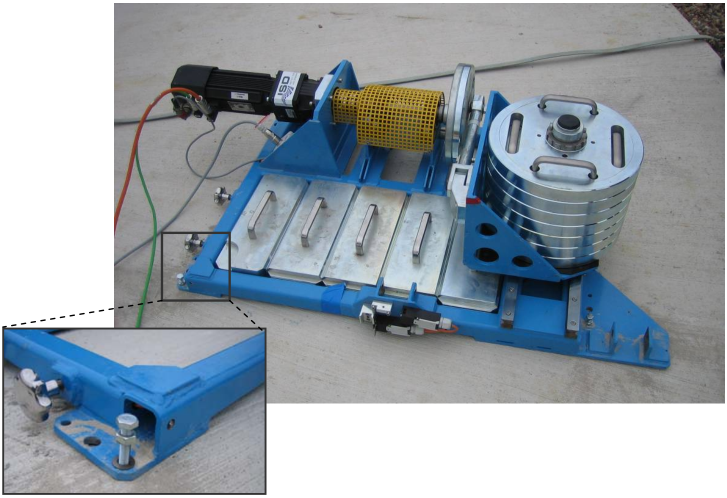

Mobile exciter and application to the structure

Measurement setup for the single foundation body and geophone

The measurement program considers different scenarios. Firstly, the response due to ambient excitation is recorded, which enables the estimation of the ambient influences to the artificially generated excitation. Then, different configurations of the mobile exciter are used in order to pass the frequency range between 1.0 Hz and 14 Hz. This range contains the eigenmodes predicted by the modal analysis. The maximal excitation force is 1,000 N, which is the upper limit of the measurement device.

- Results

The spectral density of one test due to the sweep excitation is depicted in the following figure. Spectral peaks occur at circa 1.8 Hz, at 4.0 Hz - 4.5 Hz, and around 12.0 Hz - 13.0 Hz.

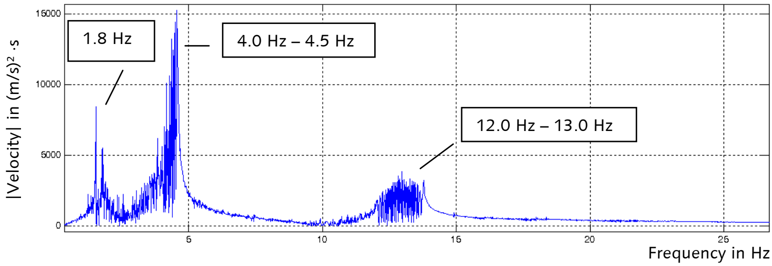

Spectral density at the foundation due to sweep excitation

In theory, a time signal caused by a sweep excitation shows an amplification of the system response at the time when the resonance frequency is passed. The recorded time signal that corresponds to the spectral density (figure above) is shown in the figure below (blue signal). The expected amplitude amplification is poorly developed. A slight increase can be seen in the time range between 0 s to 100 s, whereas a decrease is visible up to the end of the signal at 190 s. Obviously, the sweep excitation force is not able to produce a system response that clearly exceeds the response due to the ambient influences. To support this conclusion and in order to correlate the frequencies either to ambient or to artificial excitations, a band-pass filter is applied to the time signal. The filtered signals for two different band-pass filters are depicted (green signals). Part a) of the figure shows that the frequencies around 1.8 Hz relate to a nearly constant system response, most probably caused by a stochastic excitation from ambient sources. A band-pass filter that remains the time signal containing the frequencies between 4.0 Hz and 4.5 Hz is depicted in part b). The supposed amplification characteristic for a sweep excitation is visible in a time range of 80 s to 140 s. This amplification is most probably caused by resonance between the sweep excitation and the eigenfrequency of the first bending mode. This conclusion is supported by the occurrence of frequencies in the range of 12.0 Hz to 13.0 Hz, where the corresponding torsional eigenmode was predicted.

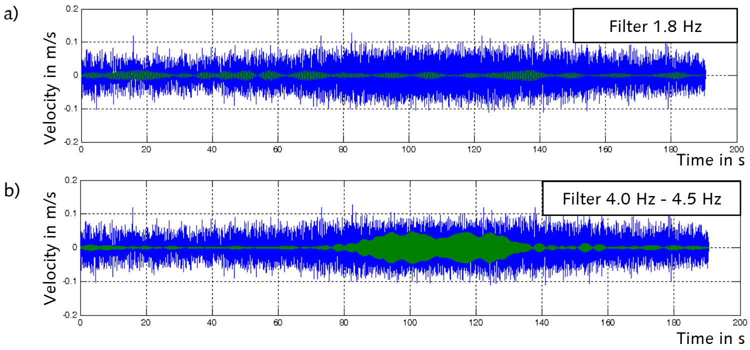

Filtered velocity signal – blue = original, green = filtered

- Conclusions

Exciting the foundation body of approximately 500 tons with the mobile exciter reaches the limit of applicability. The system response due to the sweep sine of maximal 1,000 N does not produce a clearly amplified system response in contrast to the ambient excitations.

Applying a band-pass filter to the recorded response signal allows correlating the measured frequencies to the artificial excitation.

The first bending mode of the structure is measured in a frequency range of 4.0 Hz to 4.5 Hz. The interpretation of this result is supported by the occurrence of frequencies at 12.0 Hz to 13.0 Hz. The distance of the frequencies between the bending mode and the torsional eigenmode equals the prediction from the FE-simulations.

The measured eigenfrequency (4.0 Hz to 4.5 Hz) is higher than the eigenfrequency from the modal analysis (circa 3.5 Hz). The modal analysis bases on the soil stiffness values given in the geological survey [33]. The soil stiffness of the upper layer is suggested to $E_S = 2.5$ MN/m² (see Figure 5.2).

The comparison of the modeled eigenfrequency to the measured eigenfrequencies reveals that the spring stiffness in the FE model that represent the stiffness of the upper soil layer should be increased in contrast to the soil stiffness of the upper layer proposed by the geological survey.

Measurements of the Lower Crosses of the Lattice Structure

- Objective of the measurements

While exciting one cross of bay 5 of the lattice structure (figure below) by applying a pull-back test, a free vibration is induced to all the four crosses of the Bay 5. The corresponding system response contains the eigenfrequencies of this structural part. The test is conducted during standstill to avoid influences from the operation of the wind turbine. The measurement aims on identifying the different closely located eigenfrequencies (see Figure 5.6 to Figure 5.8). The mode shapes are used to distinguish between the several modes. Additionally, the damping ratios are determined.

Right: Sensor location

Left: Structure with crane and tear-bolt system (cable highlighted)

Measurement setup at bay 5

- Measurement setup

In order to record the system responses, two accelerometers are available that are placed in the center of the excited cross (B18) and in the center of one adjacent cross (B17), as depicted in the figure above (right).

The excitation forces used to realize the statical deflection of the cross structure is designed by FE-simulations, which are presented in PAHN AND ROLFES (2011) [79]. Tear-bolts made of gray cast iron (type GG 10) are used (figure below). Gray cast iron is a brittle material that cracks abruptly. The breaking force is defined by a relieved cross-section of the tear-bolt. For redundancy, tear-bolts with breaking forces of F = 5,000 N and F = 8,000 N are used. A series of six tests is conducted for each tear-bolt type. The tear-bolts are fastened to a steel cable via special connecting pieces. On one side, this cable is attached to one cross of the lattice structure. On the other side the cable is pulled by a truck-mounted crane.

a) Steel cable with tear-bolt and connecting pieces

b) Tear-bolts and connecting pieces

Tear-bolt system with steel cable

Assuming the FE-prediction of the local eigenmodes of bay 5 to be correct, the two accelerometers allow identifying the three closely spaced modes assessing their phase relationships. As known from the modal analysis (section 5.1.2), the different mode shapes of bay 5 are characterized by in-phase vibrations of opposing crosses (Figure 5.6), by in-phase vibrations of neighboring crosses (Figure 5.7), and by in-phase vibrations of all crosses (Figure 5.8). The three mode shapes are drawn qualitatively (columns) in the following figure. During the measurements accelerations are recorded at two adjacent crosses. Thus, two mode shape orientations (rows) are possible with respect to the sensor locations. Consequently, the phase relationships between the two accelerometers either show always an out-of-phase vibration, always an in-phase vibration, or alternating phase relationships for a series of tests.

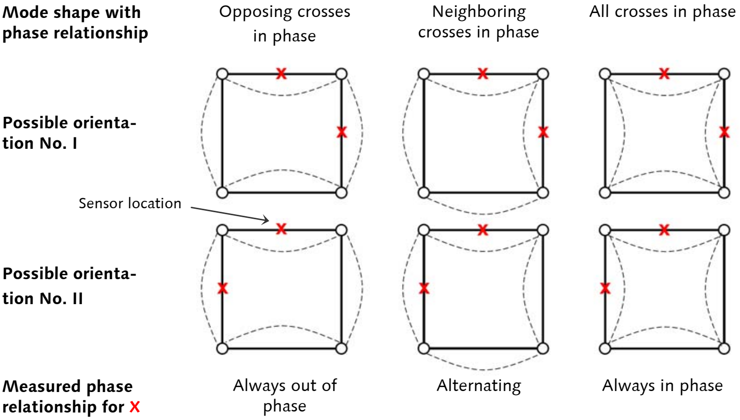

Possible sensor location w.r.t. the phase relationship of bay 5 mode shapes

Results

The time series of two acceleration responses recorded at the excited cross due to an excitation force of F = 5,000 N (left) and F = 8,000 N (right) are depicted below. The artificial excitation exceeds the ambient influences by far and the induced free vibration is clearly visible for both cases.

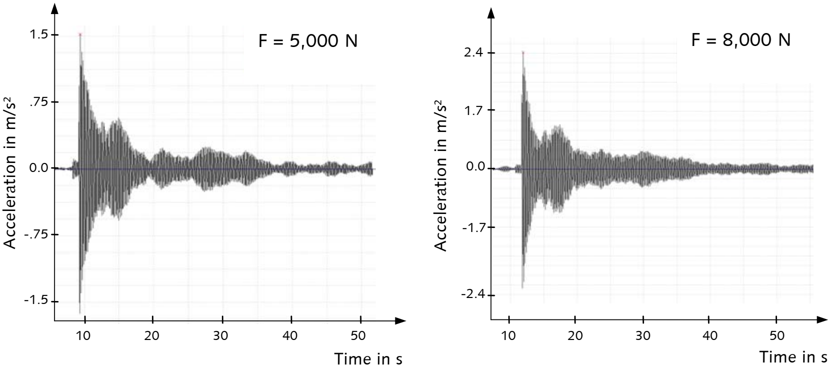

Acceleration signal due to pullback test

A further characteristic that can be derived from the measurement data is the occurrence of beat vibrations, which indicates the presence of closely spaced frequencies. This characteristic was predicted by the FE-simulations. The following figure shows a comparison of a simulated frequency response to a measured one, due to an excitation force of F = 5,000 N. Additionally, the frequency plots are completed by a qualitative graph of the corresponding acceleration signal in the time domain (each in the upper left part). As can be seen, the beat vibrations in the time-domain plots differ. The amplitude decay of the simulation signal is much smaller than the decay in the measurement signal. The reason is the negligence of damping in the simulation.[112]

Comparing the frequency spectra shows a good accordance between the simulated and the measured system response. Amplitude peaks occur between 5.1 Hz and 5.4 Hz in both spectra. Each spectrum is dominated by two peaks, whereas the higher frequency represents the maximal peak. The peaks show broad bases, what either is caused by the presence of further frequencies or by high damping. But, for the investigated structural part only light damping is expected. Comparing the frequencies of the maximal peak indicates a frequency shift of circa 0.2 Hz between the simulation and the measurement. But, this conclusion is only true if both maximal peaks are related to the same eigenmode.

---

[112] Structural damping is not considered, although method-dependent numerical damping is present.

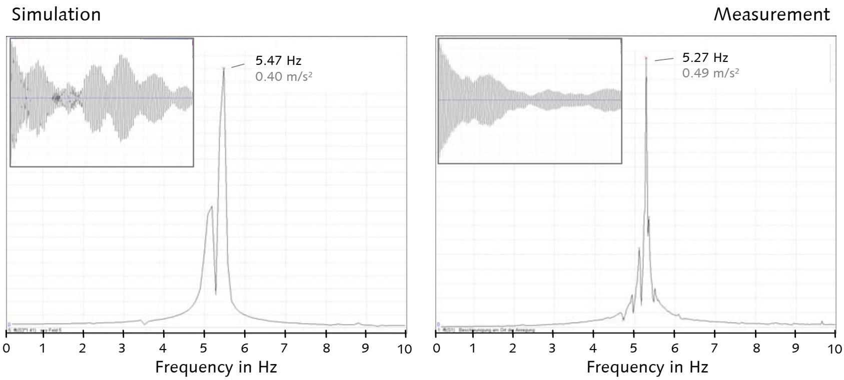

Frequency spectra of the simulation and a measured signal

In order to distinguish between the different frequencies that are present in the response signals, a stepwise identification is done. Firstly, the eigenfrequency, the phase relationship, and the damping are determined in a part of the signal where the free vibration is dominated by only one frequency (figure below, red). With this knowledge, the identification of the complete signal is accomplished (blue).

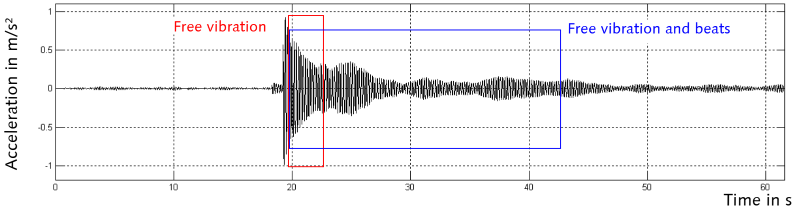

Separation of free vibrations from beat vibrations

The acceleration signals of the sensors B17 and B18 are analyzed. The results of the 12 tests are averaged. The identification reveals three eigenfrequencies that can be determined with a high accuracy, indicated by a small standard deviation between the different results. Additionally, the phase relationships between the two sensors (B17 and B18) are derived, which allows the correlation of the frequencies to the mode shapes. The identification is completed by the damping ratios. The damping ratios are given as percentage of critical damping. The results are summarized in the following table.

Summary of the identified modes of bay 5

No.	Eigenfrequency	Measured phase	Damping ratio	Mode shape
1	5.09 Hz	out of phase	0.37 %	Opposing crosses in phase
2	5.26 Hz	in phase	0.38 %	All crosses in phase
3	5.33 Hz	alternating	0.22 %	Neighboring crosses in phase

- Conclusions

The eigenfrequencies, the mode shapes, and the damping ratios for the lower crosses of the lattice structure are determined due to an artificial excitation. Three closely spaced eigenfrequencies are detected, as it is predicted by the modal analysis. Using the phase-angle relationships between the two sensors, an unequivocal correlation of the frequencies to the mode shapes is possible. Comparing the mode shapes gained by the modal analysis (see Figure 5.6 to Figure 5.8) to the identified mode shapes (table above) shows that there is a mode shape shift between the simulation and the measurement. Both in the simulation and the measurement the mode shape with the smallest frequency is described by an in-phase vibration of opposing crosses. But, the second and third mode shape is shifted. The main reason is seen in the modeling of the connecting-node stiffness, which contains simplifications in the FE model (see section 5.1.2).

As a general conclusion it can be stated that the identification of the eigenfrequencies and mode shapes can be done with a high accuracy. The damping estimation contains higher uncertainties, which is indicated by a higher standard deviation of the damping ratio results. This conclusion is in accordance with the statements derived by ANDERSEN ET AL. (1999) [1] and PEETERS AND DE ROECK (2001) [83].

Appendix M – Estimation of the Aerodynamic Damping for the REpower 5M

Estimation of the aerodynamic damping

The following equation is presented in KÜHN (2001) [58], page 105. This equation is valid for wind turbines with high tip speed ratios, especially near the rated wind speed.

$$D_{aero} = \frac{N_b \cdot \rho \cdot \Omega}{8 \cdot \pi \cdot f_0 \cdot m_0} \cdot \int_{R_{root}}^{R} \frac{dc_L}{d\alpha}\Big|_r \cdot c(r) \cdot r \; dr$$

N_b = 3 - number of rotor blades
ρ = 1.29 kg/m³ - air density
Ω = 0.20 rad/s - rotation speed at rated wind speed
f_0 = 0.31 Hz - eigenfrequency of the first fore-aft mode (result of the modal analysis in section 5.1.2)
m_0 = 528,919 kg - modal mass of the first fore-aft mode (result of the modal analysis in section 5.1.2)
R_{Root} = 3 m - radius to the blade root (see reference [85])
R = 63 m - rotor blade radius (see reference [85])
$dc_L/d\alpha|_r$ = 5.1-5.8 - lift coefficient w.r.t. the angle of attack α (reference [27], page 188)
$c(r)$ - function of the blade-chord length
r - variable along the rotor radius.

GASCH AND TWELE (2005) [27] (page 194) present an estimation for the blade-chord length that bases on the Betz Theory. The blade-chord length c(r) is calculated as follows.

$$c(r) = 2 \cdot \pi \cdot R \cdot \frac{1}{N_b} \cdot \frac{8}{9 \cdot c_A} \cdot \frac{1}{\lambda_A^2 \cdot \left(\frac{r}{R}\right)}$$

R = 63 m - length of the rotor blade
N_b = 3 - number of rotor blades
c_A = 0.8 - lift coefficient, $c_A \approx 0.6\text{-}1.2$ (assumed to be constant)
λ_A = 6 - tip speed ratio for the design
r - variable along the rotor blade length

The result for the estimation of the blade-chord length is depicted in the figure below.

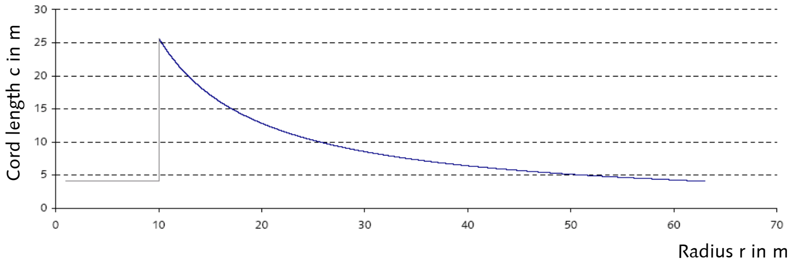

Appendix N – Data Selection for the Eigenfrequency and Damping Identification

Data selection for the eigenfrequency and mode shape identification

Operation state	Data restriction	Number of data sets
Standstill		
0 rpm	Δ Nacelle yaw < 0.05° or > 356° ∅ Wind speed > 3 m/s ∅ Rotor speed < 0.5 rpm ∅ Pitch angle < 90° Δ Pitch angle < 2.2°	19
Power production		
7 rpm	Δ Nacelle yaw < 0.05° ∅ Rotor speed 7.0-7.5 rpm Δ Rotor speed < 1 rpm ∅ Pitch angle < 1° Δ Pitch angle < 0.02°	94
8 rpm	Δ Nacelle yaw < 0.07° ∅ Rotor speed 7.5-8.5 rpm Δ Rotor speed < 2.3 rpm ∅ Pitch angle < 1° Δ Pitch angle < 0.02°	26
9 rpm	Δ Nacelle yaw < 0.03° ∅ Rotor speed 8.5-9.5 rpm Δ Rotor speed < 3 rpm ∅ Pitch angle < 1° Δ Pitch angle < 0.02°	35
10 rpm	Δ Nacelle yaw < 0.04° ∅ Rotor speed 9.5-10.5 rpm Δ Rotor speed < 3 rpm ∅ Pitch angle < 1° Δ Pitch angle < 0.02°	30
11 rpm	Δ Nacelle yaw < 0.07° ∅ Rotor speed 10.5-11.5 rpm Δ Rotor speed < 3.1 rpm ∅ Pitch angle < 1° Δ Pitch angle < 0.5°	84
12 rpm	Δ Nacelle yaw < 0.08° ∅ Rotor speed 11.5-12.1 rpm Δ Rotor speed < 1.4 rpm ∅ Pitch angle < 1° Δ Pitch angle < 3°	19

Data selection for the damping estimation

Operation state	**Data restriction**	**Number of data sets**
Standstill		
0 m/s 0 rpm	∆ Nacelle yaw < 5° ∅ Rotor speed < 0.02 rpm ∅ Pitch angle < 89° ∆ Pitch angle < 3°	42
Power production – between cut-in and rated wind speed		
3.5 m/s 7 rpm	∆ Nacelle yaw < 1° ∅ Rotor speed 7.0-7.1 rpm ∆ Rotor speed < 0.1 rpm ∅ Pitch angle < 1° ∆ Pitch angle < 0.03°	52
5.4 m/s 8 rpm	∆ Nacelle yaw < 1° ∅ Rotor speed 7.75-8.25 rpm ∆ Rotor speed < 0.5 rpm ∅ Pitch angle < 1° ∆ Pitch angle < 0.05°	12
7.3 m/s 9 rpm	∆ Nacelle yaw < 1° ∅ Rotor speed 8.75-9.25 rpm ∆ Rotor speed < 0.5 rpm ∅ Pitch angle < 1° ∆ Pitch angle < 0.02°	19
9.2 m/s 10 rpm	∆ Nacelle yaw < 1° ∅ Rotor speed 9.75-10.25 rpm ∆ Rotor speed < 0.7 rpm ∅ Pitch angle < 1° ∆ Pitch angle < 0.05°	12
11.1 m/s 11 rpm	∆ Nacelle yaw < 3° ∅ Rotor speed 10.90-11.10 rpm ∆ Rotor speed < 0.2 rpm ∅ Pitch angle < 1° ∆ Pitch angle < 0.5°	12
13.0 m/s 12 rpm	∆ Nacelle yaw < 0.05° ∅ Rotor speed 11.80-12.00 rpm ∆ Rotor speed < 0.4 rpm ∅ Pitch angle < 1° ∆ Pitch angle < 4°	10
Power production – between rated and cut-out wind speed		
16.0 m/s 12 rpm	∆ Nacelle yaw < 0.05° ∅ Rotor speed > 12.0 rpm ∅ Wind speed 15.5-16.5 m/s	61
19.0 m/s 12 rpm	∆ Nacelle yaw < 0.05° ∅ Rotor speed > 12.0 rpm ∅ Wind speed 18.5-19.5 m/s	6

Appendix O – Averaged Singular Values and Damping Estimation

Identification of the global eigenfrequencies using averaged singular value functions in standstill and operation

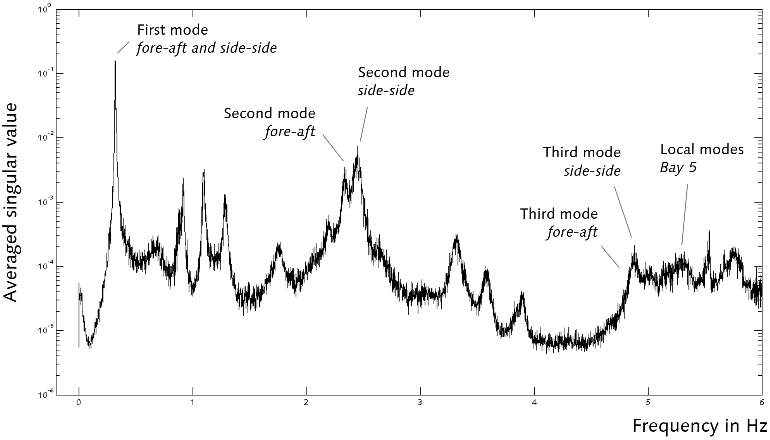

Averaged singular value – 0 rpm

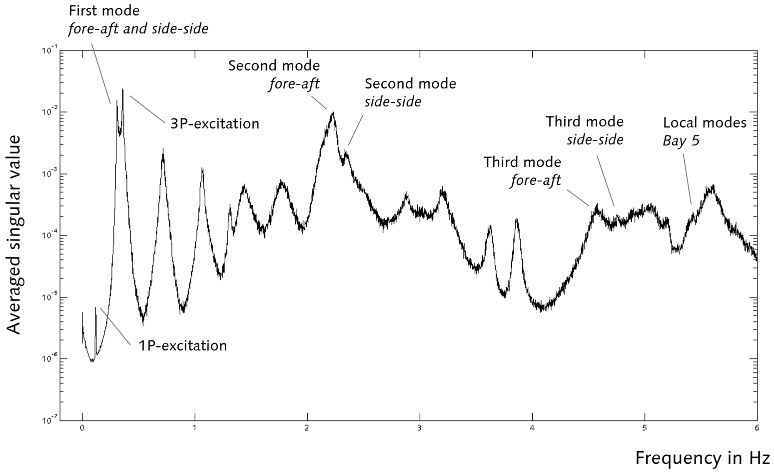

Averaged singular value – 7 rpm

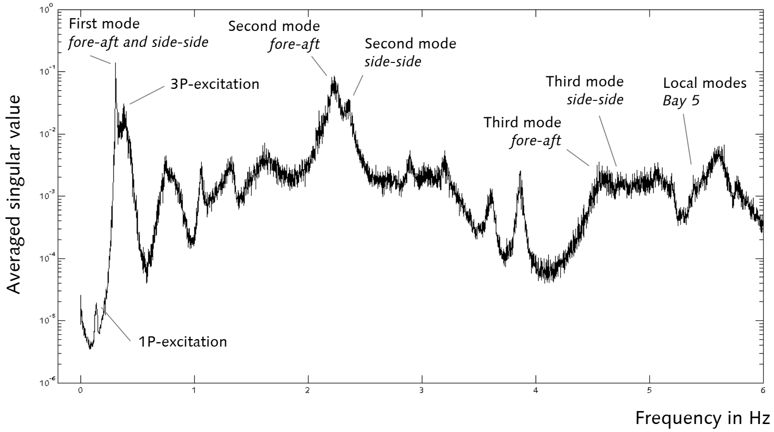

Averaged singular value – 8 rpm

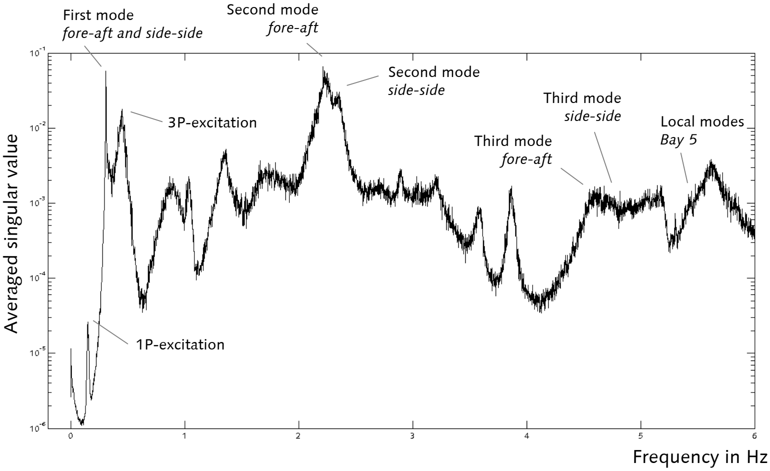

Averaged singular value – 9 rpm

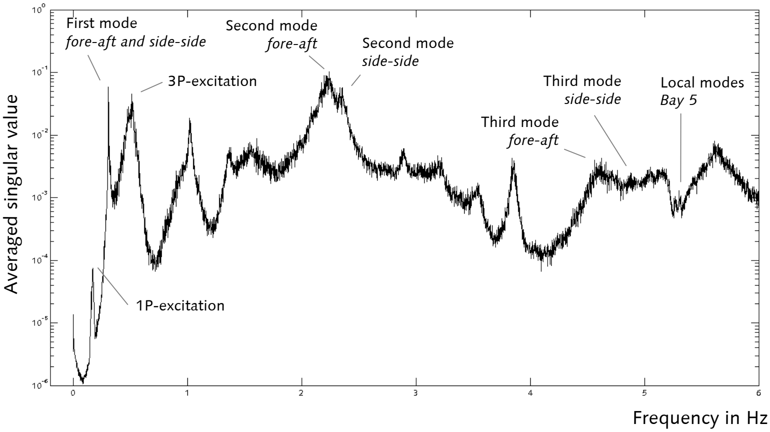

Averaged singular value – 10 rpm

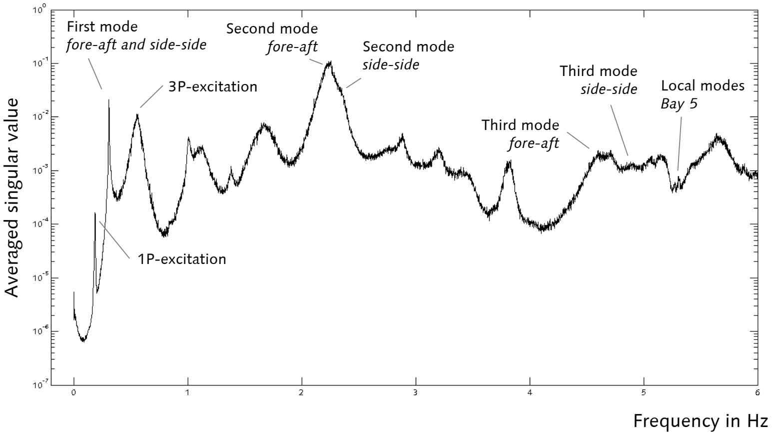

Averaged singular value – 11 rpm

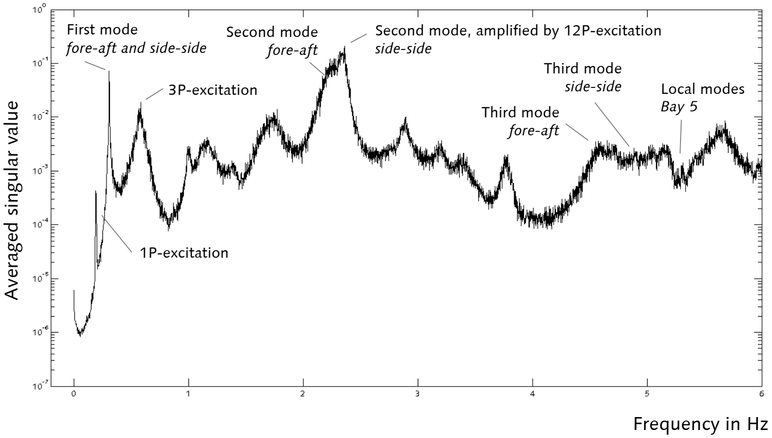

Averaged singular value – 12 rpm

Damping Estimation

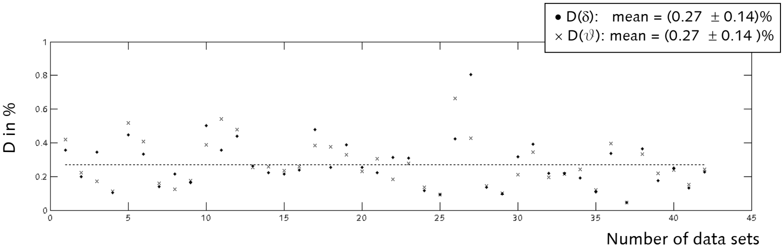

Distribution of estimated damping ratios – 0 rpm at 0 m/s

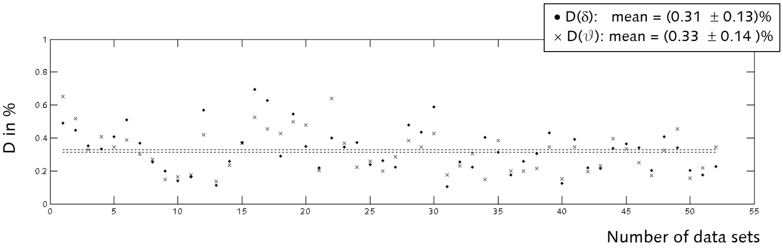

Distribution of estimated damping ratios – 7 rpm at 3.5 m/s

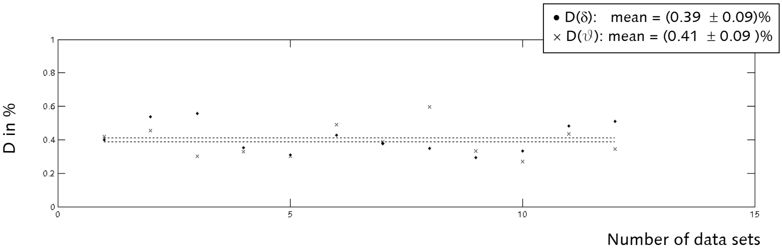

Distribution of estimated damping ratios – 8 rpm at 5.4 m/s

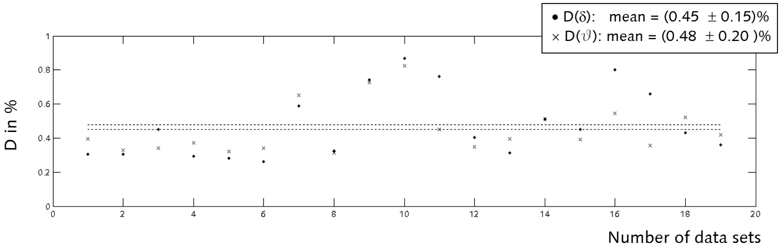

Distribution of estimated damping ratios – 9 rpm at 7.3 m/s

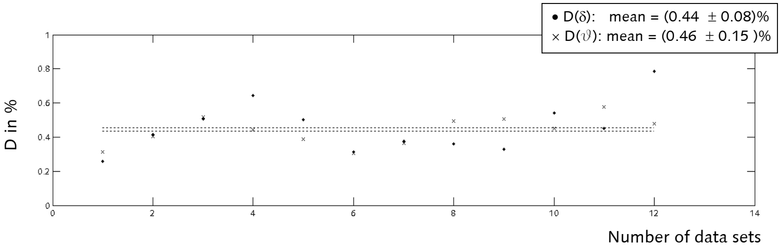

Distribution of estimated damping ratios – 10 rpm at 9.2 m/s

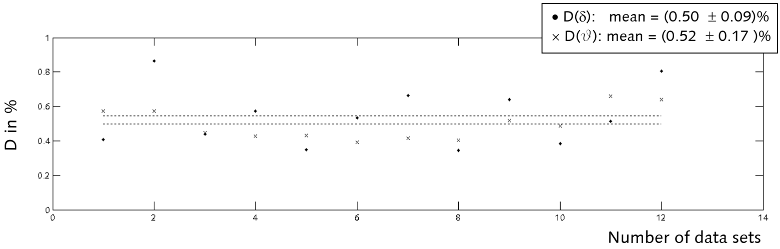

Distribution of estimated damping ratios – 11 rpm at 11.1 m/s

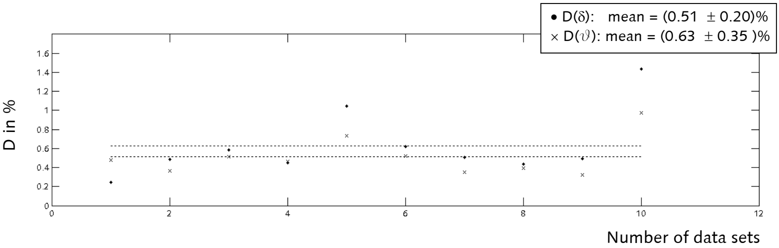

Distribution of estimated damping ratios – 12 rpm at 13.0 m/s

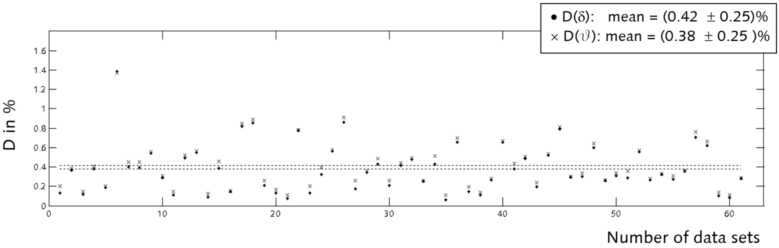

Distribution of estimated damping ratios – 12 rpm at 16.0 m/s

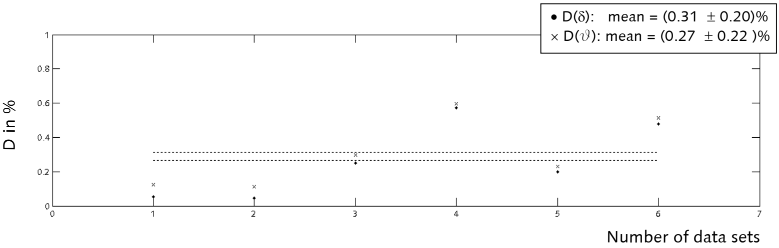

Distribution of estimated damping ratios – 12 rpm at 19.0 m/s

Appendix P – Model Updating Parameters

Sensitivity analysis of the soil parameters

The effects of changing the stiffness of the upper soil layer in the FE model are studied (see also Figure 5.2). To do so, the stiffness of the upper soil layer is changed stepwise. The initial stiffness is based on the recommendations given in the geological survey [33]. The resulting eigenfrequencies for the global bending modes are calculated and depicted in the three diagrams below.

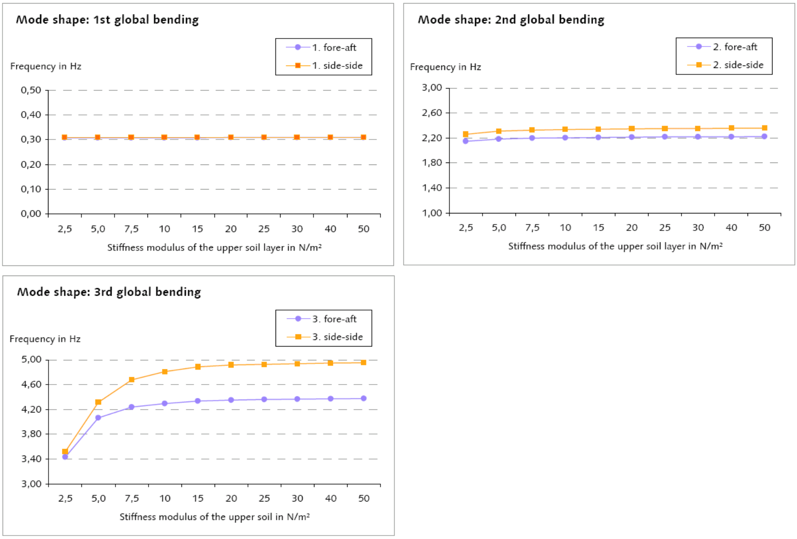

Sensitivity analysis of the stiffness modeling of the upper soil layer

The first and second global bending modes remain unaffected, as clarified by the horizontal graphs. Only the third global bending modes depend on the modeling of the stiffness of the upper soil layer. The eigenfrequencies also increase with increasing stiffness, especially in the range of 2.5 N/m² to ca. 20 N/m². Above 20 N/m², the eigenfrequencies consolidate to constant values, regardless the increase of the stiffness. Hence, the model updating of the stiffness modeling of the upper soil layer is reasonable only for the third global bending modes, within a range up to maximal 25 N/m². The stiffness modeling of the upper soil layer underlies high physical uncertainties, which is the reason for choosing this parameter for the model updating.

Discussion of the model updating parameters

The basic assumption for the model updating process is choosing parameters that are obviously connected with modeling uncertainties. Furthermore, the parameters are varied in a range that is physically meaningful. Both conditions are discussed subsequently for the chosen model updating parameters that are presented in Figure 5.21.

Bending stiffness of the rotor blades: The higher global bending modes as well as the local modes of bay 5 show a high sensitivity in terms of the rotor-blade bending stiffness. Precise structural information of the rotor blades is not available, in order to respect proprietary information. Hence, the modeling of the rotor-nacelle assembly (RNA) is based on reasonable estimations. Consequently, the modeling of the RNA includes uncertainties. For this reason, the variation of the stiffness values is partly allowed up to 50 %.

Mass of the transition piece: The transition piece has a significant influence to the second global bending mode, because it is located at the maximal deflection of the corresponding mode shape. Generally, mass is considered a parameter that can be determined with high accuracy. But, looking at the figure below shows that modeling the circular cross-section by a finite number of shell elements leads to a loss of information. The stiffness remains unaffected, but uncertainties occur in terms of the mass. For this reason, the model updating is achieved by increasing the density of the shell elements. The maximal increase is limited to 10 %, so that the resulting mass of the transition piece lies in the range of the real mass value including the built-in components.

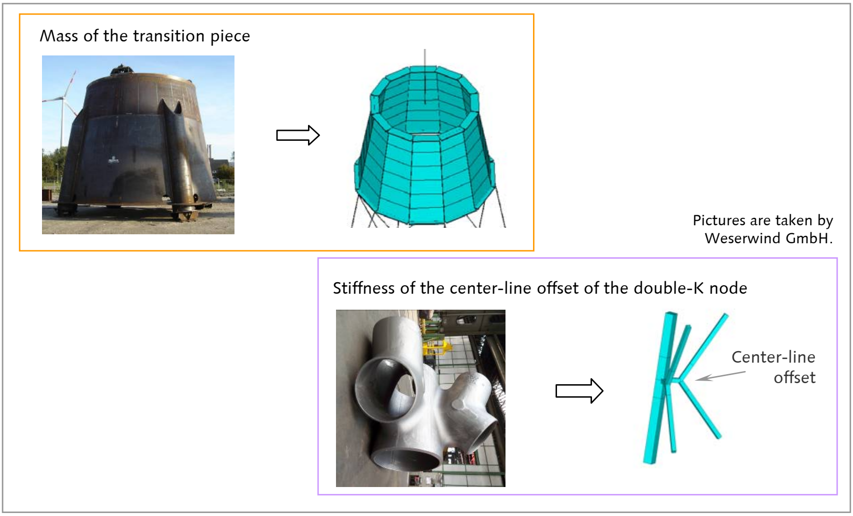
Mass of the transition piece

Pictures are taken by Weserwind GmbH.

Stiffness of the center-line offset of the double-K node

Simplification in the modeling of the transition piece and the double-K node

Stiffness of the center-line offset of the double-K node: The three-dimensional geometry of the double-K node (see figure above) is simplified to a beam construction in the FE model. This simplification requires inserting a beam element representing the center-line offset. The beam element is defined by bending stiffness and axial rigidity, which is adopted from the cross-section of the node legs. As expected, this assumption does not reflect the reality, which allows using the offset stiffness to be used as model updating parameter. In order to estimate the range of the stiffness variation, the results of numerical analysis and full-scale experiments are used, which are published in the final report of the research project OGOWin (2011) [74]. There is no particular limit for the variation of the center-line offset, since this parameter does not represent a physical structural component.

Horizontal stiffness of the upper soil layer: The three soil layers have different load-bearing capacities, with the upper layer showing a significantly lower stiffness. As pointed out in the sensitivity analysis of the soil parameters (see beginning of Appendix P), the model updating of the soil layers can be reduced to the variation of the horizontal stiffness of the upper soil layer. This parameter mainly affects the third global bending modes. The modeled soil-layer stiffness is based on soil properties gained from static in-situ tests, which are usually prone to uncertainties. In comparison to the proposed stiffness parameter from the geological survey the model updating increases the stiffness value, which is in accordance with the dynamic measurements presented in Appendix L.

Additional masses for the platforms, flanges, and built-in components: These additional masses are adjusted in a single-digit percent range.

Appendix Q – FAST with HydroDyn

Changes in FAST source code of version "FAST_v70002b-bjj_AD130000a-bjj_DLL.exe"

Objective:	Output the hydrodynamic loadings at tower nodes in fore-aft direction (surge)
Remarks:	The tower node distribution is considered uniform throughout the flexible tower length. If the number of tower nodes is extended over 99, FAST2ADAMS have to be disabled. In this version, the output of the hydrodynamic loadings is set as a constraint.

Modifications in the "FAST_IO.f90" file

Subroutine "WrOutHdr" (*generates the header for the primary FAST output file*)

- Read in "Module Tower" (to obtain the values of the variables TwrNodes and TwrFlexL)
- Read in "Module EnvCond" (to obtain the values of the variables WtrDpth and WaveHS)
- Set Integer WaveNodes = 0
- Calculate WaveNodes (for calculation see "Remark: Number of tower nodes with hydrodynamic loading")
- Output the number of all tower nodes
- Output the number of the tower nodes with hydrodynamic loading (for checking purposes – calculation of the number of tower nodes with hydrodynamic loading see below "Remark: Number of tower nodes with hydrodynamic loading")
- Add sensor name und unit (two loops over the number of tower nodes – for TabDelim and no TabDelim)

Subroutine "WrOutput"

- Read in "Module Tower" (to obtain the values of the variables TwrNodes and TwrFlexL)
- Read in "Module EnvCond" (to obtain the values of the variables WtrDpth and WaveHS)
- Set Integer WaveNodes = 0
- Calculate WaveNodes (for calculation see "Remark: Number of tower nodes with hydrodynamic loading")
- Adjust the output format for the new number of outputs
- Extend the write command to the load values of FtHydro

Mitteilungen des Instituts für Statik und Dynamik der Leibniz Universität Hannover

1	R. Rolfes/ C. Hühne	Eröffnungskolloquium (Tagungsband)	2005
2	H. Rothert/ M. Kaliske/ L. Nasdala	Entwicklung von Materialmodellen zur Alterung von Elastomerwerkstoffen unter besonderer Berücksichtigung des Sauerstoffeinflusses (DFG-Abschlußbericht)	2005
3	L. Nasdala	Simulation von Materialinelastizitäten bei Nano-, Mikro- und Makrostrukturen – Stabilitätsprobleme, Schädigungs- und Alterungsprozesse bei Kohlenstoffnanoröhren und Elastomerwerkstoffen (Habilitationsschrift)	2005
4	C. Hühne	Robuster Entwurf beulgefährdeter, unversteifter Kreiszylinderschalen aus Faserverbundwerkstoff (Dissertationsschrift)	2006
5	L. Nasdala/ K.-U. Schröder	Finite Element Applications in Structural Analysis (Skript zur Hörsaalübung)	2006
6		Klausuraufgabensammlung, 4. Auflage	2007
7	R. Rolfes/ W.-J. Gerasch/ D. Rotert	Vorlesung Tragwerksdynamik	2007
8	K.-H. Elmer/ K. Betke/ Th. Neumann	Standardverfahren zur Ermittlung und Bewertung der Belastung der Meeresumwelt durch die Schallimmission von Offshore-Windenergieanlagen (Abschlussbericht zum BMU-Forschungsvorhaben)	2007
9	K.-U. Schröder	Zur nichtlinearen Berechnung von Stahlbeton- und Verbundbauteilen (Dissertationsschrift)	2007
10	G. Ernst	Multiscale Analysis of Textile Composites – Stiffness and Strength (Dissertationsschrift)	2008
11	G. Haake	Systemidentifikation mit Autoregressiven Modellen und Validierung numerischer Strukturmodelle bei Offshore-Windenergieanlagen (Dissertationsschrift)	2010

12	T. Grießmann	Dynamisches Tragverhalten von Stahlbetonbiegebalken im Experiment und in der und in der Simulation (Dissertationsschrift)	2011
13	S. Zerbst	Global Approach for Early Damage Detection on Rotor Blades of Wind Energy Converters (Dissertationsschrift)	2011
14	N. Wieczorek	Semiaktive Schwingungsdämpfung leichter Fußgängerbrückenkonstruktionen (Dissertationsschrift)	2011
15	B. Kriegesmann	Probabilistic Design of Thin-Walled Fiber Composite Structures (Dissertationsschrift)	2012
16	J. Reetz	Schadensdiagnose an Tragstrukturen von Windenergieanlagen mit der Multiparameter-Eigenwertproblem-Methode (Dissertationsschrift)	2012
17	R. Rolfes/ D. Rotert	Vorlesung Baustatik	2012
18	R. Rolfes/ D. Rotert	Vorlesung Stabtragwerke	2012
19	H. Krüger	Ein physikalisch basiertes Ermüdungsschädigungsmodell zur Degradationsberechnung von Faser-Kunststoff-Verbunden (Dissertationsschrift)	2012
20	S. Czichon	Multi scale Failure Analysis of Fibre Reinforced Polymers with production induced Porosity Defects (Dissertationsschrift)	2013
21	T. Pahn	Inverse Load Calculation for Offshore Wind Turbines (Dissertationsschrift)	2013